Transonic Unsteady Aerodynamics and Aeroelasticity 1987

NASA

Transonic Unsteady Aerodynamics and Aeroelasticity 1987

Compiled by
Samuel R. Bland
Langley Research Center
Hampton, Virginia

NASA

PREFACE

This two-part document contains text and figures for the papers presented at the Symposium on Transonic Unsteady Aerodynamics and Aeroelasticity — 1987, held at the NASA Langley Research Center on May 20-22, 1987. The Symposium, which reviewed the subject area, was the third such meeting at Langley. The previous workshops were held in 1980 and 1983 and were an outgrowth of a meeting held at Columbus, Ohio in 1978 to assess the state of unsteady aerodynamics for use in transonic flutter analysis.

The papers were grouped in five subject areas, which may be described broadly as:

(1) Transonic small disturbance (TSD) theory for complete aircraft configurations
(2) Full potential and Euler equation methods
(3) Methods for vortex and viscous flows
(4) Aeroelastic applications
(5) Experimental results and cascade flows

The decade since the Columbus meeting has seen the wide acceptance of computational fluid dynamics methods for transonic aeroelastic analysis. In 1978, calculations with the TSD methods for two-dimensional airfoils (especially the NASA Ames LTRAN code and its derivatives) were well established, and the USAF Flight Dynamics Laboratory had initiated development of the first TSD code (XTRAN3) for three-dimensional wings. As demonstrated in the papers from the 1987 meeting contained herein, the TSD methods (the NASA Langley CAP-TSD code in particular) can now be applied to the aeroelastic analysis of complete aircraft. Methods suitable for situations in which small disturbance theory is inadequate are being aggressively pursued.

Future research should follow three main paths:

(1) Development of more exact methods using the full potential, Euler, and Navier-Stokes equations
(2) Evaluation of the TSD methods by detailed comparison with more exact methods and experiment
(3) Detailed pressure measurements and flutter tests on well-defined aeroelastic models.

Samuel R. Bland

CONTENTS

Part 1

SESSION 1

SESSION 2

---

[*]Part 2 is presented under separate cover.

SESSION 5

ATTENDEES

Adams, William M., Jr.	NASA Langley
Amos, Anthony K.	USAF AFOSR
Anderson, W. Kyle	NASA Langley
Appa, Kari	Northrop Corporation
Batina, John T.	NASA Langley
Belk, Dave	USAF AD/AFATL/FXA
Bendiksen, Oddvar O.	Princeton University
Bennett, Robert M.	NASA Langley
Beotehond, A.	Hi Tech
Bland, Samuel R.	NASA Langley
Bodapati, Satya	Naval Postgraduate School
Bohlmann, Jonathan D.	General Dynamics
Borland, Christopher J.	Boeing Military Airplane Co.
Brentner, Kenneth S.	NASA Langley
Carta, Franklin O.	United Technologies Research Center
Carter, James E.	United Technologies Research Center
Cazier, Frank W., Jr.	NASA Langley
Chu, Li-Chuan	PRC
Chaung, Hsin-Kung A.	Old Dominion University
Cunningham, Atlee	General Dynamics
Dixon, Sidney C.	NASA Langley
Durham, Michael H.	NASA Langley
Eckstrom, Clinton V.	NASA Langley
Edwards, John W.	NASA Langley
Fuglsang, Dennis F.	Purdue University
Gibbons, Michael D.	PRC
Giesing, Joesph P.	McDonnell Douglas
Gilbert, Michael G.	NASA Langley
Giles, Gary L.	NASA Langley
Gilyard, Glenn B.	NASA Ames-Dryden
Guruswamy, Guru P.	NASA Ames
Haller, Richard L.	General Dynamics
Hassig, Hermann J.	Lockheed-California Co.
Hess, Robert W.	NASA Langley
Howlett, James T.	NASA Langley
Hu, Hong	Old Dominion University
Huttsell, Larry	USAF AFWAL/FIBRC
Kandil, Osama A.	Old Dominion University
Kaza, Krishna R. V.	NASA Lewis
Kousen, Kenneth A.	Princeton University
Layton, Jeffrey B.	Purdue University
Leishman, J. Gordon	University of Maryland
Levine, Mark S.	Purdue University
Liu, Danny D.	Arizona State University
Mohr, Ross W.	Purdue University
Mook, Dean T.	VPI&SU
Mukhopadhyay, Vivekananda	PRC
Mulville, Dan	NASA Headquarters
Noll, Thomas E.	NASA Langley

Pao, S. Paul	NASA Langley
Peele, Elwood L.	NASA Langley (retired)
Perry, Boyd, III	NASA Langley
Piette, Douglas S.	Lockheed-Georgia Co.
Pitt, Dale M.	McDonnell Aircraft Co.
Pototzky, Anthony S.	PRC
Rash, L. C.	Wyle Laboratories
Rivera, Jose A., Jr.	NASA Langley
Robins, Philip C.	Texas A&M University
Rodden, William P.	Consultant
Rumsey, Christopher L.	NASA Langley
Sandford, Maynard C.	NASA Langley
Sankar, Lakshmi	Georgia Tech
Seidel, David A.	NASA Langley
Shankar, Vijaya	Rockwell International
Shifflette, James M.	Old Dominion University
Shimko, A. V.	Northrop Corp.
Shirk, Michael H.	USAF AFWAL/FIBR
Silva, Walter A.	PRC
Simpson, L. Bruce	USAF AFATL/FXA
Smedfjeld, John	Grumman Aircraft
Smith, Gregory E.	Dynamic Engineering
Soistmann, David L.	PRC
Spence, Peter L.	PRC
Strganac, Thomas W.	NASA Langley
Summers, John C.	NASA Langley
Takallu, Mohammed A.	PRC
Tatum, Kenneth E.	PRC
Thomas, James L.	NASA Langley
Tracy, Maureen B.	PRC
Verdon, Joesph M.	United Technologies Research Center
Vinh, Lam-Son	NASA Langley
Vretakis, Nicholas G.	USAF AFSCLO
Watson, Ralph D.	NASA Langley
Weatherill, Warren H.	Boeing Commercial Airplane Co.
Webster, Rosa C.	NASA Langley
Whitfield, David L.	Mississippi State University
Whitlow, Woodrow, Jr.	NASA Langley
Wieseman, Carol D.	NASA Langley
Wynne, Eleanor C.	NASA Langley
Yates, E. Carson, Jr.	NASA Langley
Yurkovich, Rudy	McDonnell Aircraft Co.
Zeiler, Thomas A.	PRC

UNSTEADY AERODYNAMICS
AND
AEROELASTIC RESEARCH AT AFWAL

L. J. Huttsell
and
W. A. Sotomayer
Air Force Wright Aeronautical Laboratories
Structures Division (AFWAL/FIBRC)
Wright-Patterson AFB, Ohio

OUTLINE

The presentation (Figure 1) will be broken into two areas: (1) transonic unsteady aerodynamic development of the XTRAN3S code and (2) some other aeroelastic research and development within the Structures Division (Air Force Wright Aeronautical Laboratories, Flight Dynamics Laboratory). The first area will cover historical development of the XTRAN3S program, the Joint AF/NASA unsteady aerodynamics program to expand and improve this code, and the new efforts for applications and improvements of XTRAN3S. The second area will cover three aeroelastic research and development efforts that may be of interest to this group. These efforts are (1) an Analog and Digital Aeroservoelasticity Method called ADAM, (2) an Automated STRuctural Optimization System called ASTROS, and (3) a new effort for improved flight loads predictions.

- **TRANSONIC UNSTEADY AERO DEVELOPMENT - XTRAN3S**

  o HISTORICAL DEVELOPMENT
  o JOINT AF/NASA PROGRAM
  o CURRENT RESEARCH AND APPLICATIONS

- **AEROELASTIC RESEARCH AND DEVELOPMENT**

  o ANALOG AND DIGITAL AEROSERVOELASTICITY METHOD
  o AUTOMATED STRUCTURAL OPTIMIZATION SYSTEM
  o FLIGHT LOADS PREDICTION METHOD

Figure 1

HISTORICAL DEVELOPMENT OF XTRAN3S

Figure 2 gives a roadmap showing the development of the XTRAN3S code. In 1974, Ballhaus and Steger published a report (NASA TM X-73,082) on fully implicit finite difference schemes for 2-D unsteady transonic flows that permitted time step selection based on accuracy rather than stability considerations. This led to the development of the LTRAN2 code which used a conservative, implicit finite-difference algorithm to integrate the non-linear, low-frequency, transonic, small-disturbance equation in time. The XTRAN3S (eXact TRANsonic 3-dimensional aerodynamics with Structural effects) code is an extension of the Ballhaus/Goorjian procedure used in LTRAN2. The XTRAN3S code was developed by Boeing under an AFWAL contract. Both NASA Ames and Langley provided valuable consultation during the contract and worked to extend and improve the code.

In 1985, a joint AFWAL and NASA (Ames and Langley) effort was initiated to extend and improve XTRAN3S and to explore promising long-term computational fluid dynamics (CFD) methods. All agreed to work to achieve a code to satisfy the needs of future Air Force fighters by the 1989 time period. The next few charts will give more details on each participant's efforts on XTRAN3S. Details of current applications and research will also be presented on a later chart.

NASA Langley's efforts on XTRAN3S and their in-house research with Approximate Factorization (AF) algorithms led to the recent development of their transonic small disturbance code called CAP-TSD. There will be several papers presented at this symposium on this code.

Figure 2

3
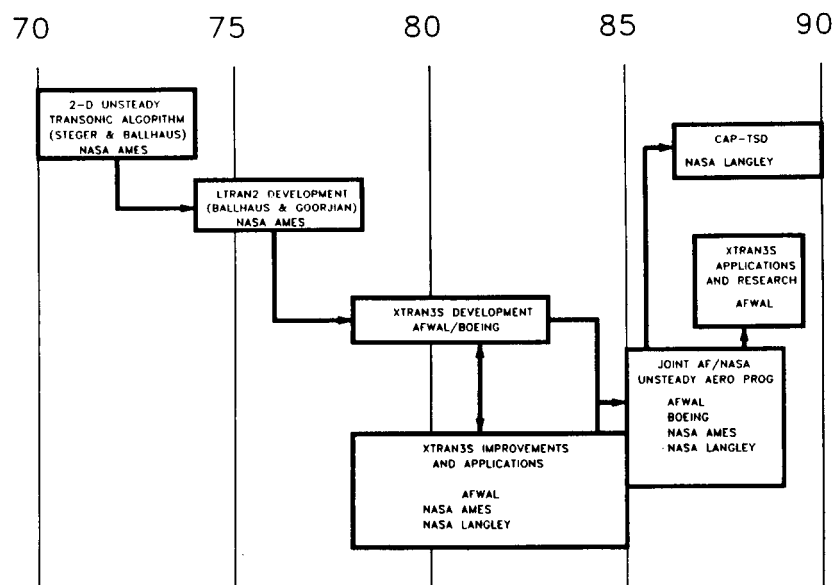
The XTRAN3S code has been used at AFWAL for steady and unsteady aerodynamic calculations and for dynamic aeroelastic analysis. Figure 3 lists some of past and on-going efforts with XTRAN3S at AFWAL. In-house unsteady aerodynamic applications have been made for the LANN wing, F-5 wing, and F-5 wing with control surface. Presently, W. Sotomayer is investigating non-reflective far-field boundary conditions for XTRAN3S. Another on-going effort involves aeroelastic calculations for the Cornell 45 degree swept wing which will be discussed in more detail on the next chart.

XTRAN3S Applications and Improvements

AFWAL FDL In-House

- F-5 Wing and Wing-Control Surface
- LANN Wing
- Non-Reflecting Boundary Conditions
- Aeroelastic Calculations for Cornell Wing

Figure 3

AEROELASTIC CALCULATIONS FOR CORNELL WING

Subsonic and supersonic aeroelastic calculations have been conducted by AFWAL for the Cornell 45° Swept Wing shown in Figure 4. A set of dynamically similar models of different mass and stiffness was tested by Cornell Aeronautical Laboratory in 1956, and the non-dimensional flutter trend versus Mach number for various mass ratios are shown in the figure. The results of this in-house effort by Pendleton and French will be presented at the AIAA Aircraft Design Conference in September 1987.

Transonic aeroelastic calculations are underway using the XTRAN3S code. The linear and nonlinear XTRAN3S calculations at M=0.8 agree very well with the doublet lattice predictions and with test data. Additional calculations will be performed in the range of M=.95 to M=1.13 to define the transonic dip and to compare with test data.

CORNELL 45° SWEPT WING FLUTTER TRENDS
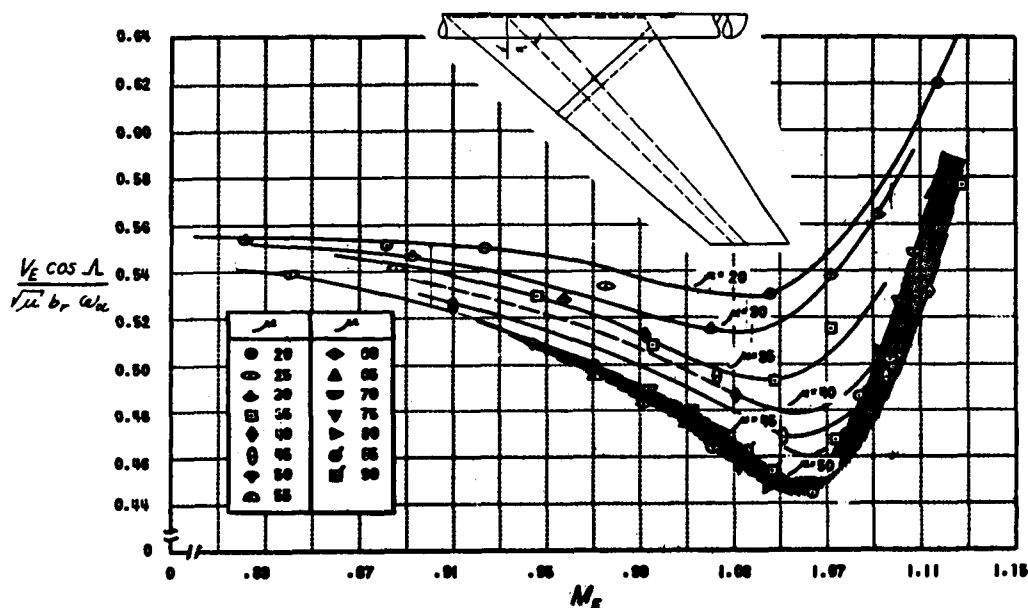
Figure 4

NASA Ames

NASA Ames has been active with the XTRAN3S program since its early development. An outline of their efforts is presented in Figure 5. Their applications include F-5 wing and F-5 wing with tip store, aeroelastic analysis of the B-1 wing, and other analyses for research configurations. Under a NASA Ames contract, Boeing developed the procedure for including inviscid/viscous interaction for three-dimensional transonic flow. NASA Ames developed algorithm improvements and gridding for wing/tip store and a full-volume fuselage capability. Supersonic boundary conditions were recently added to the XTRAN3S code by NASA Ames.

XTRAN3S Applications and Improvements

NASA Ames

- Applications (B-1, F-5, etc.)
- Algorithm Improvements
- Wing/Tip Store Capability
- Full-Volume Fuselage Capability
- Supersonic Capability

Figure 5

NASA Langley

As shown in Figure 6, NASA Langley has also been very active in the application and improvement to the XTRAN3S code. Their applications include the F-5 wing, RAE wing-fuselage, wing/canard, and several research wings. Their improvements include algorithm development, wing/fuselage capability, and wing/tail or canard/wing capability. They have also provided programmer support and managed the Boeing contract for wing/pylon/nacelle capability. Presently they are working on the development and validation of their new code called CAP-TSD (Computational Aeroelasticity Program - Transonic Small Disturbance), utilizing an Approximate Factorization (AF) scheme.

XTRAN3S Applications and Improvements

NASA Langley

- Applications (F-5, RAE Wing-Fuselage, Wing/Canard, etc.)
- Algorithm Improvements
- Wing/Fuselage and Wing/Tail Capability
- Boeing Contract for Wing/Pylon/Nacelle Capability
- Programmer Support

Figure 6

CURRENT RESEARCH AND APPLICATIONS

In June 1986, AFWAL initiated a PRDA (Program Research and Development) for applications and improvements to XTRAN3S. We anticipate three contracts will result from this PRDA (Figure 7). One contract will involve improved unsteady calculations using available experimental pressure data. The second contract will integrate existing capabilities for wing/fuselage, wing/pylon/nacelle, and supersonic analysis into an improved version of XTRAN3S. Applications to a fighter with stores and a transport configuration will be performed to validate this code. The third contract will involve applications of both XTRAN3S and CAP-TSD to a fighter configuration with flight test data.

- UNSTEADY PERTURBATIONS AROUND AN
     EXPERIMENTAL MEAN

- XTRAN3S INTEGRATION, IMPROVEMENT, AND
     APPLICATION

     o WING/FUSELAGE
     o WING/PYLON/NACELLE
     o SUPERSONIC
     o A-6 AND TRANSPORT APPLICATION

- XTRAN3S AND CAP-TSD (NASA LANGLEY)
     APPLICATIONS AND COMPARISON WITH TEST FOR
     FIGHTER CONFIGURATIONS

Figure 7

Structural dynamics, flight controls, and unsteady aerodynamics are independent technologies for the purpose of research, but for modern aircraft design, early simultaneous consideration of these disciplines is necessary to prevent aeroservoelastic problems. Without early interaction between these technologies (Figure 8) in the design process, aircraft with high-gain flight control systems may be driven unstable as a result of the feeding back of structural displacements. Several fighters, bombers, and a target drone have experienced such aeroservoelastic problems. Currently, extensive analyses and tests are required to prevent adverse control system/structural interactions. Aircraft design trends indicate that vehicles of the future will be even more flexible, emphasizing the need for integrated design and analysis procedures to obtain the desired performance.
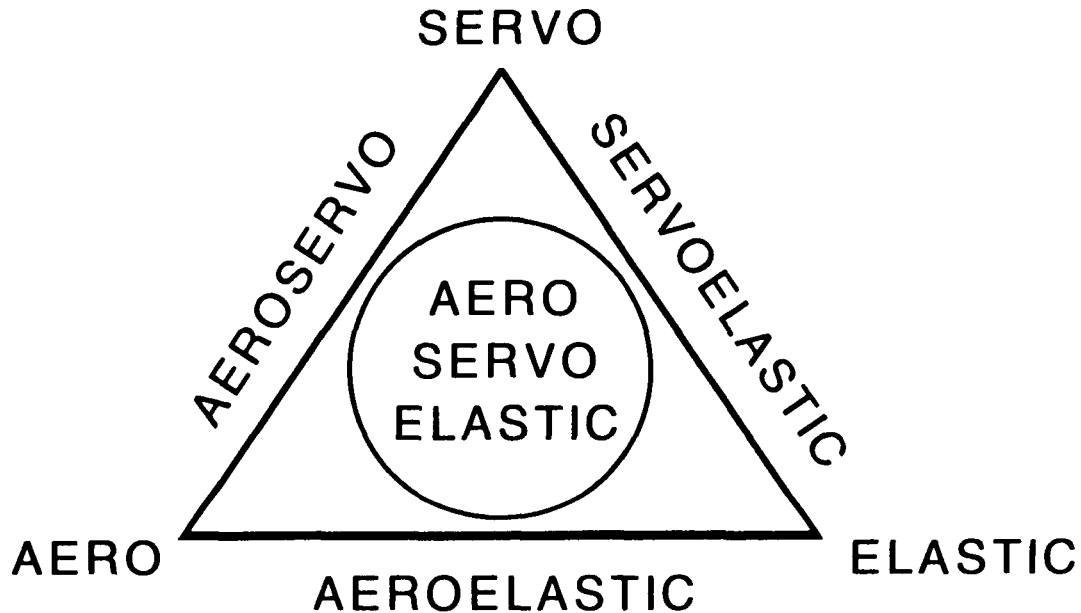
Figure 8

ANALOG AND DIGITAL AEROSERVOELASTIC METHOD (ADAM)

The Flight Dynamics Laboratory is developing techniques to analyze aircraft with either analog or digital flight control systems and is incorporating these into a new in-house analysis computer program called ADAM (Analog and Digital Aeroservoelasticity Method). The objectives of this effort are to improve the in-house capability for performing analyses, to develop the capability to audit ongoing aircraft development programs and to enable the evaluation of proposals of advanced aircraft designs from an aeroservoelastic consideration. A secondary objective is to establish a closer working relationship and to improve communication among structural dynamics, controls, and aerodynamics engineers.

ADAM is capable of analyzing the aeroservoelastic characteristics of complete aircraft in either the longitudinal or lateral/directional modes. The program is currently operational and will be continually improved to add the most desirable features for performing aeroservoelastic analysis. ADAM is now capable of analyzing aircraft stability for analog multi-input/multi-output (MIMO) control systems and for digital systems to a limited extent. The program is being modified to fully account for digital systems. For analyses involving analog control systems, classical root locus criteria are employed. If a digital control system is involved, discretization techniques are used. Figure 9 presents the operational flow diagram for ADAM.
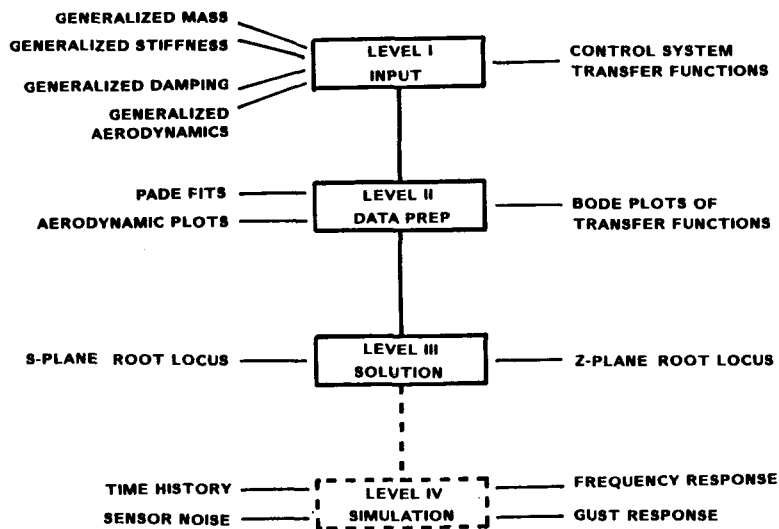
Figure 9

DEVELOPMENT OF AN "AUTOMATED STRUCTURAL OPTIMIZATION SYSTEM' (ASTROS)

The goal of this effort (Figure 10) is to combine modern optimization algorithms and proven multidisciplinary analysis programs with the latest computer software advances. The resulting state-of-the-art structural design tool can help meet performance requirements of future aerospace vehicles with the payoff in least weight and/or cost. A procedure for preliminary structural design or modification of aircraft and spacecraft is being developed.

ASTROS
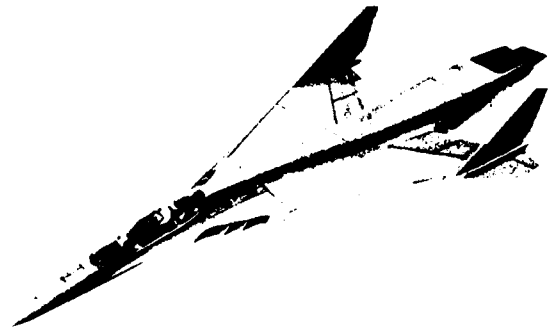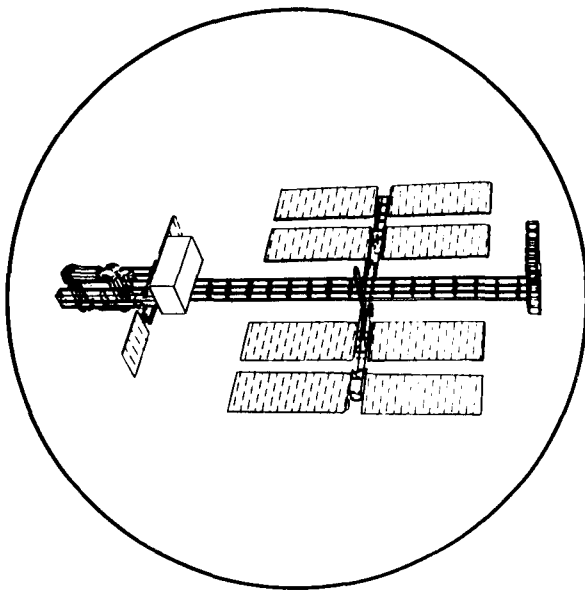
AIR FORCE STRUCTURAL OPTIMIZATION SYSTEM

Figure 10

The computer code for Automated STRuctural Optimization System (ASTROS) has an executive system and an engineering data base management system to support six technical (engineering) modules (Figure 11). The engineering modules include Structures and Dynamics, Air Loads (Subsonic and Supersonic), Aeroelasticity, Sensitivity Analysis, Optimization, and Control Response.

The Structural Analysis is based on the finite element method, incorporating static and thermal loads, buckling analysis, eigenvalue analysis, and dynamic response. The Air Loads module calculates static air loads using Woodward aerodynamics. The Aeroelasticity module calculates the unsteady aerodynamic forces using the subsonic doublet lattice and supersonic potential gradient methods, and calculates flutter speed using the p-k method. In addition to flutter, ASTROS can consider static divergence, control surface effectiveness, and roll effectiveness as design criteria. The goal of the Optimization module is to produce an optimum design starting from an arbitrary initial design, while satisfying all the requirements imposed by the constraints. The Control Response module determines the structural response to control input for the final design.

ASTROS is currently being tested in-house in anticipation of the final code delivery in March 1988. The program is proving useful not only for structural optimization, but also for its capability to do any combination of static or dynamic structural analysis, air loads, or flutter in an analysis mode.

Engineering Disciplines
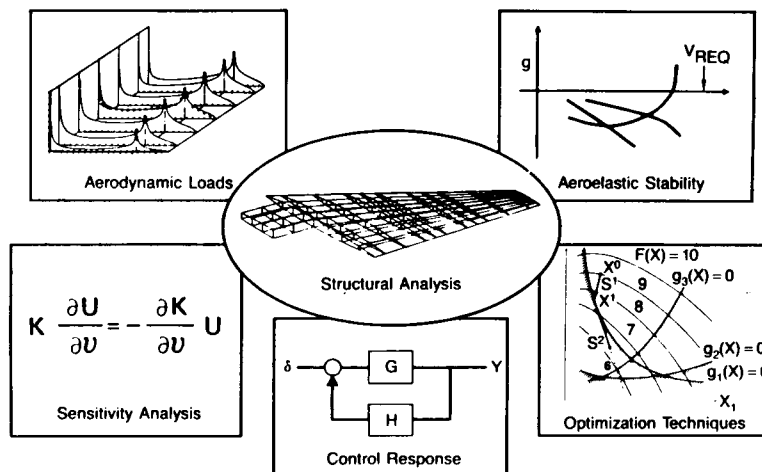
Figure 11

FLIGHT LOADS PREDICTION METHODS FOR FIGHTER AIRCRAFT

The prime motivator that has led to the significant progress in Computational Fluid Dynamics (CFD) for aircraft has been the desire to accurately predict aerodynamic flow field so that aerodynamic performance can be improved and accurate prediction of lift and drag can be obtained. These same advances can improve predictions of structural loads.

The objective of this effort is to apply advanced CFD methods to structural loads calculations (Figure 12). These advanced CFD methods are needed at high angles of attack where separation may occur and in the transonic flight regime where shock waves may significantly affect the loads. The approach is to utilize a proven CFD method coupled with finite element structural analysis software so that loads can be calculated for an elastically deformed structure.

Lockheed-Georgia was the winner of this competitive procurement. The 3-year contract is expected to start in May 1987. The CFD method that Lockheed will use is a full Navier-Stokes flow solver in conjunction with a grid generator that will generate grids about realistic 3-dimensional aircraft. Five (5) months after contract start, Lockheed will deliver an interim version of the software which will calculate the flow field about rigid generic wing/body combination. This will be run on the Cray XMP 12 at Wright Patterson and the Cray XMP 48 at NASA Ames. The AFWAL contact is Mr Elijah Turner, (513) 255-6434 or Autovon 785-6434.

OBJECTIVE: DEVELOP CFD AEROELASTIC LOADS
ANALYSIS CODE FOR SEPARATED FLOW

- FULL NAVIER-STOKES
- 2ND-ORDER ACCURATE STEADY/UNSTEADY
- 3-D AIRCRAFT

APPROACH:

- COUPLE EXISTING CFD FLOW SOLVER WITH FINITE ELEMENT STRUCTURAL ANALYSIS SOFTWARE

- VALIDATE CODE

ANTICIPATED COMPLETION: MAY 1990

Figure 12

CONCLUDING REMARKS

An efficient and accurate transonic unsteady aerodynamic method is needed for predicting flight loads, flutter, and aeroservoelastic stability for advanced aircraft. There have been new developments and many improvements to older codes. XTRAN3S which was featured at the last workshop, has been improved and will be a useful code for the near-term. However, to predict th unsteady aerodynamics for high performance maneuvering aircraft, the Euler/Navier-Stokes codes must be extended and improved for complex three-dimensional configurations. The long-term goal is development of Euler/Navier-Stokes unsteady aerodynamic methods for aeroelastic analysis (Figure 13).

- AN EFFICIENT & ACCURATE TRANSONIC UNSTEADY AERO METHOD IS NEEDED FOR ADVANCED AIRCRAFT.

- XTRAN3S WILL CONTINUE TO BE USED IN THE NEAR-TERM.

- AN AIR FORCE LONG-TERM GOAL IS DEVELOPMENT OF EULER/NAVIER-STOKES UNSTEADY AERO METHODS FOR AEROELASTIC ANALYSIS.

Figure 13

EXTENSIONS AND IMPROVEMENTS OF
XTRAN3S

C. J. Borland
Boeing Military Airplane Co.
Seattle, Washington

SUMMARY

This paper will summarize recent work that has been performed under
a NASA Langley Contract NAS1-17864, "Additional Development of the XTRAN3S
Computer Program." Work on this code, for steady and unsteady aerodynamic
and aeroelastic analysis in the transonic flow regime, has concentrated in
four areas:

1) Maintenance of the XTRAN3S code, including correction of errors,
   enhancement of operational capability, and installation on the
   Cray X-MP system at Wright-Patterson Air Force Base;

2) Extension of the vectorization concepts in XTRAN3S to include
   additional areas of the code for improved execution speed;

3) Modification of the XTRAN3S algorithm for improved numerical
   stability for swept, tapered wing cases and improved computa-
   tional efficiency;

4) Extension of the wing-only version of XTRAN3S to include pylon
   and nacelle or external store capability.

● **MISCELLANEOUS PROGRAM CORRECTIONS & ENHANCEMENTS**

● **IMPROVED VECTORIZATION OF XTRAN3S**

● **ALGORITHM IMPROVEMENT**

● **DEVELOPMENT OF WING/PYLON/STORE CAPABILITY**

MISCELLANEOUS PROGRAM CORRECTIONS

This figure lists the various UPDATE correction sets for correction of errors in the XTRAN3S code. These correction sets are to be applied to BCS Version 1.6 (equivalent to Langley Version 1.5) of the XTRAN3S code.

UPDATE NAME	FUNCTION
EXTLOFT	CORRECTS LOFTING PROCEDURE FOR EXTRAPOLATION OF AIRFOIL DATA
VISCORR	CORRECTS ERROR IN WEDGE PARAMETER DEFINITION
FIXPROMAT	CORRECTS DATA INPUT ERROR FOR INERTIA MATRIX
MISCFIX	CORRECTS GEOMETRY DEFINITION ERROR, MODIFIES CPRESS AND CFOMO TO ACCOUNT FOR MODIFIED GRID, AND VARIABLE DIMENSION ERROR IN ZSWEEP
ENCODE	CORRECTS LABELING ERROR IN TIME HISTORY OUTPUT
VECTCORR	CORRECTS INITIALIZATION ERROR IN VECTORIZATION
PARMGEO	PROVIDES VARIABLE DIMENSION FOR NUMBER OF POINTS ON AIRFOIL

MISCELLANEOUS PROGRAM ENHANCEMENTS

This and the following figure list the UPDATE correction sets for
improvement of XTRAN3S operational features. This group of correction
sets, plus the previous list of error correction modifications, constitute
upgrade of the XTRAN3S code from Version 1.6 to Version 1.10.

| UPDATE NAME	FUNCTION
BCS17	ALLOWS ALTERNATE INPUT FILE FOR AEROELASTIC DATA AND ADDS SELECTIVE DEGREE-OF-FREEDOM MATRIX
CONTROL	ADDS 2 SOLUTION TASKS: (A) STATIC RIGID ANALYSIS WITH CONTROL SURFACE DEFLECTION (B) STATIC AEROELASTIC ANALYSIS WITH CONTROL SURFACE DEFLECTION
INVERR	ADDS OUTPUT OF AEROELASTIC DATA
TASKCORR	UPDATES DOCUMENTATION AND LOGIC FOR CONTROL UPDATE
INTEQM	ADD OPTION FOR INTEGRATION OF EQUATIONS OF MOTION FOR ZERO AIR FORCES

UPDATE NAME	FUNCTION
NEWBL	REMOVES EFFECT OF SHOCK SWEEP ON BOUNDARY LATER CALCULATION
SHOCKFIX	PROVIDES PROPER SHOCK PLACEMENT FOR NEWBL
VERS110	UPDATES PROGRAM BANNERS TO VERSION 1.10
WRTWRNS	ADDS ADDITIONAL ERROR DIAGNOSTICS
WPAFB1 WPAFB2	UPDATES FOR INSTALLATION AT WPAFB.

IMPROVED VECTORIZATION OF XTRAN3S

The original version of XTRAN3S was developed using the CDC 7600 computer.
During the code development period, advanced vector machines, such as the
VPS-32 and CRAY-1S and later the CRAY X-MP became available. The code was
adapted to operate on these machines, but only minimal changes to the code
were performed to take advantage of "implicit" vectorization, i.e., those
portions of the code that could easily be adapted to vector computation
through the existing nature of the computational algorithm.

Later studies with a pilot code version of XTRAN3S, operational on the
CRAY-1S, showed that at least a factor of two improvements in computational
efficiency could be achieved by rearrangement of operations to permit a
larger degree of implicit (or automatic) vectorization. (This represents a
speed-up factor of almost five compared to an unvectorized or scalar code
operating on the same machine.) These concepts are generally applicable,
but not directly transportable, to the VPS-32 version of the code, since
VPS-32 requires longer vectors than the CRAY-1S to achieve improved
efficiency when compared with scalar computations. The improved
vectorization scheme has now been implemented on the CRAY X-MP in Version
1.10 of XTRAN3S.

In this section of the presentation the original algorithm will be
described with respect to its implications for vectorization. Then the
modifications necessary to achieve a higher degree of vectorization on the
CRAY X-MP will be discussed.
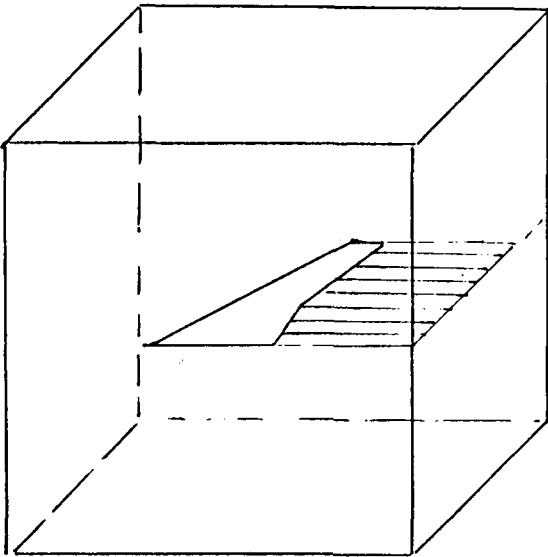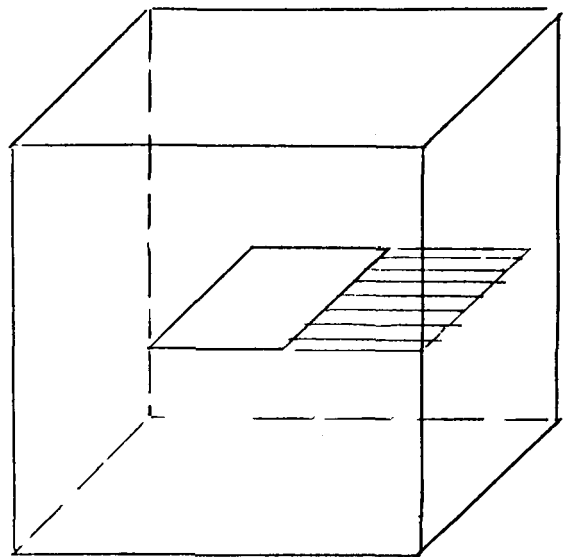
PHYSICAL SPACE   COMPUTATIONAL SPACE

ORIGINAL ALGORITHM STORAGE SCHEME (Version 1.5)

In the original version of XTRAN3S, the equations for the X-sweep are solved sequentially for each Y mesh point, with a constant Z mesh point location. Thus for the default values of $N_X = 60$, $N_Y = 20$, $N_Z = 40$, 20 equations of length 60 are solved for each X-Y plane. Then, for the same X-Y plane, the Y-sweep equations (60 equations of length 20) are solved sequentially in the downstream (increasing X) direction due to the presence of the backward spatial or "upwind" difference approximation to ϕ_{xt}. This process is then repeated for the next X-Y plane in the increasing Z direction. The Z-sweep is performed by accessing the data, formulating the equations, and solving for each X-Z plane sequentially in the increasing downstream direction, with the process then repeated for the next plane in the increasing η direction. Since solutions of the Z-sweep equations, ϕ^{n+1}, are dependent on ϕ^n, ϕ^{n-1} and the solution of the Y-sweep equations $\tilde{\phi}$, but not on the solutions to the X-sweep equations, $\bar{\phi}$ need not be stored in a three-dimensional array.

X-SWEEP

$\phi^{n\cdot} \longrightarrow \tilde{\phi}$

SOLVE 20 EQUATIONS OF LENGTH 60
REPEAT 40X
(EQUATIONS ARE INDEPENDENT)

Y-SWEEP

$\left.\begin{array}{c}\phi^n \\ \tilde{\phi}\end{array}\right\} \longrightarrow \tilde{\phi}\cdot$

SOLVE 60 EQUATIONS OF LENGTH 20
REPEAT 40X
(EQUATIONS ARE DEPENDENT—MUST BE
SOLVED SEQUENTIALLY IN i DIRECTION)

Z-SWEEP

$\left.\begin{array}{c}\phi^n \\ \tilde{\phi} \\ \phi^{n-1\cdot}\end{array}\right\} \longrightarrow \phi^{n+1}$

SOLVE 60 EQUATIONS OF LENGTH 40
REPEAT 20X
(EQUATIONS ARE DEPENDENT—MUST BE
SOLVED SEQUENTIALLY IN i DIRECTION)

*3-D STORAGE REQUIRED · 3 LEVELS = 144,000

MODIFIED ALGORITHM STORAGE SCHEME (Version 1.10)

For the CRAY X-MP, the scheme illustrated in this figure has been adopted. For the X-sweep, data is accessed for each Y-Z plane (rather than each X-Y plane), and vectorized solution is performed in the Z direction, i.e., each step in the solution is a vector operation of length 40. This is then repeated for the next Y-Z plane, and the intermediate result $\bar{\phi}$ is stored in a three-dimensional array. For the Y sweeps, the data is accessed in the Y-Z planes, and a vectorized solution of length 40 is again performed in the Z direction, with the results $\tilde{\phi}$ stored in a three-dimensional array. Finally, the Z-sweeps are performed as a vectorized solution of length 20 in the Y direction, and the advanced values of the potential ϕ^{n+1} are stored in place of the values ϕ^n at the previous time step. It should be noted that four three-dimensional "levels" of storage, ϕ^n, ϕ^{n-1}, $\bar{\phi}$ and $\tilde{\phi}$ are required for this scheme, compared with three for the original scheme. In addition, however, nine additional three-dimensional arrays for vector equation coefficients and right-hand sides have been stored to improve efficiency and decrease the amount of re-calculation required. For the default mesh, the amount of storage for three-dimensional arrays has increased from 144,000 to 624,000. The total storage requirement has thus increased from about one-half million words to over one million words. Because of the larger amounts of storage available on both the CRAY X-MP and VPS-32, compared to the CDC 7600, this has caused no difficulty.

X-SWEEP

SOLVE 1 VECTOR EQUATION
(VECTOR LENGTH 40)
REPEAT 20X

Y-SWEEP

SOLVE 1 VECTOR EQUATION
(VECTOR LENGTH 40)
REPEAT 60X

Z-SWEEP

SOLVE 1 VECTOR EQUATION
(VECTOR LENGTH 20)
REPEAT 60X

*3-D STORAGE REQUIRED - 4 LEVELS + 9 COEFFICIENTS = 624,000
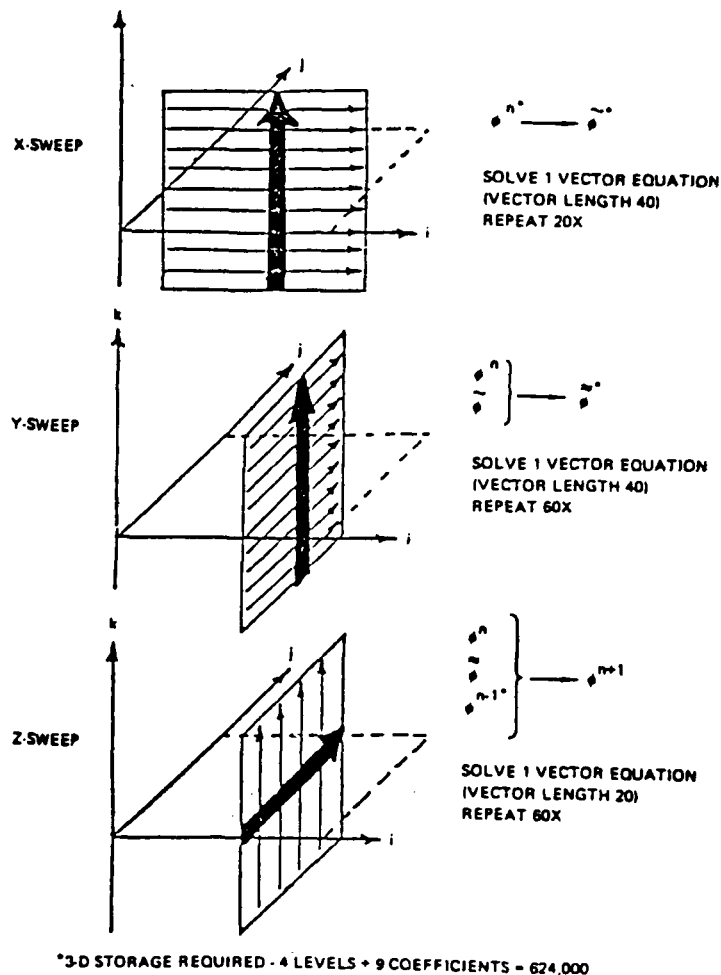
VECTORIZATION OF NASA WING-BODY MODIFICATION

This figure shows the improvements that can be achieved by careful attention to the use of vectorization concepts. The NASA-Langley developed wing-body modification update was installed in both the standard Version 1.5 and improved Version 1.10. Due to the use of conditional branching within computation loops (DO-loops), vectorization was inhibited. Version 1.5 took more than twice as long to run a wing-body case as a wing-alone case with the same dimensions, and Version 1.10 took more than three times as long. (The unmodified Version 1.10 runs more than twice as fast as Version 1.5). When the conditional branches were constrained to the outside of computation loops, permitting vectorization to occur, considerable speed-up was achieved. A wing-body case can now be run using Version 1.10 with only an increase of 4% over the cost of a wing-alone case. These constraints are applied in all the modification of XTRAN3S described below.

VERSION/CASE	WING ONLY	WING-BODY
1.5	1.0	-
1.5 + W-B	1.05	2.18
1.10	.43	-
1.10 + W-B	1.69	1.744
1.10 + W-B	.43	.45

(VECTORIZED)

(NORMALIZED CP SEC/ITERATION)

XTRAN3S ALGORITHM IMPROVEMENT

The XTRAN3S code solves the modified transonic small disturbance equation shown in this figure. After transforming the wing planform in Cartesian Coordinates (X, Y, Z) to a rectangular region in computation coordinates (ξ, η, ζ), the equation appears as shown below.

The underlined terms originate with the spanwise (Y-dependent) or cross (X-Y dependent) terms of the original equation, $G\phi_{y2}$ and $\phi y + H\phi_{x\phi y}$. The non-underlined terms depend only on original streamwise or normal derivatives. In the XTRAN3S algorithm, the original spanwise term $G\phi_{y2}$ was split into streamwise and transformed normal components. These terms were then treated separately with the streamwise component treated implicitly, and the normal component treated explicitly.

MODIFIED TRANSONIC SMALL DISTURBANCE EQ.

$$\frac{\partial}{\partial t}\left(-A\varphi_t - B\varphi_x\right) + \frac{\partial}{\partial x}\left(E\varphi_x + F\varphi_x^2 + \underline{G\varphi_y^2}\right)$$

$$+ \frac{\partial}{\partial y}\left(\underline{\varphi_y + H\varphi_x\varphi_y}\right) + \frac{\partial}{\partial z}\left(\varphi_z\right) = 0$$

TRANSFORMING TO $\xi = \xi(x,y) \; ; \; \eta = y \; ; \; \zeta = z \; ; \; \tau = t$

$$\frac{\partial}{\partial \tau}\left(-\frac{A}{\xi_x}\varphi_\tau - B\varphi_\xi\right)$$

$$+ \frac{\partial}{\partial \xi}\left\{E\xi_x\varphi_\xi + F\xi_x^2\varphi_\xi^2 + G\left(\xi_y\varphi_\xi + \varphi_\eta\right)^2 + \underline{\frac{\xi_y}{\xi_x}\left(\xi_y\varphi_\xi + \varphi_\eta\right) + H\xi_y\varphi_\xi\left(\xi_y\varphi_\xi + \varphi_\eta\right)}\right\}$$

$$+ \frac{\partial}{\partial \eta}\left\{\underline{\frac{1}{\xi_x}\left(\xi_y\varphi_\xi + \varphi_\eta\right) + H\varphi_\xi\left(\xi_y\varphi_\xi + \varphi_\eta\right)}\right\} + \frac{\partial}{\partial \zeta}\left\{\frac{1}{\xi_x}\varphi_\zeta\right\} = 0$$

The equation can be rewritten as shown by recollecting terms by coefficients of like-terms. Here a and b are the original (x-direction) streamwise terms of the governing equations, and $\hat{a}$, $\hat{b}$, etc., contain coefficients based on the spanwise terms of the equation. It has been previously noted that a time-accurate, fully conservative, implicit treatment can only be performed on the terms

$$\frac{\partial}{\partial \xi} (\hat{a}_\phi \phi_\xi + \hat{b}\phi_\xi^2) \qquad \text{and} \qquad \frac{\partial}{\partial \eta} (\frac{1}{\xi} \phi_\eta)$$

The remaining terms can be differenced in a fully conservative explicit fashion, or in a partially conservative implicit fashion. In the original XTRAN3S algorithm, only the cross-term $\frac{\partial}{\partial \xi} (G\phi_\eta^2)$ is so treated; the remaining terms are treated explicitly. In the present study, several different combinations of implicit and explicit difference treatments have been investigated. By examining the coefficients it can be seen that certain terms which were treated explicitly in the original XTRAN3S algorithm can be treated implicitly without loss of accuracy (i.e., without losing the conservation form of the equation). It has also been noted by Batina that only the original streamwise terms, represented by the coefficients $\hat{a}$ and $\hat{b}$ should be included in the type-dependent difference scheme or in the definition of the shock point operator. This treatment of these terms corresponds directly to the original 2-dimensional method of Ballhaus and Goorjian known as LTRAN2.

RECOLLECTING TERMS:

$$\frac{\partial}{\partial t} \left(-\frac{A}{\xi_x} \varphi_t - B\varphi_\xi \right)$$

$$\frac{\partial}{\partial \xi} \left(\hat{a}\varphi_\xi + \hat{b}\varphi_\xi^2 + \hat{\hat{a}}\varphi_\xi + \hat{\hat{b}}\varphi_\xi^2 + \hat{c}\varphi_\eta + \hat{d}\varphi_\eta^2 \right)$$

$$+ \frac{\partial}{\partial \eta} \left(\hat{e}\varphi_\xi + \hat{f}\varphi_\xi^2 + \hat{g}\varphi_\eta \right)$$

$$+ \frac{\partial}{\partial y} \left(\hat{h}\varphi_y \right) = 0$$

WHERE

$$\hat{a} = E\xi_x \qquad \hat{\hat{a}} = \xi_y^2/\xi_x + (2G+H)\dot{\xi}_y \varphi_\eta \qquad \hat{b} = F\xi_x^2$$

$$\hat{\hat{b}} = (G+H)\xi_y^2 \quad, \quad \hat{c} = \xi_y/\xi_x \qquad \hat{d} = G$$

$$\hat{e} = \xi_y/\xi_x \qquad \hat{f} = H\xi_y \qquad \hat{g} = \frac{1}{\xi_x} + H\varphi_\xi \qquad \hat{h} = \frac{1}{\xi_x}$$

ORIGINAL ADI ALGORITHM

The transformed streamwise sweep for the original (Version 1.5) XTRAN3S algorithm is shown in this figure.

Here D_ξ is a type-dependent mixed difference operator based on the sign of $(\hat{a}^n + 2\ G_\phi \phi_\xi^D)$, δ_ξ is a central difference operator, D_η is a mixed difference operator based upon the sign of $2G_s(\delta_\eta \phi n)$.

ξ - SWEEP:

$$B\ \tilde{\delta}_\xi \left(\frac{\tilde{\phi} - \phi^n}{\Delta t} \right) = D_\xi \left[a^n \left(\frac{\tilde{\phi}_\xi - \phi_\xi^n}{2} \right) + 6\phi_\xi^n \tilde{\phi}_\xi \right]$$

$$+ \ 2G_s\left(\delta_\eta \phi^n \right) D_\eta \left(\tilde{\delta}_\xi \phi^n \right) + \ \delta_\eta \left(\frac{1}{\xi_x} \delta_\eta \phi^n \right)$$

$$+ \ \frac{1}{\xi_x} \delta_{\xi\xi} \phi^n + \delta_\xi X^n + \delta_\eta Y^n$$

WHERE

$$X^n = G_N \left(\xi_y \phi_\xi^n + \phi_\eta \right)^2 + H\ \xi_\eta^2 \phi_\xi^{n2} + H\ \xi_y \phi_\xi^n \phi_\eta^n$$

$$+ \ \xi_y/\xi_x \phi_\eta^n + \xi_y^2/\xi_x \phi_\xi^{n2}$$

$$Y^n = \xi_y/\xi_x \phi_\xi^n + H\ \xi_y \phi_\xi^{n2} + H\ \phi_\xi^n \phi_\eta^n$$

26

MODIFIED ADI ALGORITHM

The transformed streamwise sweep for the modified (Version 1.10) XTRAN3S algorithm is shown in this figure. Here it can be seen that all but one of the explicitly-treated streamwise derivative terms $(\delta_\xi X^n)$ in the original algorithm can be treated implicitly. The remaining cross-derivative terms $\delta_\xi(\phi_\eta)$ or $\delta_\eta(\phi_\xi)$ must still be treated explicitly.

ξ - SWEEP:

$$B \overleftarrow{\delta_\xi} \left(\frac{\tilde{\tilde{\phi}} - \phi^n}{\Delta t} \right) = D_\xi \left[\hat{a}^n \left(\frac{\tilde{\tilde{\phi}}_\xi + \phi^n_\xi}{2} \right) + \hat{b} \, \phi^n_\xi \tilde{\tilde{\phi}}_\xi \right]$$

$$+ \, \delta_\xi \left[\hat{\hat{a}}^n \left(\frac{\tilde{\tilde{\phi}}_\xi + \phi^n_\xi}{2} \right) + \hat{\hat{b}} \, \phi^n_\xi \tilde{\tilde{\phi}}_\xi \right]$$

$$+ \, 2G \left(\delta_\eta \phi^n \right) D_\eta \left(\overleftarrow{\delta_\xi} \phi^n \right) + \delta_\eta \left(\frac{1}{\xi_x} \delta_\eta \phi^n \right)$$

$$+ \quad \frac{1}{\xi_x} \delta_{\xi\xi} \phi^n \quad + \quad \delta_\xi X^n \quad + \quad \delta_\eta Y^n$$

WHERE

$$X^n = \xi_y/\xi_x \, \phi^n_\eta$$

$$Y^n = \xi_y/\xi_x \, \phi^n_\xi + H \xi_\eta \phi^2_\xi + H \phi^n_\xi \phi^n_\eta$$

The transformed spanwise and vertical sweeps are unmodified in the new algorithm since these solutions are fully implicit.

η - SWEEP:

$$B \, \overset{\leftarrow}{\delta_\zeta} \left(\frac{\overset{\approx}{\varphi} - \varphi^n}{\Delta t} \right) = \frac{1}{2} \, \delta_\eta \left(\frac{1}{\xi_x} \, \delta_\eta \overset{\approx}{\varphi} - \frac{1}{\xi_x} \, \delta_\eta \varphi^n \right)$$

$$+ \; G \left(\delta_\eta \varphi^n \right) \, D_\eta \left(\overset{\leftarrow}{\delta_\zeta} \overset{\approx}{\varphi} - \overset{\leftarrow}{\delta_\zeta} \varphi^n \right)$$

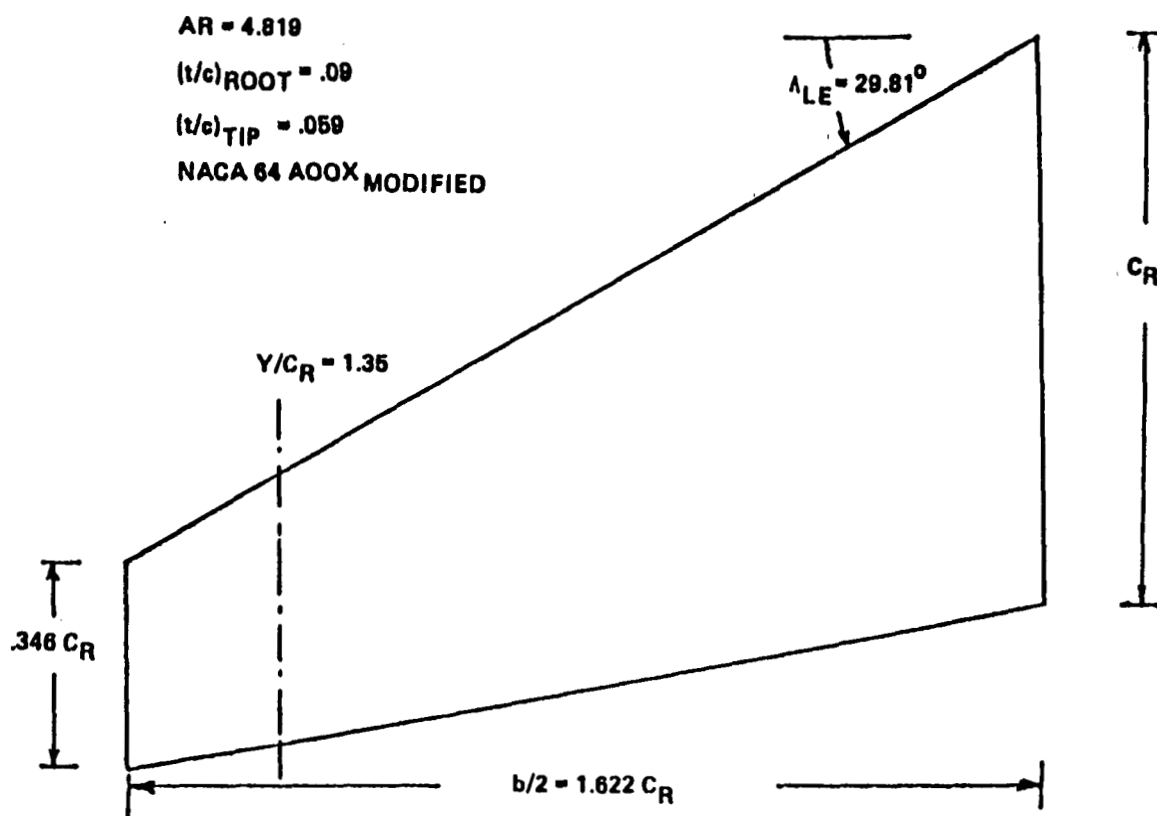ζ - SWEEP:

$$\frac{A}{\xi_x} \left(\frac{\varphi^{n+1} - 2\varphi^n + \varphi^{n-1}}{\Delta t^2} \right) + B \, \overset{\leftarrow}{\delta_\zeta} \left(\frac{\varphi^{n+1} - \overset{\approx}{\varphi}}{\Delta t} \right)$$

$$+ \frac{1}{2} \cdot \frac{1}{\xi_x} \, \delta_{\zeta\zeta} \left(\varphi^{n+1} - \varphi^n \right)$$

(THESE SWEEPS UNMODIFIED)

A-6E TEST PROBLEM

The modified ADI algorithm has been tested on the wing planform for the
A-6E attack aircraft with a moderate sweep and taper. The computation time
step could be increased by a factor of ten with numerical stability
maintained. For a more severely swept and tapered planform (the F-5 wing)
an increase of more than fifteen has been reported.

AR = 4.819

$(t/c)_{ROOT}$ = .09

$(t/c)_{TIP}$ = .059

NACA 64 A00X MODIFIED

Λ_{LE} = 29.81°

C_R

Y/C_R = 1.35

.346 C_R

b/2 = 1.622 C_R

A-6E Planform in XTRAN3S Calculations

This figure shows the resulting steady pressure distributions for the original and modified ADI algorithms. In the modified algorithm the shock has moved one grid point upstream. Otherwise results are essentially identical.

Comparison of Pressure Distribution Calculated by the
Original and Revised XTRAN3S Algorithms
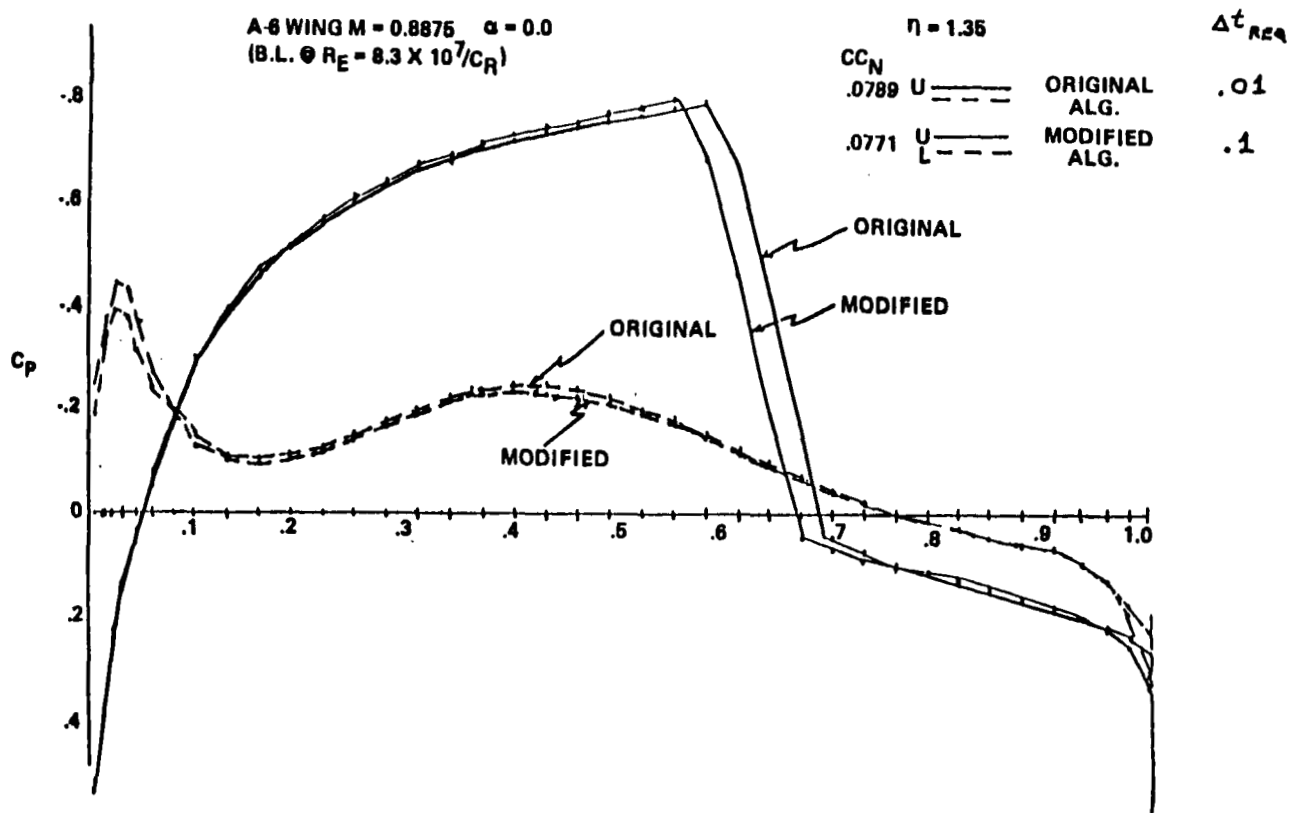
WING-PYLON STORE TRANSONIC ANALYSIS

This section of the presentation will describe the development and current status of a pylon/external store or nacelle capability in XTRAN3S.
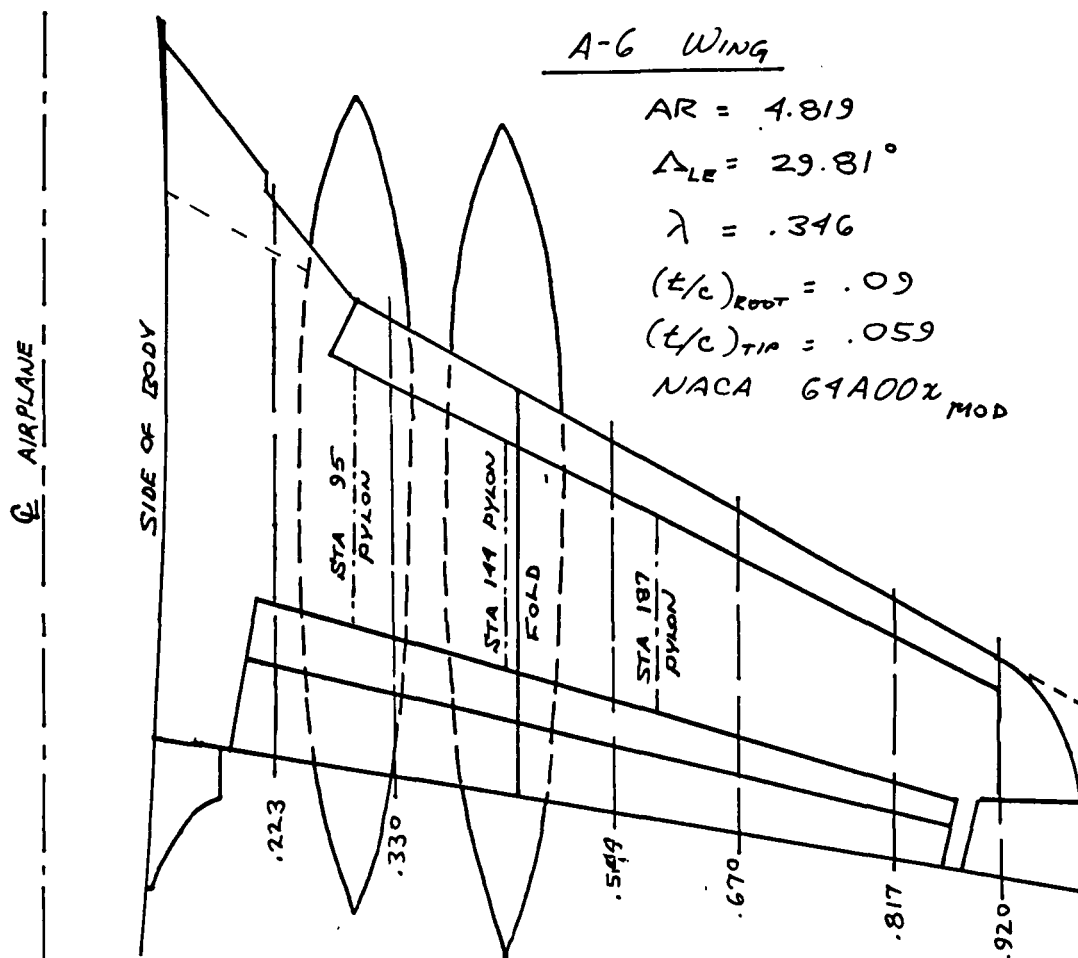
Wing - Pylon - Store

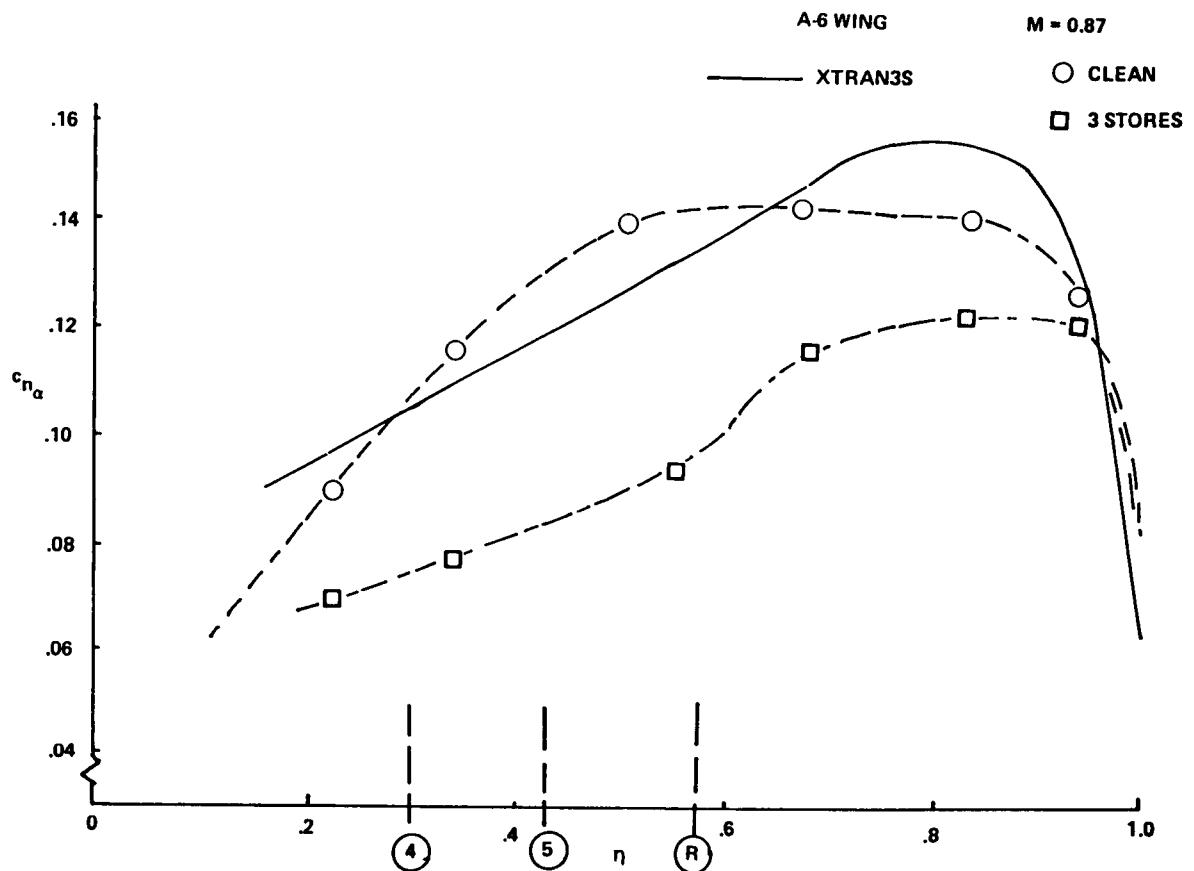# Transonic Analysis

With XTRAN3S

A-6 WING WITH STORES

Flutter characteristics of military aircraft may be severely affected by
the presence of external stores. These stores may affect the flow field
characteristics as well as the structural dynamic characteristics of the
aircraft. Flutter speeds with carriage of external stores are usually
lower than for the clean wing and may require severe operational
restrictions. This figure shows a schematic of the wing of the Navy A-6E
attack aircraft. As a part of the flutter clearance program for the newly-
designed graphite-epoxy A-6 Replacement Wing, Boeing performed wind tunnel
tests on both rigid and aeroelastic transonic models. The A-6 wing is
shown here with 2 -400 gallon external fuel tanks mounted on pylons under
the wings at two inboard stations (the third station is used to mount a
small air-air missile such as the AIM-9L Sidewinder). The wing is
moderately swept and tapered. Simulations conducted to date with XTRAN3S
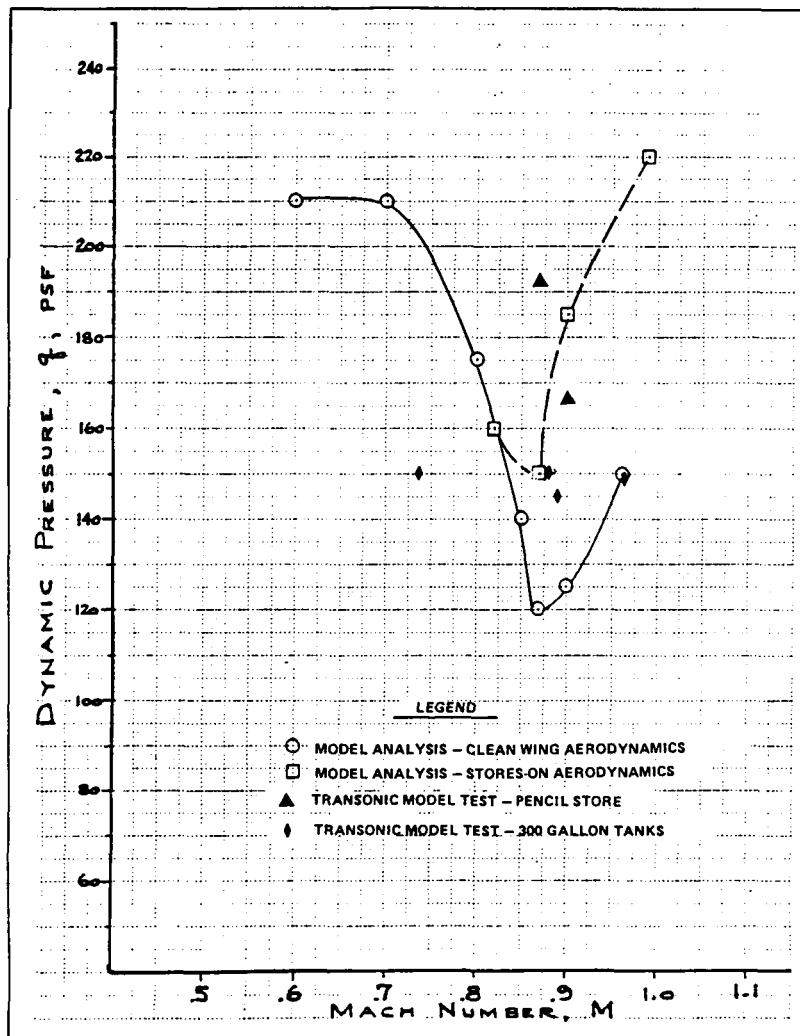did not include the inboard strake, fuselage, or nacelle.

$A-6$ WING

$AR = 4.819$

$\Lambda_{LE} = 29.81°$

$\lambda = .346$

$(t/c)_{ROOT} = .09$

$(t/c)_{TIP} = .059$

NACA $64A00x_{MOD}$

As seen in this figure, aerodynamic interference due to the presence of the stores has a significant effect on the sectional lift distribution of the wing. (Symbols represent data from a static rigid test). Also shown is a prediction of the static lift curve slopes by XTRAN3S for the clean wing. Flutter results using the clean wing XTRAN3S aerodynamics and the clean wing test data as correction factors in an interfering modified strip theory analysis are essentially the same.

FLUTTER TEST COMPARISON - ONE STORE

In this figure, analysis of the A-6 wind tunnel flutter model tested in NASA's Transonic Dynamics Tunnel for both the "clean wing" and "stores on" aerodynamics correction factors (section lift curve slopes and aerodynamic centers) are compared with measured flutter dynamic pressures. The analysis for both sets of corrections shows the typical "transonic bucket" as a function of Mach number. The model test with an actual stores representing a single 300 gallon external fuel tank showed essentially no effect of Mach number - a completely unexpected result! An effort to explain this phenomenon, a "pencil store", or simulator with identical mass and inertia properties but minimum aerodynamic interference was also tested. Here the results showed the expected Mach effect of decreasing flutter speed up to a critical Mach number. A "no-flutter" run (not shown) at higher speeds demonstrated the classical transonic bucket behavior. Thus the importance of wing-store aerodynamic interference and potential aerodynamics of the store itself were demonstrated.
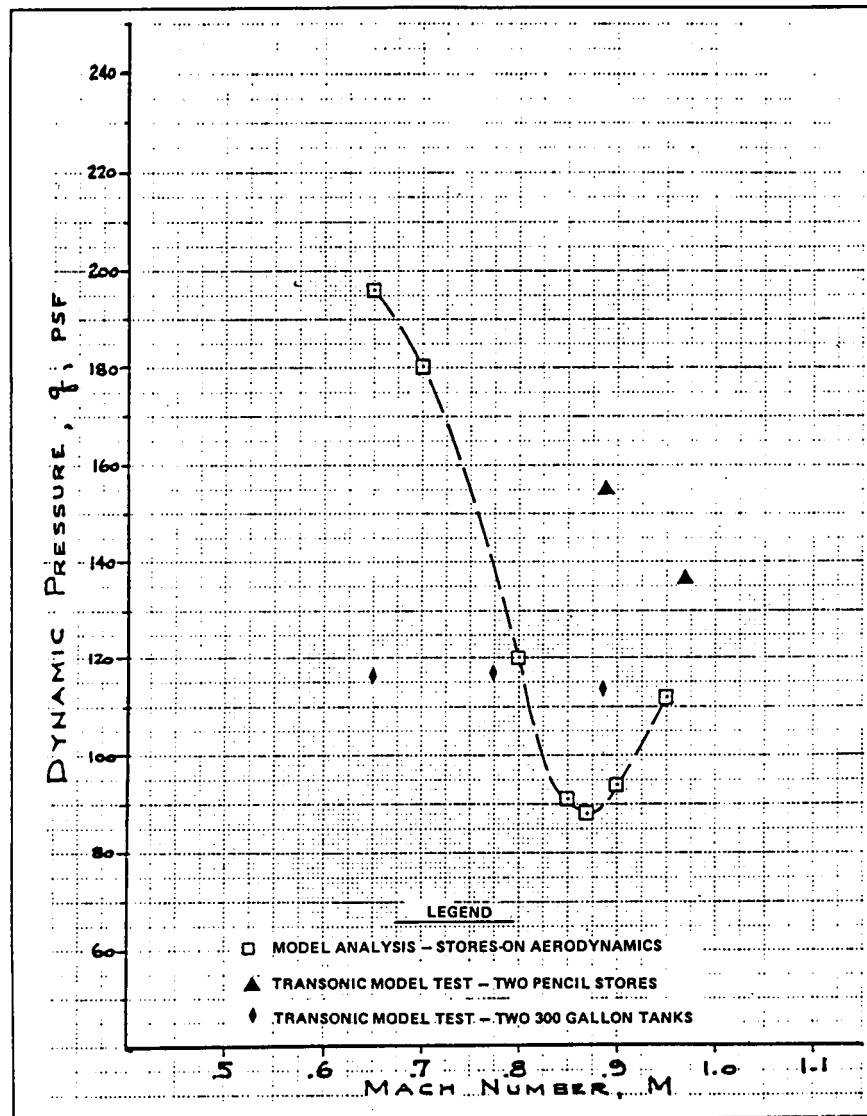

LEGEND
- ⊙ MODEL ANALYSIS – CLEAN WING AERODYNAMICS
- ⊡ MODEL ANALYSIS – STORES-ON AERODYNAMICS
- ▲ TRANSONIC MODEL TEST – PENCIL STORE
- ◆ TRANSONIC MODEL TEST – 300 GALLON TANKS

FLUTTER ANALYSIS,
300 GALLON TANK ON PYLON 5

FLUTTER TEST COMPARISON - TWO STORES

This figure shows a similar comparison of analysis and test results for two 300 gallon tanks and pencil stores. Although the measured flutter boundary shows a much higher Mach number for the same dynamic pressure at flutter (or vise versa), the bucket behavior for the pencil stores is again confirmed. The actual stores show no appreciable effect of Mach number on flutter. One principal difference between the actual stores and the simulators was the rapidity of the onset of flutter. With the actual stores, flutter was approached quite slowly with fairly long times to double amplitude (5-10 seconds) allowing good confirmation of actual flutter behavior without risk to the model. On the second flutter point shown with the simulators (at a q of 155 psf) violent flutter was encountered (.1 sec to double amplitude) and the model was destroyed.


LEGEND
□ MODEL ANALYSIS – STORES-ON AERODYNAMICS
▲ TRANSONIC MODEL TEST – TWO PENCIL STORES
♦ TRANSONIC MODEL TEST – TWO 300 GALLON TANKS

FLUTTER ANALYSIS,
TWO 300 GALLON TANKS ON PYLONS 4&5

35

INITIAL XTRAN3S STORE-PYLON SIMULATION

This figure shows a portion of the grid (Y-Z plane) used in the internal XTRAN3S simulation of the A-6 wing-pylon-store geometry. The pylons are located in planes midway between spanwise grid lines. The stores are simulated as a single line, with stores boundary conditions being satisfied at the four neighboring grid points. Shown in this figure are the maximum diameters of the 400 and 300 gallon tanks in relation to the wing and an approximate side of body location. The rigid model was tested with the store configuration shown plus a Sidewinder at the outboard station (which has not been modeled).

INITIAL   XTRAN3S   STORE-PYLON   SIMULATION

(WING LOWER SURFACE)
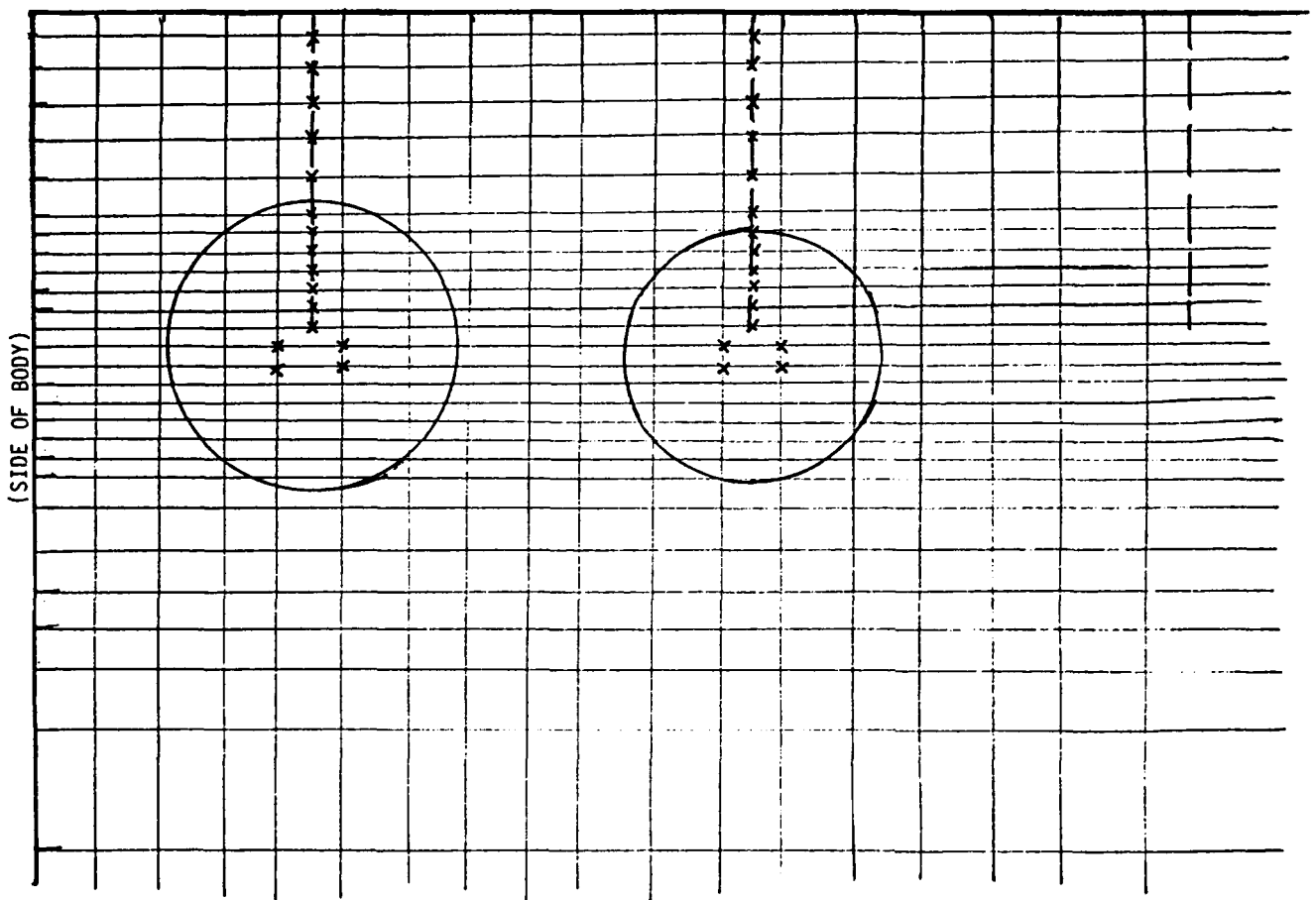
A-6 CLEAN WING

This figure and the next show the measured pressures on the wing upper and lower surface at a location just outboard of the inboard pylon station. Shown are the clean wing and pylons only cases. Also shown are the pressures predicted by XTRAN3S including surface boundary layers. Other than difference at the leading edge and slight pressure differences on the lower surface, the comparison is good.
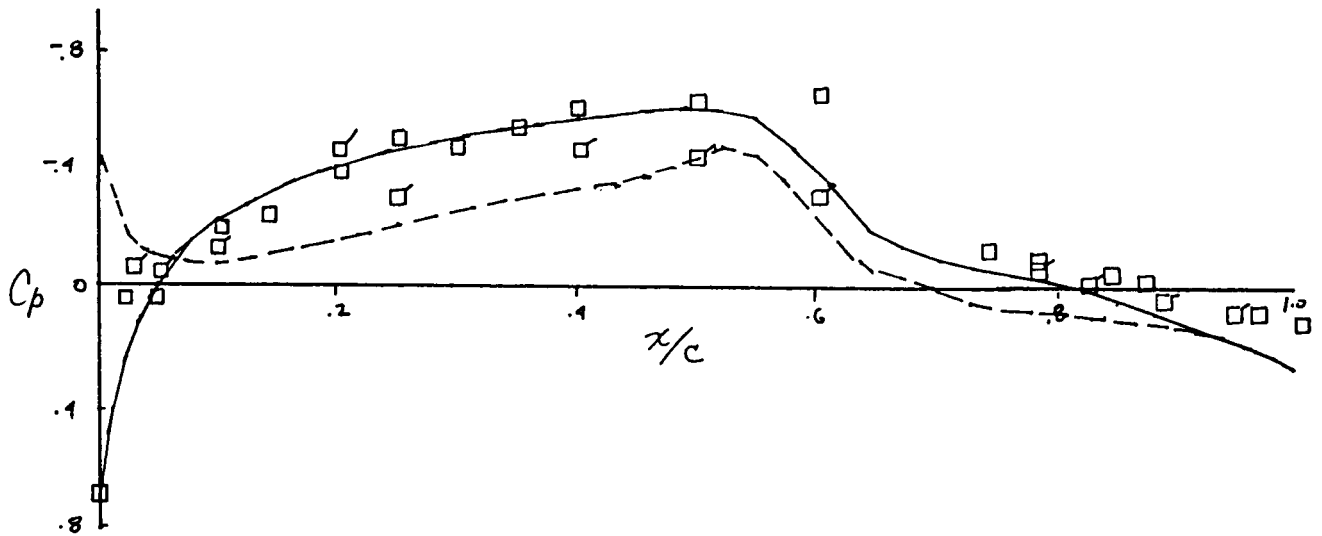
A-6 CLEAN WING

$M = .87$ $\alpha = .0$ $\eta = .33$

	TEST	XTRAN3S
C_{p_u}	□	——
C_{p_ℓ}	◨	— —
C_n	.071	.120
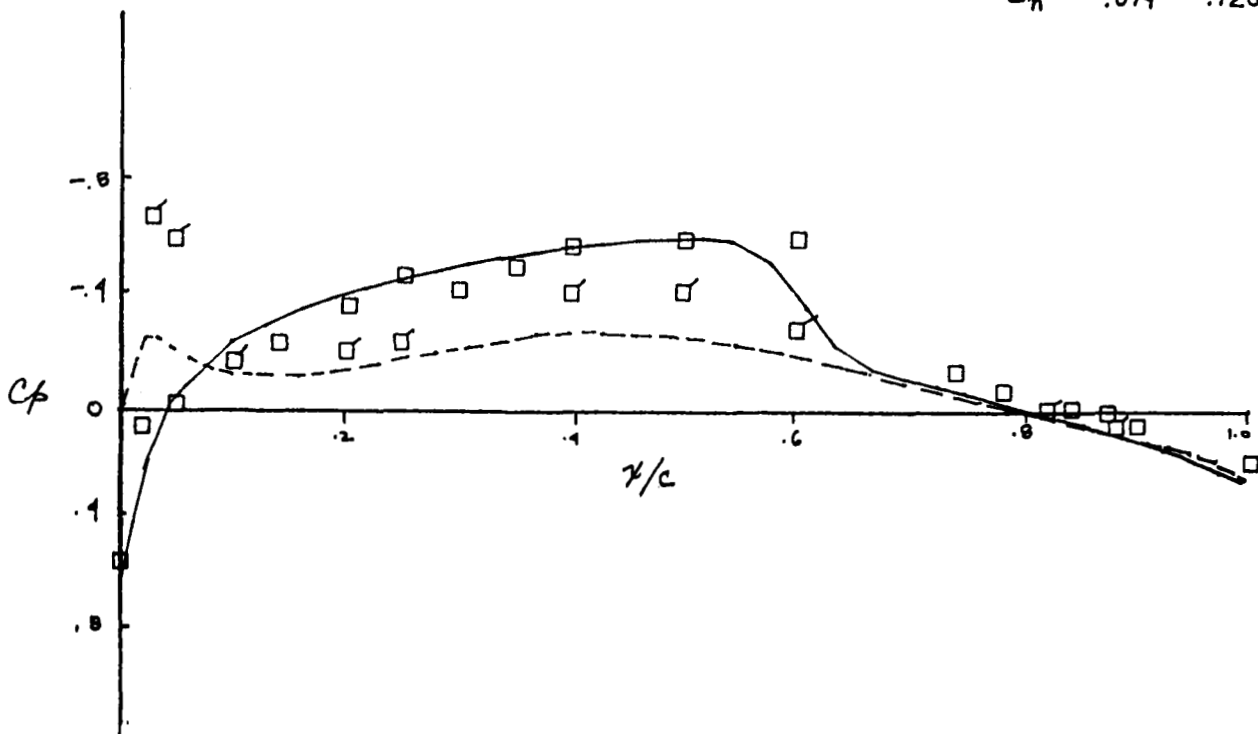
$M = .97 \quad \alpha = 0.0 \quad \eta = .33$

|	TEST	XTRAN3S'
C_{p_u}	□	——
C_{p_ℓ}	◰	— —
C_n	.103	.098

A-6 PYLON + STORES

This figure shows the comparison of measured and predicted pressures for the pylon-stores case. Although there is additional interference due to this "slender-body" modeling of the store, the comparison is neither qualitatively nor quantitatively good. Thus is was seen that a more complete modeling of the store is required.

$M = .87$ $\alpha = 0.0$ $\eta = .33$

	TEST	XTRAN3S
C_{p_u}	□	———
C_{p_l}	◻	— — —
C_n	.098	.030
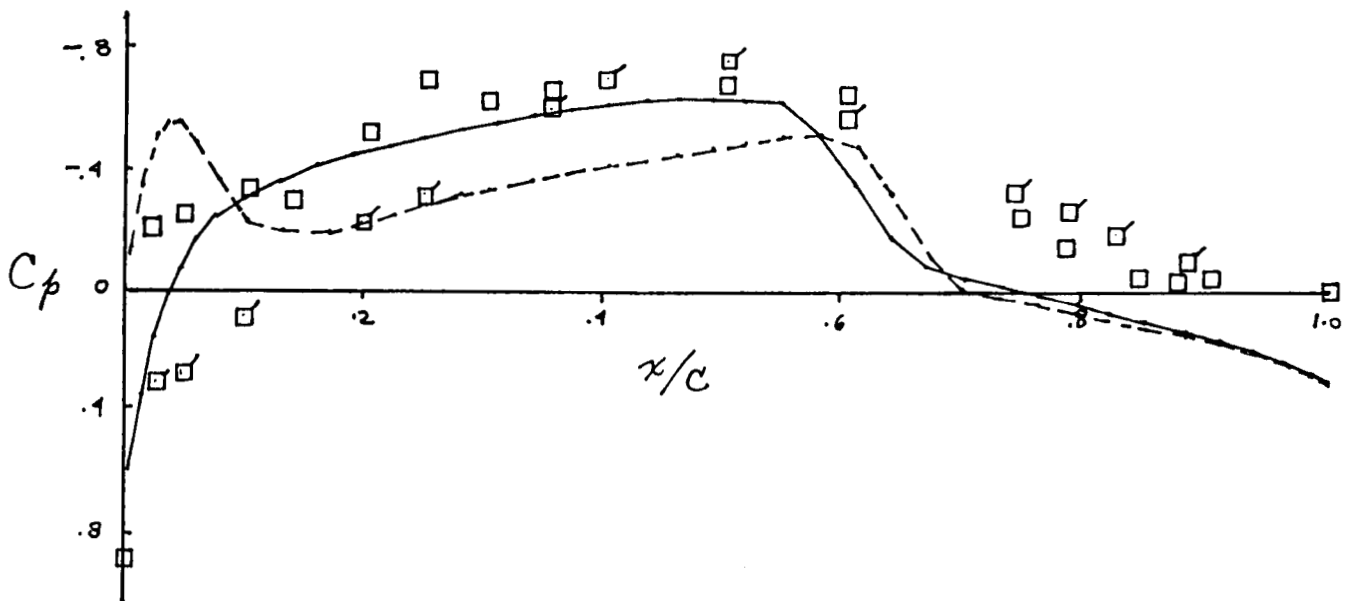
INTERFERENCE SHELL GEOMETRY

This figure shows the effective geometry of an "interference shell" or surface on which the boundary conditions are satisfied, surrounding the store. In the manner of Batina's Wing-Fuselage modification, slender-body corrections are used to modify the local surface boundary condition applied on the shell.

$$\phi_z = \frac{\Delta C}{A\bar{c}} F_z - \frac{S'}{S} \alpha_s$$

$$\phi_y = \frac{\Delta C}{A\bar{c}} F_y - \frac{S'}{S} \beta_s$$
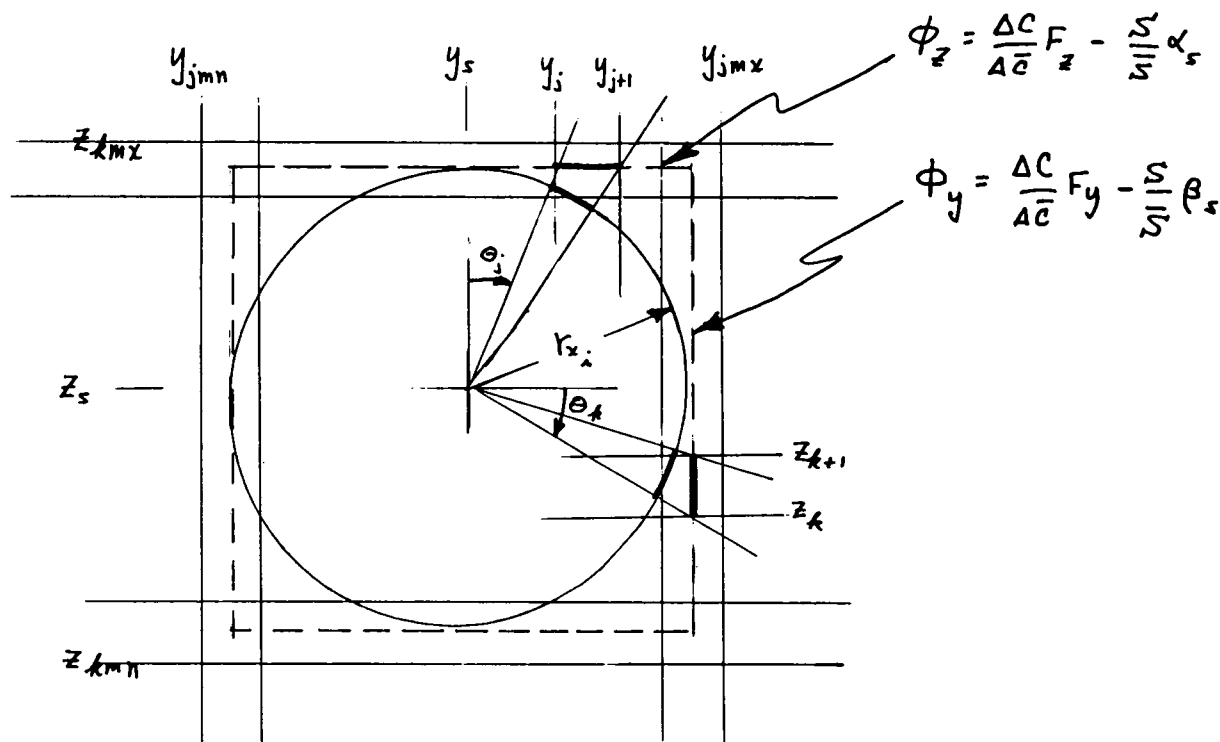
$$C_{i_j} = r_{x_i} |\Theta_{j+1} - \Theta_j| \qquad S_i = \pi r_{x_i}^2$$

$$\bar{C}_i = y_{j+1} - y_j \qquad \bar{S}_i = (y_{jmx} - y)(z_{\ell mx-\frac{1}{2}} - z_{\ell mn+\frac{1}{2}})$$

XTRAN3S STORE-PYLON SIMULATION

This figure shows the grid geometry for the store-pylon simulation with interference shells.

(WING LOWER SURFACE)
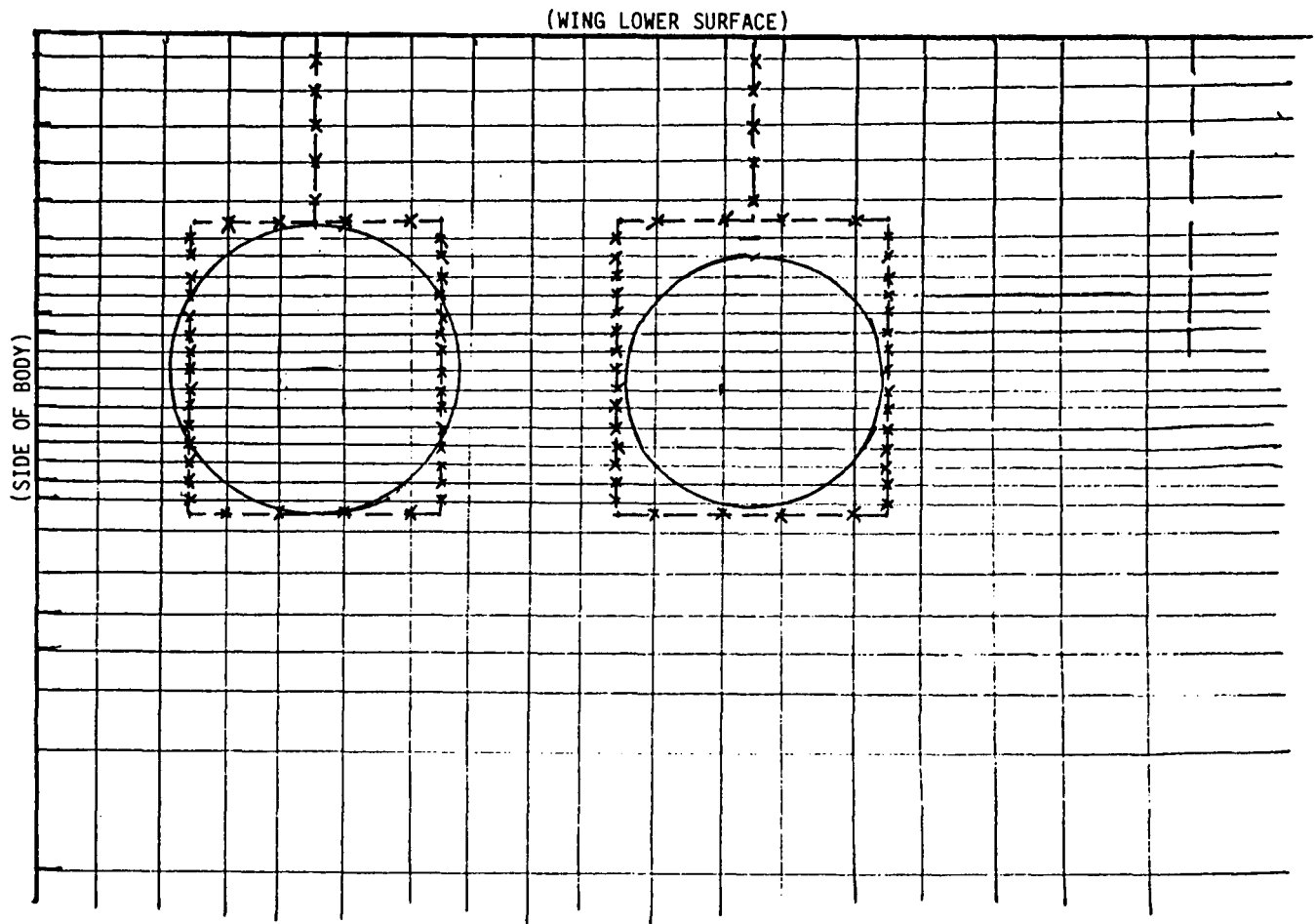
(SIDE OF BODY)

## A-6 PYLONS + STORES (INTERFERENCE SHELL)

In this figure the XTRAN3S prediction with the interference shell is compared with measured data. The analysis predicts a much stronger shock, located closer to the trailing edge of the wing, than the data indicated. (The boundary layer calculation for this case was unstable; thus the result shown is an inviscid calculation.)

(At the symposium, the possibility of flow field separation causing the behavior shown was suggested by Joe Giesing of McDonnell-Douglas. This has been simulated and the results are shown in the next figure.)
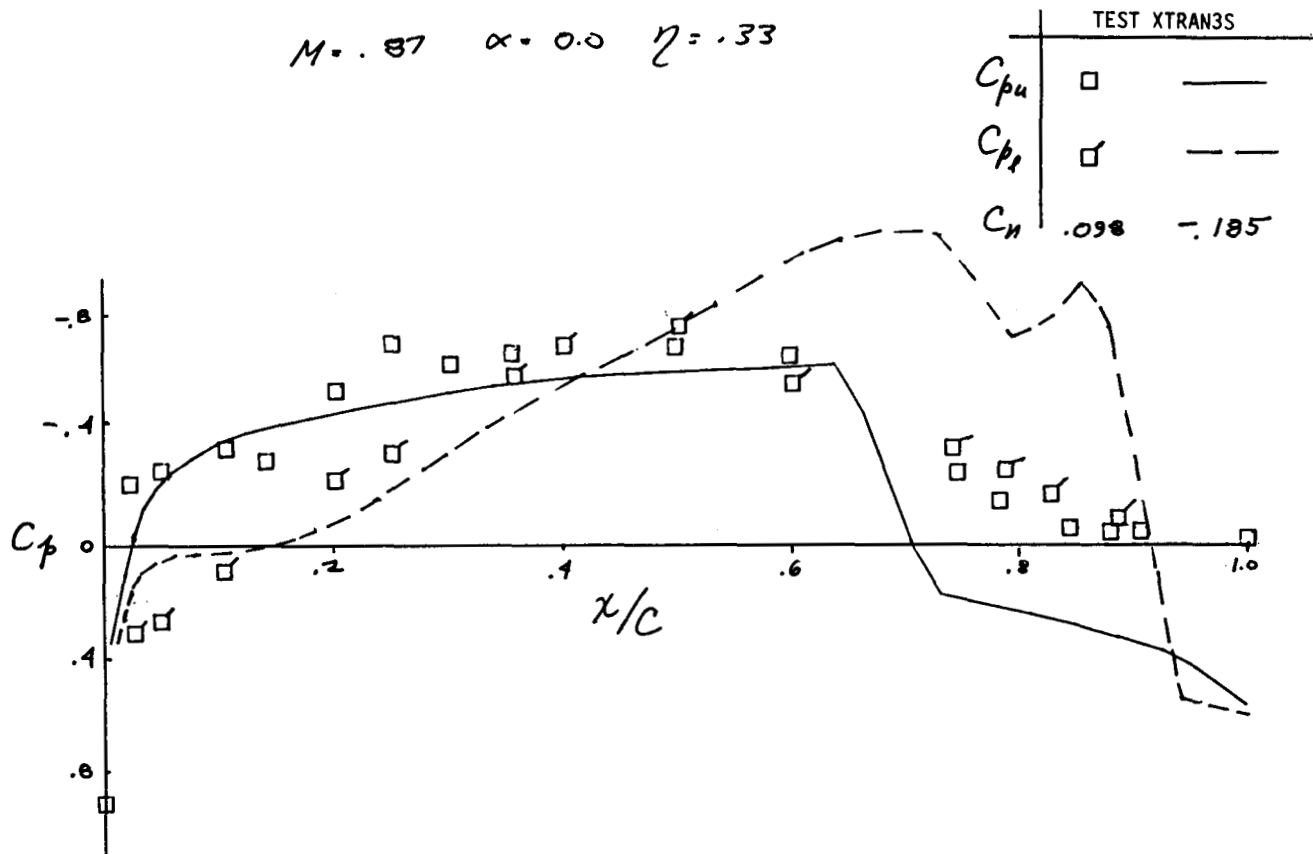
A-6 PYLON + STORES WITH AFT SEPARATION

Flow separation on the aft portion of the stores was simulated by use of a constant store radius and zero slope for the portion of the store aft of the maximum radius. This geometry modification has considerably improved the correlation with measured data, as shown in this figure. This calculation is shown with the boundary layer present. (This figure was not shown at the symposium.)

$M = .87 \quad \alpha = 0.0 \quad \eta = .33$

		TEST	XTRAN3S
C_{pu}	▫		———
C_{pl}	▫		– – –
C_n		.098	.067
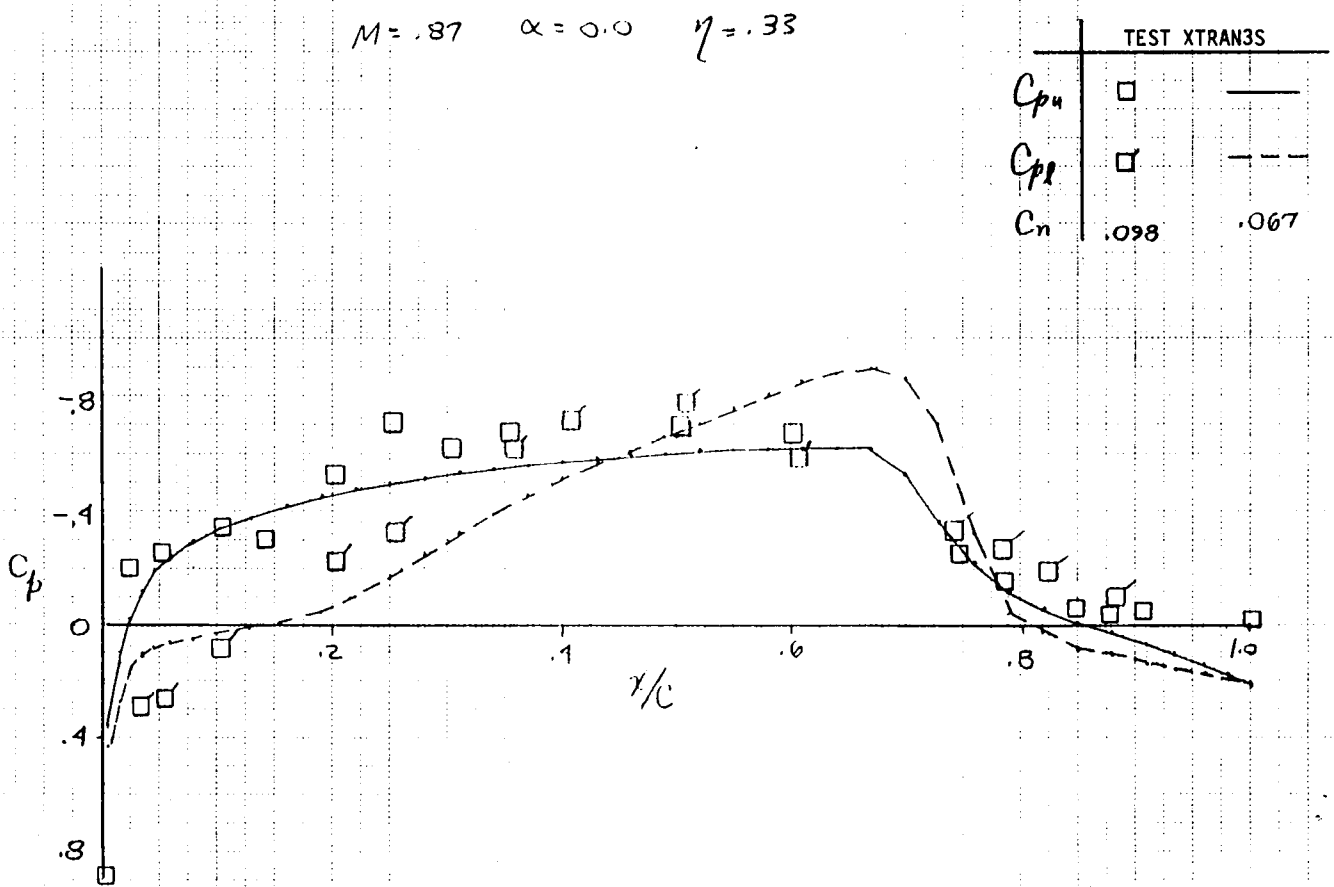
SUMMARY

In summary, modifications to the XTRAN3S code, implemented in Version 1.10, have provided a speed-up of twenty to thirty times over the previous released Version 1.5.

The pylon-store modification, under development, has shown that the presence of pylons and stores can be simulated although attention to geometric and flow field details is required.

- IMPROVED VECTORIZATION and ALGORITHM MODIFICATIONS PROVIDE 20-30X SPEED-UP IN XTRAN3S VERSION 1.10

- PYLON-STORE MODIFICATION DEVELOPED

  - SIMPLE SLENDER BODY INSUFFICIENT

  - INTERFERENCE SHELL OVERPREDICTS STORE INTERFERENCE ON WING

44

FUTURE EFFORTS

Future developments of the XTRAN3S code, to be initiated shortly under AFWAL sponsorship, are shown in this figure. Some comparisons with NASA-Langley's CAP-TSD code will be made at a later date.

- CONTINUE DEVELOPMENT ON PYLON-STORE MODIFICATION

- INCORPORATE WING-BODY AND PYLON-STORE MODIFICATIONS IN SINGLE VERSION

- ADD SUPERSONIC AND FOURIER ANALYSIS CAPABILITIES

- CONTINUE EVALUATIONS WITH TRANSPORT AND ATTACK AIRCRAFT AEROELASTIC MODELS

Role of Computational Fluid Dynamics in
Unsteady Aerodynamics for Aeroelasticity

Guru P. Guruswamy
Sterling Federal Systems
Applied Computational Fluids Branch
NASA Ames Research Center
Moffett Field, California

Peter M. Goorjian
Applied Computational Fluids Branch
NASA Ames Research Center
Moffett Field, California

Introduction

In the last two decades, there have been extensive developments in computational unsteady transonic aerodynamics (ref. 1). Such developments are essential since the transonic regime plays an important role in the design of modern aircraft. Consequently, there has been a large effort to develop computational tools with which to accurately perform flutter analysis at transonic speeds. In the area of Computational Fluid Dynamics(CFD), unsteady transonic aerodynamics are characterized by the feature of modeling the motion of shock waves over aerodynamic bodies, such as wings. This modeling requires the solution of nonlinear partial differential equations. At the present time, the most advanced codes such as XTRAN3S, the Air Force/NASA code for transonic aeroelastic analysis of aircraft, use the transonic small perturbation (TSP) equation(ref. 2). Currently XTRAN3S is being used for generic research in unsteady aerodynamics and aeroelasticity of almost full aircraft configurations(ref. 3). Use of Euler/Navier Stokes equations for simple typical sections has just begun. In comparison, for steady flows, Euler/Navier Stokes equations are being used for wing-bodies and complex separated flows(ref. 4). A brief history of the development of CFD for aeroelastic applications has been summarized in figure 1. The present paper summarizes the development of unsteady transonic aerodynamics and aeroelasticity at NASA-Ames in coordination with Air Force, other NASA centers and industries since 1978.
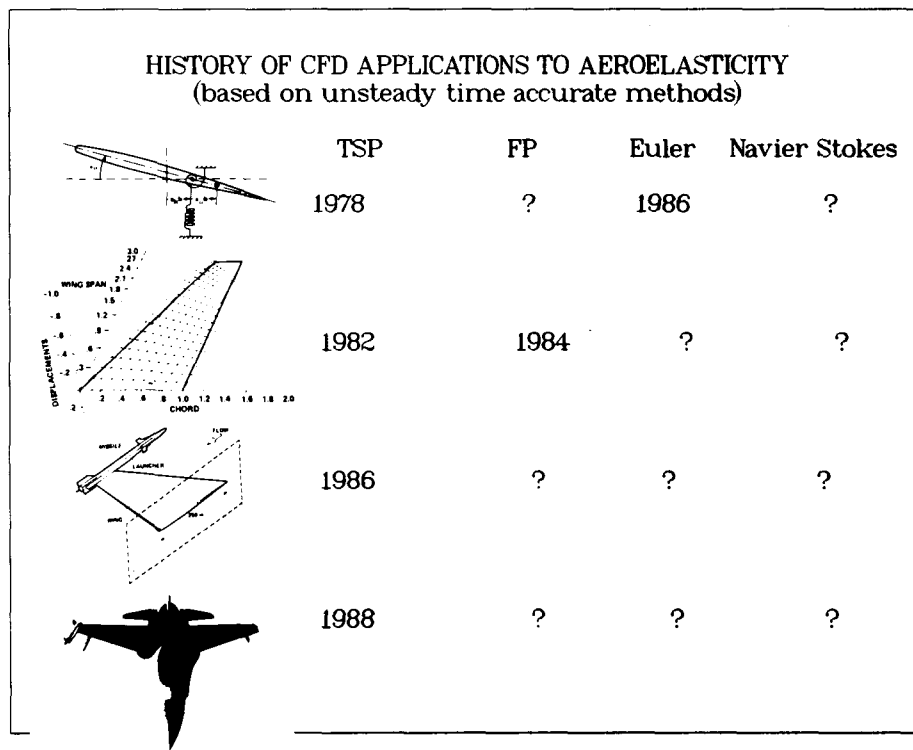

HISTORY OF CFD APPLICATIONS TO AEROELASTICITY
(based on unsteady time accurate methods)

	TSP	FP	Euler	Navier Stokes
	1978	?	1986	?
	1982	1984	?	?
	1986	?	?	?
	1988	?	?	?

FIGURE 1

Need for Time Accuracy for Aeroelastic Calculations

Transonic aeroelasticity is a highly coupled phenomenon between struc-
tures and fluids due to flow nonlinearities. The presence of moving shock
waves in the transonic flows further intensifies this coupling and leads to several
non-classical aeroelastic phenomenon such as a dip in the flutter boundary
curve. In order to make accurate computations in transonic aeroelasticity, it
is important to use time accurate methods. The first efficient time accurate
method of solving unsteady transonic flows was developed for airfoils using the
TSP equations and was implemented in the code LTRAN2 (ref. 5). Based on
LTRAN2 several improved codes have been developed and are in routine use
for transonic aeroelastic computations of typical sections. A time accurate way
of simultaneously integrating unsteady transonic aerodynamics and structural
equations of a typical section was first presented in reference 6. From figure
2, taken from reference 6, it can be seen that time linearized computations
based on the indicial method and harmonic method fail to predict the neu-
tral stability condition. On the other hand the computations based on the
time accurate method succeed. Though the time linearized techniques are
sometimes computationally more efficient than the time accurate techniques,
one should watch for the non-physical solutions from time linearized meth-
ods (indicial, UTRANS2-harmonic method) as shown in figure 2. In this paper
several results from time accurate transonic aeroelastic calculations will be
presented.

IMPORTANCE OF TIME ACCURACY IN AEROELASTICITY
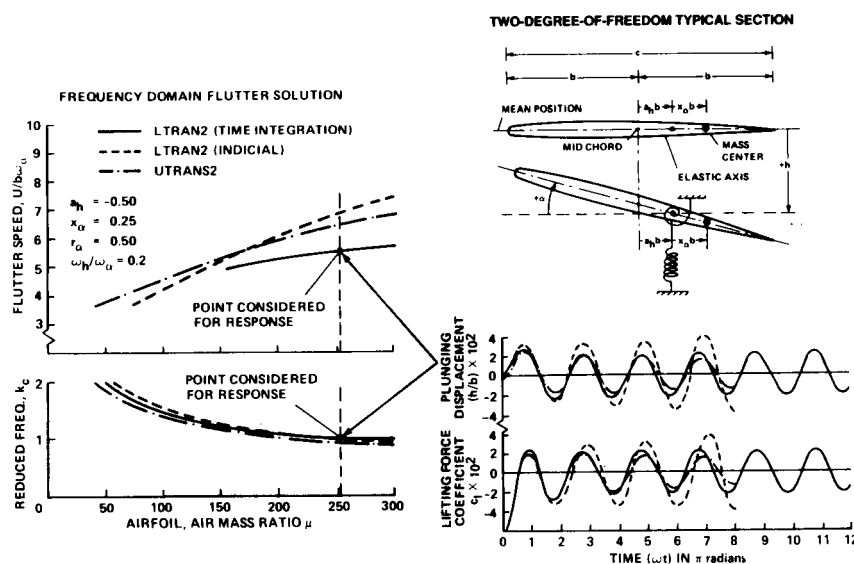
• RESULTS ARE FROM TIME ACCURATE ADI ALGORITHM

FIGURE 2

Time Accurate Unsteady Calculations of Rectangular Wings

The successful development of the two-dimensional code LTRAN2, which employs an alternating-direction-implicit(ADI), finite-difference scheme, and the availability of faster computers with more memory, made possible the development and use of three-dimensional unsteady transonic aerodynamic codes. LTRAN3, the earlier low-frequency version of XTRAN3S was developed for time accurate calculations (ref. 7). The time accuracy of this code was validated against unsteady experimental data in reference 8. Figure 3 shows the magnitude and the phase angle of the unsteady pressures for a rectangular wing oscillating in its first bending mode. Time accurate computations have accurately captured the effects of unsteady motion of the shock wave. The rise in the phase angle behind the shock wave, which is one of the salient features of the unsteady transonic flow, has been predicted accurately by the alternating direction implicit scheme using the Murman-Cole switch incorporated in LTRAN3. This code was successfully applied to compute the flutter boundaries of rectangular wings by using coupled (ref. 7) and uncoupled (ref. 8) methods. Figure 3, shows the good comparison of unsteady pressures and flutter boundary computed from LTRAN3 with the experiment and NASTRAN, respectively.
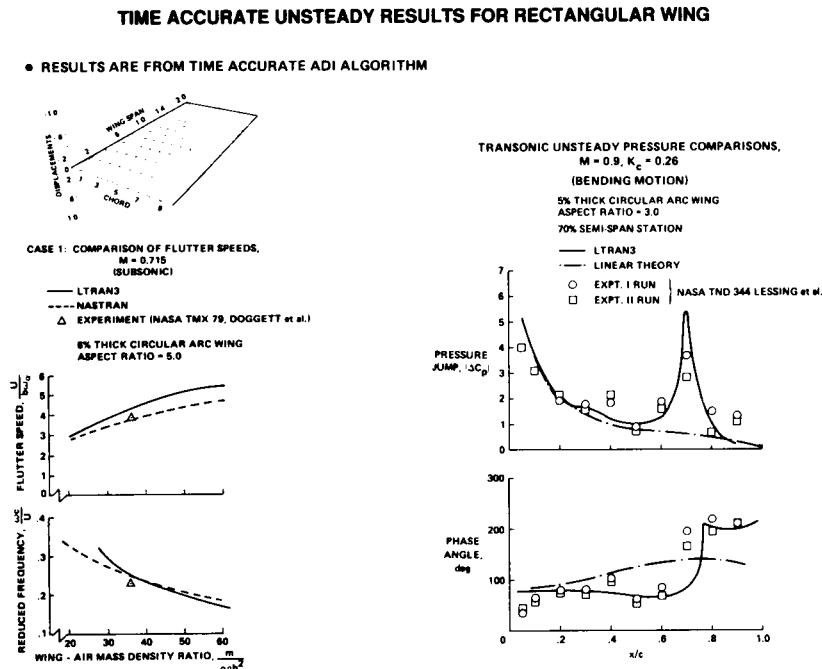
TIME ACCURATE UNSTEADY RESULTS FOR RECTANGULAR WING

● RESULTS ARE FROM TIME ACCURATE ADI ALGORITHM

FIGURE 3

Transonic Aeroelasticity of a Transport Wing

The successful aerodynamic and aeroelastic computations for rectangular wings lead to further applications for more practical configurations. At the same time, the capability of LTRAN3 was extended to account for integration with structures and also high frequency terms. The successful time integration method developed in reference 3 was implemented in XTRAN3S. Using this code, aeroelastic computations were made for a Japanese transport wing and results were compared with the experiment (ref. 9). Figure 4 shows steady pressures and also the flutter boundary curve obtained by using XTRAN3S. During this study several errors in XTRAN3S, such as one in the far span boundary conditions, were corrected. This study also indicated the time step size restriction of XTRAN3S based on sweep angle. Because of the time step size restriction it was not practical to use XTRAN3S for computing flows over low aspect ratio fighter wings. Though several limitations were found in XTRAN3S, this study on a practical wing configuration with favorable comparison with the experiment showed the potential of the code for further development.
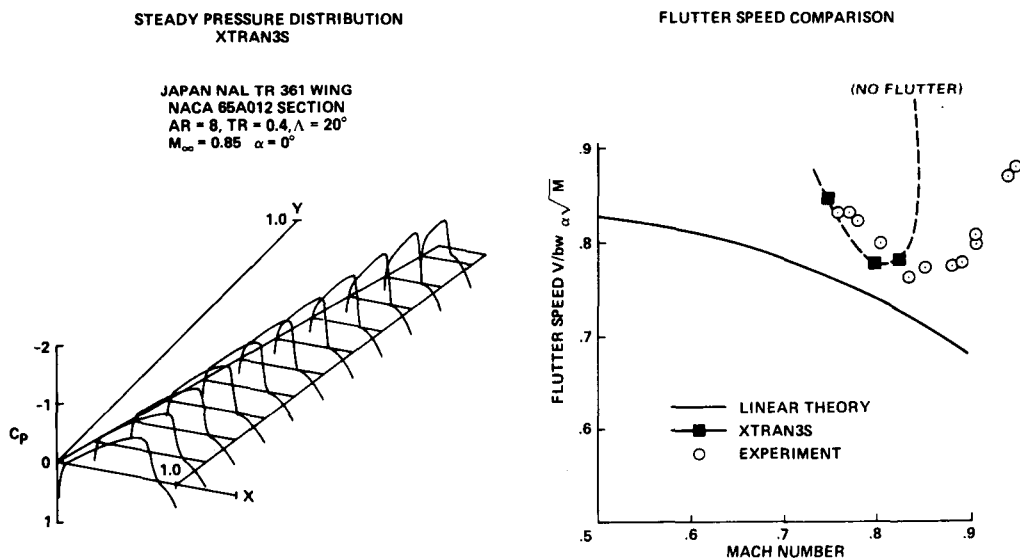
TYPICAL TRANSPORT WING

FIGURE 4

Unsteady Transonics of Fighter Wings

Research was further conducted to study the time step size restriction of XTRAN3S. Detailed studies showed that conventional shearing transformation used in XTRAN3S yielded computations that were numerically unstable. The physical grid was dependent upon the planform and was highly skewed for low aspect ratio fighter wings. To correct this, a new modified coordinate transformation technique was developed in reference 10. This modified transformation removed the skewness in the physical grid and led to computations that are stable, fast and accurate. It was first implemented in XTRAN3S-Ames(ATRAN3S), a parallel NASA Ames version of XTRAN3S. Using the modified transformation, for the first time, successful unsteady computations were made for the F-5 fighter wing in the transonic regime. Figure 5 shows the unsteady modal motion and the corresponding unsteady pressures of the F-5 wing at a transonic Mach number of 0.9. Theory compares very well with the experiment. The success of the modified shearing transformation was first reported by the present authors in '1983 Symposium on Transonic Unsteady Aerodynamics and Aeroelasticity and it was implemented in other versions of XTRAN3S.

TYPICAL FIGHTER WING

UNSTEADY MODAL MOTION
F-5 WING, FREQUENCY = 40 Hz
PITCHING ABOUT 50% ROOT CHORD

TRANSONIC UNSTEADY PRESSURES
M = 0.90, f = 40 Hz, $\alpha = 0°$
MODIFIED TRANSFORMATION
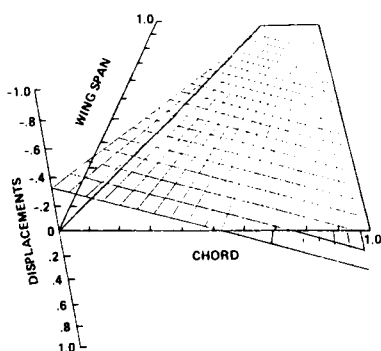
F5 WING
AR = 2.98
TR = 0.31
LE SWEEP = 32°

NLR EXPERIMENT
□ REAL
△ IMAGINARY

ATRAN3S, $\Delta T = 0.01$
—— REAL
---- IMAGINARY

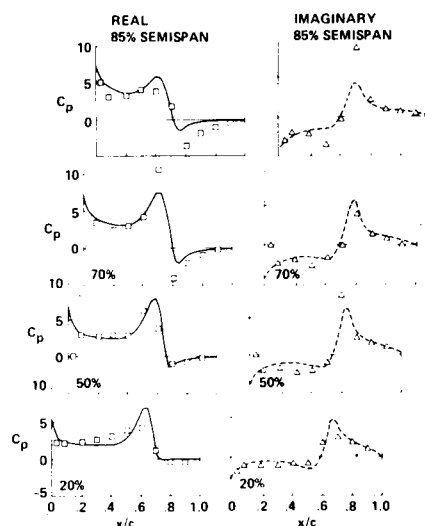## FIGURE 5

Transonic Aeroelasticity of Variable Sweep B-1 Wing

The variable sweep B-1 wing has been observed to undergo angle of attack dependent aeroelastic oscillations in both flight and wind tunnel tests. These oscillations were more significant at high sweep angles. Motivated by these observations, the flow over the B-1 wing was studied computationally, including the aeroelastic response of the wing. In the low sweep case, the comparisons demonstrated the capability of XTRAN3S-Ames to properly simulate the flow in the presence of shock waves. In the high sweep case, where the sweep angle is equal to $67.5°$ the comparisons at a low angle of attack demonstrated the capability of the modified shearing transformation to properly simulate the flow at an extreme sweep angle. Computations at the high sweep case for a higher angle of attack at which oscillations were observed did not show any shock waves. Their absence leads support to a new hypothesis that the observed oscillations at the high sweep angle are separation induced oscillations(SIO) due to the presence of leading edge separation vorticies and not due to shock induced oscillations as previously proposed before this study. Figure 6 shows the aeroelastic responses at $25°$ and $67.5°$ sweep angles. Low damping at high sweep as predicted by XTRAN3S-Ames might have made the wing susceptible to the observed oscillations. Details are given in reference 11. This research demonstrated an important application of time accurate CFD to a crucial practical problem.
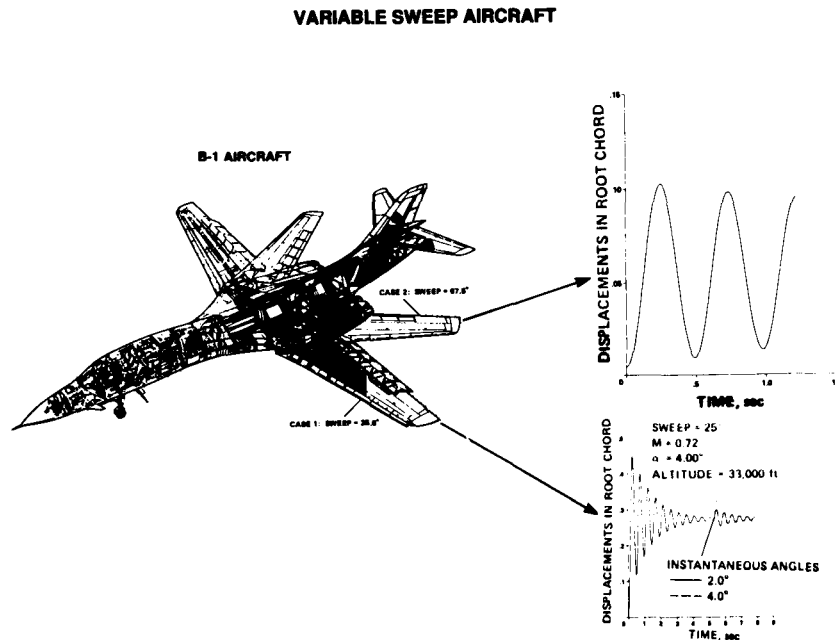
VARIABLE SWEEP AIRCRAFT

FIGURE 6

Transonic Aeroelasticity Wings with Tip Stores

The presence of tip stores influences both aerodynamic and aeroelastic performances of wings. Such effects are more pronounced in the transonic regime. One of the major advantages of TSP equations is the simplicity of adding new geometry capability to the finite difference grid. As a result, transonic aeroelasticity of wings with tip stores was studied by a theoretical method using the TSP equations coupled with modal structural equations of motion. This new capability was added to XTRAN3S-Ames. Unsteady aerodynamics on the oscillating F-5 wing with a tip missile compared well with the experiment. Aeroelastic computations on a typical rectangular wing indicated that tip store unsteady aerodynamics can make the wing aeroelastically less stable. Aeroelastic computations were also made for a typical fighter wing with a tip store. Computations showed that it is important to account for the aerodynamics of the tip store particularly in the transonic regime where the tip store can make the wing aeroelastically less stable. Details of this work are presented in reference 12. Figure 7 shows the effect of a tip missile on the aeroelastic response of a fighter wing. The unsteady aerodynamic forces of the tip missile decreases the aeroelastic damping of the wing response.

EFFECT OF TIP MISSILE ON FIGHTER WING RESPONSE

10% TIP MASS
M = 0.90, ALTITUDE = 30,000 ft

——— WITH MISSILE — — —WITHOUT MISSILE

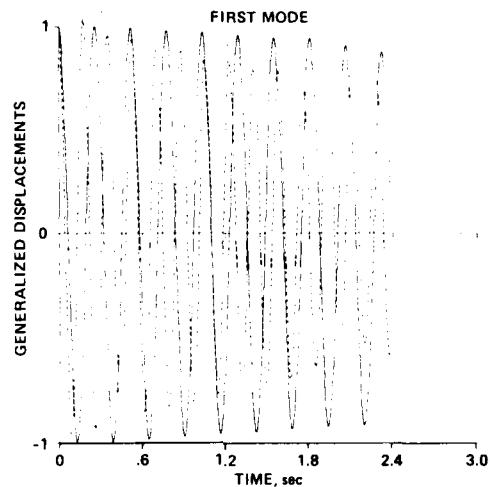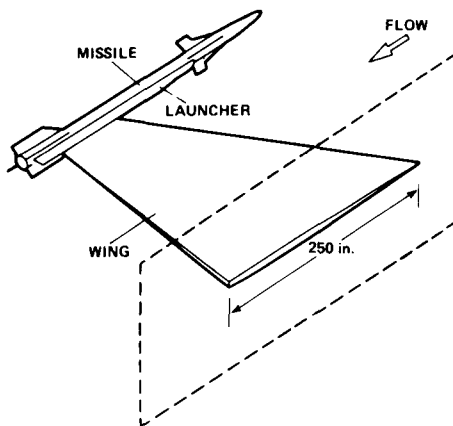A TYPICAL FIGHTER WING CONFIGURATION WITH TIP MISSILE

FIGURE 7

An Integrated Approach for Aeroelasticity of Actively Controlled Wings

Use of active controls is important for future aircraft which will tend to be more flexible for high maneuverability. So far, the theoretical aeroelastic studies with active control surfaces have been restricted to the linear subsonic and supersonic regimes. In the non-linear transonic flows, the combined effect of the shock wave and the flow discontinuity due to the presence of the hinge line of the control surface can have a strongly coupled influence on aeroelastic performances of wings. To study such a strongly coupled phenomenon, an integrated approach was developed and has been implemented in XTRAN3S-Ames. It is noted that to study the coupling of complex physical systems like non-linear flows and wing structures, it is important to use well understood equations and solution procedures such as those used in XTRAN3S. Studies showed that shock waves play an important role in active controls and the control laws which do not account for strong coupled phenomena of fluids and structures may not be effective in the transonic regime. Details are presented in reference 13. Figure 8 shows the effect of the active control surface on the twisting modal response of a typical fighter wing. Since the present study is in the time domain, it can be used as a "numerical flight simulator" to complement wind tunnel and flight tests.

EFFECT OF CONTROL SURFACE ON RESPONSES OF FIGHTER WING
CONTROLLING THE TWISTING MODE

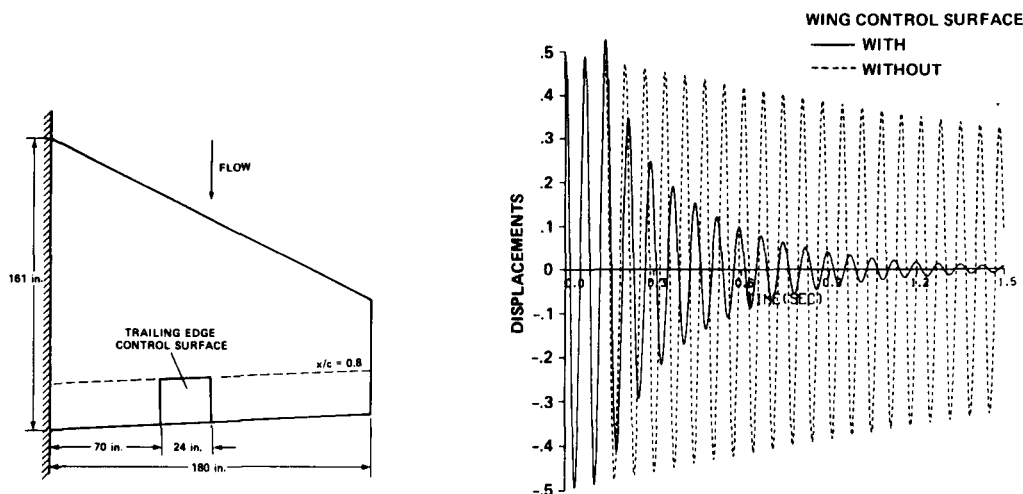M = 0.90, Q = 2.476 psi, GAIN = 40.0
TWISTING MODE

FIGURE 8

Unsteady Transonics of Wings at Supersonic Freestreams

Flow remains nonlinear and transonic in nature for Mach numbers slightly above one. As a result, rapid variations in aerodynamic forces can still occur due to unsteady motions of the wing. Therefore it is important to study the aeroelastic characteristics at low supersonic freestream conditions since critical aeroelastic phenomenon similar to that for transonic freestream conditions can still occur. Supersonic freestream capability was first implemented in the transonic code ATRAN2 (ref. 14). the improved version of LTRAN2. This required the use of different far field boundary conditions than those used for transonic freestream conditions. Due to the lack of manpower and need, no effort was made to implement these modifications into early versions of XTRAN3S. Now there is a need for time accurate aeroelastic computations at supersonic freestreams for advanced fighter aircraft. In this work the capability of XTRAN3S-Ames has been extended to handle supersonic freestream conditions. The far field boundary conditions were modified following the approach given in ref. 13 which is based on the propagation of pressure waves along the flow characteristics. Successful steady and unsteady computations were made for the rectangular and fighter wings at supersonic freestream conditions. Figure 9 shows the good comparison of unsteady pressures computed from XTRAN3S with the experimental data at M = 1.3. This new capability is being incorporated in the official XTRAN3S with wing body capability.
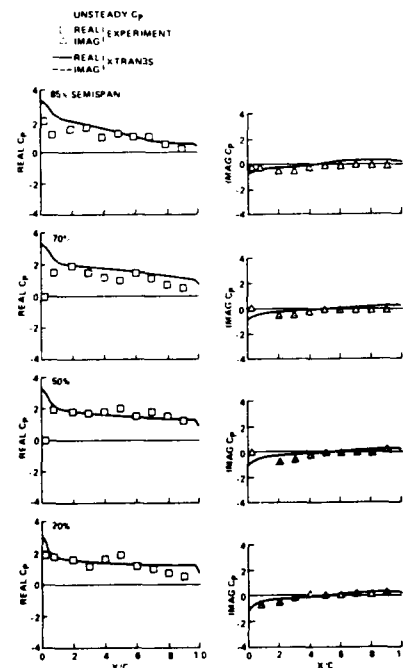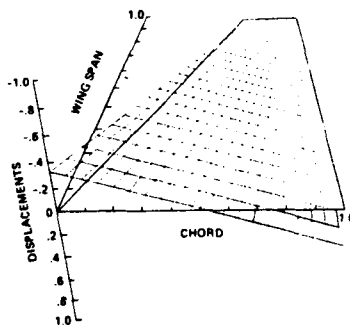
F5-WING, M = 1.33, α = 0°, k = 0.396 (40 Hz)

FIGURE 9

56

Unsteady Transonics of Full-Span Wing-Body Configurations

In the development of CFD it appears that there is more emphasis on using new equations and methods than on adding the geometry and flow physics capabilities. For example, limited effort has been put into extending the powerful TSP theory for unsteady computations of full aircraft, though the steady wing-body computations using TSP were done a decade ago. The presence of a body influences both the aerodynamic and aeroelastic performance of wings. Such effects are more pronounced in the transonic regime. To accurately account for the effect of the body, particularly when the wings are experiencing asymmetric modal motions, it is necessary to model the full configuration in the nonlinear transonic regime. In this study, full-span wing-body configurations are simulated for the first time by using the unsteady TSP equations and it has been incorporated in XTRAN3S-Ames. The body geometry is modeled exactly as the physical shape, instead of as a rectangular box, which has been done in the past. Steady pressure computations for wing-body configurations compare well with the available experimental data. Unsteady pressure computations when the wings are oscillating in asymmetric modes show significant influence of the body. The details are given in reference 15. Figure 10 shows steady pressures on the body (comparing well with the experiment) and also the effect of asymmetry on the unsteady lifting forces of the wing.
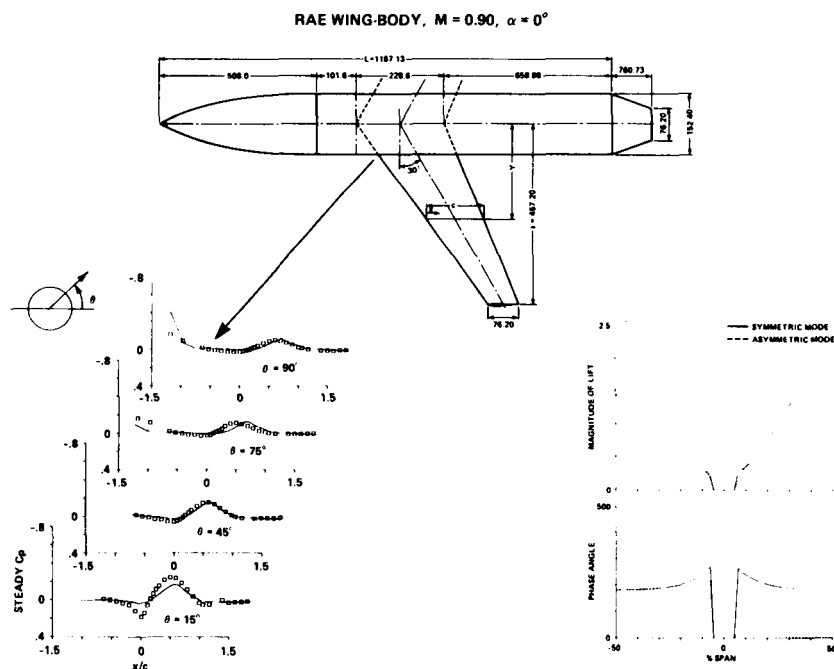

FIGURE 10

A New Algorithm for Unsteady Euler Equations

One of the most successful ideas used in the calculation of transonic flows is the one of Murman-Cole to use different types of differencing for the regions of subsonic and supersonic flows. Central differencing is used in subsonic regions of the flow and upwind differencing is used in supersonic regions of the flow. This change of the algorithm takes into account the fundamentally different characteristics of subsonic and supersonic flows. The previous section of this paper has shown the successful application of the Murman-Cole switch modified by Jameson's rotated differencing scheme to unsteady transonic flow computations on wing-body configurations. Motivated by the success of the type dependent differencing for potential equations, a similar method has been developed (ref. 16) for the Euler equations. This new algorithm uses flux vector splitting in combination with the concept of rotating the coordinate system to the local streamwise direction. The flux vector biasing is switched from upwind for supersonic flow to downwind for subsonic flow. Several one-dimensional calculations for steady and unsteady transonic flows demonstrated the stability and accuracy of the algorithm. Unsteady results were demonstrated for an airfoil whose thickness varies in time. Figure 11 shows the pressure coefficient plots for three times at which the shock wave is increasing in strength and time accurately moving downstream.

UNSTEADY EULER ALGORITHM FOR TRANSONIC FLOW

- NEW ALGORITHM IS BASED ON ADI, FLUX SPLITTING, SWITCHING AT SHOCKS, AND ROTATING DIFFERENCING
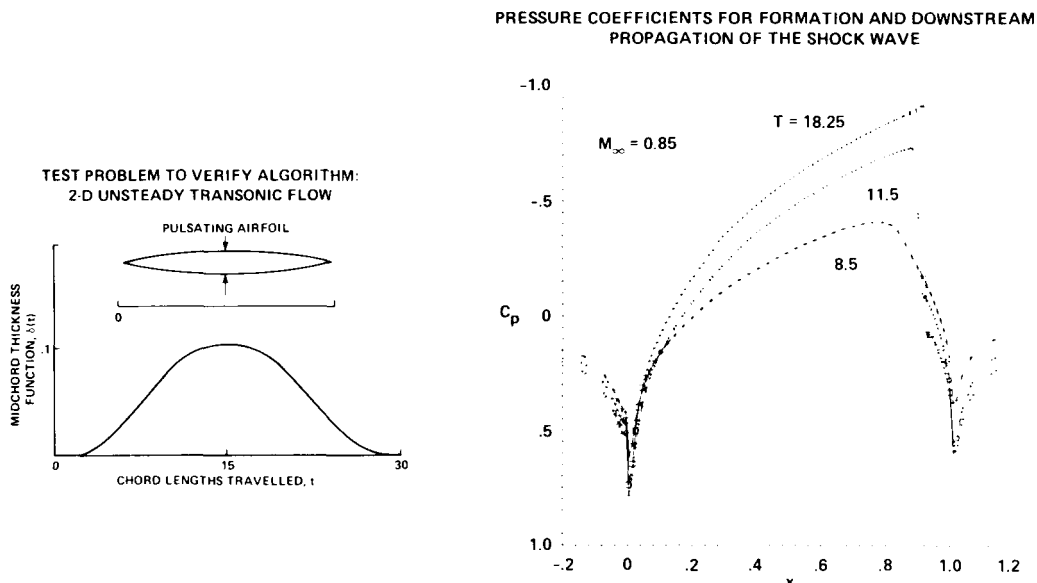
PRESSURE COEFFICIENTS FOR FORMATION AND DOWNSTREAM PROPAGATION OF THE SHOCK WAVE

TEST PROBLEM TO VERIFY ALGORITHM: 2-D UNSTEADY TRANSONIC FLOW

PULSATING AIRFOIL

FIGURE 11

Future Directions and Concluding Remarks

Since about 1978 to date, CFD for aeroelasticity has progressed from solving simple airfoils to almost complete aircraft by using TSP theory. Now industry has a computational tool such as XTRAN3S to simultaneously solve structures and aerodynamics for transonic flows at small angles of attack. Most of the aeroelastic phenomena such as flutter occurs at small angles of attack. As illustrated in this paper, time accurate simultaneous solution of structures and aerodyamics is essential to properly understand the physics of real world aeroelastic problems. The computational efficiency of XTRAN3S has been improved by a factor of about 100 since its first release. The present version, 1.10, of XTRAN3S can make time accurate unsteady transonic computations on fighter wings such as the F-5 in about 10 minutes of CRAY-XMP time. XTRAN3S can further be applied to investigate practically important time dependent aeroelastic phenomenon such as the one illustrated for active controls in this paper. During the last decade CFD without structural coupling has advanced fairly well to the use of Euler/Navier Stokes equations. This has lead to the development of codes such as TNS, a Transonic Navier Stokes code for full aircraft analysis(ref. 4). However, these developments have been mostly restricted to steady computations. New algorithms are being developed to make time accurate unsteady computations(ref. 16). These new tools along with other CFD techniques, such as the zonal grid approach developed for the TNS code(see Figure 12 for typical steady results), need to be extended for aeroelastic computations of full aircraft with complex flows.
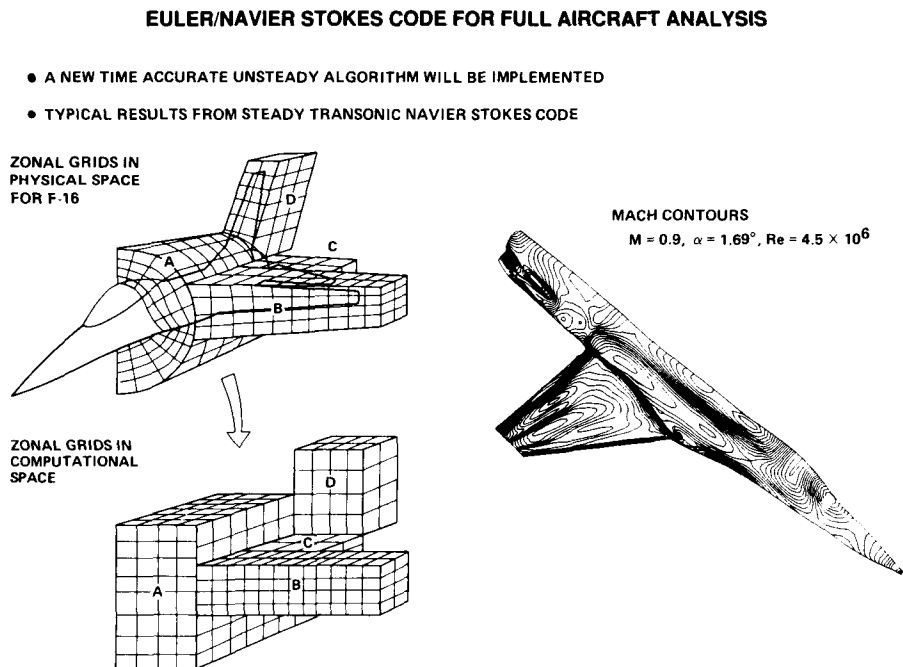
EULER/NAVIER STOKES CODE FOR FULL AIRCRAFT ANALYSIS

- A NEW TIME ACCURATE UNSTEADY ALGORITHM WILL BE IMPLEMENTED

- TYPICAL RESULTS FROM STEADY TRANSONIC NAVIER STOKES CODE

FIGURE 12

References

[1] Goorjian, P. M., "Computations of Unsteady Transonic Flows," Advances in Computational Transonic; Vol. IV in the series: Recent Advances in Numerical Methods in Fluids, Ed. W. G. Habashi, Pineridge Press Ltd. (U. K.), March, 1984.

[2] Huttsell, L. J. and Cooley, D. E., "The Background and Status of the Joint Air Force/NASA Transonic Unsteady Aerodynamic Program (XTRAN3S)," AFWAL-TM-86-154-FIBRC, Jan. 1986.

[3] Guruswamy, G. P. and Goorjian, P. M. ,"Unsteady Transonic Flow Simulation on a Full-Span Wing-Body Configuration," AIAA-87-1240. 19th Fluid Dynamics Conference, June 1987, Honolulu, Hawaii.

[4] Flores, J. "Simulation of Transonic Viscous Wing and Wing-Fuselage Flows Using Zonal Methods," NASA TM 89421, Mar. 1987.

[5] Ballhaus, W.F. and Goorjian, P.M., "Implicit Finite Difference Computations of Unsteady Transonic Flows About Airfoils," AIAA Journal, Vol. 15, Dec. 1977, pp. 1728-1735.

[6] Guruswamy, P. and Yang, T. Y., "Aeroelastic Time Response Analysis of Thin Airfoils by Transonic Code LTRAN2," Computers and Fluids, Vol. 9, No. 4, Dec. 1980, pp. 409-425.

[7] Borland, C. J. and Rizzetta, D. P., "Nonlinear Transonic Flutter Analysis About Airfoils," AIAA Journal, Vol. 20, No. 11, Nov. 1982, pp. 1606-1605.

[8] Guruswamy, P. and Goorjian, P. M., "Computations and Aeroelastic Applications of Unsteady Transonic Aerodynamics About Wings," Journal of Aircraft, Vol. 21, No. 1, Jan. 1984, pp. 37-43.

[9] Myers, M. R., Guruswamy, P. and Goorjian, P. M. "Flutter Analysis of a Transport Wing Using XTRAN3S," AIAA paper No. 83-0922, May 1983.

[10] Guruswamy, P. and Goorjian, P. M., "Efficient Algorithm for Unsteady Transonic Aerodynamics of Low-Aspect Ratio Wings," Journal of Aircraft, Vol. 22, No. 3, March 1985, (Also AIAA Paper No. 84-0872-CP, May 1984.)

[11] Guruswamy, G. P., Goorjian, P. M., Ide, H. and Miller, G. D.,"Transonic Aeroelastic Analysis of the B-1 Wing," Journal of Aircraft, Vol. 23, No. 7, July 1986, pp. 547-553.

[12] Guruswamy, G. P., Goorjian, P. M., and Tu, E. L, "Transonic Aeroelasticity of Wings Tip Stores," AIAA-86-1007-CP, April, 1987. (will appear in the Journal of Aircraft)

[13] Guruswamy, G. P., Tu, E. L, and Goorjian, P. M., "Transonic Aeroelasticity of Wings with Active Control Surfaces," AIAA-87-0709-CP, 28 Structural Dynamics Conf., Monterey, California, April, 1987.

[14] Chow, L. J. and Goorjian, P. M., "Implicit Unsteady Transonic Airfoil Calculations at Supersonic Freestreams," AIAA-82-0934, AIAA/ASME 3rd Joint Thermophysics Fluids, Plasma and Heat Transfer Conference, St. Louis, Missouri, June 1982.

[15] Guruswamy, G. P. and Goorjian, P. M., "Unsteady Transonic Flow Simulation on a Full-Span-Wing-Body Configuration," AIAA-87-1240-CP, 19 Fluid Dynamics Conf., Honolulu, Hawaii, June 1987.

[16] Goorjian, P. M., "Algorithm Developments for the Euler Equations with Transonic Calculations of Transonic Flows," AIAA-87-0536, AIAA 25th Aerospace Sciences Meeting, Reno, Jan 1987.

CAP-TSD: A PROGRAM FOR UNSTEADY TRANSONIC ANALYSIS OF REALISTIC AIRCRAFT CONFIGURATIONS

John T. Batina
David A. Seidel
Samuel R. Bland
Robert M. Bennett
Unsteady Aerodynamics Branch
NASA Langley Research Center
Hampton, Virginia

OVERVIEW

The presentation describes the development of a new transonic code to predict unsteady flows about realistic aircraft configurations. The work has been a major research activity over the past year within the Unsteady Aerodynamics Branch at NASA Langley Research Center. The presentation first describes an approximate factorization algorithm for solution of the unsteady transonic small-disturbance (TSD) equation. Because of the superior stability characteristics of the AF algorithm, a new transonic aeroelasticity code has been developed which is described in some detail. The new code was very easy to modify to include the additional aircraft components, so in a very short period of time the code has been developed to treat complete aircraft configurations. Finally, applications are presented which demonstrate many of the geometry capabilities of the new code.

- Describe Approximate Factorization (AF) algorithm

- Demonstrate superior stability characteristics of AF algorithm

- Introduce new transonic aeroelasticity code

- Describe complete aircraft modeling

- Applications

APPROXIMATE FACTORIZATION ALGORITHM DEVELOPED

A new algorithm based on approximate factorization (AF) was recently developed by Batina (Ref. 1) for the time-accurate solution of the unsteady TSD equation. The AF algorithm involves a Newton linearization procedure coupled with an internal iteration technique. In Ref. 1 the AF algorithm was shown to be very robust and efficient for application to either steady or oscillatory transonic flows with subsonic or supersonic freestream conditions. The new algorithm can provide accurate solutions in only several hundred time steps yielding a significant computational cost savings when compared to alternative methods. Furthermore, the AF algorithm is fully vectorizable which results in an additional saving of computer resources.

- Time-accurate solution of TSD equation

- Involves Newton linearization coupled with internal iterations

- Stable for relatively large time steps

- Fully implicit and vectorizable in all three coordinate directions

- Enables supersonic freestream calculations

APPROXIMATE FACTORIZATION ALGORITHM OVERVIEW

Shown here is a brief overview of the AF algorithm. A much more detailed description is given in Ref. 1. Basically, if the TSD equation is written in general form as $R(\phi^{n+1}) = 0$, then the solution is given by iteration of the Newton linearization. In this equation, $\Delta\phi$ is equal to $\phi^{n+1} - \phi^*$ where ϕ^* is the currently available value of ϕ^{n+1}. During convergence of the iteration procedure, $\Delta\phi$ is driven to zero so the solution is given by ϕ^*. The equation is solved numerically by approximately factoring $\partial R/\partial\phi$ into a triple product of operators and then sequentially applying the operators using three sweeps through the grid.

- ● TSD equation general form

$$R(\phi^{n+1}) = 0$$

- ● Solution by Newton linearization and internal iteration

$$R(\phi^*) + \left(\frac{\partial R}{\partial\phi}\right)_{\phi = \phi^*} \Delta\phi = 0$$

$$\text{where } \Delta\phi = \phi^{n+1} - \phi^*$$

- ● AF Algorithm

$$L_\xi L_\eta L_\zeta \Delta\phi = -R(\phi^*)$$

$$\text{where } L_\xi L_\eta L_\zeta \approx \left(\frac{\partial R}{\partial\phi}\right)_{\phi = \phi^*}$$

66

CONVERGENCE STUDY FOR UNSTEADY APPLICATIONS

With the AF algorithm, the step size may now be selected based on accuracy, rather than on numerical stability. To demonstrate this, a convergence study was performed for the F-5 wing at M = 0.9, to determine the largest step size that would produce converged results. Unsteady results were obtained using 100, 200, 300, and 400 steps per cycle of motion which required Δt = 0.2293, 0.1147, 0.0764, and 0.0573, respectively. The calculation for 100 steps per cycle produced reasonable results but fairly large differences were observed with the 200 steps per cycle calculation. As shown in this figure, the results for 200 and 300 steps per cycle are very similar, although there are small differences near the leading edge and in the shock pulse region. The results for 400 steps per cycle are essentially the same as those for 300. Therefore, it takes about 300 steps per cycle to produce converged results, although the results for 200 steps per cycle may be acceptable for engineering purposes.

- F-5 wing upper surface pressures for rigid pitching at M = 0.9 and k = 0.137
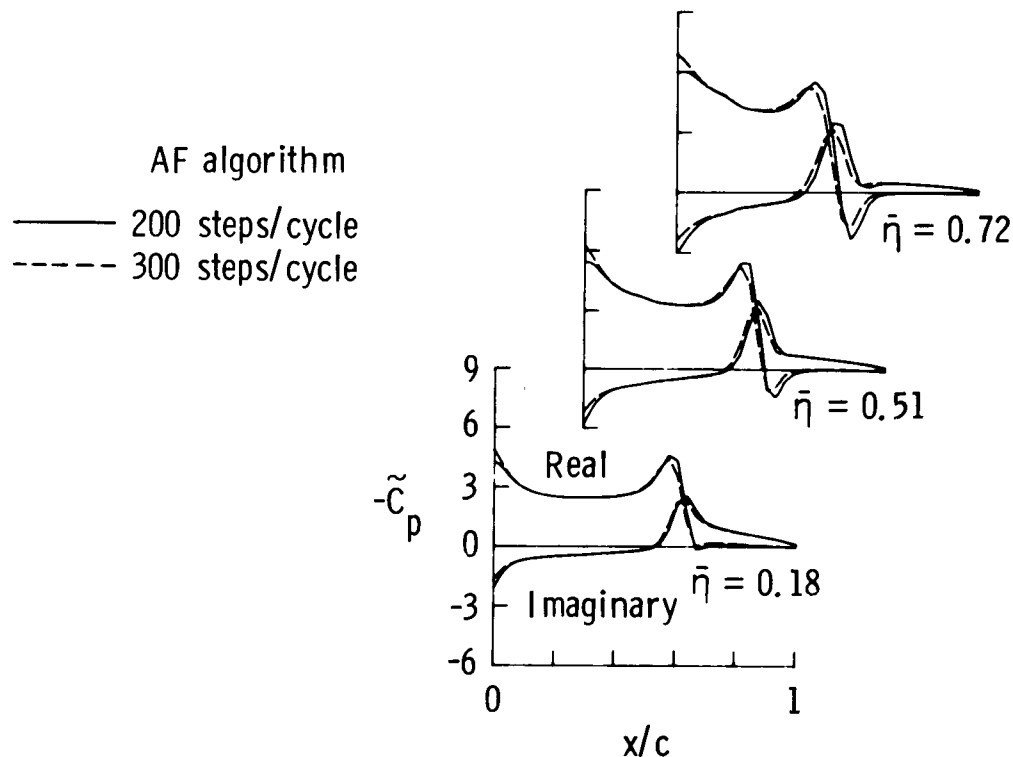
CAP-TSD: COMPUTATIONAL AEROELASTICITY PROGRAM - TRANSONIC SMALL DISTURBANCE

Because of the superior stability characteristics and computational efficiency of the AF algorithm, a new transonic code has been developed for aeroelastic applications. The new code is called CAP-TSD (Ref. 2) which is an acronym for Computational Aeroelasticity Program - Transonic Small Disturbance. As the name implies, the code solves the unsteady transonic small-disturbance equation based on the AF algorithm. The purpose of the CAP-TSD code is for static and dynamic aeroelastic applications. The code is highly vectorized and thus is very fast. In comparison with XTRAN3S, for example, CAP-TSD is about six times faster on a per time step basis. Also, the code is capable of treating complete aircraft configurations.

● Based on approximate factorization algorithm

● Static and dynamic aeroelastic applications

● Code is highly vectorized: very fast

XTRAN3S V1.5	CAP - TSD
0.62 CPU SEC/Δt	0.1 CPU SEC/Δt

● Computational expense ~ N $(=\frac{T}{\Delta t}) \times$ CPU SEC/Δt

Potential savings factor ~ $20 \times 6 \geq 100$

● Capable of treating complete aircraft configurations

# COMPLETE AIRCRAFT MODELING WITH CAP-TSD

This includes multiple lifting surfaces, the fuselage, pylons/stores/nacelles, as well as leading and trailing edge control surfaces. Furthermore, these components may be arbitrarily placed within the computational domain to allow for a full-span modeling capability. With this capability, one can then treat antisymmetric mode shapes or unsymmetric geometries such as an oblique wing or even unsymmetric store configurations.

- Multiple lifting surfaces (canard/wing/tail)

- Fuselage

- Pylons/stores/nacelles

- Leading and trailing edge control surfaces

- Components may be arbitrarily placed within computational domain
  - Full span capability
  - Antisymmetric mode shapes or unsymmetric geometries allowed

COMPLETE AIRCRAFT MODELING WITH CAP-TSD

Shown here are several of the complex configurations that have been modeled using CAP-TSD. The figure illustrates how combinations of lifting surfaces and bodies are used to model realistic geometries.

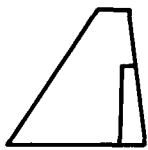- NLR F-5 wing/tiptank/pylon/store
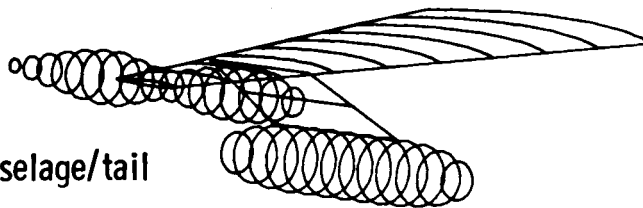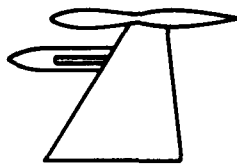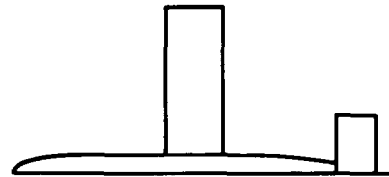
- DFVLR wing/fuselage/tail
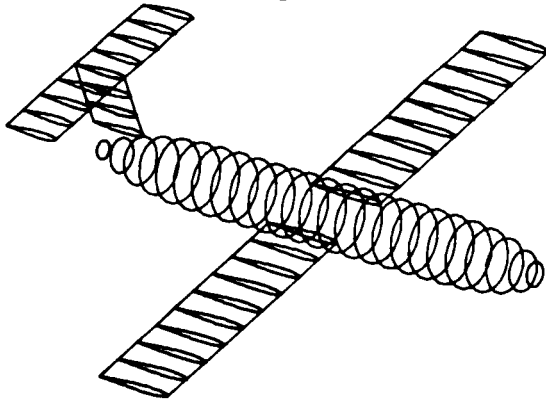
- F-16 aircraft
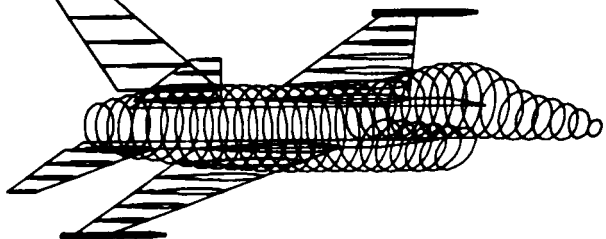
CONFIGURATIONS ANALYZED USING CAP-TSD

Results are presented next for the five configurations shown here, which demonstrate many of the CAP-TSD geometry capabilities. These configurations range in geometrical complexity from a simple wing with control surface to a realistic fighter geometry. The five configurations were selected to assess various geometry capabilities of CAP-TSD by making comparisons with the experimental pressure data of Refs. 3-9. The configurations include: The F-5 wing with an inboard trailing edge control surface (Ref. 3); the F-5 wing with an area-ruled tiptank and underwing pylon/store (Refs. 4 and 5); a simple wing/fuselage/tail configuration that was tested at the DFVLR (Ref. 6); a canard/wing/fuselage model tested by Rockwell (Ref. 7); and finally, the General Dynamics one-ninth scale F-16C aircraft model (Ref. 8).
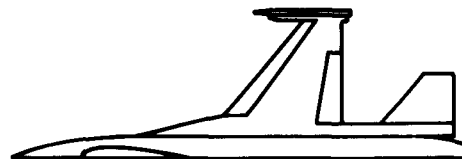
F-5 wing/
control surface

F-5 wing/tiptank/
pylon/store

DFVLR wing/
fuselage/tail

Rockwell canard/
wing/fuselage

General Dynamics
F-16C aircraft model

RESULTS FOR F-5 WING/CONTROL SURFACE CONFIGURATION

Results were obtained for the F-5 wing/control surface configuration to assess the accuracy and efficiency of the CAP-TSD code for oscillatory control surface applications. The wing has a panel aspect ratio of 1.58, a leading edge sweep angle of 31.9°, and a taper ratio of 0.28. The airfoil section of the F-5 wing is a modified NACA 65A004.8 airfoil which has a drooped nose and is symmetric aft of 40% chord. The control surface has a constant-percent-chord hinge line at 82% chord, inboard side edge at the wing root, and outboard side edge at 58% semispan. The calculations are compared with the experimental oscillatory pressure data from an F-5 wing model tested by Persoon, Roos, and Schippers (Ref. 3). Both subsonic and supersonic freestream cases are presented. Steady pressure distributions for these cases were presented and compared with the experimental data in Ref. 1, and therefore are not repeated here. Unsteady pressure results are described as follows.

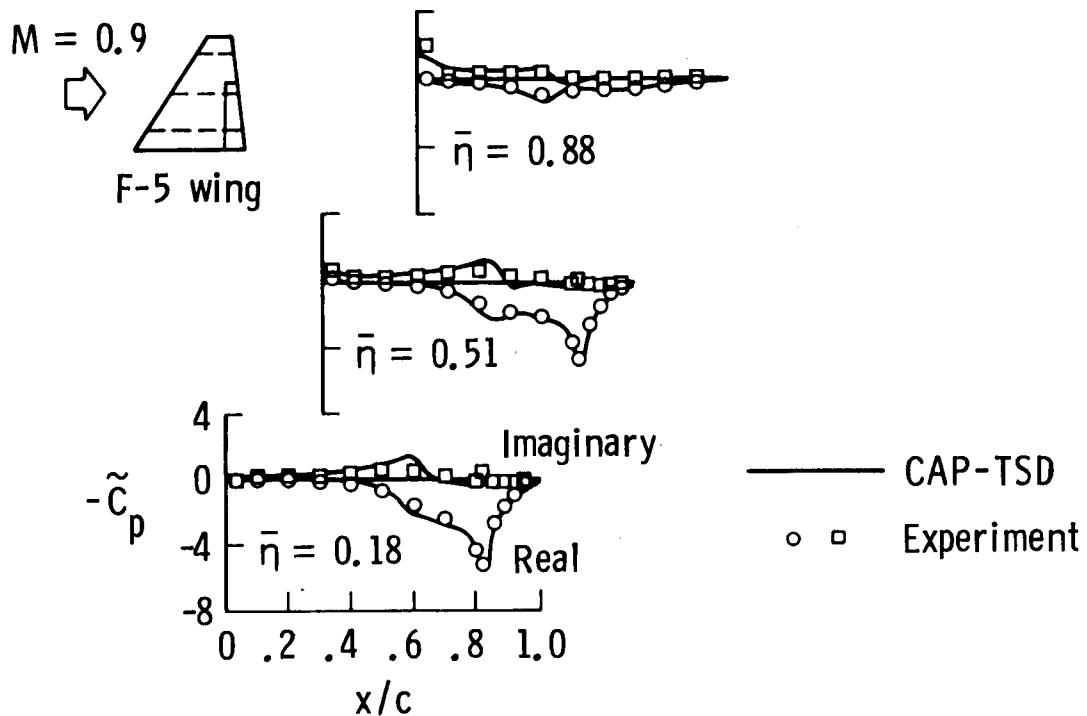- Case 1: $M = 0.9$, unsteady flow
- Case 2: $M = 1.1$, unsteady flow
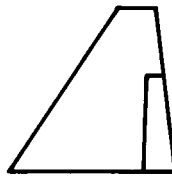
F-5 wing/
control surface

F-5 WING/OSCILLATING CONTROL SURFACE APPLICATION

At the subsonic freestream Mach number of 0.9, unsteady results were obtained for the control surface oscillating with an amplitude of 0.471° at a reduced frequency of 0.139. The calculations were performed using only 300 steps per cycle of motion which corresponds to a step size of $\Delta t = 0.07354$. Three cycles of motion were computed to obtain a periodic solution. Unsteady pressure distributions along three chords of the wing are shown in this figure along with the experimental data. These pressures are plotted as real and imaginary components corresponding to the in-phase and out-of-phase unsteady pressure distributions normalized by the amplitude of motion. The CAP-TSD results agree well with the data, especially in predicting the control surface pressures and the hinge-line singularity at 82% chord.
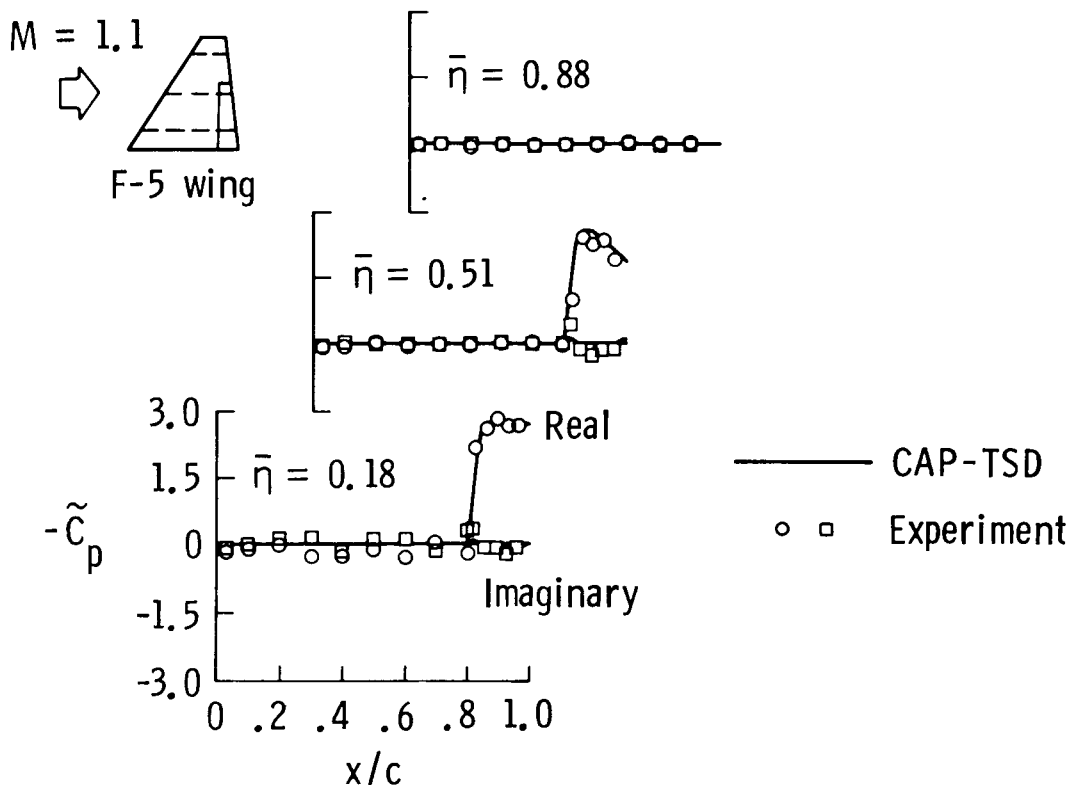
● Lower surface unsteady pressures at $\delta_1 = 0.471^{\circ}$ and $k = 0.139$

F-5 WING/OSCILLATING CONTROL SURFACE APPLICATION

At the supersonic freestream Mach number of 1.1, the unsteady results were obtained for the control surface oscillating with an amplitude of 0.45° at a reduced frequency of 0.118. These calculations were also performed using only 300 steps per cycle of motion which corresponds to a step size of Δt = 0.08875. Only two cycles of motion were required to obtain a periodic solution. Calculations for the third cycle of motion produced results that were identical to the second cycle results, to plotting accuracy. This faster convergence is due to the lack of upstream signal propagation resulting from the supersonic nature of the flow. The results indicate that the pressures on the control surface are nearly in-phase with the motion since the imaginary components are very small in comparison with the real components. Also, the pressures are zero outside of the domain of influence of the control surface which is expected for supersonic flow. The CAP-TSD results are in very good agreement with the experimental data. Further applications of CAP-TSD including comparisons with experiment for supersonic freestream cases are reported in Ref. 10.

● Upper surface unsteady pressures at δ_1 = 0.45° and k = 0.118

M = 1.1

F-5 wing

$\bar{\eta}$ = 0.88

$\bar{\eta}$ = 0.51

$\bar{\eta}$ = 0.18

3.0
1.5
0
-1.5
-3.0

$-\tilde{C}_p$

Real

Imaginary

0 .2 .4 .6 .8 1.0
x/c

———— CAP-TSD

o □ Experiment

RESULTS FOR
F-5 WING/TIPTANK/PYLON/STORE CONFIGURATION

Results were next obtained for the F-5 wing with tiptank and pylon/store to assess CAP-TSD for multiple body geometries. For this configuration, three components have been modeled in addition to the F-5 wing: (1) an area-ruled tiptank which is an axisymmetric body of revolution with a fineness ratio (length/maximum diameter) of 10.88; (2) an underwing store which is also an axisymmetric body of revolution with a fineness ratio of 7.04; and (3) a pylon which connects the store to the lower surface of the wing at 77% semispan. The tiptank and store have angles of incidence relative to the wing zero angle of attack of -2.0º and -2.5º, respectively. A more detailed description of the F-5 wing/tiptank/pylon/store configuration is given in Refs. 4 and 5 along with the experimental pressure data. The calculations were performed for combinations of F-5 components to investigate aerodynamic interference effects on steady and unsteady wing pressures. In these calculations the freestream Mach number was selected as 0.45 for comparison with the subsonic data published by the NLR.

● Case 3:   M = 0.45,   steady and unsteady flows
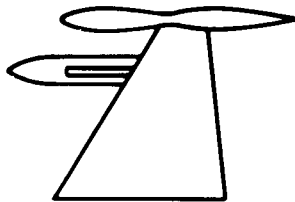
F-5 wing/tiptank/
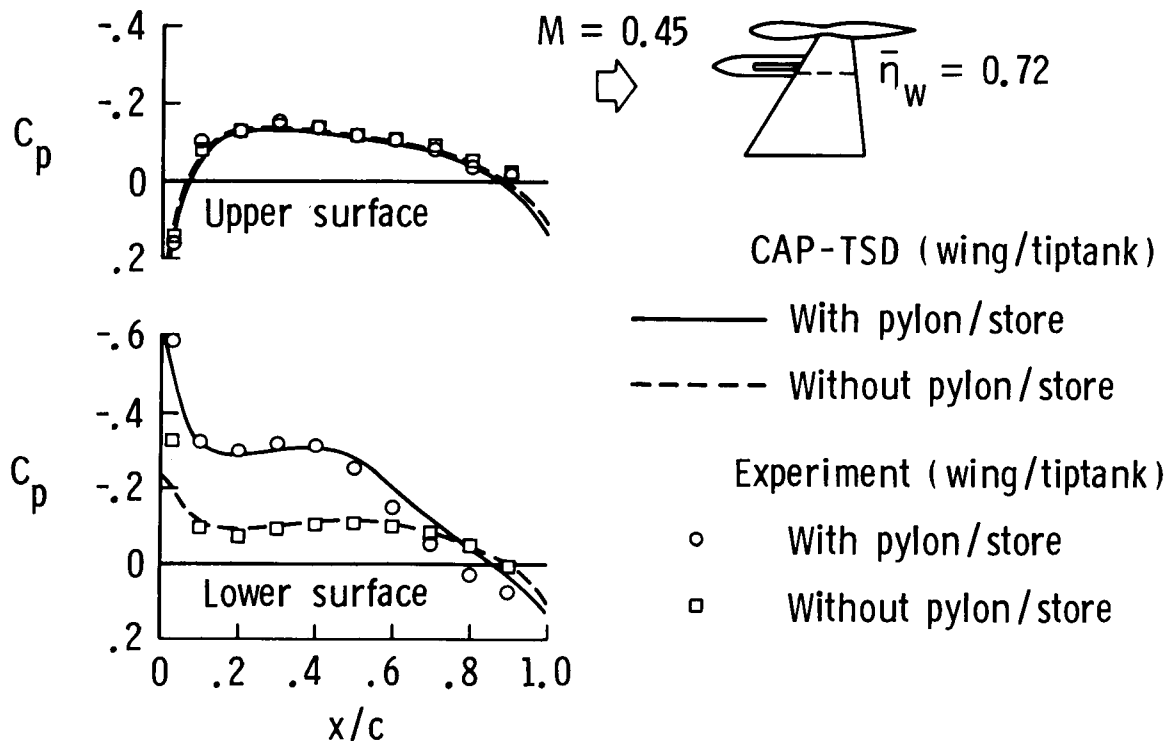pylon/store

F-5 TIPTANK STEADY PRESSURE COMPARISONS

For this case, steady pressure distributions are presented first for the tiptank, to assess the accuracy of the body modeling. Two sets of pressures are plotted corresponding to inboard (θ = 157.5°) and outboard (θ = 22.5°) longitudinal lines along the tiptank. These pressure distributions show expansions near the fore and aft maximum diameter locations and a compression near the area-ruled middle region. The calculated tiptank pressures are in good agreement with the experimental data.
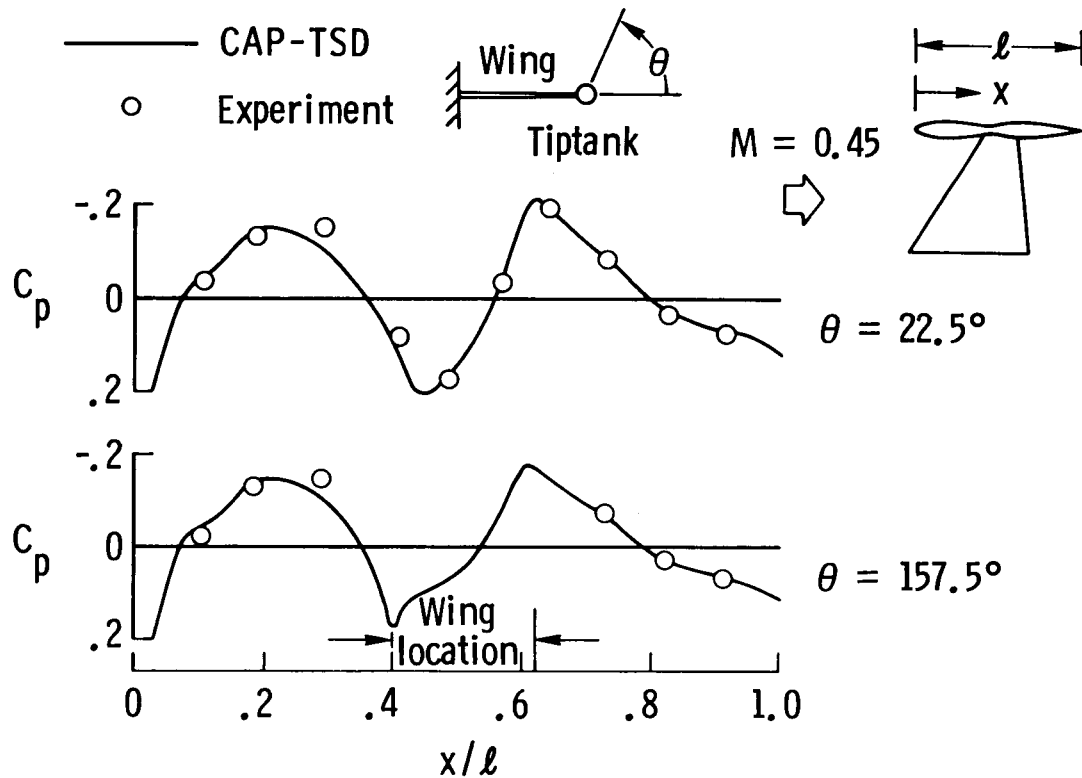
EFFECT OF PYLON/STORE ON STEADY PRESSURES

Steady pressure distributions on the wing are presented here for the 72% semispan station. Two sets of calculated and experimental results are plotted corresponding to the wing/tiptank configuration with and without the pylon/store. As shown in the lower part of the figure, inclusion of the pylon and store significantly increased the lower surface pressures from the wing leading edge to approximately 60% chord. The effect of the pylon/store on the upper surface pressures is negligible, as shown in the upper part of the figure. The calculated steady pressures for cases with and without the pylon/store compare well with the experimental data.

● F-5 wing pressures at 72% semispan station

$M = 0.45$

$\bar{\eta}_w = 0.72$

CAP-TSD (wing/tiptank)

——— With pylon/store

– – – – Without pylon/store

Experiment (wing/tiptank)

○   With pylon/store

□   Without pylon/store

EFFECT OF PYLON/STORE ON UNSTEADY PRESSURES

This figure shows the effect of the pylon/store on the unsteady pressure distributions. The unsteady calculations were performed for the configuration pitching harmonically at a reduced frequency of k = 0.147. The configuration was forced to pitch about a line perpendicular to the root at 15% chord from the wing apex. The results were obtained using 300 steps per cycle of motion which corresponds to a step size of Δt = 0.07135. Two sets of results are again presented corresponding to the wing/tiptank configuration with and without the pylon/store. As shown in the upper part of the figure, inclusion of the pylon and store increased the real component of the unsteady lifting pressure, similar to the steady-state interference effect. The effect on the imaginary part is negligible. The CAP-TSD results are again in good agreement with the experimental pressure data in predicting the aerodynamic interference effects of the pylon/store.

- F-5 configuration pitching about 15% root chord at k = 0.147
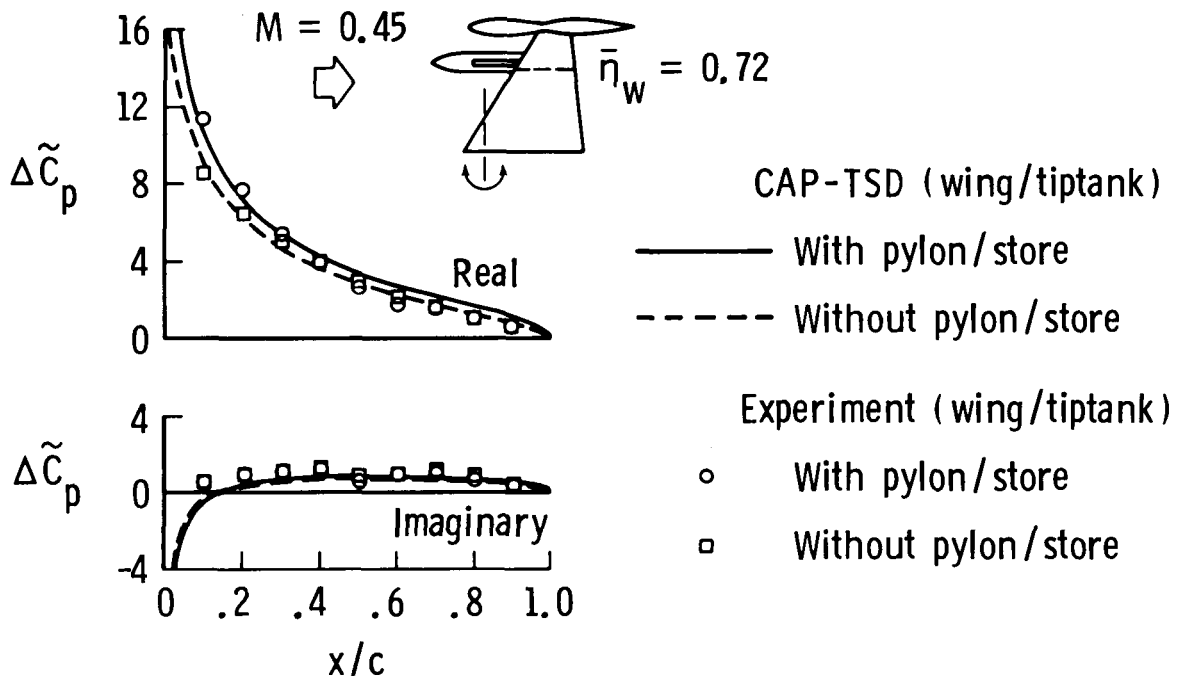
RESULTS FOR
DFVLR WING/FUSELAGE/TAIL CONFIGURATION

For the DFVLR wing/fuselage/tail configuration, results were obtained to assess the accuracy of CAP-TSD for multiple lifting surface and fuselage applications. The DFVLR configuration consists of a rectangular-planform wing that is centrally mounted to a circular cross-section fuselage with a T-tail. The wing has a panel (exposed) aspect ratio of 2.66 and an RAE 101 airfoil section (9% maximum thickness-to-chord ratio). The axisymmetric fuselage has a fineness ratio of 9.75. The horizontal tail has a panel aspect ratio of 1.5 and an RAE 101 airfoil section (12.7% maximum thickness-to-chord ratio). It is located above the wing mean plane, a distance equal to the fuselage maximum diameter, and is connected to the fuselage by the rectangular vertical tail. The DFVLR wing/fuselage/tail configuration is further described in Ref. 6 along with the low-speed experimental steady pressure data. In these calculations, the freestream Mach number was selected as 0.2 for comparison with the data. For this case as well as for the remaining complex configurations, only steady-state comparisons with experiment are given. This is because, in general, there is a lack of experimental unsteady pressure data on complex configurations to validate time-accurate computer codes.
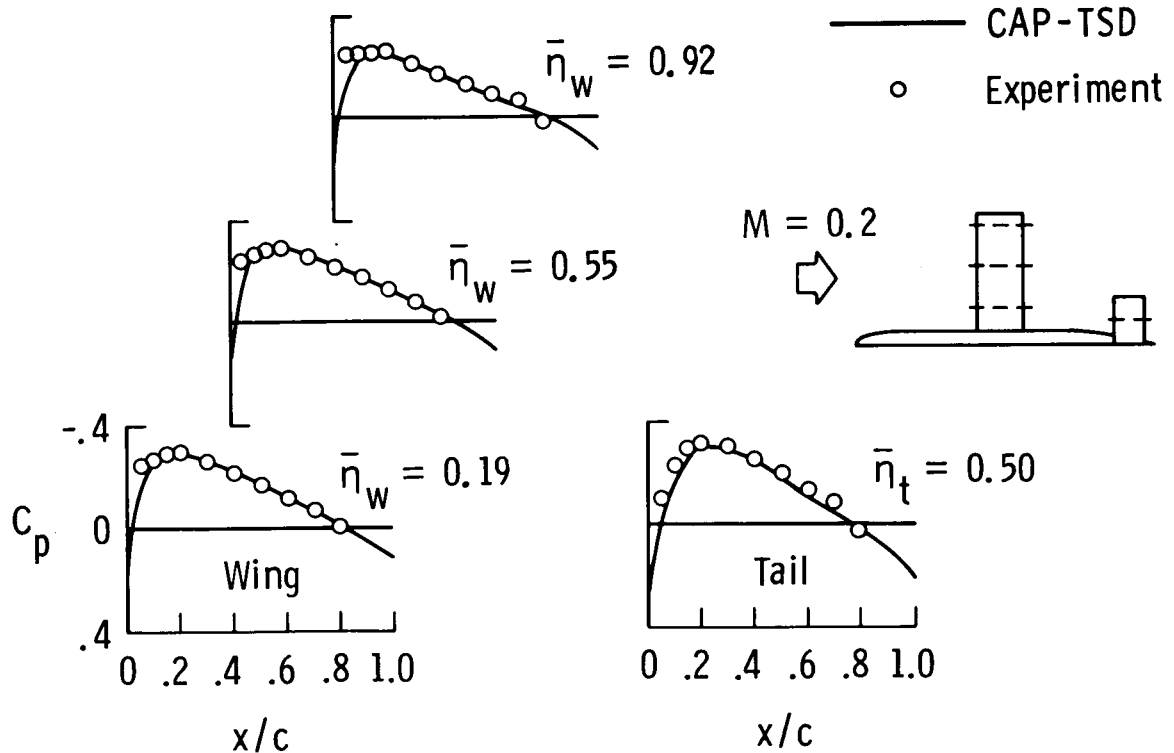
● Case 4: M = 0.2, steady flow
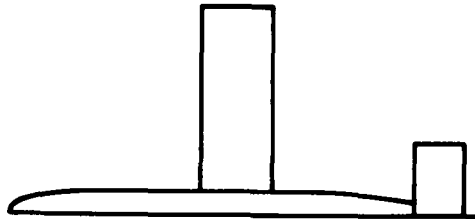
DFVLR wing/
fuselage/tail

# DFVLR CONFIGURATION STEADY PRESSURE COMPARISON

For the DFVLR configuration, comparisons of CAP-TSD and experimental steady pressures on the upper surfaces of the wing and tail are shown in the figure. Chordwise pressures along three span stations of the wing and along one span station of the tail were selected for comparison with the data. The angle of attack of the wing was 0.25°. The angle of attack for the tail and fuselage was 0.15°. The CAP-TSD results compare very well with the data along both lifting surfaces except in the vicinity of the wing leading edge.

● Wing and tail upper surface pressures at M = 0.2

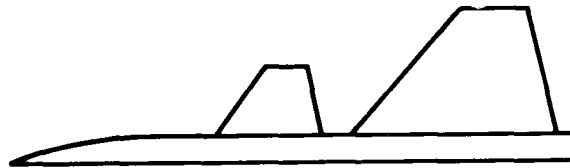# DFVLR CONFIGURATION STEADY PRESSURE COMPARISON
FOR FUSELAGE

This figure shows similar comparisons between CAP-TSD and experiment for the fuselage of the DFVLR configuration. Two sets of longitudinal pressures are plotted corresponding to the fuselage upper centerline ($\theta = 90°$) and to a line that passes close to the wing-fuselage junction ($\theta = 20°$). The calculated pressures are again in good agreement with the experimental data even in the critical wing-fuselage junction region. This good agreement thus validates the CAP-TSD code for application to multiple-component configurations such as the DFVLR wing/fuselage/tail.

● Fuselage pressures at M = 0.2
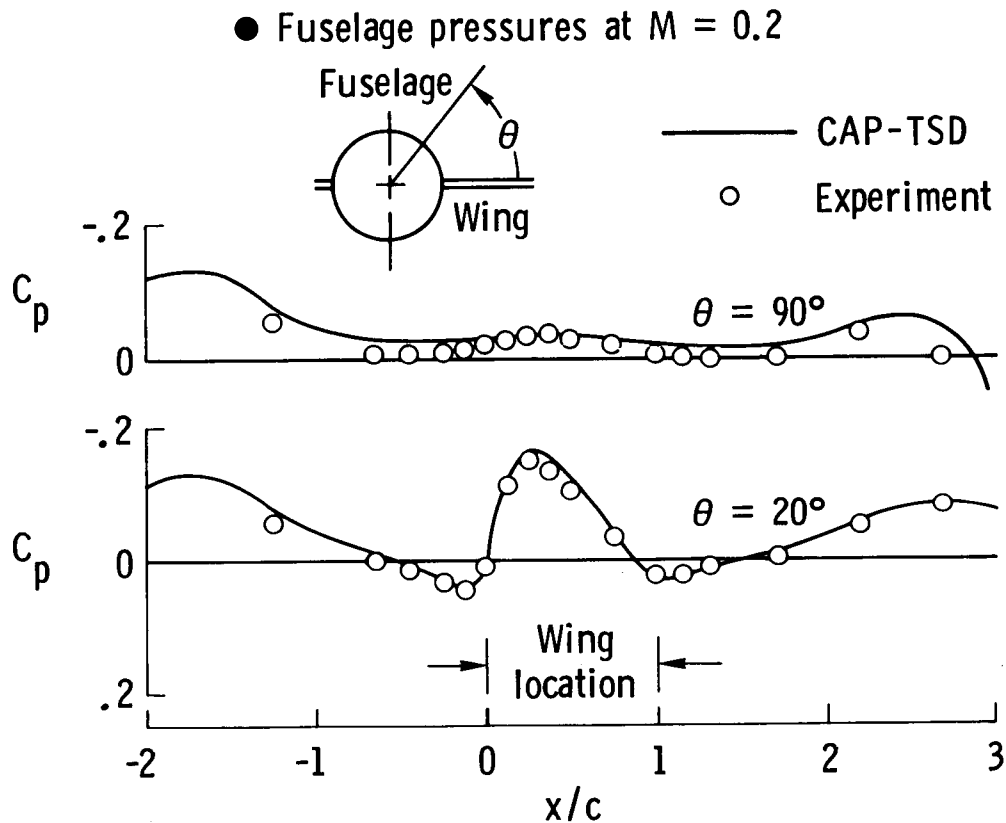
RESULTS FOR
ROCKWELL CANARD/WING/FUSELAGE CONFIGURATION

To further assess CAP-TSD for multiple lifting surface and fuselage applications, results were obtained for the Rockwell canard/wing/fuselage configuration. This configuration consists of a swept-tapered canard and wing mounted to a relatively simple half-span fuselage. Each of the non-coplanar lifting surfaces has a panel (exposed) aspect ratio of approximately 1.0, a leading edge sweep angle of 40°, a taper ratio slightly greater than 0.25, and a supercritical airfoil section. The wing also has 4° of incidence relative to the fuselage and 5° of parabolic twist washout. The Rockwell canard/wing/fuselage configuration is further described in Ref. 7 along with the experimental steady pressure data. In the CAP-TSD comparisons presented here, the freestream Mach number was 0.8.

● Case 5: M = 0.8, steady flow

Rockwell canard/
wing/fuselage

ROCKWELL CONFIGURATION STEADY PRESSURE COMPARISON

For this case, the angle of attack for both the canard and the wing was 2.05°. For the wing, this angle is added to the incidence and twist so that the root and tip are effectively at 6.05° and 1.05°, respectively. The figure shows chordwise pressures along one span station of the canard and along three span stations of the wing. The CAP-TSD pressures are in favorable agreement with the experimental data along both lifting surfaces. The small differences between calculation and experiment in the wing upper surface trailing edge region, are due to flow separation. The overpredicted pressures along the lower surface of both the canard and the wing, aft of approximately 85% chord, are due to viscous effects. Of course, flow separation and viscous effects are outside the scope of the present capability.

- Canard and wing pressures at $M = 0.8$ and $\alpha_0 = 2°$
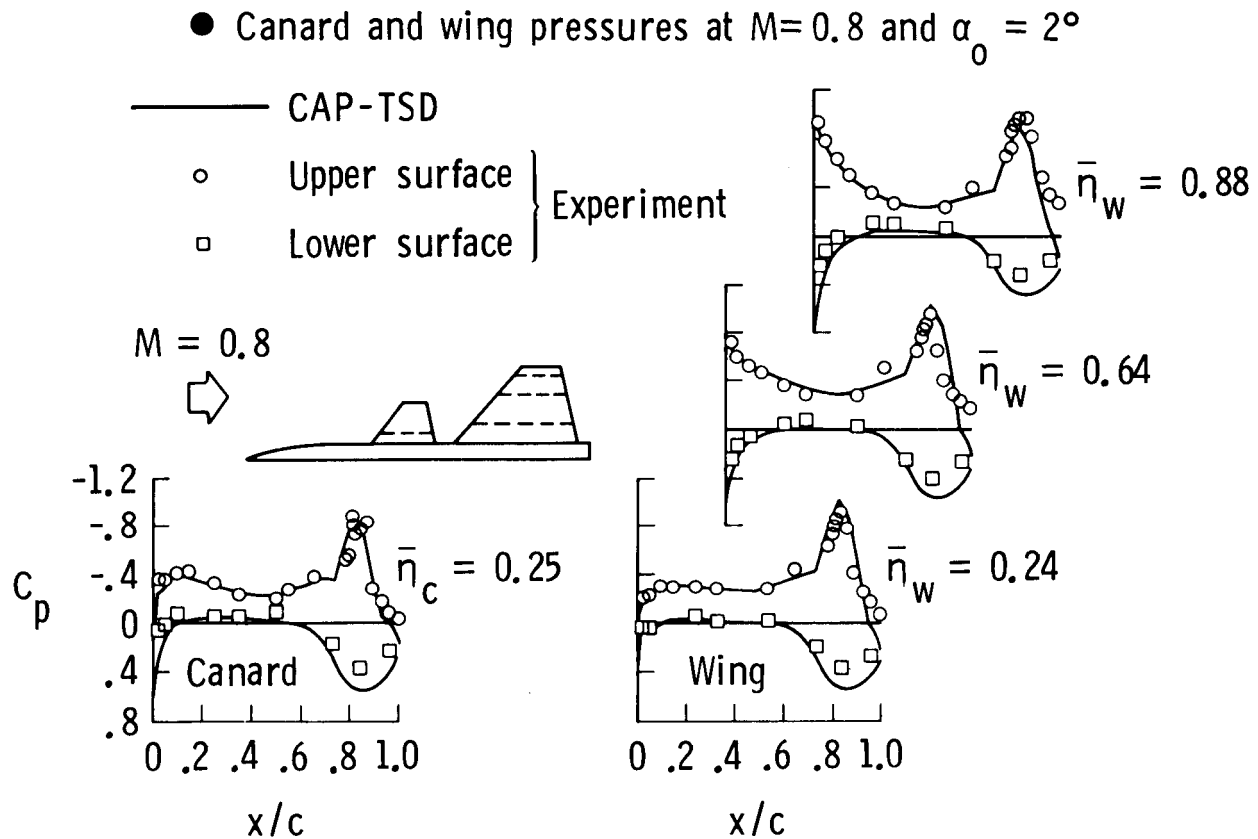
RESULTS FOR
GENERAL DYNAMICS F-16C AIRCRAFT MODEL

Finally, results were obtained for the General Dynamics F-16C aircraft model to demonstrate application of CAP-TSD to a realistic configuration. The calculations were performed for three Mach numbers including 0.85, 0.9, and 1.1. In each case, CAP-TSD results were obtained for the F-16C aircraft at approximately 2.3° angle of attack and with the leading edge control surface of the wing deflected upwards 2° for comparison with the experimental steady pressure data of Ref. 9. These steady pressure comparisons were made to assess the accuracy of CAP-TSD for complete airplane applications. All of the results were originally reported in Ref. 1. The results presented here are for the M = 0.9 case.

- Case 6: M = 0.85, steady flow
- Case 7: M = 0.90, steady and unsteady flows
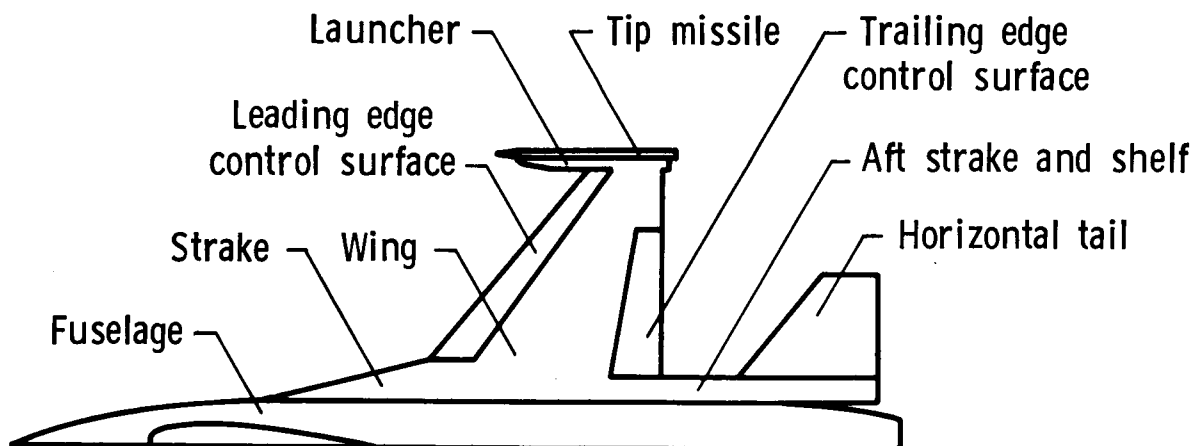- Case 8: M = 1.10, steady flow
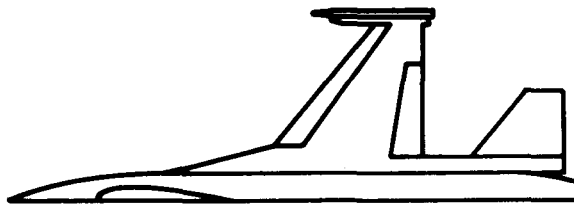
General Dynamics
F-16C aircraft model

CAP-TSD MODELING OF F-16C AIRCRAFT

In these calculations, the F-16C is modeled using four lifting surfaces and two bodies. The lifting surfaces include: (1) the wing with leading and trailing edge control surfaces; (2) the launcher; (3) a highly-swept strake, and shelf surface; and (4) the horizontal tail. The bodies include: (1) the tip missile and (2) the fuselage. Other salient features of the F-16C modeling include 3° linear twist washout for the wing, a leading edge control surface hinge line that is straight but not of constant-percent chord, and 10° anhedral for the horizontal tail. The rather detailed geometry description for the one-ninth scale F-16C aircraft model was obtained from Ref. 8 and the experimental steady pressure data is tabulated in Ref. 9. All of the calculations were performed on a cartesian grid that conforms to the leading and trailing edges of the lifting surfaces which contains 324,000 points. The grid was fairly easy to generate, even for a complex configuration such as the F-16, because it is cartesian.

There are no unsteady experimental data to validate the CAP-TSD code for time-accurate F-16C calculations. Nonetheless, an unsteady calculation was performed for the M = 0.9 case, to demonstrate the time-accurate capability. For simplicity, the calculation was performed for a rigid pitching motion where the entire F-16C aircraft was forced to oscillate about the model moment reference axis. Parallel calculations were also performed for the wing alone, to investigate the effects of aerodynamic interference by making comparisons with the complete airplane results. These wing-alone calculations were performed for the outer wing panel only, with a plane of symmetry assumed at the wing root.
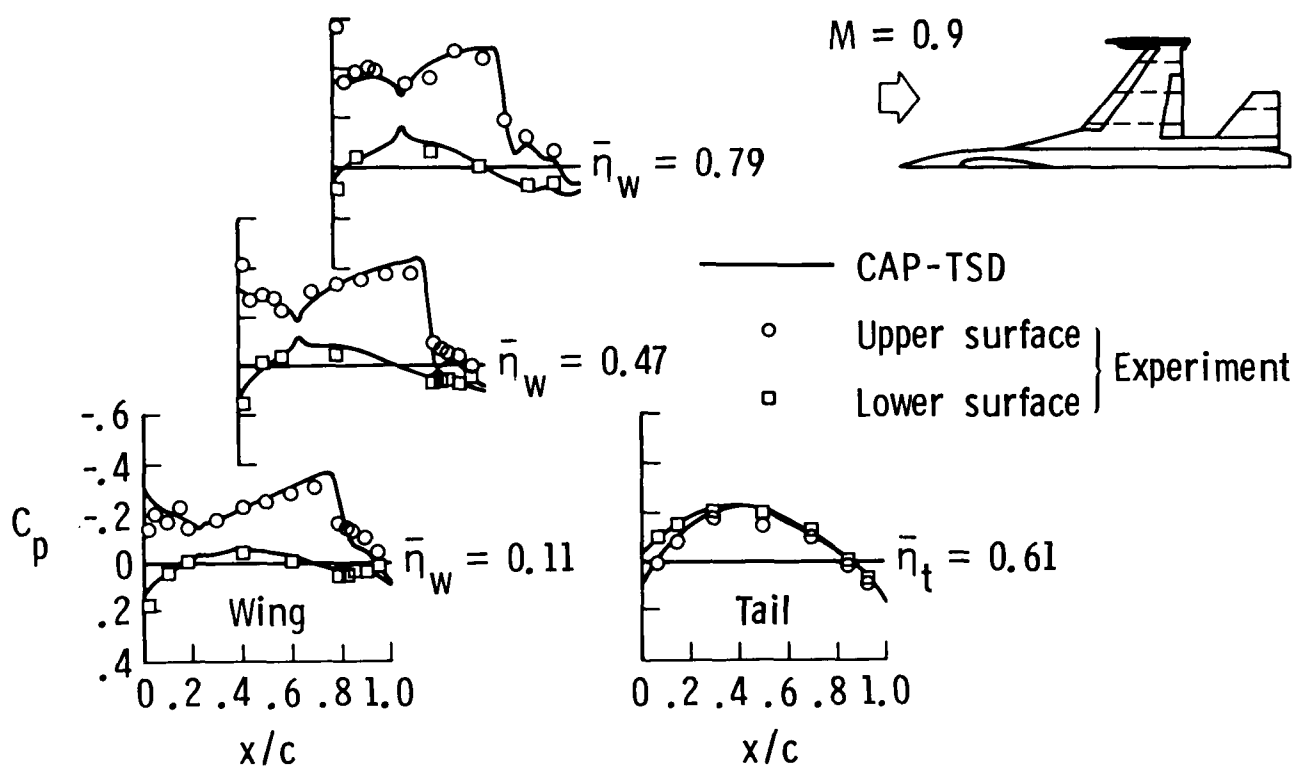
- Modeled using four lifting surfaces and two bodies
- Cartesian grid with 324 000 points

Launcher — ⌐ Tip missile ⌐ Trailing edge control surface

Leading edge control surface —

Aft strake and shelf

Strake ⌐ Wing ⌐

Horizontal tail

Fuselage ⌐

F-16C AIRCRAFT STEADY PRESSURE COMPARISON

Steady pressure comparisons are presented here for three span stations of the wing and one span station of the tail. For this case (M = 0.9), there is a moderately strong shock wave on the upper surface of the wing and the CAP-TSD pressures again generally agree well with the experimental pressures. The shock is slightly overpredicted in strength and located slightly aft of the experimental location which is expected from a conservative inviscid potential flow code. The inclusion of the nonisentropic effects (Ref. 11) and viscous effects (Ref. 12) could be expected to improve the correlation between calculation and experiment. For the tail, the flow is predominantly subcritical and the CAP-TSD pressures agree well with the experimental data. Also, the calculations required only 0.88 CPU seconds per time step on the VPS-32 computer at NASA Langley Research Center.

- **Wing and tail pressures at M = 0.9 and α_o = 2.38°**

$$M = 0.9$$

$$\bar{\eta}_W = 0.79$$

—— CAP-TSD

o   Upper surface ⎫
                  ⎬ Experiment
□   Lower surface ⎭

$$\bar{\eta}_W = 0.47$$

$$\bar{\eta}_W = 0.11$$

$$\bar{\eta}_t = 0.61$$

Wing

Tail

C_p

-.6 -.4 -.2 0 .2 .4

0 .2 .4 .6 .8 1.0
x/c

0 .2 .4 .6 .8 1.0
x/c

F-16C AIRCRAFT UNSTEADY PRESSURE COMPARISON

This figure shows the unsteady pressures for the entire F-16C aircraft undergoing a rigid pitching oscillation. Two sets of calculated pressures are compared, corresponding to complete airplane and wing alone modeling. The reduced frequency was selected as 0.1, the oscillation amplitude was chosen as $\alpha_1 = 0.5^o$, and 300 steps per cycle of motion were used. As shown in the figure, there is a relatively large shock pulse in the real part of the wing upper surface pressures. This shock pulse is of larger magnitude and is located further downstream in the complete airplane model. These features are attributed to a stronger steady-state shock on the upper surface of the wing produced by the accelerated flow about the fuselage and the launcher/tip missile. The unsteady pressures near the leading edge of the wing are also generally of larger magnitude for the complete airplane. For the tail, the unsteady pressures are relatively small in comparison with the wing pressures and thus were plotted on an expanded scale. The tail is located considerably aft of the pitch axis and thus its motion is plunge dominated which results in smaller airloads for the low value of k considered. Furthermore, these pressures are nearly 90° out of phase with the aircraft motion since the real components are small compared to the imaginary components. Also, the differences between complete airplane and wing-alone results emphasize the importance of including all of the aircraft components in the calculation.

● Upper surface pressures due to airplane pitching at $k = 0.1$

87
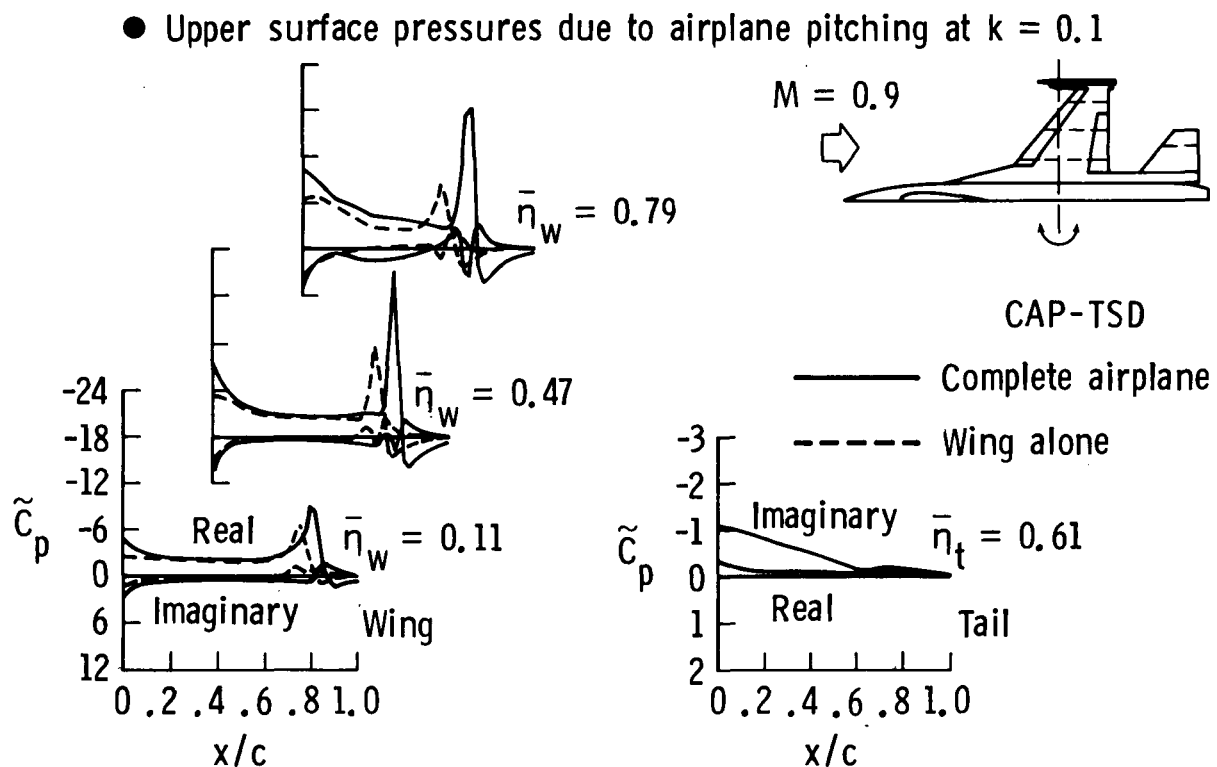
STEADY FLOW FIELD PRESSURES FOR F-16C AIRCRAFT

The following sequence of figures shows steady and unsteady pressure contours for the F-16C aircraft. The view shown in the first set of figures is an oblique projection of the aircraft. In this view, contours are plotted in vertical planes at four span stations along each wing as well as along the vehicle centerline. This figure shows the steady flow field pressures at M = 0.9 and α_0 = 2.38°. The contours indicate that there is flow compression along the leading and trailing edges of the wing and forward along the canopy. Flow expansion is indicated above the wing and fuselage, and above the canopy.
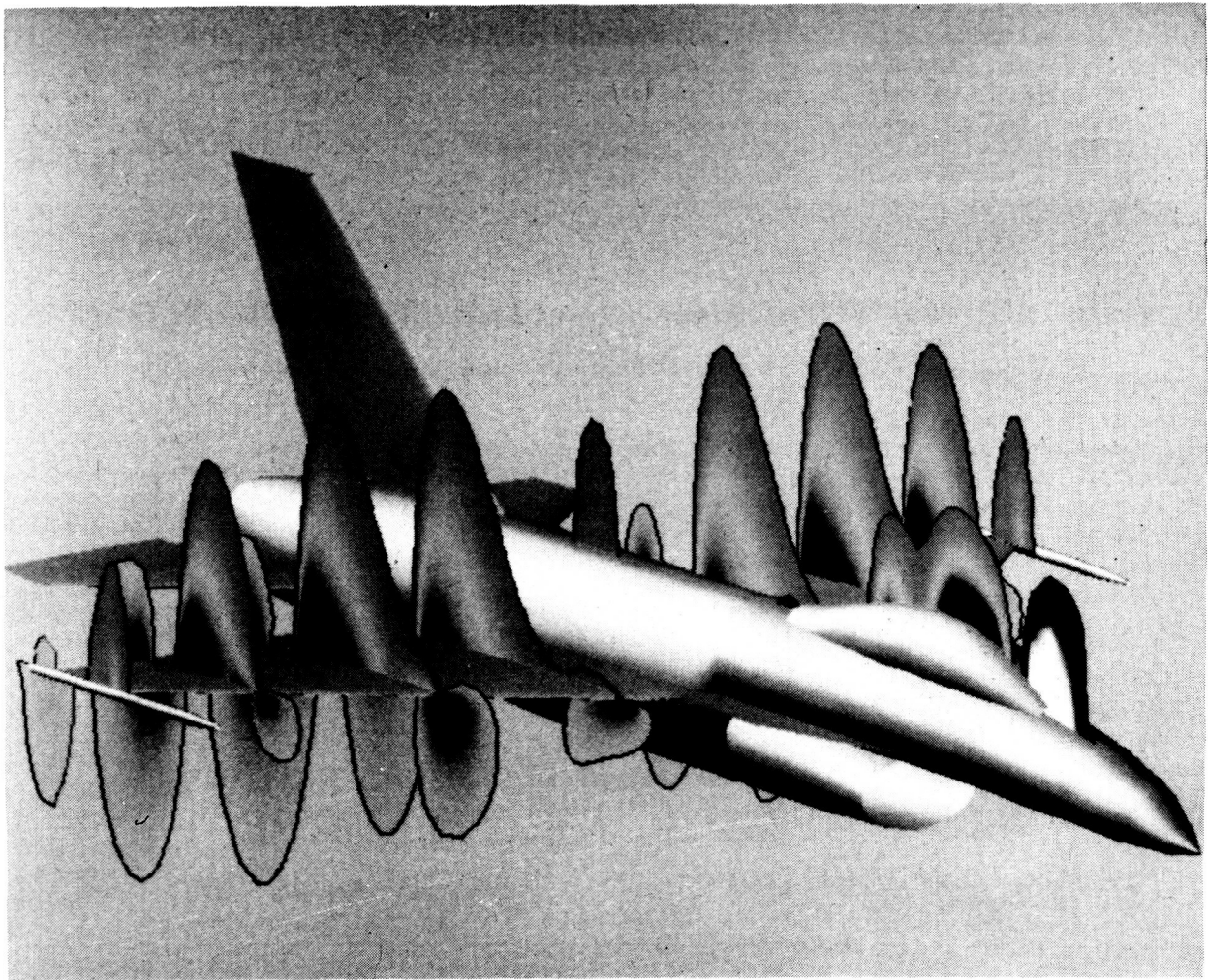
C-2

UNSTEADY FLOW FIELD PRESSURES FOR F-16C AIRCRAFT AT MAXIMUM PITCH ANGLE

Instantaneous flow field pressures at two points during a cycle of the rigid aircraft pitching calculations are shown in the next two figures. This figure shows contours at the aircraft maximum pitch angle; the next figure shows contours at the aircraft minimum pitch angle. The pressures shown here indicate an increase in the overall levels of both compression and expansion as the aircraft pitches up.
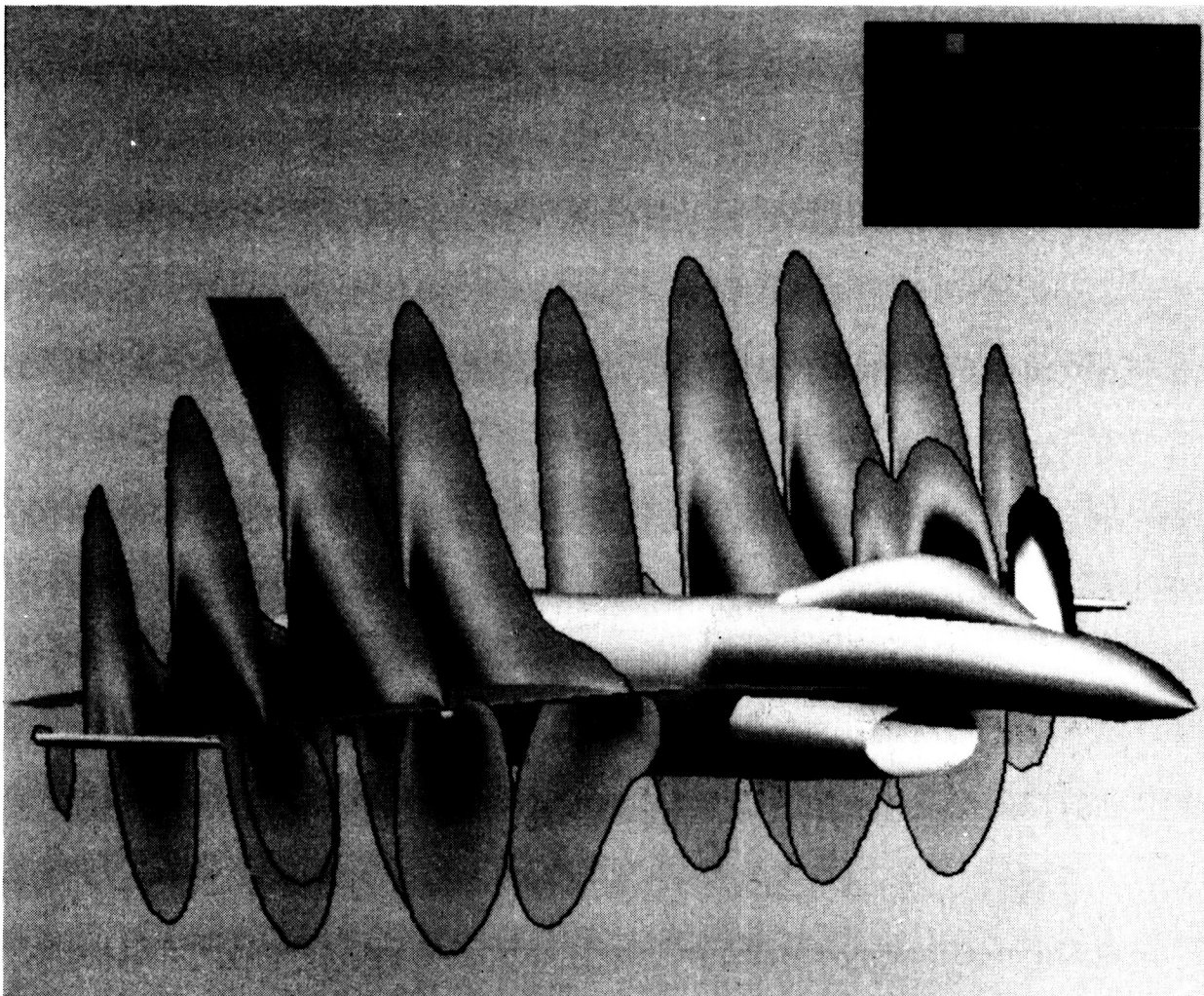
UNSTEADY FLOW FIELD PRESSURES FOR F-16C AIRCRAFT AT MINIMUM PITCH ANGLE

As the aircraft pitches down, the pressure levels decrease significantly along the wing, as shown in the figure.
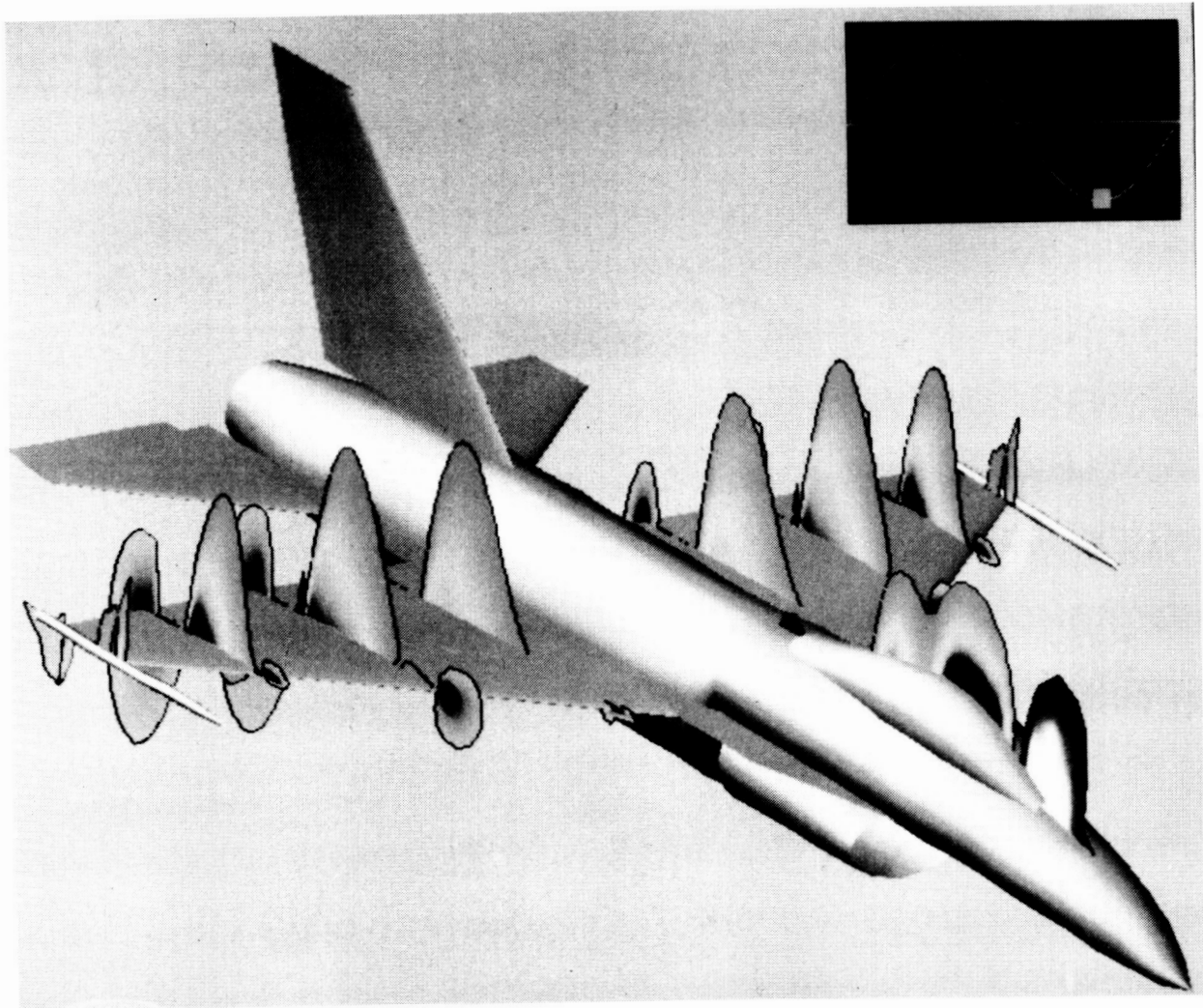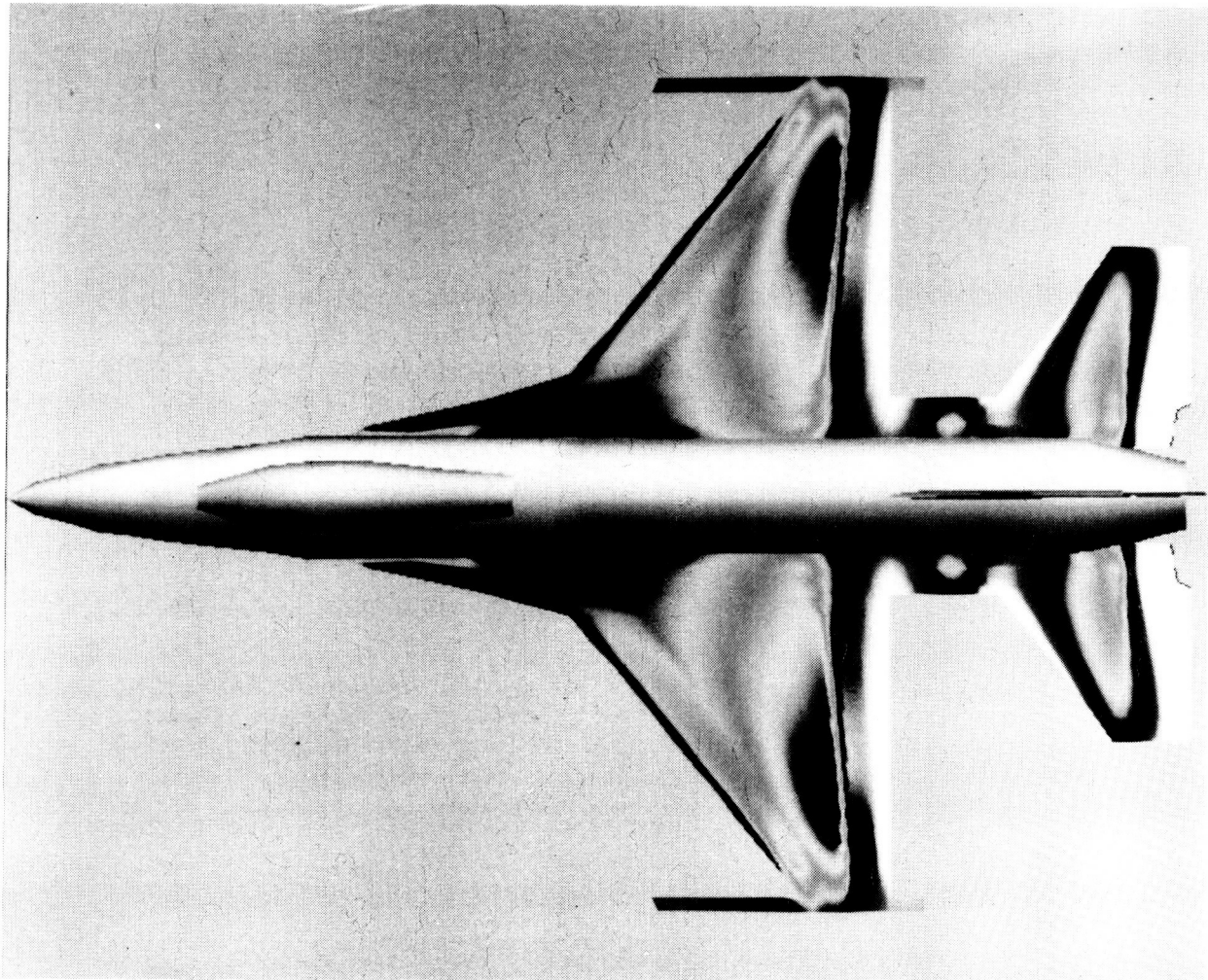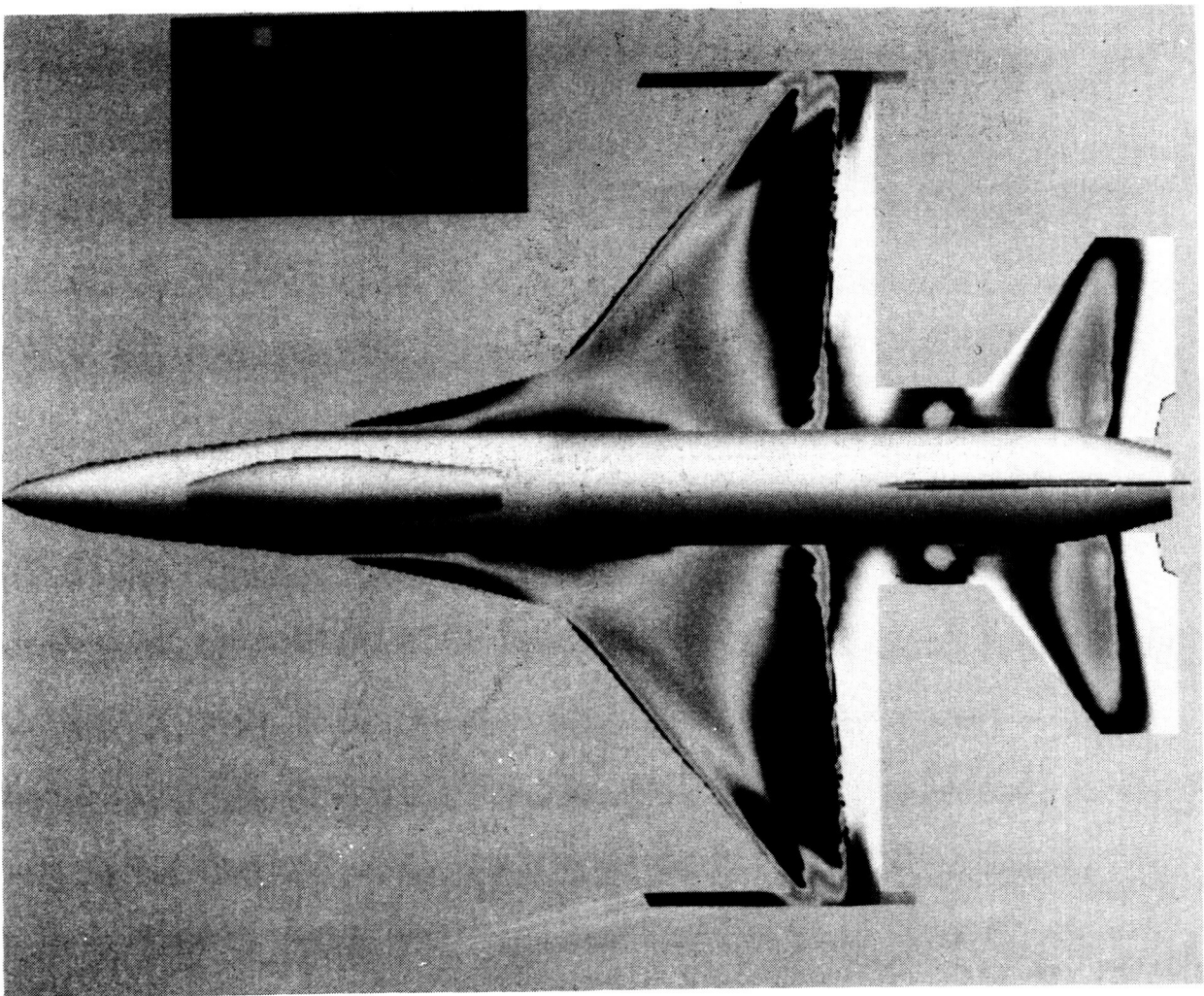
STEADY SURFACE PRESSURES FOR F-16C AIRCRAFT

The other view plotted is the planform view of the aircraft. Here the upper surface pressures are contoured similarly to the oblique projection results. This figure shows the steady surface pressures at $M = 0.9$ and $\alpha_0 = 2.38^\circ$. In this view, the shock wave is clearly represented by the lateral line on the wing near 75 - 80% chord. The shock is strongest outboard where there is a rapid change in contour level.

UNSTEADY SURFACE PRESSURES FOR F-16C AIRCRAFT
AT MAXIMUM PITCH ANGLE

Instantaneous pressures at two points during the cycle of rigid aircraft pitching are shown in the next two figures. Near the aircraft maximum pitch angle (shown here) the embedded supersonic region becomes larger as indicated by the increased size of the black contouring on the upper surface of the wing. Also, the shock becomes relatively strong as indicated by the rapid change in contour level, from black to white.
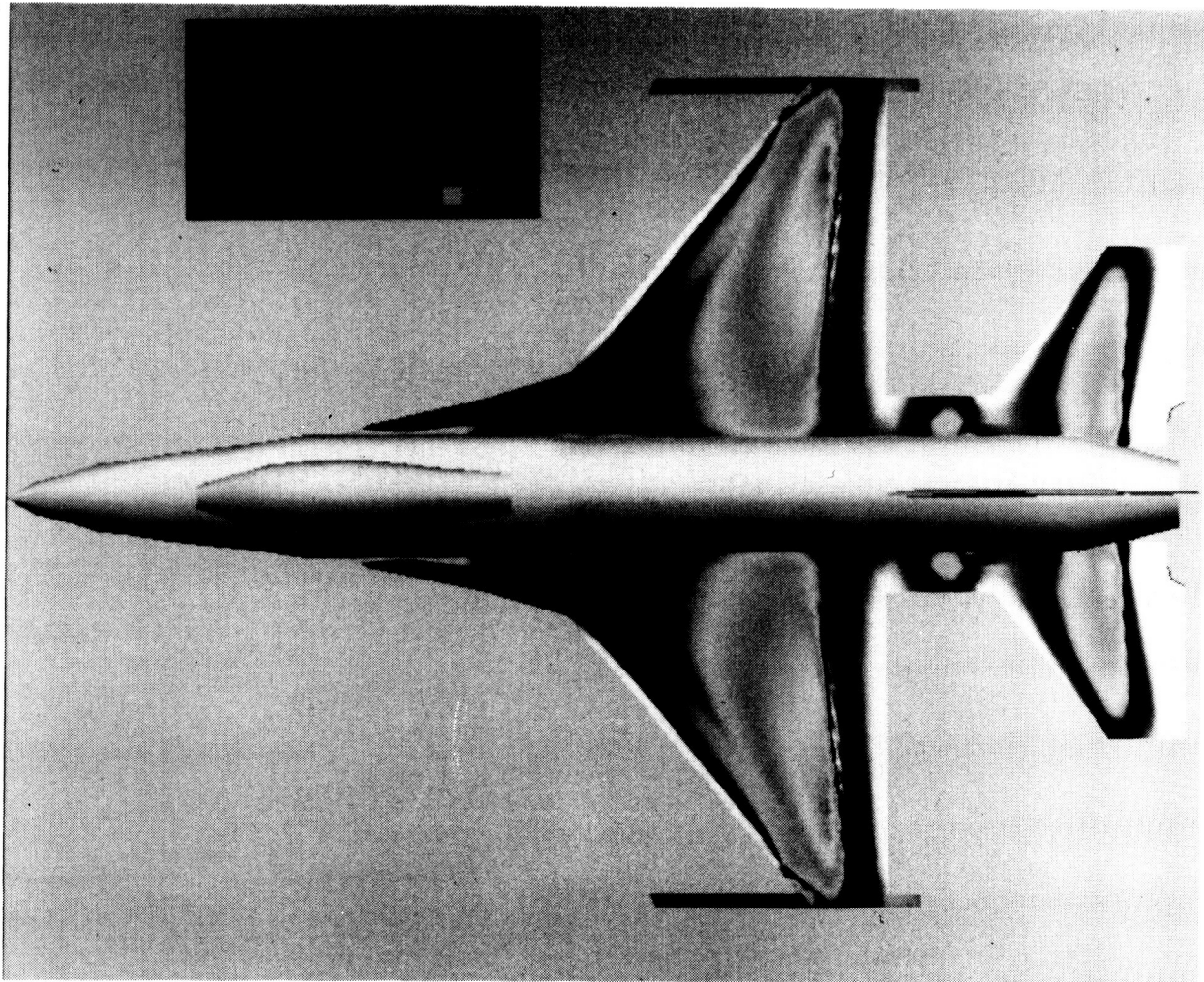
UNSTEADY SURFACE PRESSURES FOR F-16C AIRCRAFT AT MINIMUM PITCH ANGLE

Near the aircraft minimum pitch angle, shown in this figure, the shock on the wing upper surface becomes relatively weak and the flow is more compressed in the inboard region along the strake.

CONCLUDING REMARKS

A transonic unsteady aerodynamic and aeroelasticity code called CAP-TSD has been developed for application to realistic aircraft configurations. The name CAP-TSD is an acronym for Computational Aeroelasticity Program - Transonic Small Disturbance. The new code now permits the calculation of unsteady flows about complete aircraft configurations for aeroelastic analysis in the flutter critical transonic speed range. The CAP-TSD code uses a time-accurate approximate factorization (AF) algorithm for solution of the unsteady transonic small-disturbance equation. The AF algorithm has been shown to be very efficient for steady or unsteady transonic flow problems. It can provide accurate solutions in only several hundred time steps yielding a significant computational cost savings when compared to alternative methods. For reasons of practicality and affordability, an efficient algorithm and a fast computer code are requirements for realistic aircraft applications.

Results were presented for several complex aircraft configurations which demonstrated the geometrical applicability of CAP-TSD. The code can treat configurations with arbitrary combinations of lifting surfaces and bodies including canard, wing, tail, control surfaces, tip launchers, pylons, fuselage, stores, and nacelles. These calculated results were in good agreement with the experimental pressure data which assessed CAP-TSD for multiple components applications with mutual interference effects.

Finally, results were presented for the General Dynamics one-ninth scale F-16C aircraft model which demonstrated application to a realistic configuration. Steady results compared well with the experimental data. Unsteady results for the entire F-16C aircraft undergoing a rigid pitching motion were presented. Comparisons with parallel wing alone results revealed aerodynamic interference effects of the additional aircraft components on wing unsteady pressures. These effects emphasize the importance of including all components in the calculation. The CAP-TSD code thus provides the capability of modeling complete aircraft configurations for realistic transonic unsteady aerodynamic and aeroelastic analyses. Further pressure correlations and aeroelastic calculations are presently underway to continue assessing and validating the code.

- CAP-TSD code models complete aircraft configurations for transonic unsteady aerodynamic and aeroelastic analyses

- Initial pressure comparisons show good agreement

- Further pressure correlations and aeroelastic calculations presently underway to continue validating code

REFERENCES

[1]Batina, J. T.: "An Efficient Algorithm for Solution of the Unsteady Transonic Small-Disturbance Equation," AIAA Paper No. 87-0109, Presented at the AIAA 25th Aerospace Sciences Meeting, Reno, Nevada, January 12-15, 1987. (Also available as NASA TM 89014, December 1986).

[2]Batina, J. T.; Seidel, D. A.; Bland, S. R.; and Bennett, R. M.: "Unsteady Transonic Flow Calculations for Realistic Aircraft Configurations," AIAA Paper No. 87-0850, Presented at the AIAA/ASME/ASCE/AHS 28th Structures, Structural Dynamics, and Materials Conference, Monterey, California, April 6-8, 1987. (Also available as NASA TM 89120, March 1987).

[3]Persoon, A. J.; Roos, R.; and Schippers, P.: "Transonic and Low Supersonic Wind-Tunnel Tests on a Wing with Inboard Control Surface," AFWAL-TR-80-3146, December 1980.

[4]Renirie, L.: "Analysis of Measured Aerodynamic Loads on an Oscillating Wing-Store Combination in Subsonic Flow," NLR MP 74026 U, September 1974.

[5]Bennekers, B.; Roos, R.; and Zwaan, R. J.: "Calculation of Aerodynamic Loads on Oscillating Wing/Store Combinations in Subsonic Flow," NLR MP 74028 U, September 1974.

[6]Korner, H.; and Schroder, W.: "Druckverteilungs- und Kraftmessungen an einer Flugel-Rumpf-Leitwerk-Anordnung," DFVLR-IB-080-72/13, 1972.

[7]Stewart, V. R.: "Evaluation of a Propulsive Wing/Canard Concept at Subsonic and Supersonic Speeds," Rockwell International Report NR82H-85, February 1983.

[8]Fox, M. C.; and Feldman, C. S.: "Model and Test Information Report, 1/9-Scale F-16C and F-16D Force and Loads Model," General Dynamics Report 16PR2179, January 1982.

[9]Feldman, C. S.: "Wind Tunnel Data Report, 1/9-Scale F-16C Pressure Loads Test," General Dynamics Report 16PR2252, July 1982.

[10]Bennett, R. M.; Bland, S. R.; Batina, J. T.; Gibbons, M. D.; and Mabey, D. G.: "Calculation of Steady and Unsteady Pressures on Wings at Supersonic Speeds with a Transonic Small-Disturbance Code," AIAA Paper No. 87-0851, Presented at the AIAA/ASME/ASCE/AHS 28th Structures, Structural Dynamics, and Materials Conference, Monterey, CA, April 6-8, 1987.

[11]Gibbons, M. D.; Whitlow, W., Jr.; and Williams, M. H.: "Nonisentropic Unsteady Three Dimensional Small Disturbance Potential Theory," AIAA Paper No. 86-0863, Presented at the AIAA/ASME/ASCE/AHS 27th Structures, Structural Dynamics, and Materials Conference, San Antonio, Texas, May 19-21, 1986.

[12]Howlett, J. T.: "Efficient Self-Consistent Viscous-Inviscid Solutions for Unsteady Transonic Flow," AIAA Paper No. 85-0482, Presented at the AIAA 23rd Aerospace Sciences Meeting, Reno, Nevada, January 14-17, 1985.

CAP-TSD ANALYSIS OF THE F-15 AIRCRAFT

Dale M. Pitt
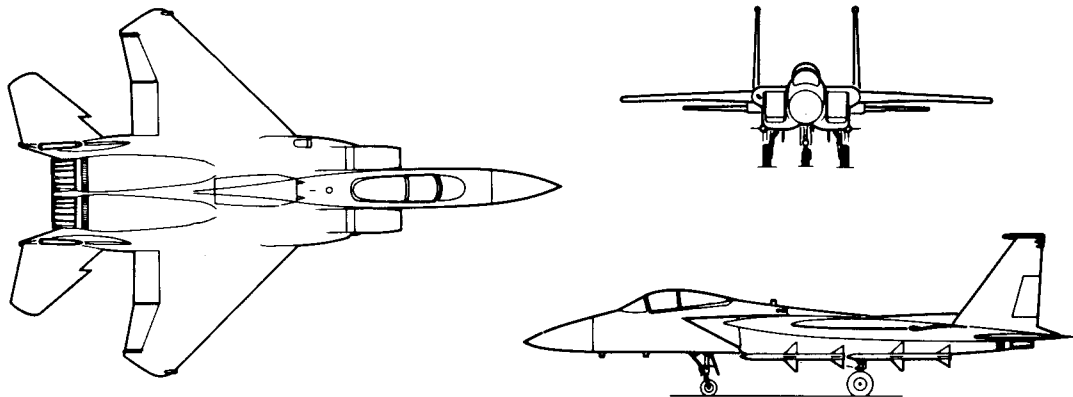McDonnell Aircraft Company
St. Louis, MO

The F-15 is a twin engine high performance fighter aircraft and is shown in the three view drawing of Figure 1. The large wing area allows for a low wing loading in cruise flight. Figure 2 also shows some of the wing and stabilator geometry characteristics.

F-15 Geometry

	Wing	Stabilator
Aspect Ratio:	3.01	2.05
Taper Ratio:	0.25	0.34
Sweep (LE):	45°	50°
Dihedral:	− 1°	0°

Figure 1

Figure 2 shows the airfoil sections of the F-15 wing. The wing root is a 6 percent thick symmetric airfoil. The wing decreases in thickness towards the tip, which is a 3 percent highly cambered airfoil. The F-15 wing has conical camber outboard of the 20 percent semi-span location.
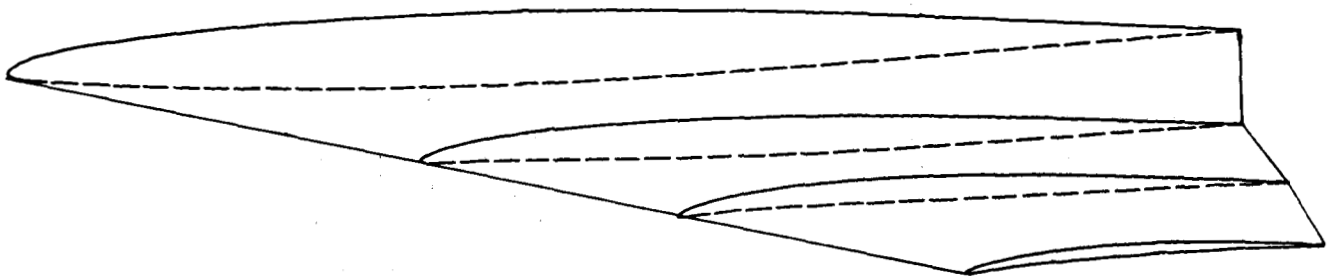
F·15 Wing and Airfoil Shapes

Figure 2

A 4.7 percent rigid model of the F-15 was tested in the MCAIR Polysonic Wind Tunnel in January of 1971. Wing pressures were measured at four span stations. The semi-span stations were located at 36.2, 58.7, 77.0 and 86.2 percent. Nominally, there were 16 upper surface pressure taps and 7 lower surface pressure taps. All data shown are for undeflected ailerons and flaps. The forward fuselage had 70 pressure taps located at 10 fuselage stations as shown in Figure 3. The fuselage taps were located at fuselage rotation angles of 0 (top), 44, 68, 90, 114, 138 and 180 (bottom) degrees.

F-15 4.7% SCALE MODEL
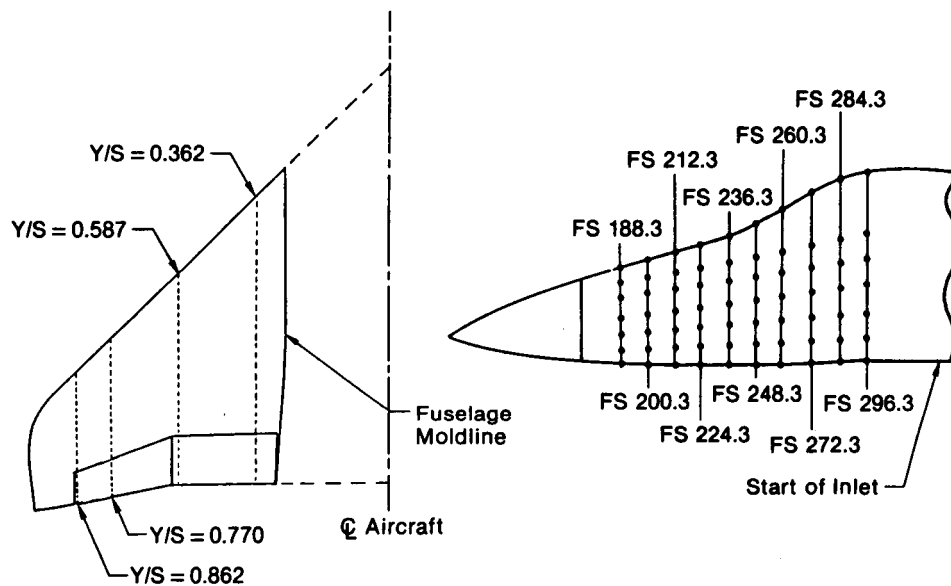## Wing and Fuselage Pressure Tap Location

Figure 3

F-15 CAP-TSD runs were made for the angle-of-attack and Mach range shown in Figure 4. The Mach number ranged from subsonic, through the transonic to the supersonic range. The angle-of-attack ranged from 0 to about 5 degrees. The F-15 CAP-TSD model includes the wing, wing-glove, stabilator, flow through inlets and fuselage body. Various pressures from these runs will be compared with test data. Also, two wing alone cases will be shown to highlight the fuselage effects.

F-15 CAP-TSD STEADY RUNS

Mach 0.80	Mach 0.90	Mach 0.95	Mach 1.208
$\alpha = 0.08°$	$\alpha = 0.08°$	$\alpha = 0.08°$	$\alpha = 0.08°$
$= 2.46°$	$= 2.46°$ *	$= 2.58°$	$= 2.70°$ *
$= 4.84°$	$= 4.84°$		

F-15 CAP-TSD Model Includes:

- Wing, Wing-Glove, Stabilator, Flow Through Inlets, Fuselage Body

*Runs were also made for wing alone case.

Figure 4

102

Figure 5 is a picture of the CAP-TSD X-Y grid for the F-15 complete aircraft configuration. There are 150 X grid points, 32 Y grid points and 72 Z grid points. Thus, the total number of grid points is 345,600. There are 22 Eta grid points along the wing span and 50 grid points along the wing chord. The stabilator has 15 Eta grid points and 23 chordwise points.

F-15 CAP-TSD GRID

$n_x = 150 \qquad n_y = 32 \qquad n_z = 72$

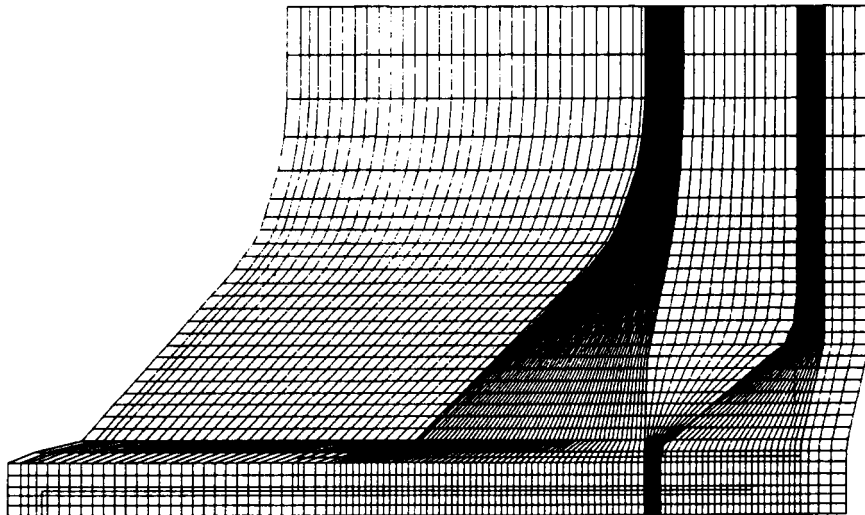### Total Number of Grid Points = 345,600

Figure 5

The first CAP-TSD results to be shown will be for the F-15 forward
fuselage section. Figure 6 shows the pressure coefficients for the top and
bottom of the fuselage versus fuselage station. For M = 0.9 and an
angle-of-attack of 0.08 degrees, the CAP-TSD lower surface pressures agree
well with the wind tunnel data. The upper surface CAP-TSD pressures agree
qualitatively with the data. However, CAP-TSD shows the compression over the
canopy starting a little sooner than the test data at a fuselage station of
225 inches. CAP-TSD predicts more compression than the data shows. In the
area where the flow expands over the canopy, Fuselage station 250 inches, the
agreement is better. Refer to Figure 3 for a side view of the canopy. It is
felt that more grid points along the fuselage will improve the CAP-TSD
correlation of the upper surface pressure.

F-15 COMPLETE AIRCRAFT, MACH 0.9, $\alpha = 0.08°$
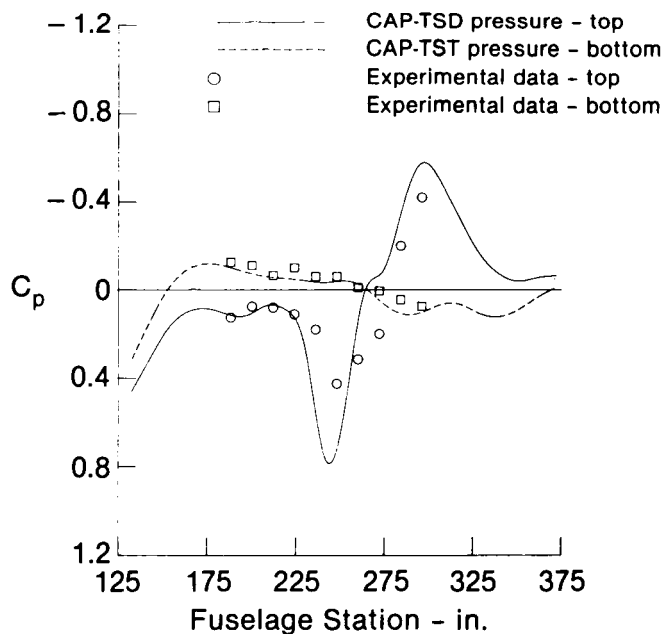
Fuselage Pressures

Figure 6

The F-15 fuselage pressures for a supersonic case are shown in Figure 7. The lower surface pressures show good correlation between CAP-TSD results and the test data. The upper surface pressures show a more severe compression than the data. However, the overall comparison is encouraging.

F·15 COMPLETE AIRCRAFT, MACH 1.208, $\alpha = 0.08°$

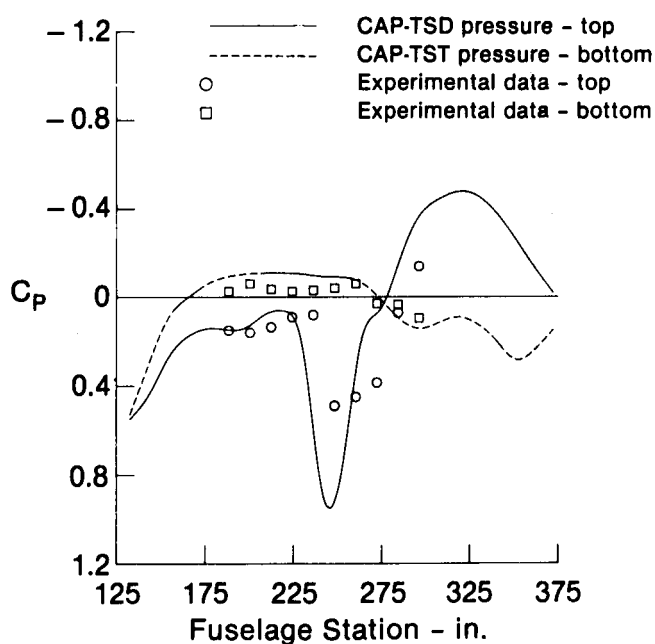|	
———————	CAP-TSD pressure - top
- - - - - - - - -	CAP-TST pressure - bottom
O	Experimental data - top
□	Experimental data - bottom

Figure 7

Figures 8-10 are comparisons of CAP-TSD results and measured data
for the outer most wing pressures. The Mach number is 0.81 and the
angles-of-attack are 0.08, 2.46 and 4.84 degrees. These three figures show
the effects that increasing angle-of-attack has on the wing flow. It should be
noted that the airfoil shape at this outboard section is highly cambered.
(Refer to Figure 2.) Figure 8 shows very good agreement between CAP-TSD
results and wind tunnel pressures.

F-15 COMPLETE AIRCRAFT, MACH 0.810
Y/S = 0.862 $\alpha = 0.08°$

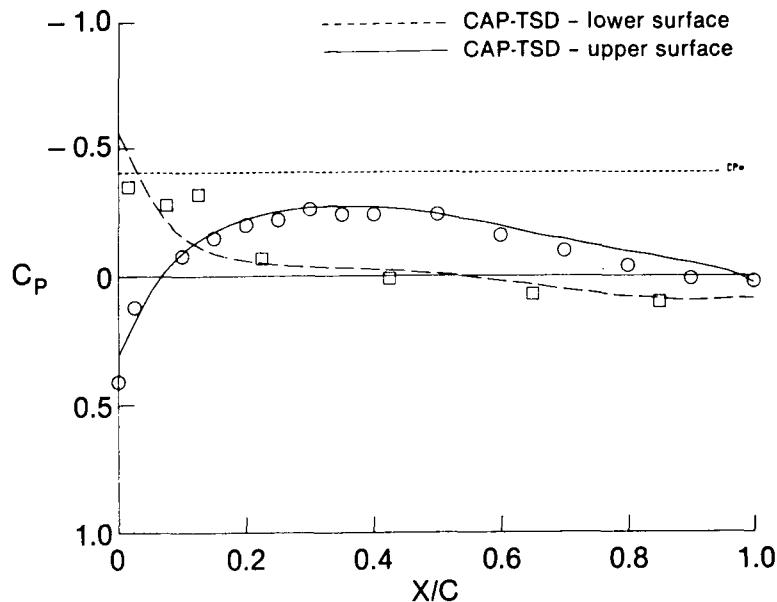Figure 8

Figure 9 is the comparison of experimental wing pressures with CAP-TSD results for M = 0.81, alpha = 2.46 degree at an 86 percent semi-span location. The flow on the upper surface is barely supersonic at X/C = 0.2. Agreement between CAP-TSD and experiment is very good.
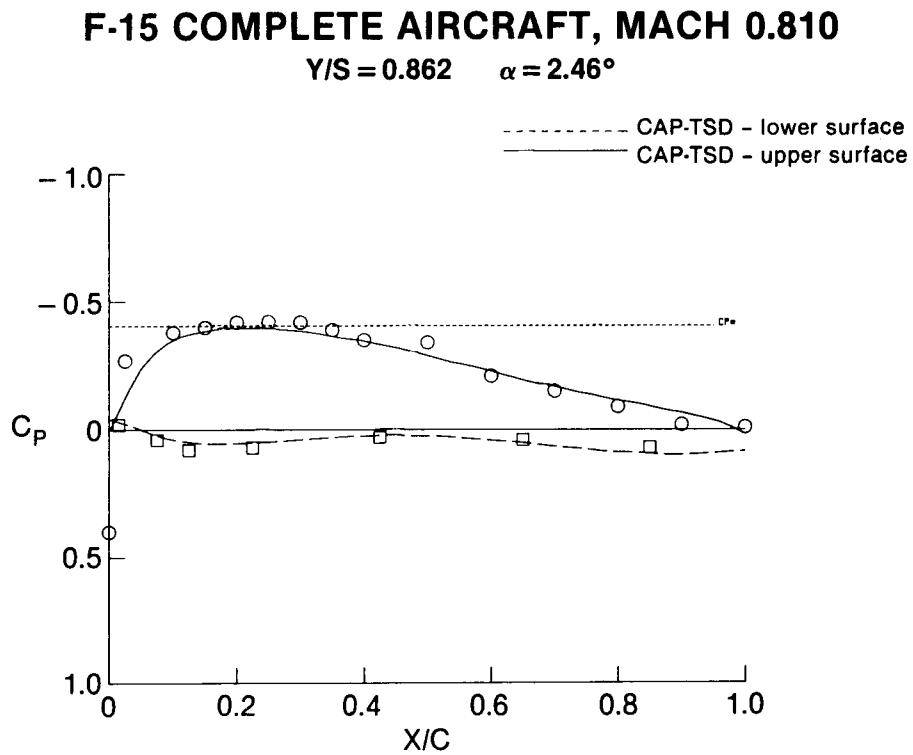
F-15 COMPLETE AIRCRAFT, MACH 0.810
Y/S = 0.862 $\alpha = 2.46°$

Figure 9

The F-15 outer wing pressure comparison for M = 0.81, alpha = 4.84 degree is shown in Figure 10. The lower surface pressures as predicted by CAP-TSD agree well with the experimental data. The upper surface CAP-TSD pressures are not quite showing the degree of suction suggested by the test data.

F-15 COMPLETE AIRCRAFT, MACH 0.810
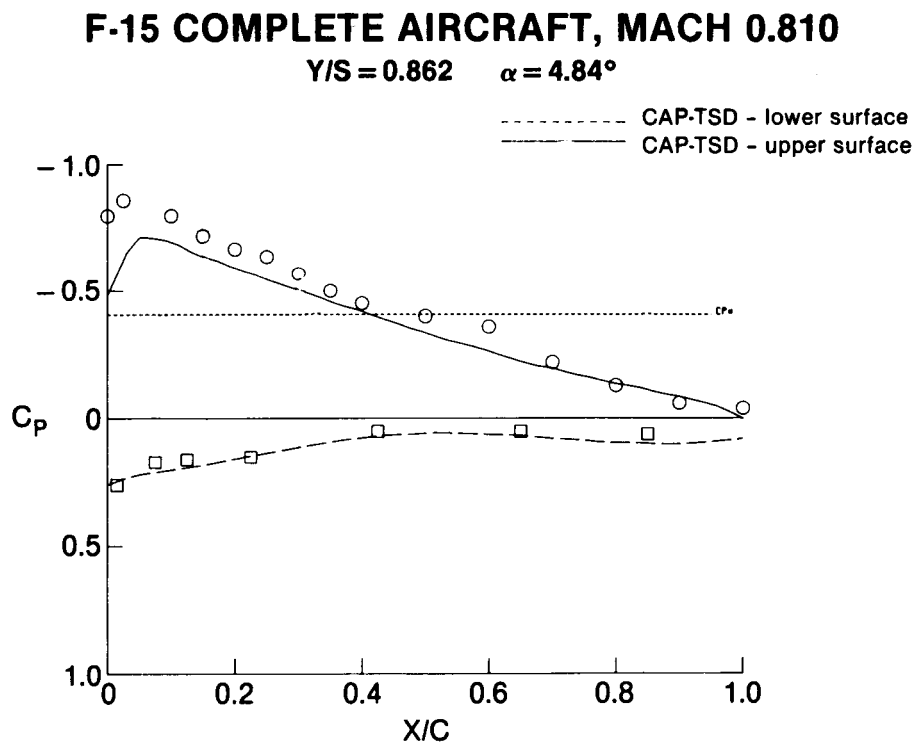### Y/S = 0.862 α = 4.84°

Figure 10

Some representative Mach 0.9 cases are shown in Figures 11 and 12.
Figure 11 shows data for the wing pressure at a 77.8 percent semi-span
location for an angle-of-attack of 0.08 degrees. The upper surface pressures
are in good agreement between CAP-TSD results and wind tunnel data. The
lower surface pressures also agree well, with a slight discrepancy at $0.1 \leq$
X/C < 0.2. This is an area of extreme lower surface camber and rapid change
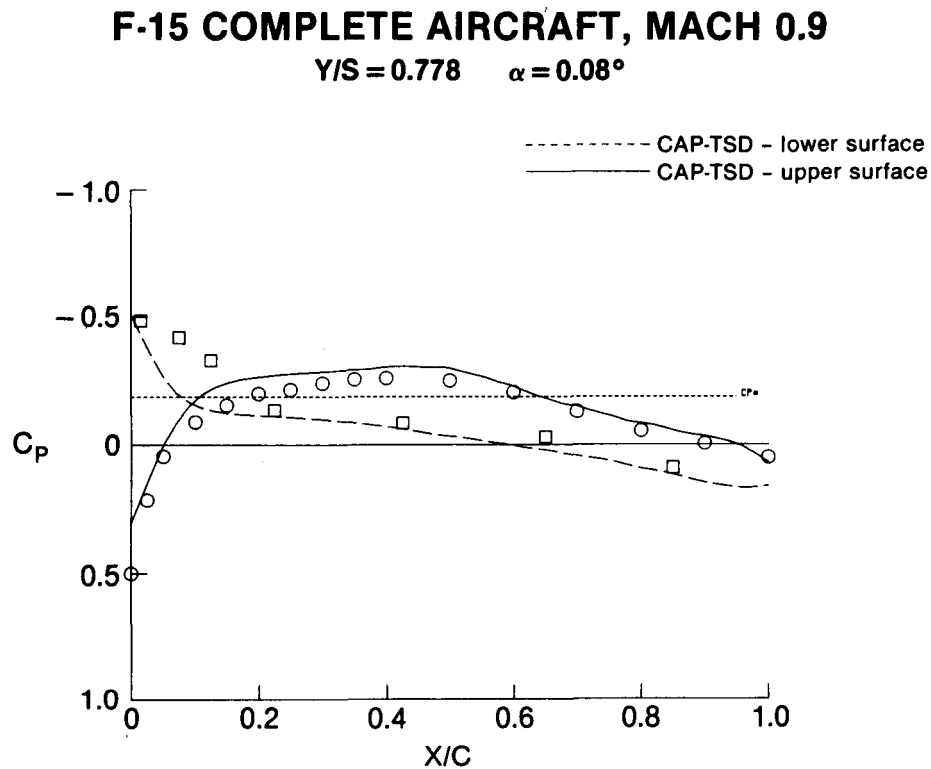in airfoil slopes.

F-15 COMPLETE AIRCRAFT, MACH 0.9
Y/S = 0.778 α = 0.08°

Figure 11

Figure 12 shows results for the inboard wing pressures for M = 0.9 and alpha of 2.46 degrees. The figure compares CAP-TSD wing alone results with the CAP-TSD complete fuselage model results and wind tunnel data. It is apparent that the modeling of the fuselage improves the upper surface pressures over the last 60 percent of the wing chord. The fuselage effects also increase the upper surface leading edge suction.

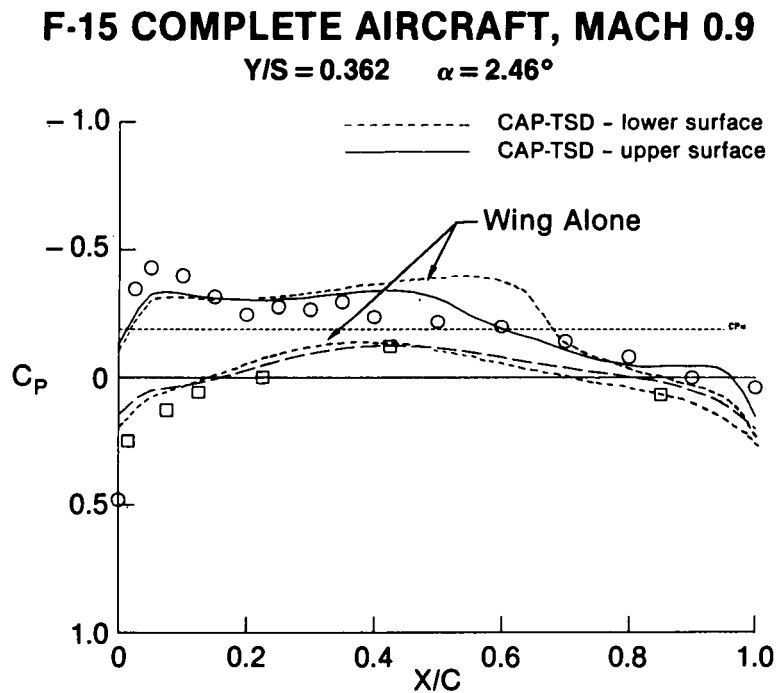## F-15 COMPLETE AIRCRAFT, MACH 0.9

Y/S = 0.362 α = 2.46°

Figure 12

Figures 13 and 14 show some of the wing pressure results for the Mach = 0.95 case. Figure 13 is a comparison of the F-15 wing pressures with those predicted by CAP-TSD at a semi-span location of 77 percent and alpha = 0.08 degrees. Both the experimental data and CAP-TSD results show a strong upper surface shock at 75% local chord location. The agreement between the test data and CAP-TSD pressures is excellent for both the upper and lower surfaces.
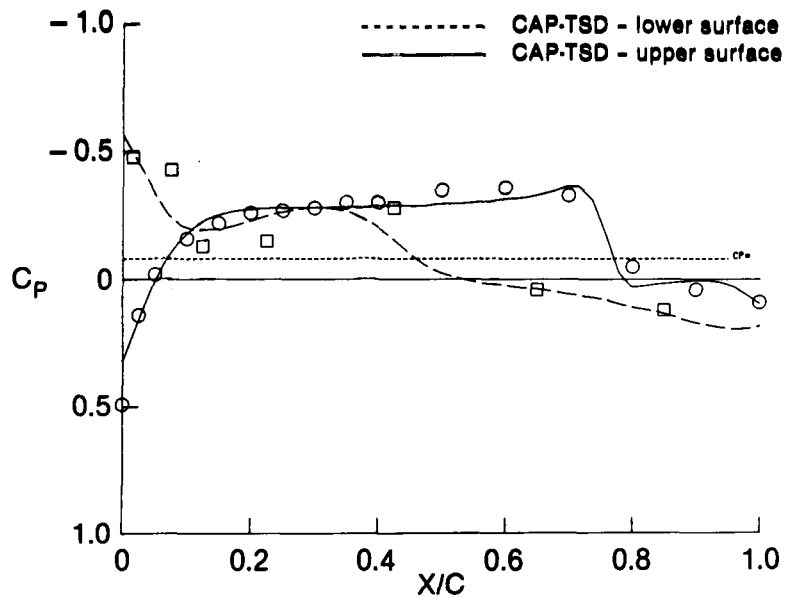
Figure 13

Figure 14 shows the wing pressures for the same Mach number and semi-span as reported in Figure 13, but for an increased angle-of-attack of 2.58 degrees. The lower surface measured pressures are in good agreement with CAP-TSD results. The upper surface CAP-TSD pressures are slightly below the test data, with the predicted shock being slightly forward of the position shown by the test data.

F-15 COMPLETE AIRCRAFT, MACH 0.952
Y/S = 0.770 $\alpha = 2.58°$

Figure 14

Some representative supersonic, Mach = 1.208, cases are shown in Figures 15 thru 17. Figure 15 is the CAP-TSD results for the complete F-15 compared to wind tunnel data at the 58.7 percent semi span and alpha of 0.08 degrees. Generally the agreement between theory and test is excellent for both upper and lower surface.

F-15 COMPLETE AIRCRAFT, MACH 1.208
Y/S = 0.587 $\alpha = 0.08°$
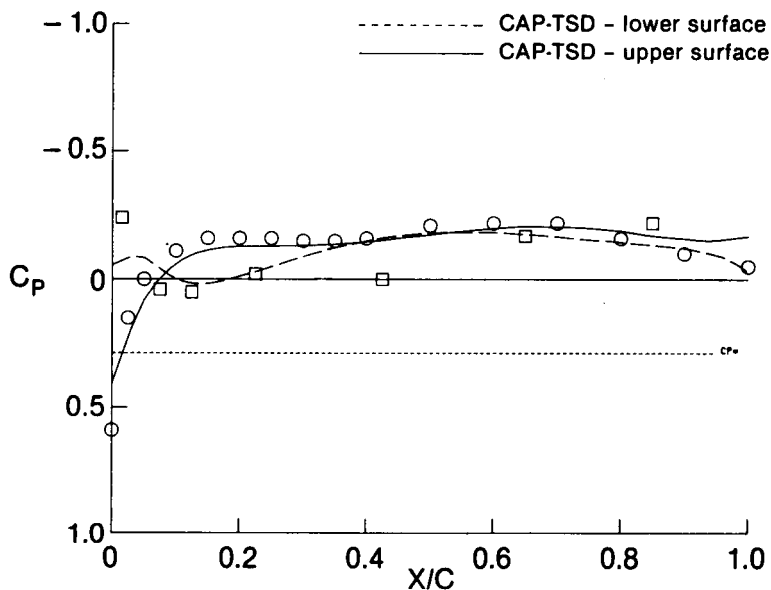
Figure 15

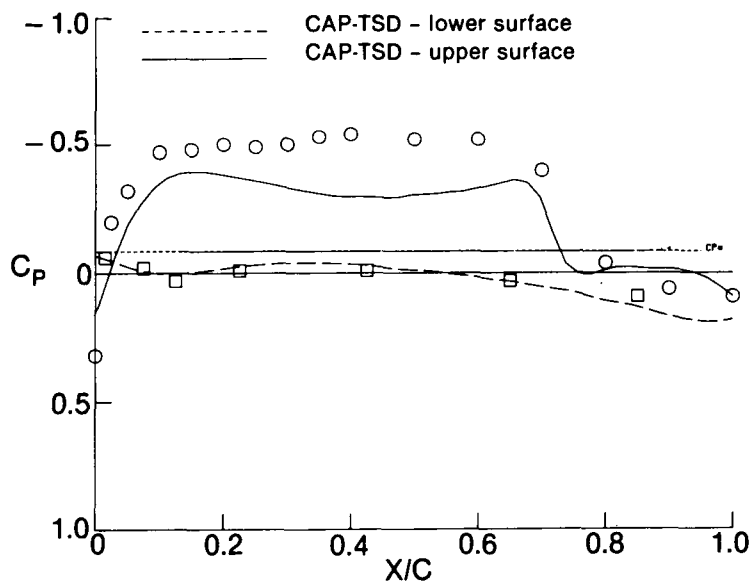The wing pressures for the same supersonic case as Figure 15 but at a more outboard semi-span location of 86.2 percent are shown in Figure 16. The upper surface experimental pressures are in very good agreement with CAP-TSD results. The lower surface CAP-TSD results also agree very well with experiment and show the effects of the lower surface camber in the leading edge area.

F-15 COMPLETE AIRCRAFT, MACH 1.208
Y/S = 0.862 α = 0.08°
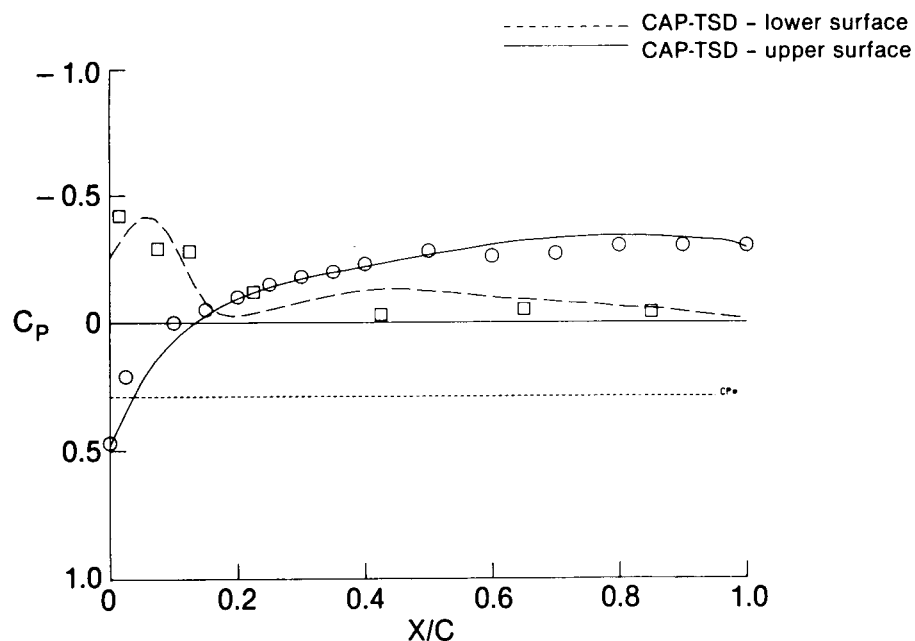
Figure 16

Figure 17 is the inboard wing pressures for a Mach of 1.208 and an alpha of 2.70 degrees. This figure compares CAP-TSD complete fuselage wing pressures with CAP-TSD wing alone results and wind tunnel data. The fuselage effects improve the correlation for the upper surface pressures. The largest improvement is over the last 40% of the local chord on the upper surface.

F-15 COMPLETE AIRCRAFT, MACH 1.208
Y/S = 0.362 α = 2.70°
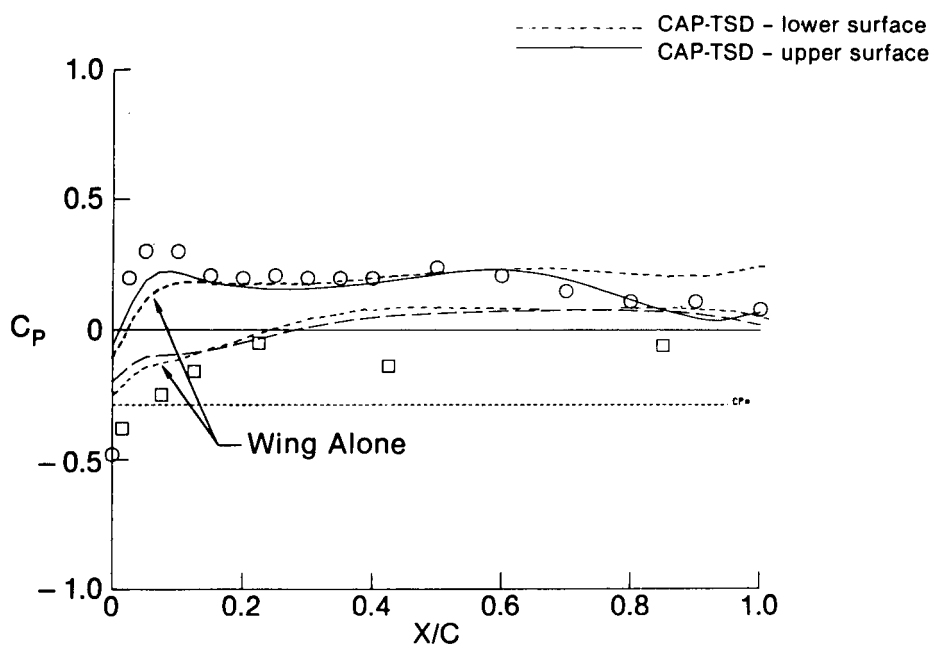
Figure 17

In summary, the F-15 fighter aircraft was modeled using CAP-TSD. The complete aircraft was model including the wing, stabilator, flow through inlets, and fuselage body. CAP-TSD was used to make static pressure runs for Mach numbers of 0.8, 0.9, 0.95 and 1.2. The angle-of-attack for these runs ranged from 0 to 5 degrees.

The CAP-TSD program showed good agreement between the computed fuselage and wing pressures and the measured wind tunnel pressures. Including the fuselage and inlets in the CAP-TSD analysis is important and improves the correlation of wing pressures with test data (Figure 18).

SUMMARY/CONCLUSIONS

- CAP-TSD Used to Model F-15, Model Includes:
  - Wing, Stabilator, Inlets, and Fuselage Body

- Static Runs Made for Following Conditions:
  - Mach Range - 0.8 to 1.2
  - Alpha Range - 0 to 5 deg

- CAP-TSD Generally Showed Good Agreement With Test Data

- Fuselage Effects Are Important in Modeling the F-15

Figure 18

CALCULATION OF STEADY AND UNSTEADY PRESSURES AT SUPERSONIC SPEEDS WITH CAP-TSD

Robert M. Bennett, Samuel R. Bland,
and John T. Batina
Unsteady Aerodynamics Branch
NASA Langley Research Center
Hampton, Virginia

Michael D. Gibbons
Planning Research Corp.
Hampton, Virginia

and

Dennis G. Mabey
Royal Aircraft Establishment
Bedford, England

INTRODUCTION

Currently there is considerable interest in the development of methods for calculating supersonic unsteady aerodynamics for application to advanced configurations. Although flutter is oftentimes critical at transonic speeds, critical conditions can also be encountered at both low and high supersonic speeds depending upon configuration and operating envelopes. Linear theory has been the primary analytical tool for analyzing flutter in the low supersonic region with recent efforts directed towards refining the potential gradient methods. In linear theory the loading on a wing is determined by the relationship of the Mach lines to the planform which can lead to complex logic for configurations. In this study a finite-difference technique is used to solve the transonic small-disturbance flow equation making use of shock-capturing to treat wave discontinuities. Thus the nonlinear effects of thickness and angle of attack are considered. Such an approach is made feasible by the development of an efficient new code by the Unsteady Aerodynamics Branch of the NASA Langley Research Center. The new code is called CAP-TSD for Computational Aeroelasticity Program - Transonic Small Disturbance and is based on a fully implicit approximate-factorization (AF) finite-difference method to solve the time-dependent transonic small-disturbance equation and has been described by Batina* in an earlier presentation at this workshop. This paper presents the application of the CAP-TSD code to the calculation of low to moderate supersonic steady and unsteady flows. In particular, comparisons with exact linear theory solutions are made for steady and unsteady cases to evaluate the shock capturing and other features of the current method. In addition, steady solutions obtained from an Euler code are used to evaluate the small disturbance aspects of the code. Steady and unsteady pressure comparisons are made with measurements for an F-5 wing model and for the RAE tailplane model. (Fig. 1.).

*Batina et al., NASA CP-3022, 1989, Paper No. 4.

INTRODUCTION

- Significant interest in unsteady supersonic aerodynamics
  - Configurations can be flutter critical at supersonic speeds
  - New configurations are under development

- Linear theory currently used
  - Mach box, potential gradient, etc
  - Treats mach lines and mach cones explicitly = complex logic for configurations

- Present study applies CAP-TSD to wings
  - Computational Aeroelasticity Program - Transonic Small Disturbance
  - Previous presentation*described application to configurations
  - Comparisons presented: Linear theory, F-5 model, and RAE tailplane model   *Pitt, this CP

Figure 1

118

CAP-TSD

As previously indicated, CAP-TSD is based on a fully implicit approximate-factorization (AF) algorithm. The program solves the modified transonic small disturbance (TSD) equation including the ϕ_{tt} term. The program has been developed for configurations and is highly vectorized. A TSD code called XTRAN3S has been previously developed and used extensively; however, the partially-explicit alternating direction implicit algorithm used in XTRAN3S was unstable for swept and tapered wings at supersonic speeds. The AF algorithm used in CAP-TSD is stable for such cases. The finite-difference method treats discrete waves by shock capturing.

For all the cases presented here, a finite-difference grid was used that consisted of 90 x 30 x 60 points in the x-y-z directions giving a total of 162,000 grid points. The grid extended 10 root chord lengths ahead and aft of the wing, nearly 13 chord lengths above and below, and one semispan outboard of the tip. On the wing, 50 points were used along each chord and 20 points along the span. This grid is one that would be used for a subsonic freestream and extends further than may be necessary for the supersonic cases. The outer boundary conditions for the cases considered herein are the "reflecting" outer boundary conditions, but care has been taken to ensure that the wing is located within the "Mach diamond" such that waves do not reflect from the outer boundaries back onto the wing surface. For the oscillating wings the calculations were made at 360 steps per cycle which corresponds to a time step of the order of 0.1. Only two cycles of motion were calculated because the flow field converges rapidly for supersonic flow. The second cycle was used for Fourier analysis. One Newton iteration per step was used for flow field convergence. (Fig. 2.)

CAP - TSD

- Fully implicit approximate-factorization (AF) algorithm

- Solves general frequency modified transonic small disturbance (TSD) equation

- Developed for configurations

- Vectorized

- Stable for supersonic flow

- Treats discontinuous waves by shock-capturing

- Reflecting outer boundary conditions and large grid extent used for supersonic flow

- Fine grid: 90x30x60 (x-y-z) 162,000 points

Figure 2

COMPARISON OF CAP-TSD AND EXACT LINEAR THEORY
RECTANGULAR WING, AR = 4, M = 1.30

The first comparison with linear theory is for tip loading on a wing in steady flow. The loading within the tip Mach line for a wing with a supersonic leading edge has an exact conical flow solution. A typical result is shown in figure 3 and is compared with a corresponding CAP-TSD calculation for a rectangular wing. For this case the loading has a discontinuous slope at the Mach line which is smeared by the finite-difference scheme but the overall trend of the loading is reproduced.
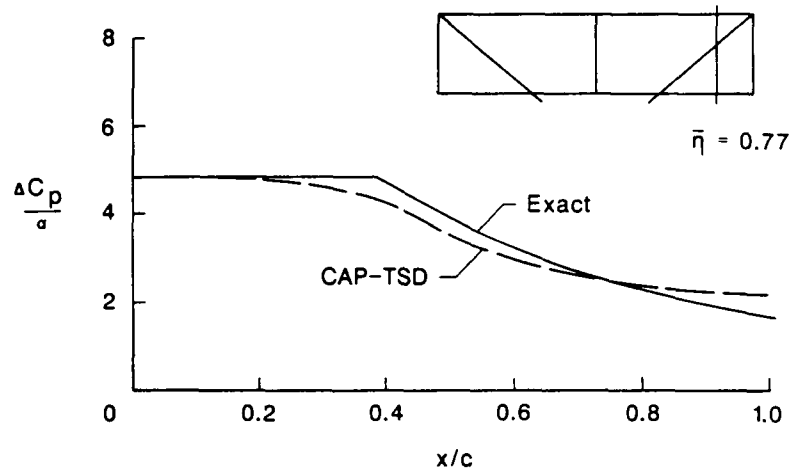
Figure 3

COMPARISON OF CAP-TSD AND EXACT LINEAR THEORY
L.E. SWEEP = 40°, TAPER RATIO = 0.5, M = 1.12

The next comparison is for a more complex situation. For a wing with a subsonic leading edge, the loading at the tip Mach line has a jump. A loading of this type is shown in figure 4 for a hexagonal wing planform of 40° leading-edge sweep, taper ratio of 0.50, and at M = 1.12. The over-all trend of the loading again is given by CAP-TSD but there is considerable smearing of the jump discontinuity. For this severe test case further development of the finite differencing is desirable, but the agreement of the overall trend is encouraging.
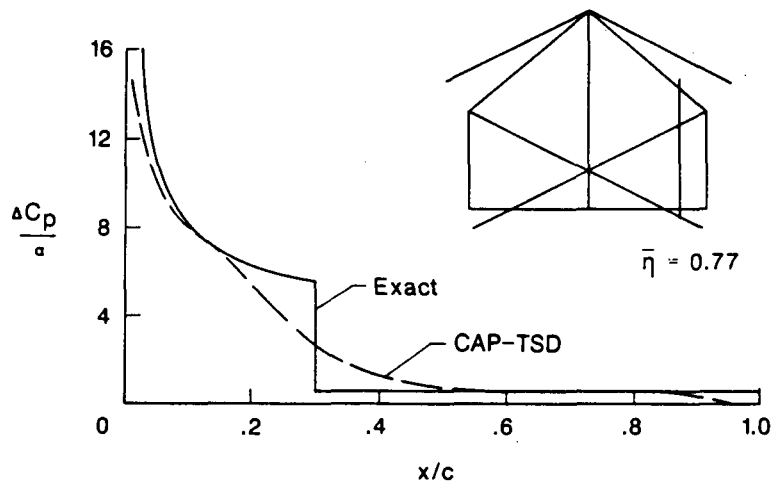

Figure 4

COMPARISON OF CAP-TSD AND EXACT LINEAR THEORY
2-D FLAT PLATE PITCHING ABOUT 41.3% C, M = 1.30

For unsteady flow, exact solutions for a two-dimensional flat plate airfoil are given in NACA Report 846 by Garrick and Rubinow (1946). Solutions for a rectangular wing of aspect-ratio-4 oscillating in pitch at M = 1.30 about the 41.3% chord are presented in NACA TN 3076 by Nelson, et al. (1954). Several cases have been run with CAP-TSD for the rectangular wing. Since the inboard portion of the wing has two dimensional flow, the inboard solutions can be compared to the 2-D results of Garrick and Rubinow. The comparison for unsteady lift is shown in figure 5. The agreement with the exact solution up to k = 1.0 is excellent.

Figure 5

122
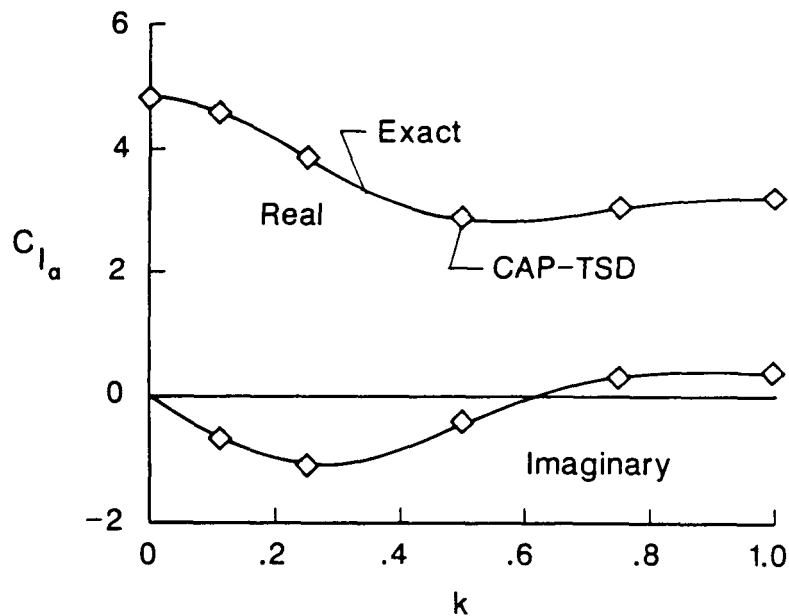
COMPARISON OF CAP-TSD AND EXACT LINEAR THEORY
FLAT PLATE WING, PITCHING ABOUT 41.3% C, M = 1.30, K = 0.111

For the oscillating rectangular wing of aspect ratio 4 at M = 1.30, the spanwise distribution of lift magnitude and phase over the wing for K = 0.116 is shown in figure 6. Good agreement is evident with some slight overprediction at the tip. Note that the phase angle is shown with a highly expanded scale. These cases indicate that the overall loading is well reproduced by CAP-TSD in supersonic unsteady flows.

Figure 6

COMPARISON OF CAP-TSD AND EXPERIMENT
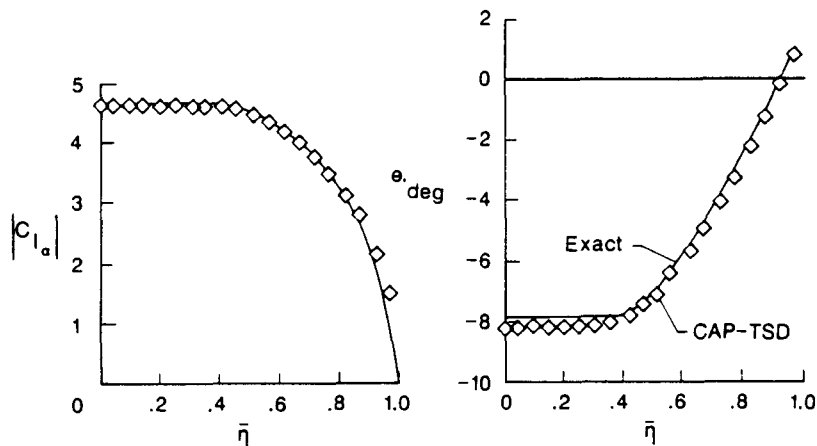## F-5 MODEL, STEADY FLOW, M = 1.10, α_0 = 0°

The first comparisons with experimental data are for an F-5 wing model tested by the Dutch NLR. The F-5 wing model is a typical supersonic wing with a panel aspect ratio of 1.58, a leading edge sweep angle of 31.9° and a taper ratio of 0.28. The airfoil section is a modified NACA 65A004.8 which has a slightly drooped nose and is symmetric aft of 40% chord. Subsonic and transonic calculations for this model have been made previously by several investigators using TSD codes and have been in generally good agreement with the experimental data. Calculations with CAP-TSD are compared with steady flow data for α_0 = 0° and for Mach numbers of 1.10 in figure 7. Generally good agreement is demonstrated. There is a shock on the lower surface near the leading edge which is swept aft slightly more than the leading edge. Some deviation of the results obtained with CAP-TSD from the data in this region is noted.
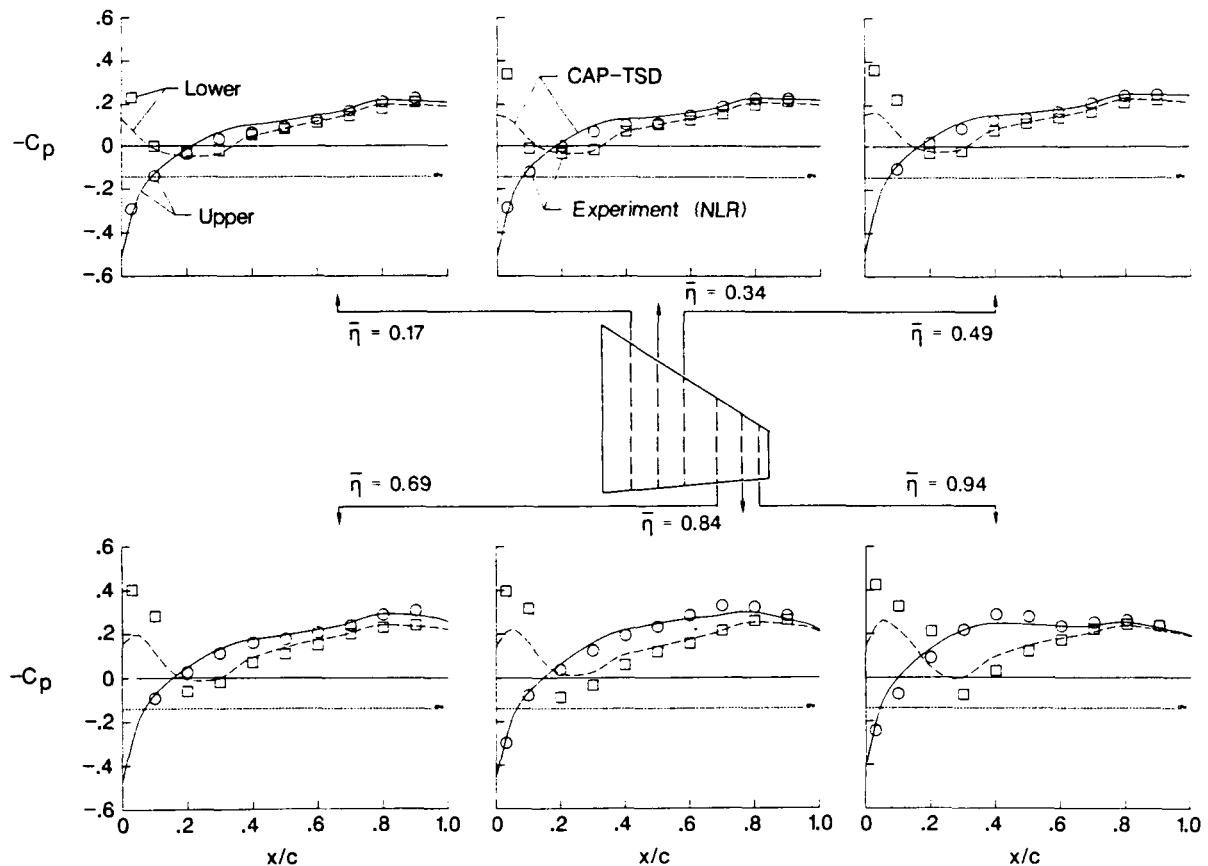
Figure 7

124

COMPARISON OF CAP-TSD AND EXPERIMENT
F-5 MODEL, STEADY FLOW, M = 1.32, α_0 = 0°

Corresponding calculations for the F-5 wing at M = 1.32 are shown in figure 8. Generally good agreement is also evident at this higher Mach number. The shock on the lower leading-edge surface that was present for M = 1.10 is no longer evident.
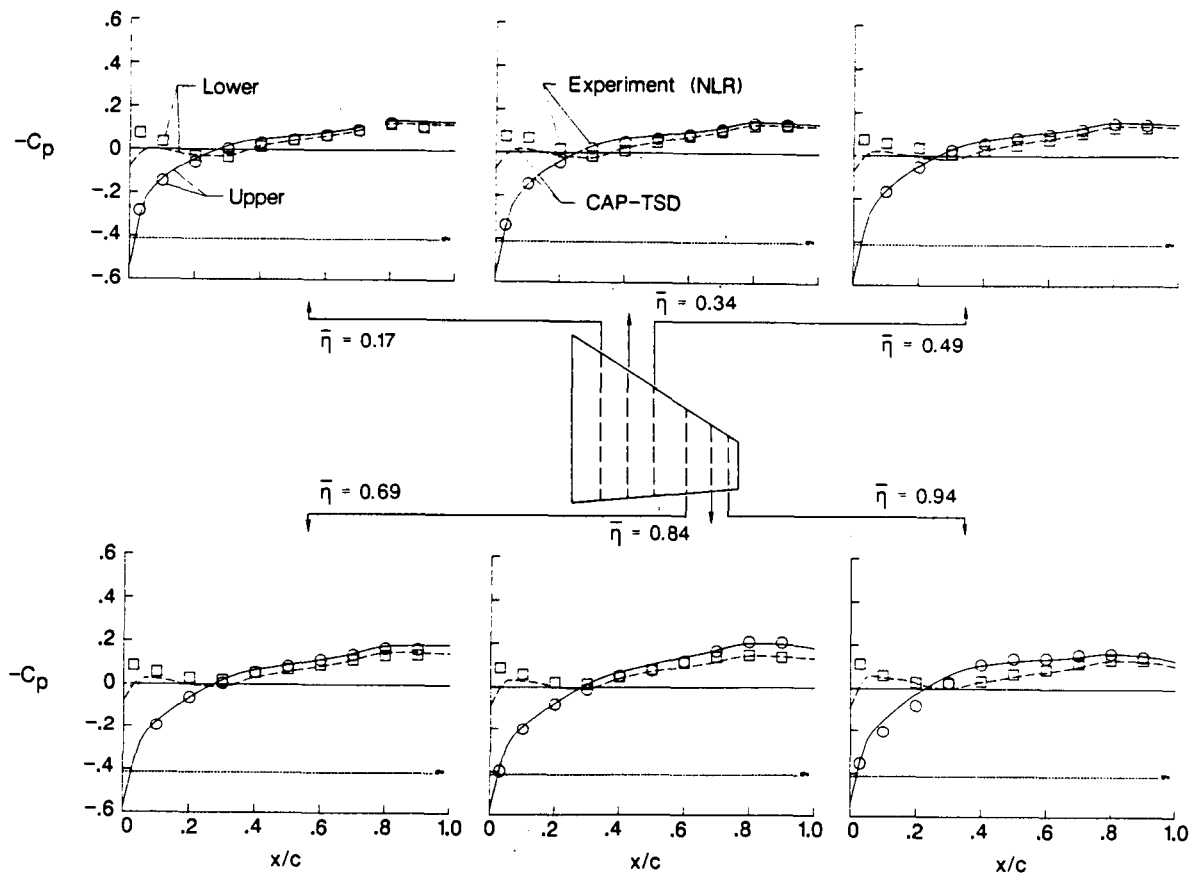
Figure 8

COMPARISON OF CAP-TSD FL057MG (EULER), AND EXPERIMENT
F-5 MODEL, STEADY FLOW, M = 1.10, $\alpha_o = 0°$

A further comparison for M = 1.10 with a steady-flow Euler code (FLO57MG) is given in figure 9. The Euler calculation uses a C-type grid which wraps around the nose of the airfoil and is able to resolve the leading-edge shock in more detail. The pressures over the remainder of the wing are in reasonable agreement taking into account the coarseness of the grid for the Euler calculation (approximately 24,000 points).

Figure 9

COMPARISON OF CAP-TSD AND EXPERIMENT
F-5 MODEL OSCILLATING IN PITCH ABOUT 50% C_r
M = 1.10, k = 0.116, α_0 = 0°, α_1 = 0.267°
UPPER SURFACE

Unsteady pressures are calculated with CAP-TSD for one reduced frequency for each of these two Mach numbers for the F-5 model wing. Upper and lower surface pressures are compared with experiment separately. The upper surface pressures for M = 1.10 and k = 0.116 are shown in figure 10. There is generally good agreement with the data. A typical supersonic loading is evident with only modest variations along the chord.

Figure 10

COMPARISON OF CAP-TSD AND EXPERIMENT
F-5 MODEL OSCILLATING IN PITCH ABOUT 50% C_r
M = 1.10, k = 0.116, α_0 = 0°, α_1 = 0.267°
LOWER SURFACE

The lower surface pressures corresponding to the upper surface results of the previous figure are shown in figure 11. In the region of the lower surface shock, a large peak in unsteady loading is apparent which appears to be due to an embedded transonic flow region. CAP-TSD gives reasonable trends for this case even for the very large unsteady loading at the tip station.
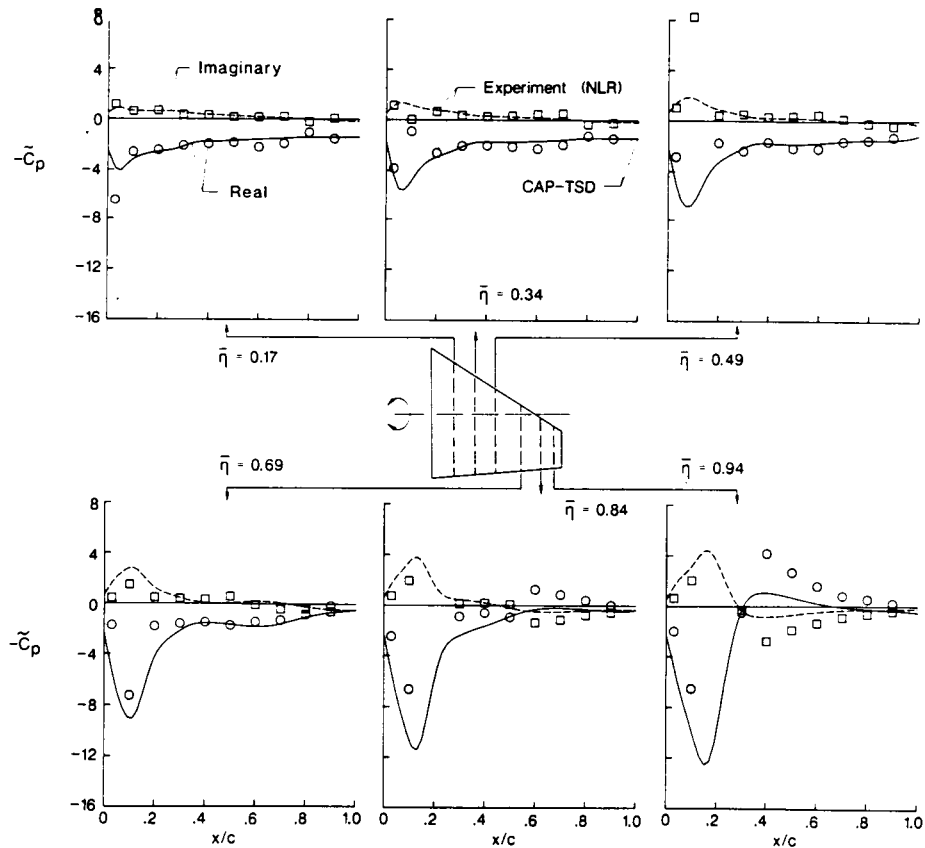
Figure 11

128
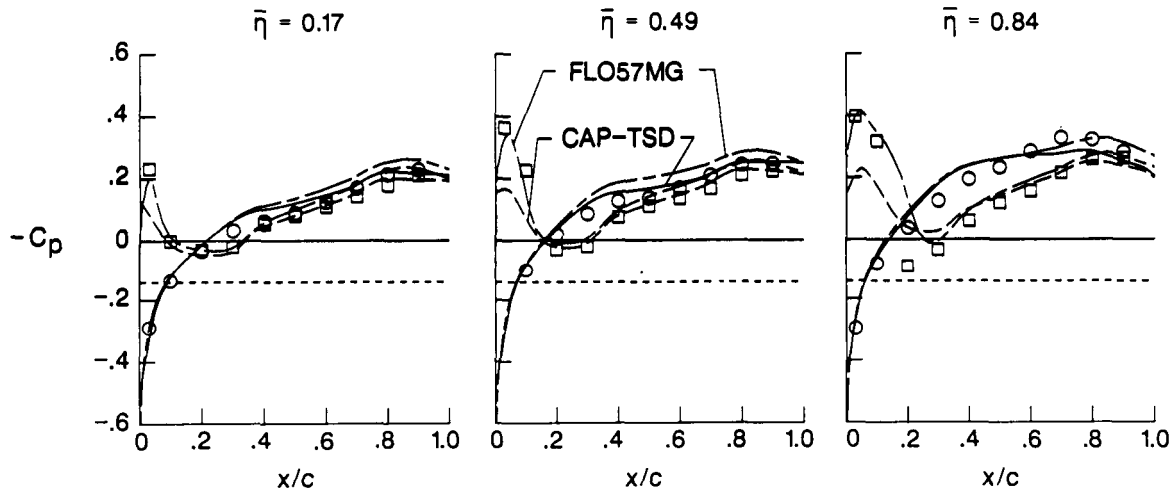
COMPARISON OF CAP-TSD AND EXPERIMENT
F-5 MODEL OSCILLATING IN PITCH ABOUT 50% C_r
M = 1.32, k = 0.198, α_0 = 0°, α_1 = 0.222°
UPPER SURFACE

Unsteady pressures for the upper surface of the F-5 model oscillating in pitch at M = 1.32 are shown in figure 12. Again there is generally good agreement with the data in a similar manner to the agreement for M = 1.10 for the upper surface.
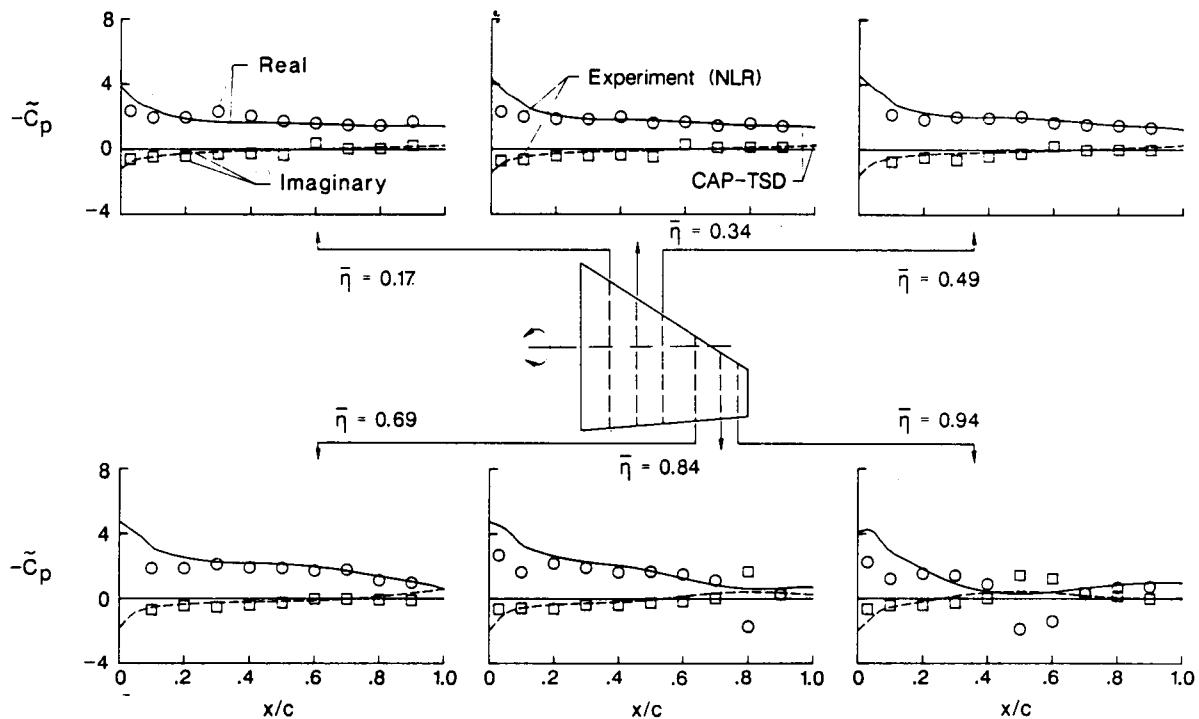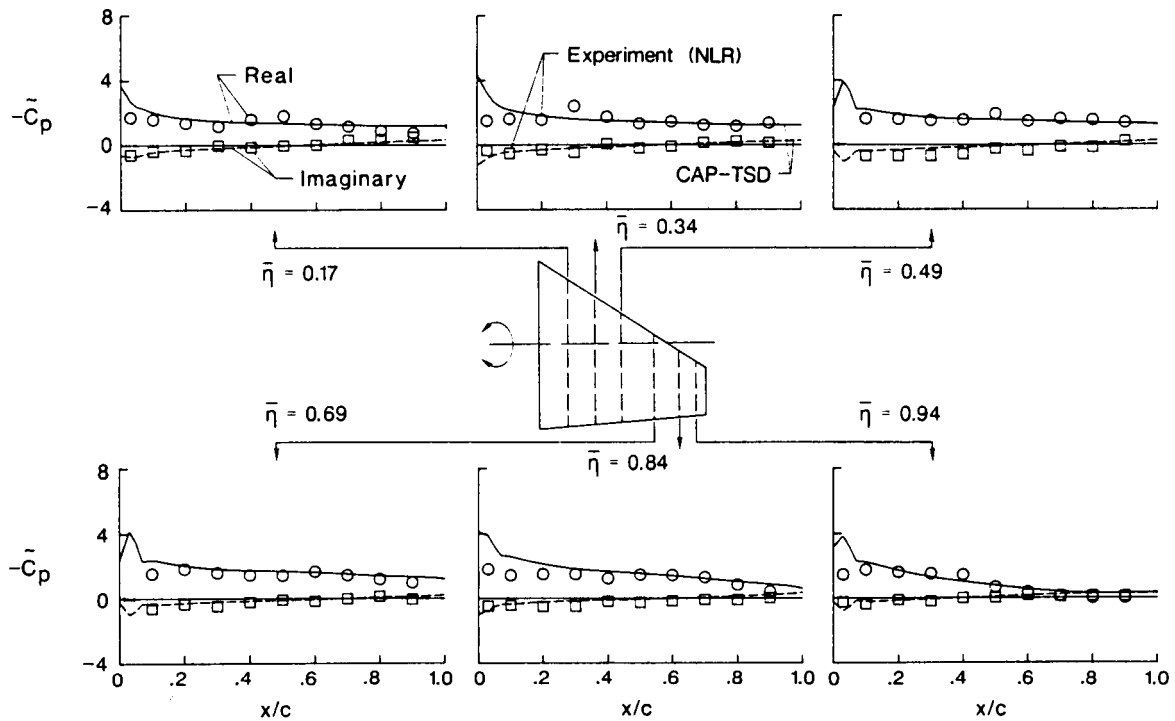

Figure 12

COMPARISON OF CAP-TSD AND EXPERIMENT
F-5 MODEL OSCILLATING IN PITCH ABOUT 50% C_r
M = 1.32, k = 0.198, α_0 = 0°, α_1 = 0.222°
LOWER SURFACE

The lower surface pressures for the F-5 model at M = 1.32 are presented in figure 13. The large peak near the leading edge that was evident at M = 1.10 does not appear in these results. Generally good agreement with the data is again obtained.
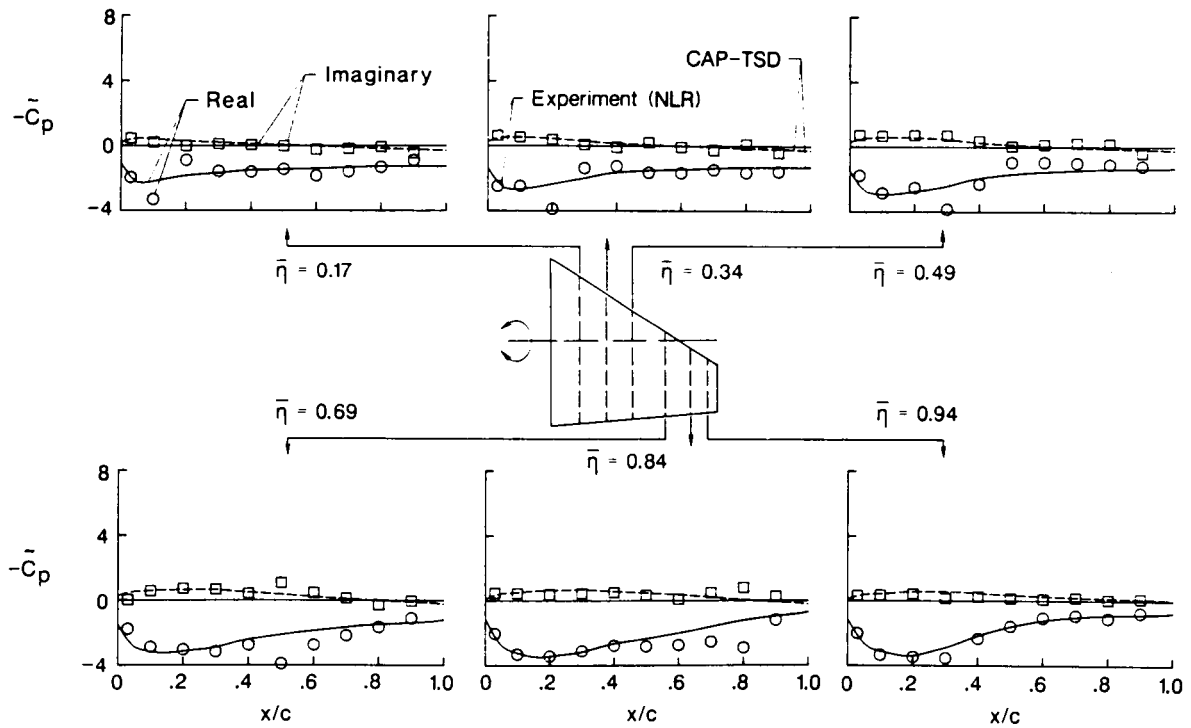
Figure 13

COMPARISON OF CAP-TSD AND EXPERIMENT
RAE TAILPLANE MODEL, STEADY FLOW, M = 1.20, α_0 = 0.0°

The RAE tailplane model was built and tested by the British RAE. The tailplane is a planform that is typical of a tailplane for a supersonic fighter. It has a panel aspect ratio of 1.20, a taper ratio of 0.27, and a leading-edge sweep angle of 50.2°. The airfoil is approximately a NACA 64A010.2 which is thicker (10.2% thick) than is typical for supersonic wings. Only upper surface pressures were measured for this model.

Calculated steady results from CAP-TSD for $\alpha_0 \approx 0°$ and M = 1.20 are compared with measured pressures in figure 14. The measured pressures shown are the mean values measured at 3 Hz (k < 0.015) as steady pressures were not measured for these Mach numbers. The agreement is quite good at all five span stations.
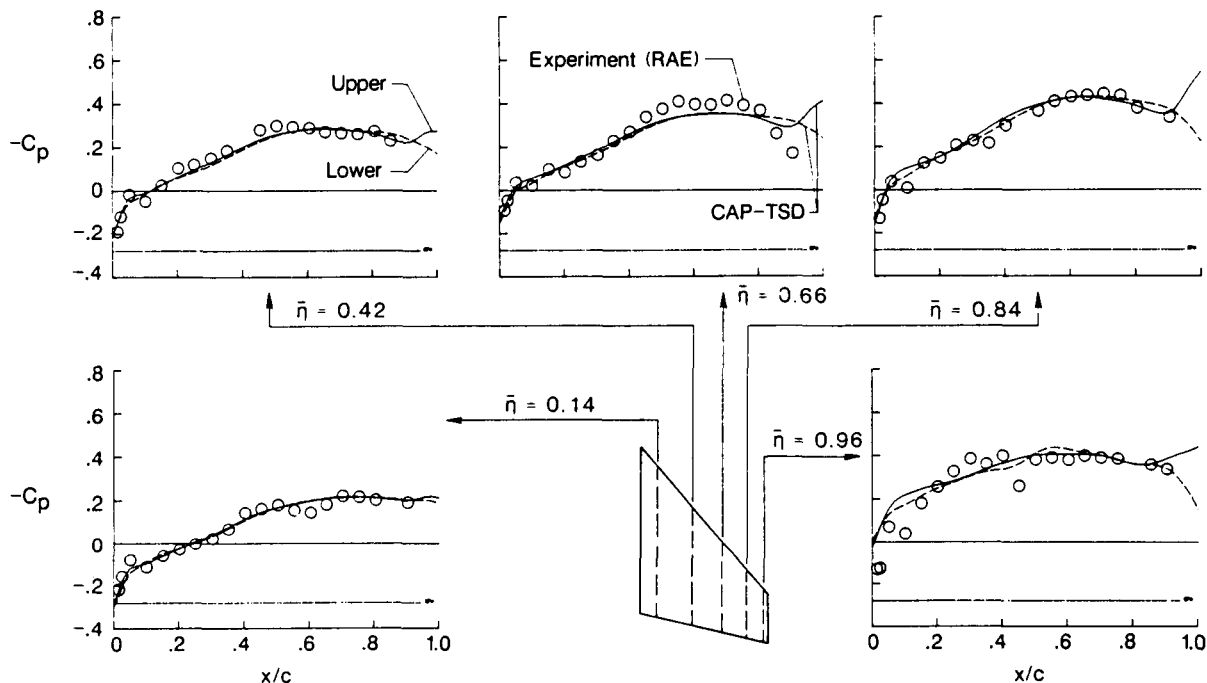
Figure 14

131

COMPARISON OF CAP-TSD AND EXPERIMENT
RAE TAILPLANE MODEL, STEADY FLOW, M = 1.71, α_0 = 0.14°

The calculated steady results for M = 1.32 are compared with the experimental results in figure 15. Here the agreement is good inboard, but some deviation is shown near the tip.
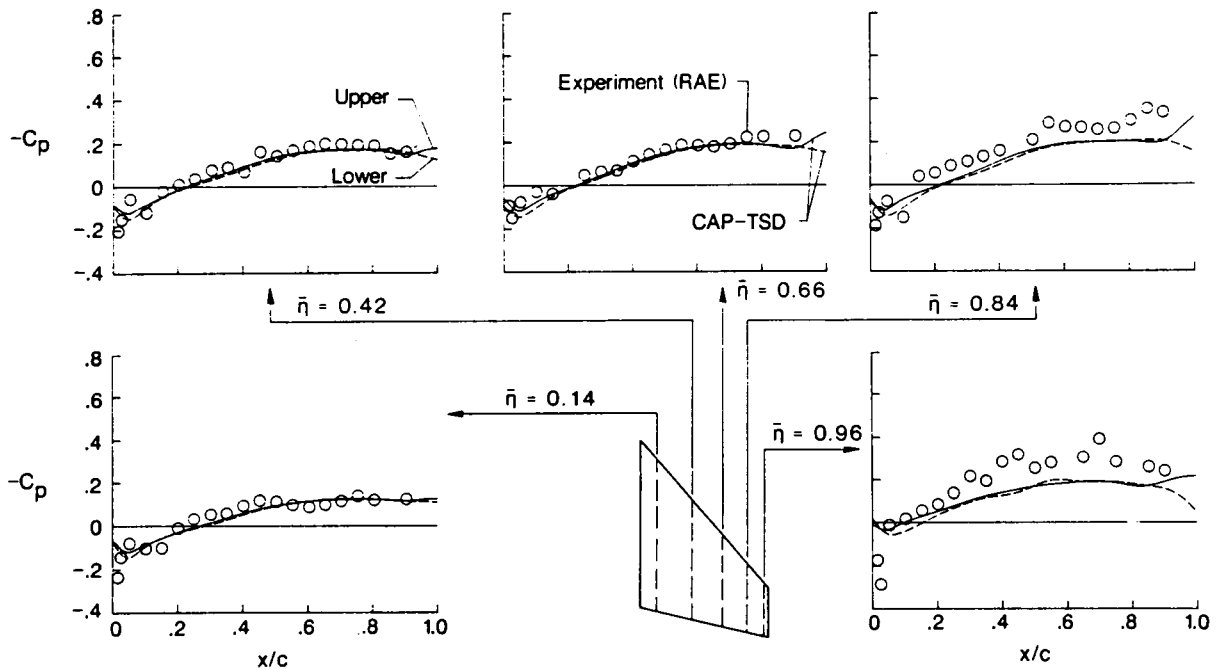
Figure 15

COMPARISON OF CAP-TSD, FL057MG (EULER) AND EXPERIMENT
RAE TAILPLANE MODEL, STEADY FLOW, M = 1.71, $\alpha_0 = 0.14°$

Corresponding calculations for M = 1.71 with FLO57MG using the Euler equations are presented in figure 16. The results from CAP-TSD and the Euler results are in close agreement. The results from FLO57MG also show the deviation from the data near the tip.
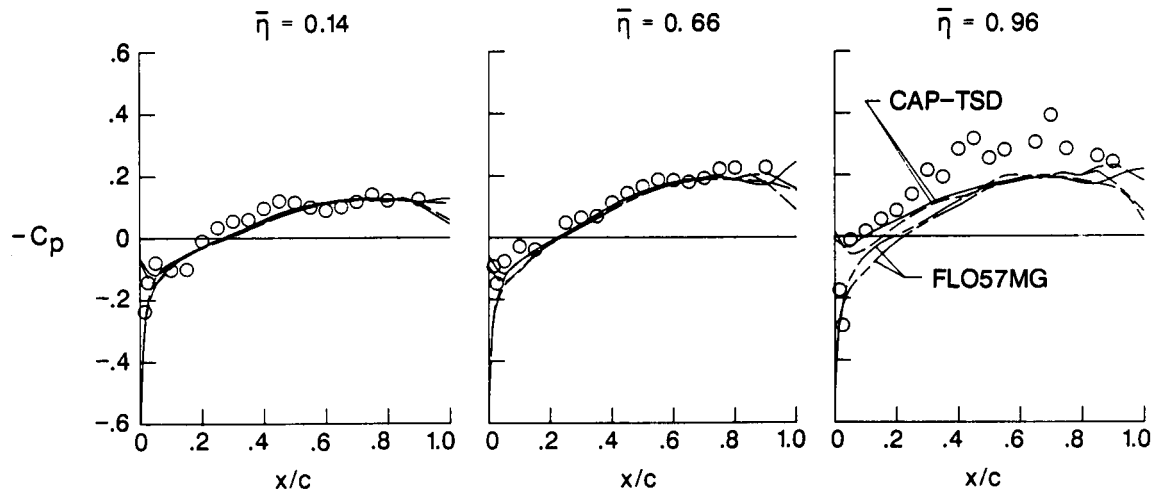
Figure 16

COMPARISON OF CAP-TSD AND EXPERIMENT
RAE TAILPLANE MODEL OSCILLATING IN PITCH ABOUT 68% C_r
$M = 1.20$, $K = 0.346$, $\alpha_0 = 0°$, $\alpha_1 = .378°$

Unsteady pressures for pitching oscillations of the RAE tailplane model at $M = 1.20$ and 70 Hz are presented in figure 17. Good overall agreement for the in phase (or real) data is obtained but the out-of-phase components (imaginary) are under predicted somewhat. As previously indicated, pressures were measured only on one surface.
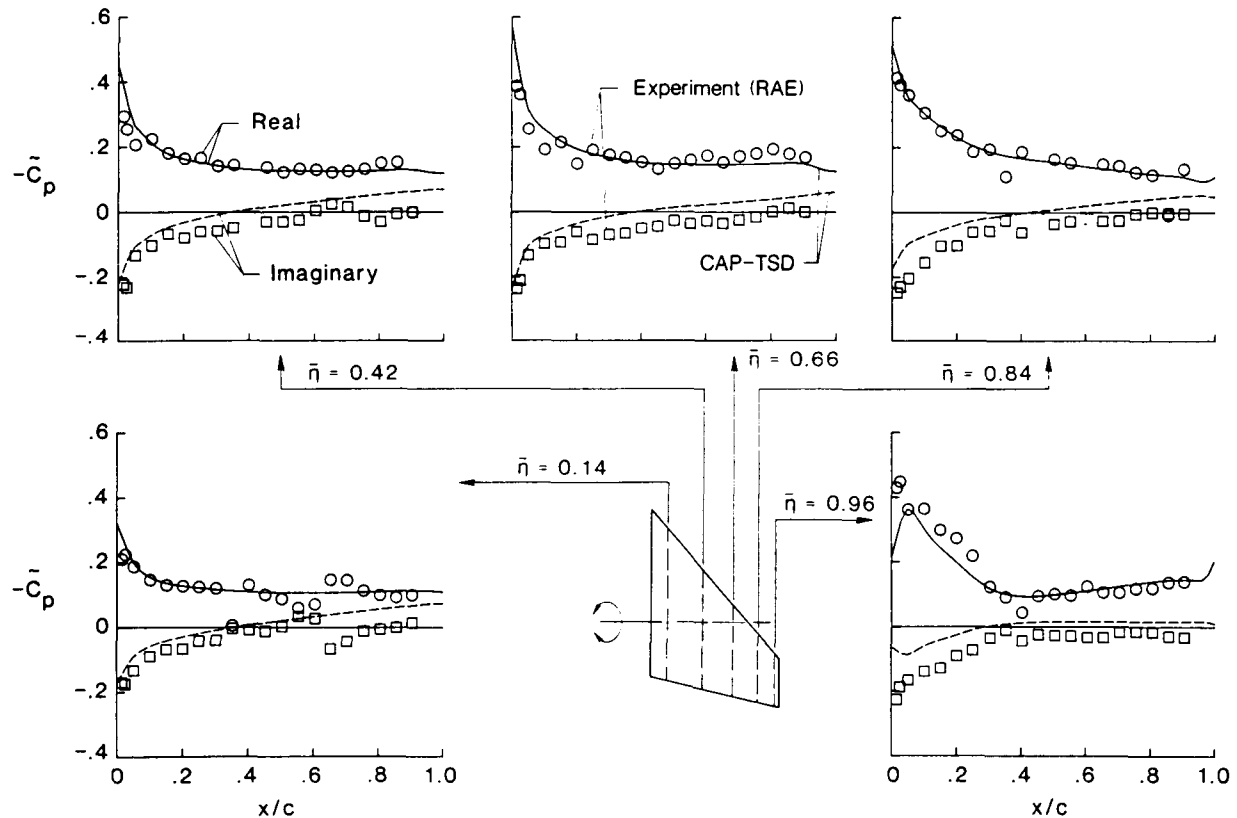
Figure 17

134

COMPARISON OF CAP-TSD AND EXPERIMENT
RAE TAILPLANE MODEL OSCILLATING IN PITCH ABOUT 68% C_r
$M = 1.71$, $K = .270$, $\alpha_0 = .14°$, $\alpha_1 = .570°$

The unsteady results for the tailplane oscillating at 70 Hz at $M = 1.71$ are shown in figure 18. The agreement is comparable to that of $M = 1.20$. The unsteady loading has less of a peak near the leading edge for $M = 1.71$ than for $M = 1.20$.
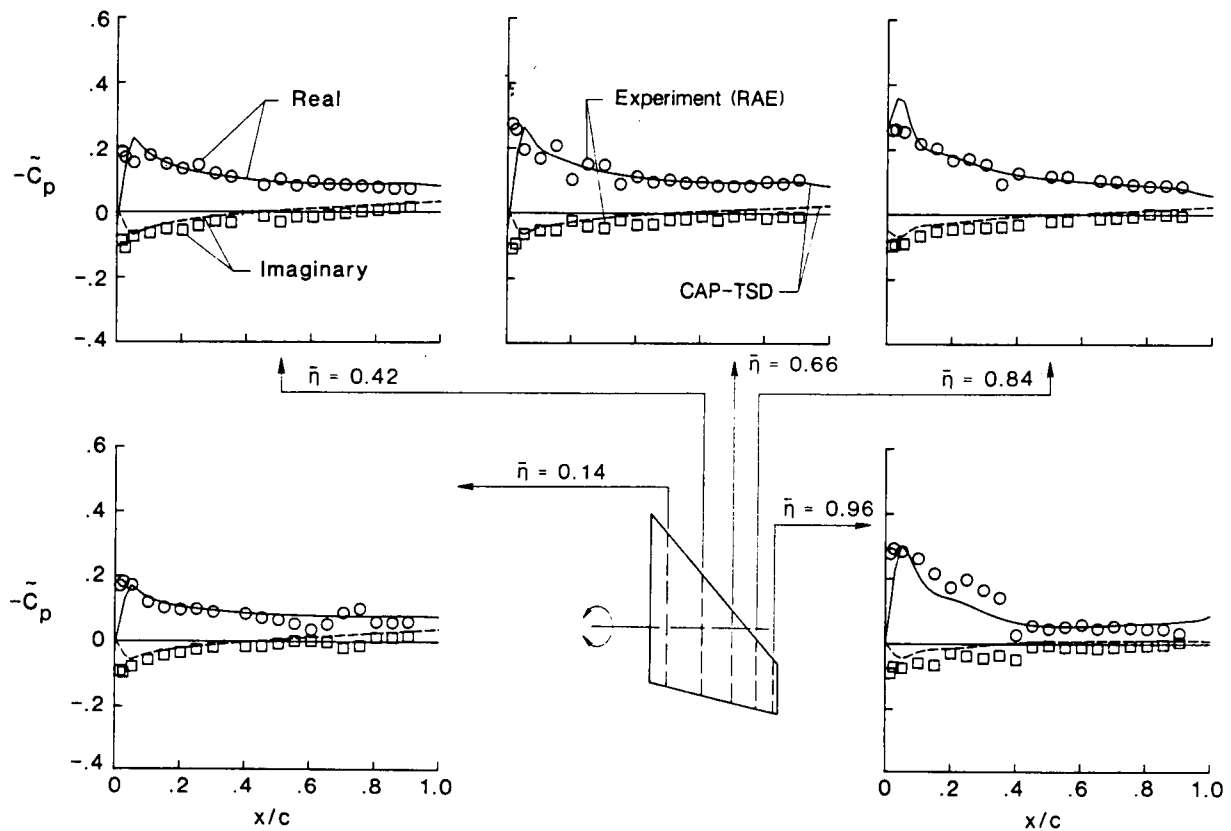
Figure 18

COMPARISON OF CAP-TSD AND EXPERIMENT
RAE TAILPLANE MODEL M = 1.71, α_o = 5.14, STEADY FLOW

Some measurements were made at 5° mean angle of attack for this model. Pressures on the lower surface were obtained by testing the upper surface at the corresponding negative angle of attack. The steady pressures for $\alpha_o = 5°$ and M = 1.71 are compared with results from CAP-TSD in figure 19. Both the thickness loading and the pressure difference are reasonably well predicted even at this large angle of attack and Mach number. Again some deviation of the results from the data is evident on the upper surface near the tip.
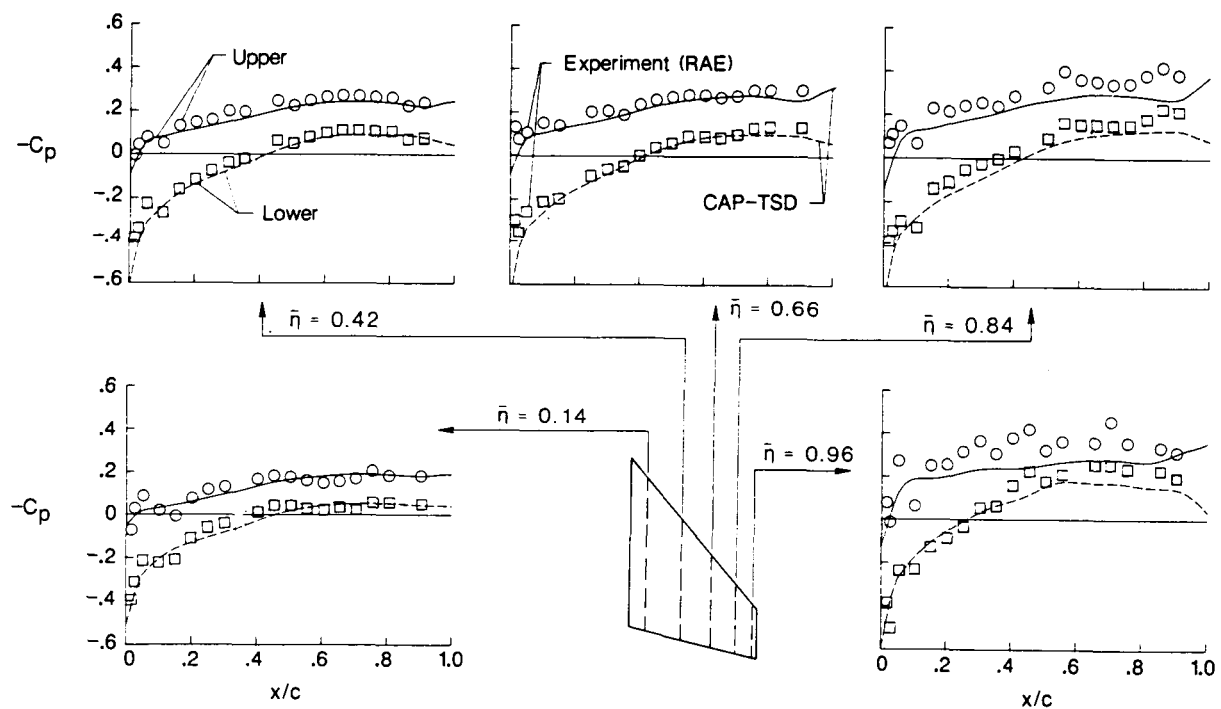
Figure 19

CONCLUDING REMARKS

A transonic unsteady aerodynamic and aeroelastic analysis code called CAP-TSD has been developed for application to realistic aircraft configurations. The new code now permits the calculation of unsteady flows about complete aircraft configurations for aeroelastic analysis in the flutter critical transonic speed range. It uses an AF algorithm that has been shown to be very efficient for steady or unsteady transonic flow problems including supersonic freestream flows.

Results were presented for several wings that demonstrate the applicability of CAP-TSD for supersonic flows including embedded transonic flows. Comparisons with known exact analytical solutions from linear theory demonstrated that CAP-TSD gives reasonably good fidelity to approximating weak shock waves, but with smearing of strong discontinuities. Unsteady lift was well predicted for a two-dimensional flat plate airfoil and for an oscillating rectangular wing. CAP-TSD results for the thin F-5 wing were in good overall agreement with experimental steady and unsteady pressures and with a steady flow Euler code. One case with an embedded swept shock near the lower surface leading edge indicated that embedded transonic flows can be treated. Results for the RAE tailplane model were in good agreement with the measured data for both steady and unsteady cases, and with a steady calculation with an Euler code. Good agreement was also found for a steady flow case at a Mach number of 1.71 and five degrees mean angle of attack. The present study has demonstrated the applicability of the CAP-TSD code to flows with supersonic freestream with favorable comparisons of selected cases. Improvements to the shock capturing characteristics and the supersonic outer boundary conditions for supersonic flows are desirable. (Fig. 20.)

CONCLUDING REMARKS

- CAP-TSD applied to wings in supersonic flow

- Results compare favorably with exact linear theory solutions

- Generally good agreement with experiment for F-5 and tailplane models

- Improvements needed in shock capturing and outer boundary conditions

Figure 20

AN EFFICIENT METHOD FOR COMPUTING UNSTEADY TRANSONIC AERODYNAMICS
OF SWEPT WINGS WITH CONTROL SURFACES

D. D. Liu[*] and Y. F. Kao[†]
Department of Mechanical and Aerospace Engineering
Arizona State University
Tempe, Arizona

and

K. Y. Fung[*]
Department of Aerospace and Mechanical Engineering
University of Arizona
Tucson, Arizona,.

ABSTRACT [#]

A transonic equivalent strip (TES) method has been further developed for unsteady flow computations of arbitrary wing planforms. The TES method consists of two consecutive correction steps to a given nonlinear code such as LTRAN2; namely, the chordwise mean-flow correction and the spanwise phase correction. The computation procedure requires direct pressure input from other computed or measured data. Otherwise, it does not require airfoil shape or grid-generation for given planforms. To validate the computed results, four swept, tapered wings of various aspect ratios, including those with control surfaces, are selected as computational examples. Overall trends in unsteady pressures are established with those obtained by XTRAN3S codes, Isogai's full potential code and measured data by NLR and RAE. In comparison with these methods, the TES has achieved considerable saving in computer time and reasonable accuracy which suggests immediate industrial applications.

INTRODUCTION

Considerable attention has been directed in recent years towards the technology development of transonic aeroelastic applications with particular emphasis on transonic flutter predictions. Based on transonic small-disturbance equations (TSDE), computational methods for unsteady transonic flow have been developed extensively both in two and three dimensions, notably LTRAN2 (now ATRAN2) (Refs. 1,2) and XTRAN3S computer codes. Various versions of XTRAN3S codes (Refs. 3,4,5) and a number of full potential methods (Refs. 6,7) are all in good progress. Recently, Guruswamy and Goorjian (Ref. 3), and Borland and Sotomayer (Refs. 4,8) have applied their XTRAN3S codes to Northrop F-5 wing planform. Bennett et al. (Ref. 9) have applied Langley XTRAN3S code for a RAE swept wing; Ruo and Malone (Ref. 10) have applied the same code for LANN wing computations. Isogai and Suetsugu (Ref. 6) have applied their full potential code to various planforms including the AGARD standard RAE wing with an oscillating flap. Most of these results have shown good agreement with the measured data of NLR and RAE.

Although these methods could produce reasonably accurate results, computation efficiency and the grid generation procedures remain to be improved before these codes can be adopted for industrial applications. For flutter predictions and aeroelastic optimizations, a more efficient computer code capable of rapid computations is sought by the aerospace industries, since cost-effectiveness is one of their main concerns.

Motivated by these considerations, we have set forth to develop a simple and more efficient method for unsteady, three-dimensional flow computations. Our objective is to achieve: (1) computation efficiency, (2) flexibility and ease of applications for flutter and (3) a unified subsonic/transonic method for arbitrary planforms. Consequently, a preliminary version of the transonic equivalent strip (TES) method has been developed (Ref. 11). The results obtained for rectangular-wing studies show promise for the TES formulation. Hence, it prompts further development. In this paper, the TES method is further developed so that all procedures are automated for aerodynamic computations. Thus it can be readily adopted by the flutter prediction and the aeroelastic optimization programs. To validate the present method, a fairly comprehensive comparison with available data is given for a number of wing planforms including those with control surfaces.

TRANSONIC EQUIVALENT STRIP (TES) METHOD

The use of strip concept for unsteady transonic computations was first proposed by the ONERA group (Ref. 12). A similar strip approach, but involving quasi-steady approximations, was recently implemented at NLR (Ref. 13). In both cases, however, only wing planforms of large aspect-ratio are treated and possible applications of their methods to low aspect-ratio wings are not forthcoming. By contrast, the present TES method has developed a more general scheme which could handle arbitrary planforms including oscillating control surfaces.

Correction Procedures

Specifically, the present method consists of the applications of two correction steps to a given two dimensional code; it could be a nonlinear code such as LTRAN2 or it could be a time linearized one. The basic correction steps are: (1) the mean-flow correction applied in the chordwise direction and (2) the phase correction in the spanwise direction (see Fig. 1 for flow chart). The first correction is fully automated by an inverse design procedure (IAF2 code) in that the local shock structure is properly recovered according to the given mean flow input provided by a selected computational method or by measured data. In this inverse problem, as solved by Fung and Chung (Ref. 14), the velocity

[†] Associate Professor, Member AIAA
[†] Graduate Student

[#] Also published as AIAA-85-4058.

potential from integrating the pressure on the slit representing an airfoil is known up to an arbitrary constant. To determine this constant, a closure condition is imposed, e.g., the resulting slope distribution being equivalent to a closed body. This constant is being updated during the numerical iteration process until a converged solution satisfying the closure requirement is obtained. Once the slope distribution of the new equivalent airfoil is found and the steady flow field fixed, unsteady responses can then be calculated by varying the slopes to account for unsteady motions. The latter step can be accomplished by applying LTRAN2 code to the equivalent airfoil.

For the second correction, we make use of the three-dimensional linear wave analogy in the sense that the phase angles are redistributed along the span according to the physical model of acoustic wave propagations in a uniform medium. This is to say that while the first correction accounts for reproducing the nonlinear structure of the three-dimensional mean flow, the second correction is responsible for the adjustment of the spanwise phase lag of the pressure according to an equivalent linear three-dimensional flow. In practice, a typical lifting surface method such as Doublet Lattice code (Ref. 15) is adopted for the second correction. Clearly, shock waves cannot be created or destroyed by any process of these corrections.

We should note that the present terminology of "strip method" is defined only by the stripwise computation procedure and is otherwise irrelevant to the classical strip theory. The above correction procedures clearly indicate that the present TES approach is equivalently three-dimensional, since there is no restriction to the wing aspect-ratio.

Justification

It has been pointed out by Fung and Lambourne (Ref. 16,17), among others, that an accurate steady state with correct shock jump and location is essential for correct unsteady aerodynamic computations. It is believed that TSDE in general should be adequate for computation of unsteady disturbances, which are acoustic signals assumed to be small in conventional flutter analysis. However, when applying TSDE methods, inaccuracy may occur as a result of the local failure at the wing leading edge and the limitation in the prediction of the shock strength. Since an accurate steady state pressure field is desired, an alternative is to find the airfoil slopes, or equivalently the airfoil, that corresponds to a given pressure distribution. This, in turn, suggests the inverse design procedure used in the first correction.

Meanwhile, the unsteady aerodynamics of wing flutter at transonic speed is complicated by the embedded supersonic region. Disturbances downstream cannot be felt directly at an upstream point. As a result, the phase lag between unsteady motion of the wing and corresponding aerodynamic response increases as the supersonic region gets larger. While this effect is important in the chordwise direction of a wing, the existence of supersonic region should not affect the way an acoustic signal propagates in the spanwise direction. With the exception of highly-swept wings, the flow-induction effect in the spanwise direction should be subsonic in nature. It is therefore conceivable that the correlation between the aerodynamic responses at different spanwise stations is a linear one as assumed in conventional flutter analysis, and that the unsteady aerodynamic responses due to structural deformations of a wing at transonic speeds are

similar in nature to those at the corresponding subsonic speeds, except in the streamwise direction.

ANALYSIS

Governing Equations

The simplest form of the time-dependent three-dimensional TSDE can be expressed as

$$C\phi_{xx} + D\phi_{yy} + \phi_{zz} = 2B\phi_{xt} + A\phi_{tt} , \qquad (1)$$

where

$$A = M_\infty^2 k^2/\delta^{2/3} , \quad B = M_\infty^2 k/\delta^{2/3}, \quad C = K - \Gamma\phi_x,$$

$$K = (1-M_\infty^2)/\delta^{2/3}, \quad \Gamma = (\gamma+1)M_\infty^2 \quad \text{and}$$

$$D = c^2/b^2\delta^{2/3}.$$

The nondimensional quantities and coordinates are defined as

$$\phi = \bar{\phi}/(c\delta^{2/3}U_\infty) ,$$

$$(x,y,z) = (\bar{x}/c, \bar{y}/b, \bar{z}\delta^{1/3}/c),$$

$$t = \bar{t}\omega \quad \text{and} \quad k = \omega c/U_\infty ,$$

where all barred symbols denote the true physical quantities, parameters c, b, δ and ω represent the root chord, the semi-span, the airfoil thickness ratio and the circular frequency of oscillation, respectively.

The potential ϕ can be split into two components, i.e.,

$$\phi = \phi_0(x,z,t) + \phi_1(x,y,z,t;\Delta\alpha) \qquad (2)$$

where ϕ_0 satisfies the nonlinear, two-dimensional equation (set D = 0 in Eq. (1)) as can be solved by LTRAN2 code; ϕ_1 is the correction potential accounting for the three-dimensional effect attributed to a small unsteady disturbance due to the amplitude Δα. The three-dimensional unsteady disturbance is assumed to be small as compared to the two-dimensional one at all times; hence, the nonlinear term in the ϕ_1-equation can be neglected, resulting in a linear equation for ϕ_1, i.e.

$$K\phi_{1_{xx}} - \Gamma(\phi_{0_x}\phi_{1_x})_x + D\phi_{1_{yy}} + \phi_{1_{zz}} = 2B\phi_{1_{xt}} + A\phi_{1_{tt}} \quad (3)$$

Foregoing physical argument in the TES method allows for further simplification of Eq. (3) by ignoring the coupling term $(\phi_{0_x}\phi_{1_x})_x$. In so doing, Eq. (3) is reduced to the acoustic equation, where ϕ_1 can be simply solved by the conventional subsonic lifting surface method (Ref. 15).

To further justify the spanwise connection procedure, it is helpful to investigate the characteristic surfaces due to Eq. (1),

$$(x-\frac{B}{A}t)^2 + (C+\frac{B^2}{A})z^2 + (\frac{C}{D} + \frac{B^2}{AD})y^2 = (\frac{B^2}{A^2} + \frac{C}{A})t^2 \qquad (4)$$

Expressed in the dimensional form and for t > 0, Eq. (4) can be recast into a general form, see Fig. 2A

$$(\bar{x} - U_\infty\bar{t})^2 + (\lambda\bar{y})^2 + (\lambda\bar{z})^2 = (\lambda a_\infty\bar{t})^2 \qquad (5)$$

where $\lambda^2 = 1$, for linearized subsonic flow,

$\lambda^2 = 1-(\gamma+1)M_\infty M_\ell$, for transonic flow.

141

M_ℓ is a local, small-disturbance Mach number, defined as $M_\ell = \phi_x^-/a_\infty$; hence, λ^2 must be positive or zero. Eq. (5) indicates that the traveling source of small disturbance is emitted from $(U_\infty t, 0, 0)$ at the instant t, whose wave front is a sphere for linearized subsonic flow and an ellipsoid for transonic flow (Fig. 2A). Hence, the expanding wave fronts propagate at wave speeds in the chordwise- and spanwise-strip planes, for $y = y_i$ and $x = x_i$, respectively, with

$$\frac{d\bar{R}}{dt} = \frac{a_\infty^2\, \bar{t}}{\sqrt{a_\infty^2 \bar{t}^2 - \bar{y}_i^2}} \qquad \text{(chordwise)}$$

and

$$\frac{d\bar{R}}{dt} = \frac{(a_\infty^2 - U_\infty^2)\bar{t} + U_\infty \bar{x}_i}{\sqrt{a_\infty^2 \bar{t}^2 - (\bar{x}_i - U_\infty \bar{t})^2}} \qquad \text{(spanwise)}$$

Note that at $x_i = U_\infty t$ or $y_i = 0$, the rate of propagation becomes identically sonic; otherwise it is time-dependent. Most importantly, along these strip planes, the event diagrams (x–t diagrams) clearly show that while the propagation in the chordwise strip plane is of mixed type which could be either locally subsonic or supersonic, depending on the difference between a_∞ and U_∞, the propagation in the spanwise strip is unconditionally subsonic, which is independent of the a_∞ and U_∞ relations (Fig. 2B).

Boundary Conditions

On the mean surface of the wing planform the potentials must satisfy the tangency condition, i.e. at $z = 0$,

$$\phi_{0_z} = \delta F_x(x, y_i) + \alpha_0 + \alpha_1 \cdot (H_x + kH_t) , \qquad (6)$$

$$\phi_{1_z} = \Delta\alpha \cdot (H_x + kH_t) , \qquad (7)$$

where $F(x, y_i)$ is the stripwise wing surface geometry, y_i is the "ith" spanwise location, α_0 is the mean angle of attack, and $H(x, t)$ depicts the wing motion with oscillation amplitude $\alpha_1 + \Delta\alpha$. While $\Delta\alpha$ is the small amplitude which induces the three-dimensional unsteady disturbances, $\Delta\alpha$ is actually related to the two-dimensional amplitude α_1 by $\Delta\alpha = o(\alpha_1)$.

Outside of the wing planform, the potential ϕ must satisfy the radiation condition in the lateral and the upstream far fields. The zero pressure jump condition across the wake sheet and along which there is no flow discontinuity must be maintained. Also, an unsteady pressure wave must attenuate far downstream. Since these boundary conditions are linearized consistent with the small-disturbance assumption, expressions for ϕ_0 and ϕ_1 become decoupled. Thus, it renders the correction steps to be applied in a consecutive manner.

Pressure Coefficients

Due to a small oscillatory amplitude α, the pressure coefficient can be decomposed into

$$\bar{c}_p = c_p + \Delta c_p \cdot \alpha$$

where c_p is the steady mean pressure coefficient and Δc_p is the unsteady pressure coefficient defined as

$$\Delta c_p^j = \left(\frac{p_u^j - p_\ell^j}{\frac{1}{2}\rho_\infty U_\infty^2}\right) / \alpha^j \qquad (8)$$

with P_u and P_ℓ denoting the pressure at upper and lower surfaces, the superscript $j = \ell$, N and "ℓ" denotes the linear subsonic values and "N" denotes the nonlinear transonic values. Clearly,

$$\alpha^N = \alpha_1 \quad \text{and} \quad \alpha^\ell = \Delta\alpha .$$

In terms of the strip concept, Eq. (6) can be written as

$$\Delta c_{p_1}^j = c_1\, p_1^j\, (x, y, z; k) , \qquad (9)$$

$$\Delta c_{p_0}^j = c_0\, p_0^j\, (x, y_i, z; k) , \qquad (10)$$

where c_1 and c_0 are constants and the subscripts 0 and 1 denote, respectively, the two-dimensional strip value and the three-dimensional value at the spanwise location $y = y_i$. While the first correction is applied at the level of Eq. (8), the spanwise correction is implied by the pressure-mode relation between p_1^j and p_0^j which can be expressed as

$$p_1^j = p_0^j\, f^j(y; k) . \qquad (11)$$

According to the foregoing arguments of wave propagations in the stripwise characteristic plane, the nonlinear spanwise pressure function $f^N(y; k)$ can be approximated by its linear counterpart $f^\ell(y; k)$ throughout the spanwise correction procedure.

In passing, we note that in all the figures presented, $\Delta c_p'$ and $\Delta c_p''$ are the real and imaginary parts of the unsteady pressure Δc_p representing the in-phase and out-of-phase pressure coefficients.

RESULTS AND DISCUSSION

To demonstrate the present TES method and to validate its computed results, four different wing planforms are selected for comparison with available data. These include Northrop F-5 Wing in pitching motion and with an oscillating flap, LANN wing in pitching motion, RAE/AGARD tailplane in pitching motion and AGARD standard RAE wing with an oscillating flap. The sections selected are given in the table 1 below:

Table 1   Selected Wing Sections

Planforms	Sections /	Semi-Span %
F-5 Wing	1, 2, 3, 5, /	18.1, 35.2, 51.2, 72.1,
	6, 7, 8 /	81.7, 87.5, 97.7
LANN Wing	2, 3, 4, /	32.5, 47.5, 65.0
	5, 6 /	82.5, 95.0
RAE Tailplane	1, 2, 3, 5 /	14.0, 42.0, 66.0, 96.0

Steady Mean-Flow Results: Equivalent Airfoil Design

For all steady mean-flow pressure design outputs, the present computed results using the IAF2 code for equivalent airfoil design are shown by solid lines, whereas the input data in general are

shown by open symbols. Figure 3A and 3B display the pressure inputs for upper and lower surfaces at selected sections listed above at M_∞ = 0.9 for LANN wing and F-5 wing based on NLR's measured data (Refs. 18,19). For the case of F-5 wing at M_∞ = 0.95, it can be seen from Figure 3C that "strong" shock occurs near the wing trailing edge. Hence some care must be exercised to input the pressure data. To demonstrate the flexibility of the TES method, we adopt the computed results of XTRAN3S-Ames (Ref. 3) as our pressure inputs. Notice that minor discrepancies between input and output results appear behind the mean shock. Figure 10A shows the comparison of input data measured by RAE (Ref. 9) and the TES output results for a RAE tailplane at M_∞ = 0.9. Figure 11 presents the steady pressures for the RAE wing at 45% spanwise location using the computed results of the Bailey-Ballhaus code (or GACBOPPE code) as inputs, as no measured data were provided for this section in Ref. 20. For all cases considered, the comparison between the input data and the output computed results are generally in good agreement.

Unsteady Pressure Results: LTRAN2/TES Computations

For unsteady computations, the LTRAN2 code is adopted as our computation basis because of its inclusion of nonlinearity and ease of application. In all figures presented for unsteady pressures, solid lines denote the present TES method, whereas lines attached with triangular symbols represent various versions of XTRAN3S codes, with the exception of Figure 11. The open square and circle symbols denote the NLR or RAE measured data for in-phase and out-of-phase pressures, respectively.

Figures 4, 5 and 6 contain unsteady results at various spanwise sections of Northrop F-5 wing in pitching oscillation at M_∞ = 0.9 and at given reduced frequencies k_c = 0.274, 0.55 and 0.136, respectively. Figure 7 presents the unsteady results for the same wing in pitching oscillation at M_∞ = 0.95. The pitching axes for all cases of F-5 wing are located at 50% root chord. For all cases at M_∞ = 0.9, it can be observed that the present results practically follow the same trend as those of XTRAN3S codes. Better correlations are found at lower frequencies than for those at higher frequencies. In Figure 5, overpredicted unsteady shock appears in section 5 which suggests that the three-dimensional, wave cancelling mechanism acts at high frequencies more effectively than a locally two-dimensional one. In Figure 7, the resulting unsteady pressures at M_∞ = 0.95 appear also to follow the same trend as those of NLR and XTRAN3S code, except that the unsteady shock strength is again overpredicted by the present method. To investigate this problem further, we change over the pressure input as predicted by XTRAN3S to the NLR measured data which contains a weaker mean shock. As shown in Figure 8, the unsteady pressures are indeed improved near the shock and are otherwise unaffected. This further verifies our contention that the steady shock strength and position are the most crucial for unsteady pressure predictions.

Figure 9 presents the in-phase and out-of-phase pressures of the LANN wing with pitching axis located at 62% root chord. Throughout five spanwise locations considered, the present results for upper-surface compare more favorably with the NLR measured data than do the XTRAN3S results. Meanwhile, subcritical flows are predicted for lower surfaces; hence, the unsteady pressures do not contain shock-jump. Figure 10 presents pressure results for a highly-swept RAE tailplane of Λ = 50.2° at M_∞ = 0.9 and at zero mean incidence. Because the present method uses the measured data inputs, it can be seen that the predicted unsteady shock positions correlate better with the RAE data than do the XTRAN3S results. It should be cautioned that Eq. (1) may not be suitable for wings with large sweepback angles, as the side wash could be of the same order as the mean convective velocity. One would therefore expect that for both steady and unsteady flow, discrepancies will occur near the wing tip, particularly for wings with low aspect ratios. Such deterioration in pressure estimates was observed in Ref. 9.

In general, overall trends of unsteady pressures were obtained with TES method from Figures 4 to 10. In some cases, insufficient adjustment of the phase angle causes the underprediction of the unsteady pressure level. It is believed that this type of discrepancy may result from the linear approximation inherent in the spanwise correction procedure.

Oscillating Flap

Figure 11 presents the computed and measured data at 45% semi-span of AGARD standard RAE wing with an oscillating flap starting at 70% chord. It is interesting to observe that the present results and Isogai's full potential method (Ref. 6) are in good agreement with RAE measured data. Figure 12 compares in- and out-of-phase pressures at two flap sections of F-5 wing at M_∞ = 0.9; the hinge line is located at 82% chord. Closed agreements are found with XTRAN3S results of Sotomayor and Borland (Ref. 8) and NLR measured data (Ref. 21). It should be pointed out that in presenting the flap oscillation data, usual practice in computational methods is to connect the data points across the hinge line, in the same manner as connecting the shock points; such are the cases of Refs. 6 and 8. However, control surface singularities in subsonic flow have been well established by White and Landahl (Ref. 22). Since the flow is assumed inviscid and is locally subsonic, hinge line singularity, as we have presented in these figures, should prevail.

Computation Time

In performing the first correction of the present TES code (LTRAN2/IAF2), we used typically 103 x 97 grid points and assigned 240 time steps for each cycle. Pressure data are read usually in the fourth cycle, as the aerodynamic response normally becomes periodic or harmonic after the third cycle. Typically, it takes 700 iterations to achieve the IAF2 steady pressure output. In an IBM 3081, the CPU time for the first correction amounts to some 620 seconds. With 10 x 10 panels, the Doublet Lattice code requires 40 seconds, with the additional procedure, the CPU time amounts to roughly 100 seconds. Hence, the total CPU time required for running TES code on one strip adds up to 720 seconds. The same case (e.g., Northrop F-5 wing) computed by XTRAN3S code would require reportedly 2000 to 4000 seconds CPU time in the CRAY-1S supercomputer. This would amount to an equivalent CPU time in an IBM 3081 of about 10 hours or more. With four strips chosen in this case, present TES method usually takes up no more than 3000 seconds. Therefore, a saving of about ten- to twelve-fold in CPU time can be achieved. With further improvement to the TES pilot code, it is expected that at least another reduction factor of two in CPU time can be achieved.

CONCLUDING REMARKS

A TES method has been developed for unsteady transonic computations about wing planforms. Four swept, tapered wings of various aspect ratios including control surfaces are selected as computational examples for validation of the TES computer code. Computed results of TES code practically follow the same trends as those of XTRAN3S codes and full-potential code; all of them have been verified with available measured data by NLR and RAE.

In view of the satisfactory results obtained and the effective procedures established by the TES method, we believe that it is useful for immediate aeroelastic applications. To summarize, the following special features of the TES method are worthy of notice:

Applicability to General Planforms

In addition to its applicability to rectangular wings, the TES method is equally applicable to swept and tapered wing planforms with any given aspect-ratio, including those with control surfaces.

No Need for Grid Generation

Any time-domain three dimensional computational methods generally requires a grid generation procedure, which could be planform-dependent in most cases. The present TES method does not require such a procedure.

Computation Efficiency

A rough estimate in CPU time indicates that to compute aerodynamics for one given mode, using the present TES code, is at least ten times faster than using the XTRAN3S code. With further improvement of the current TES pilot code, it is expected that at least another reduction factor of two in CPU time can be achieved.

Flexibility and Ease of Application

Unlike other unsteady computational methods, TES method makes use of the steady-flow pressures supplied either by measurement or by steady computational method. The flexibility of the TES method lies in the pressure input scheme which does not require airfoil shapes. For ease of application, the input format of TES code will be unified with that of the subsonic doublet lattice code.

Transonic A.I.C. and Flutter

With the exclusion of chordwise bending modes, the present TES method can be extended to the construction of a three-dimensional aerodynamic-influence-coefficient matrix, hence, the generalized forces. These are the essential building blocks for the TES method to become an efficient aerodynamic tool for flutter analysis.

ACKNOWLEDGEMENTS

REFERENCES

1. Ballhaus, W.F. and Goorjian, P.M., "Implicit Finite-Difference Computations of Unsteady Transonic Flows about Airfoils," AIAA Journal, Vol. 15, No. 12, December 1977, pp. 1728-1735.

2. Ballhaus, W.F. and Goorjian, P.M., "Computation of Unsteady Transonic Flows by the Indicial Method," AIAA Journal, Vol. 16, No. 2, February 1978, pp. 117-124.

3. Guruswamy, P. and Goorjian, P.M., "An Efficient Coordinate Transformation Technique for Unsteady Transonic Aerodynamic Analysis of Low-Aspect-Ratio Wings," AIAA Paper 84-0872-CP.

4. Borland, C.J. and Sotomayer, W.A., "An Algorithm for Unsteady Transonic Flow about Tapered Wings," AIAA Paper 84-1567.

5. Edwards, C.J., Bland, S.R. and Seidel, D.A., "Experience with Transonic Unsteady Aerodynamic Calculations," NASA TM 86278, August 1984.

6. Isogai, K. and Suetsugu, K., "Numerical Calculations of Unsteady Transonic Potential Flow Over Three-Dimensional Wings with Oscillating Control Surfaces," AIAA Journal, Vol. 22, No. 4, April 1984, pp. 478-485.

7. Malone, J.B. and Ruo, S.Y., "Computation of Unsteady Transonic Flows about Two-Dimensional and Three-Dimensional AGARD Standard Configurations," AGARD Specialist Meeting on Transonic Unsteady Aerodynamics and Its Aeroelastic Applications, Toulouse, France, September 3-6, 1984.

8. Sotomayer, W.A. and Borland, C.J., "Numerical Computation of Unsteady Transonic Flow about Wings and Flaps," AIAA Paper 85-1712.

9. Bennett, R.M., Wynne, E.C. and Mabey, D.G., "Calculations of Transonic Steady and Oscillatory Pressures on A Low Aspect Ratio Model and Comparison with Experiment," Paper 85-17, 2nd International Symposium on Aeroelasticity and Structural Dynamics, Aachen, Germany, April 1-3, 1985.

10. Malone, J.B. and Ruo, S.Y., "LANN Wing Test Program: Acquisition and Application of Unsteady Transonic Data for Evaluation of Three-Dimenssional Computational Methods," AFWAL-TR-83-3006, February 1983.

11. Liu, D.D., "Computational Transonic Equivalent Strip Method for Applications to Unsteady 3D Aerodynamics," AIAA Paper 83-0261.

12. Couston, M., Angelini, J.J. and Meurzec, J.P., "Comparison des Champs de Pression Instationnaire Calcules et Mesure sur le Modele ZKP," AGARD-R-688, April 1980, pp. 1-1 to 1-16.

13. Zwann, R.J., "Verifications of Calculation Methods for Unsteady Airloads in the Prediction of Transonic Flutter," AIAA Paper 84-0871.

14. Fung, K.Y. and Chung, A., "Computations of Unsteady Transonic Aerodynamics Using Prescribed Steady Pressures," Journal of Aircraft, Vol. 20, No. 12, December 1983, pp. 1058-1061.

15. Rodden, W.P., Giesing, J.P. and Kalman, T.P., "New Developments and Applications of the Subsonic Doublet Lattice Method for Nonplanar Configurations," AGARD Symposium on Unsteady Aerodynamics for Aeroelastic Analyses of Interfering Surfaces, Paper No. 4, May 1970.

16. Fung, K.Y., "A Simple, Accurate and Efficient Algorithm for Unsteady Transonic Flow," Recent Advances in Numerical Methods in Fluid Dynamics, W.G. Habashi, Ed., Pineridge Press, Swansea, U.K., 1984.

17. Lambourne, N.C., "Experimental Techniques in Unsteady Aerodynamics," AGARD Report No. 679, Special Course on Unsteady Aerodynamics, June 18, 1980, pp. 10-1 to 10-26.

18. Horsten, J.J., Den Boer, R.G. and Zwaan, R.J., "Unsteady Transonic Pressure Measurements on a Semi-Span Wing Tunnel Model of a Transport-Type Supercritical Wing (LANN Model)," NLR TR-82-069U, Parts I and II and AFWAL-TR-83-3039, Part I and II, March 1983.

19. Tijdeman et al., "Transonic Wing Tunnel Tests on an Oscillating With with External Store, Part II: The Clean Wing," NLR TR 78106U, Part II, also AFFD; -TR-78-194, January 1978.

20. Mabey, D.G., McOwat, D.M. and Welsh, B.L., "Aerodyanamic Characteristics of Moving Trailing-Edge Control at Subsonic and Transonic Speeds," Aerodynamic Characteristics of Controls, AGARD-CP-262, May 1982, pp. 20-1 to 20-25.

21. Persoon, A.J., Roos, R. and Schippers, P., "Transonic and Low Supersonic Wind-Tunnel Tests on a Wing with Inboard Control Surface," AFWAL-TR-80-3146, December 1980.

22. White, R.B. and Landahl, M.T., "Effect of Gaps on the Loading Distribution of Planar Lifting Surfaces," AIAA Journal, Vol. 6, No. 4, April 1968, pp. 626-631.
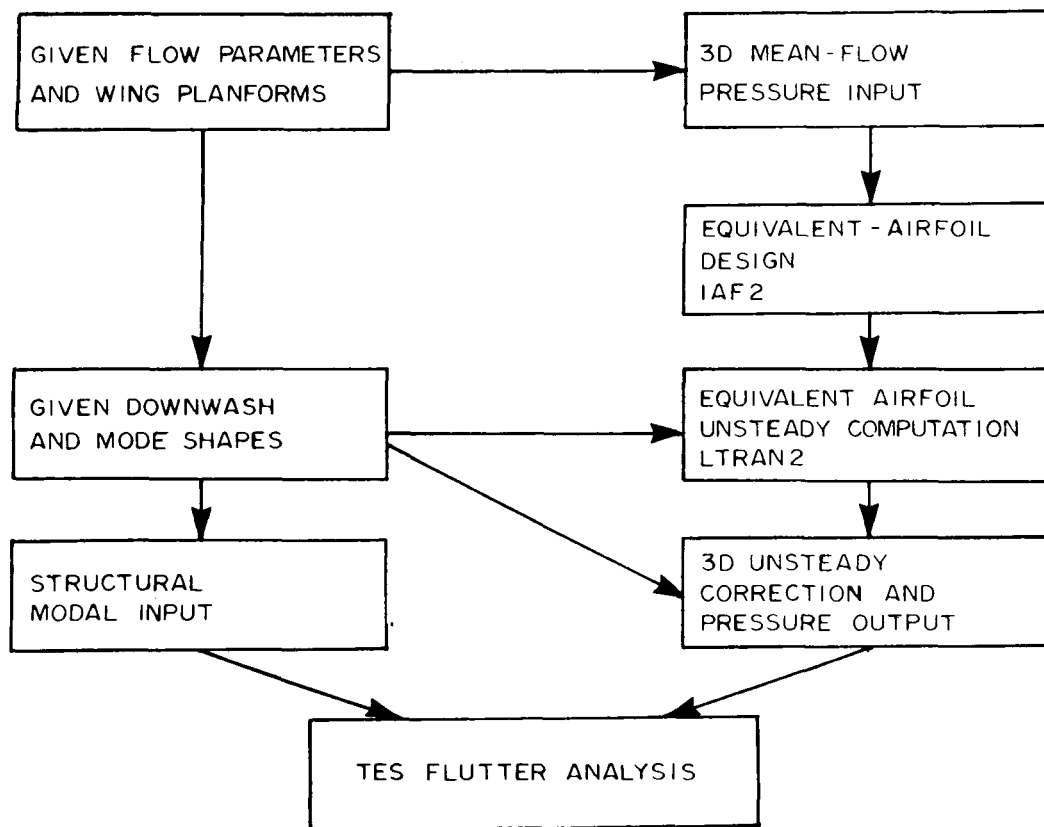
Fig. 1 Flow Chart Showing TES Computation Procedure

$$R_1 = \sqrt{(\lambda a_\infty \bar{t})^2 - (\lambda \bar{y}_0)^2}$$

$$R_2 = \sqrt{(\lambda a_\infty \bar{t})^2 - (\bar{x}_0 - U_\infty \bar{t})^2}$$
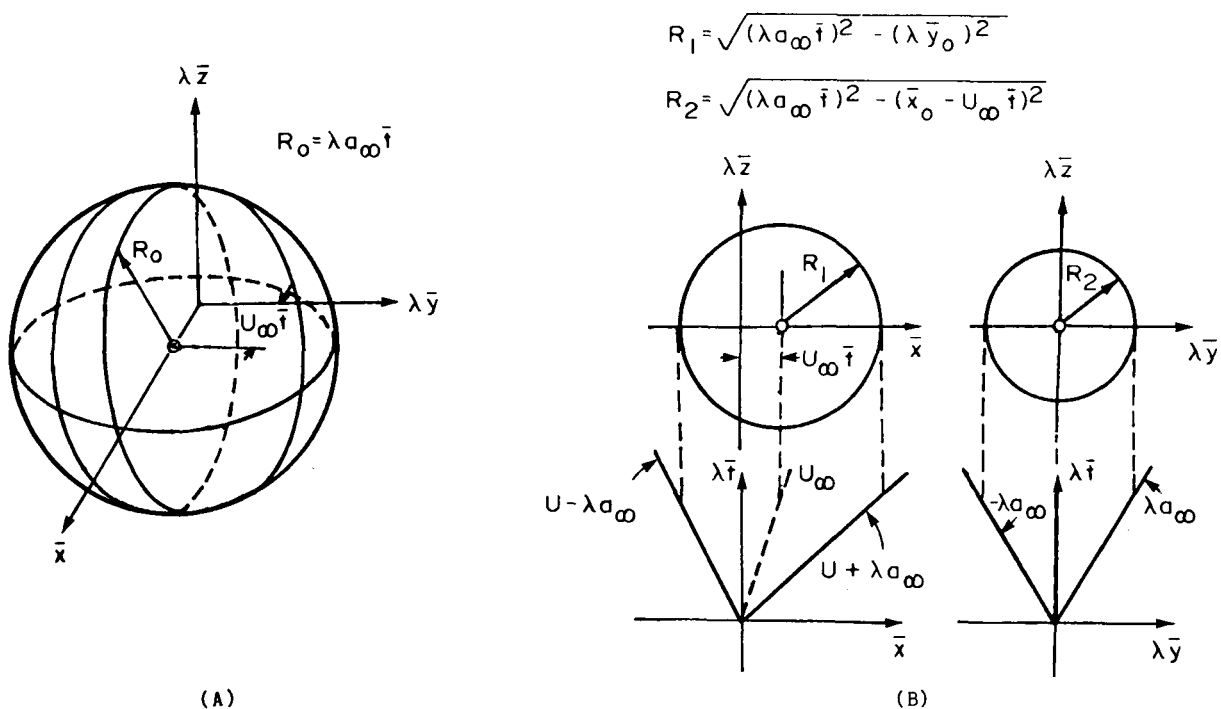

(A)

(B)

Fig. 2 (A) Characteristic Sphere
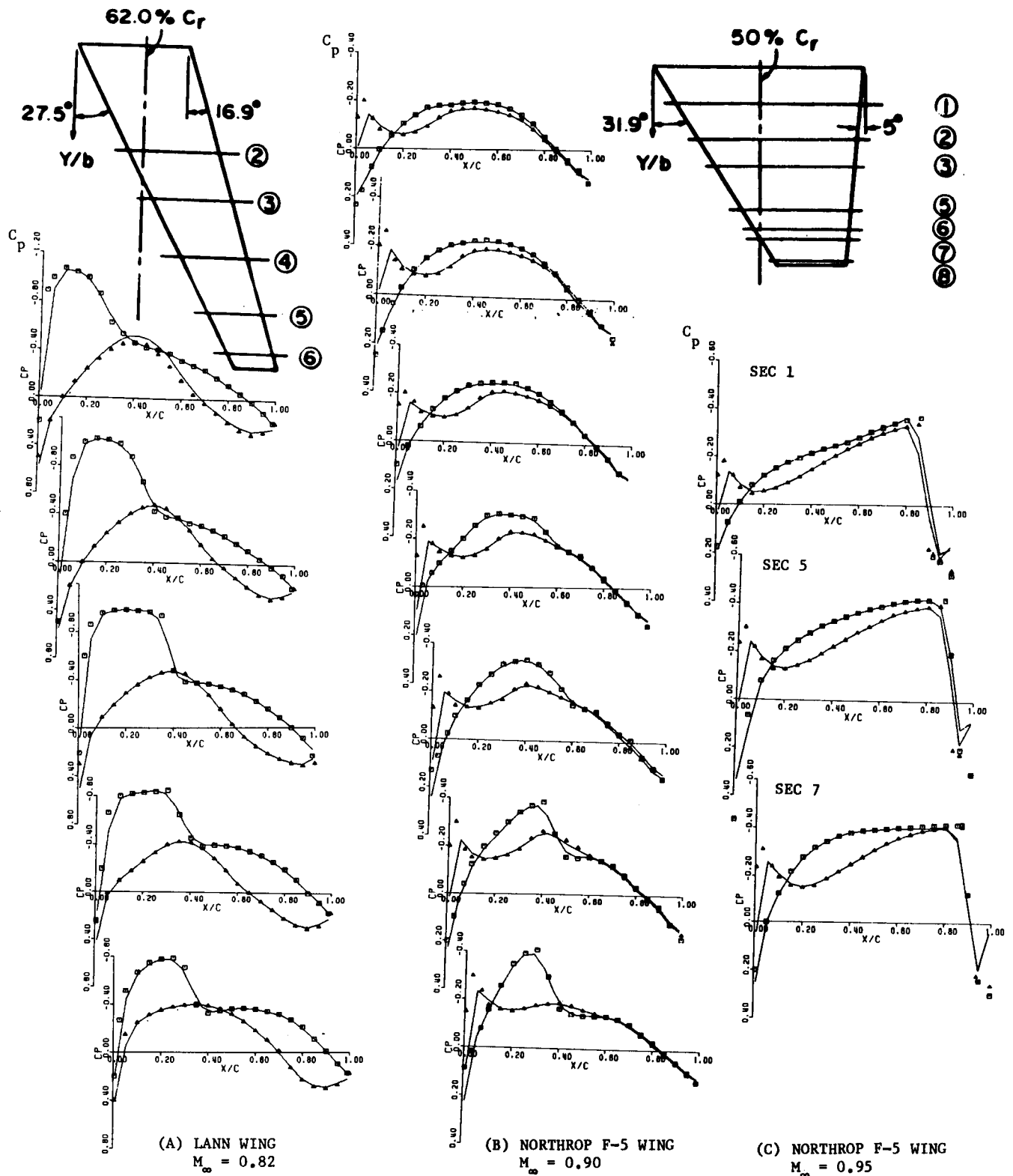   (B) Wave Propagations in Strip Planes

Fig. 3   Steady Pressure Inputs and Equivalent-Airfoil Outputs at Various Spanwise Locations for:
(A)   LANN WING at Mean Incidence α_0 = 0.62°
(B) and (C)   NORTHROP F-5 WING at Mean Incidence α_0 = 0°
(▣ Upper and △ Lower Surfaces - Measured Data: (A) NLR/Horsten, (B) NLR/Tijdeman and
(C) Computed Data XTRAN3S/Ames; ——— Present Equivalent-Airfoil Output)

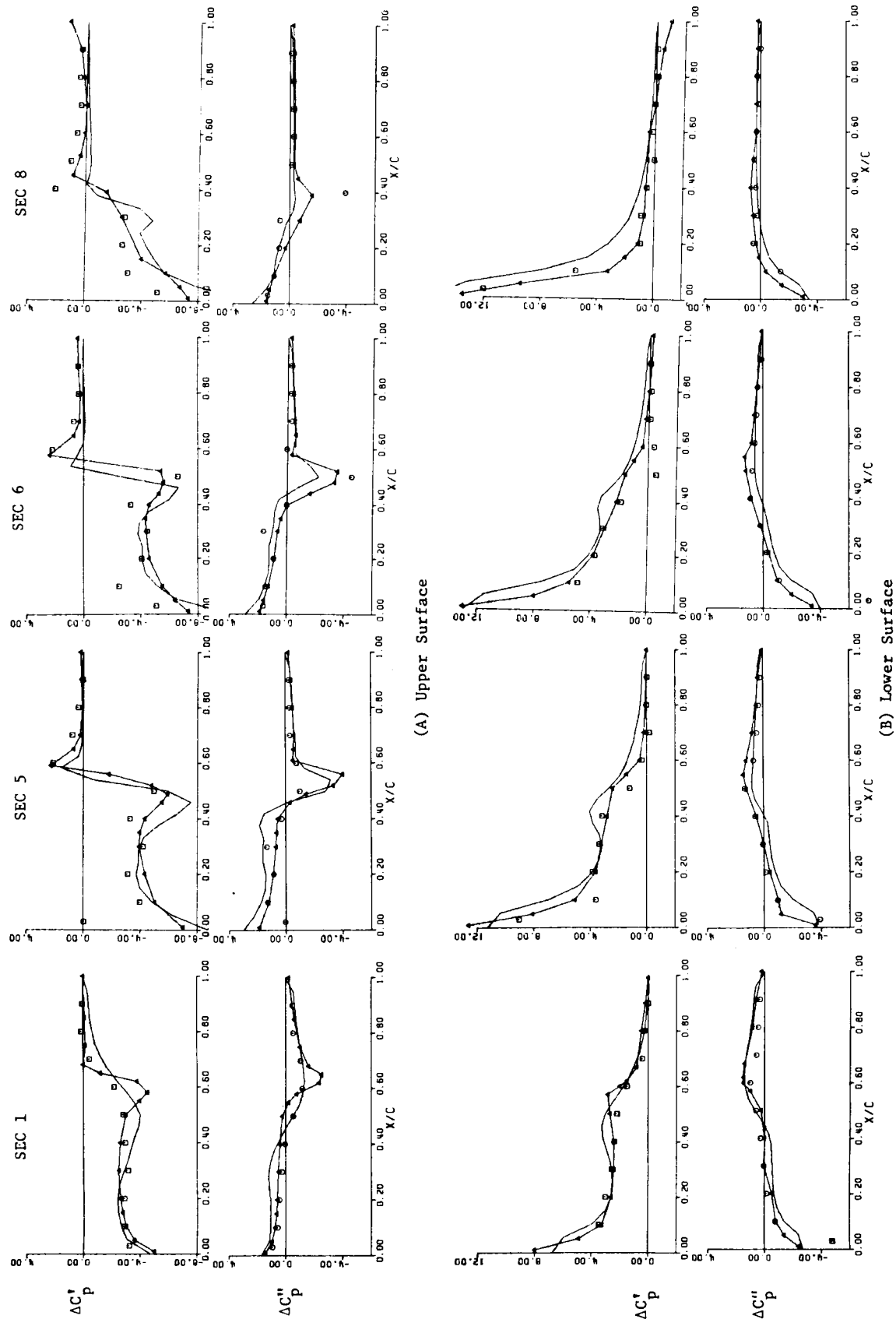Fig. 4 NORTHROP F-5 WING Comparison of In-phase and Out-of-phase Pressures at Four Spanwise Locations: Pitching Oscillation about Mid Root-Chord at Mach Number $M_\infty = 0.90$ and Reduced Frequency $k = 0.274$. (—— Present TES Method; —△— XTRAN3S/Borland et al.; ⊡ Real and ⊙ Imaginary - NLR/Tijdeman et al. Measured Data)
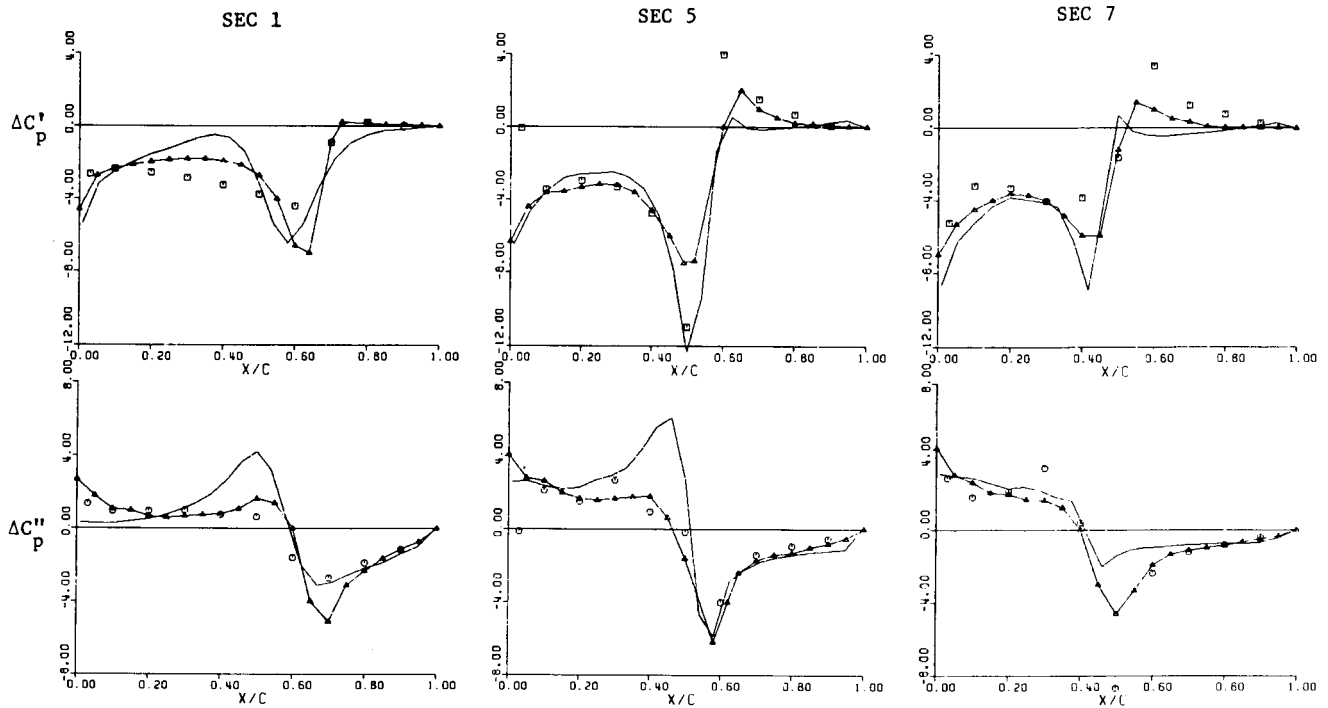
Fig. 5   NORTHROP F-5 WING Comparison of In-phase and Out-of-phase Pressures on Upper Surface at Three
Spanwise Locations: Pitching Oscillation about Mid Root-Chord at Mach Number M_∞ = 0.90 and
Reduced Frequency k_c = 0.550.
(———— Present TES Method; —△— XTRAN3S/Ames; ⊡ Real and ⊙ Imaginary - NLR/Tijdeman et al.
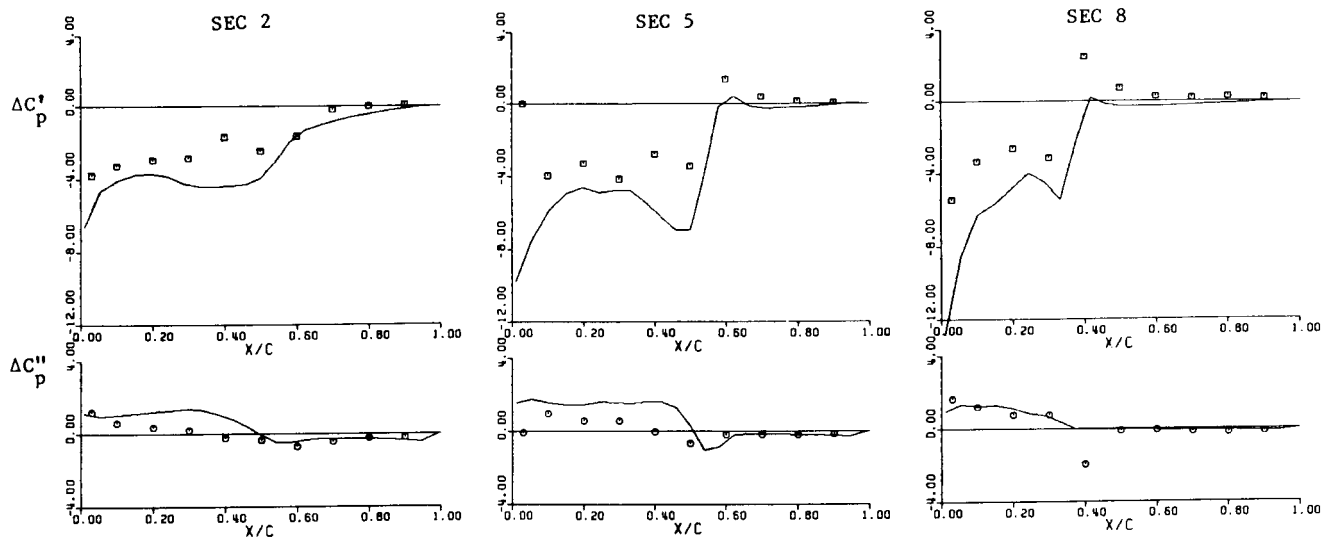Measured Data)

Fig. 6   NORTHROP F-5 WING Comparison of In-phase and Out-of-phase Pressures on Upper Surface at Three
Spanwise Locations: Pitching Oscillation about Mid Root-Chord at Mach Number M_∞ = 0.90 and
Reduced Frequency k_c = 0.136.
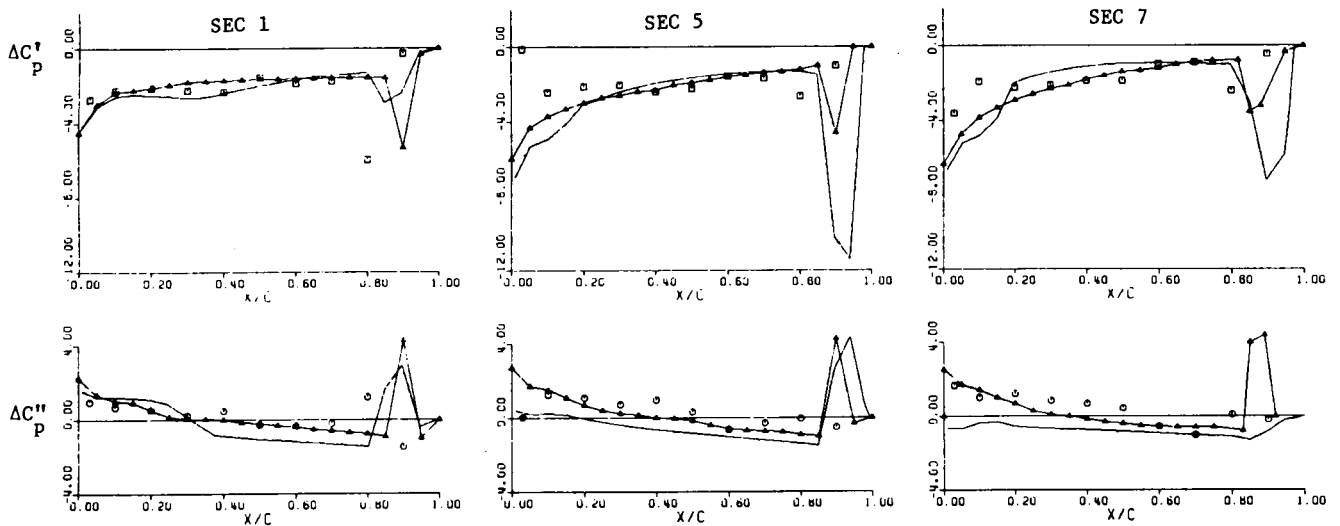(———— Present TES Method; ⊡ Real and ⊙ Imaginary - NLR/Tijdeman et al. Measured Data)
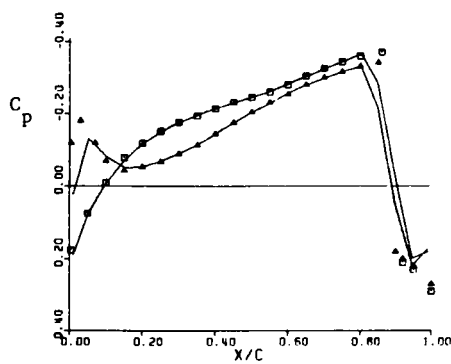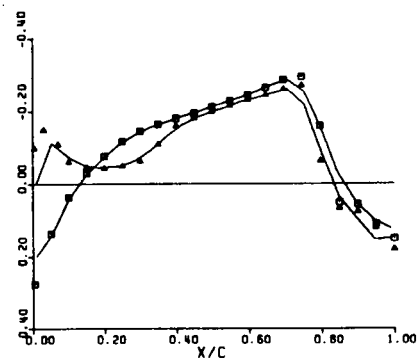
149

Fig. 7 NORTHROP F-5 WING Comparison of In-phase and Out-of-phase Pressures on Upper Surface at Three Spanwise Locations: Pitching Oscillation about Mid Root-Chord at Mach Number M_∞ = 0.95 and Reduced Frequency k_c = 0.528.
(———— Present TES Method; —△— XTRAN3S/Ames; ▣ Real and ⊙ Imaginary - NLR/Tijdeman et al. Measured Data)

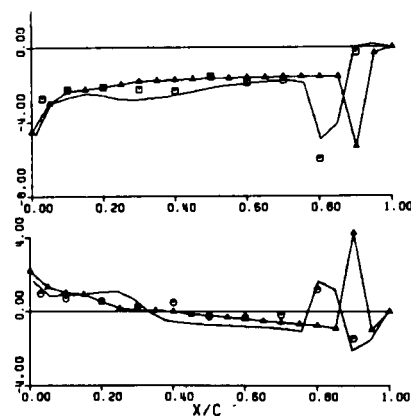(A) XTRAN3S/Ames Input
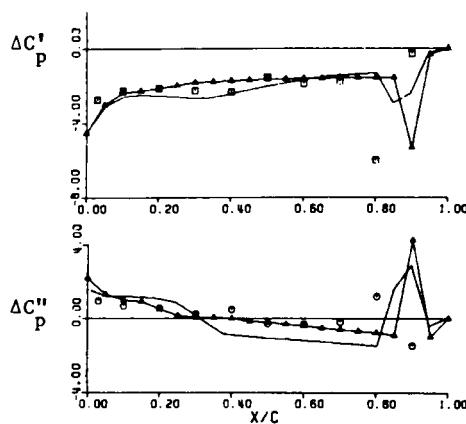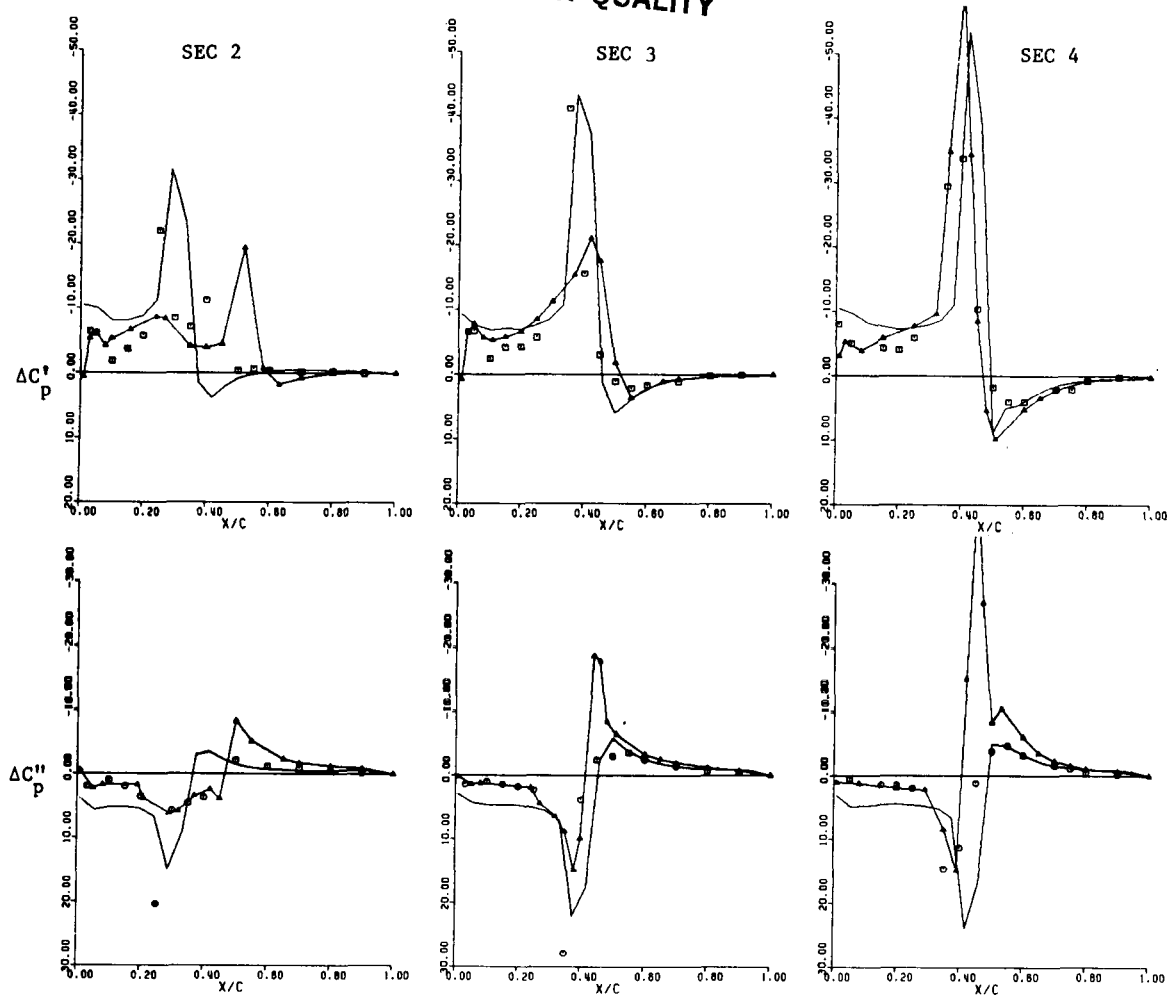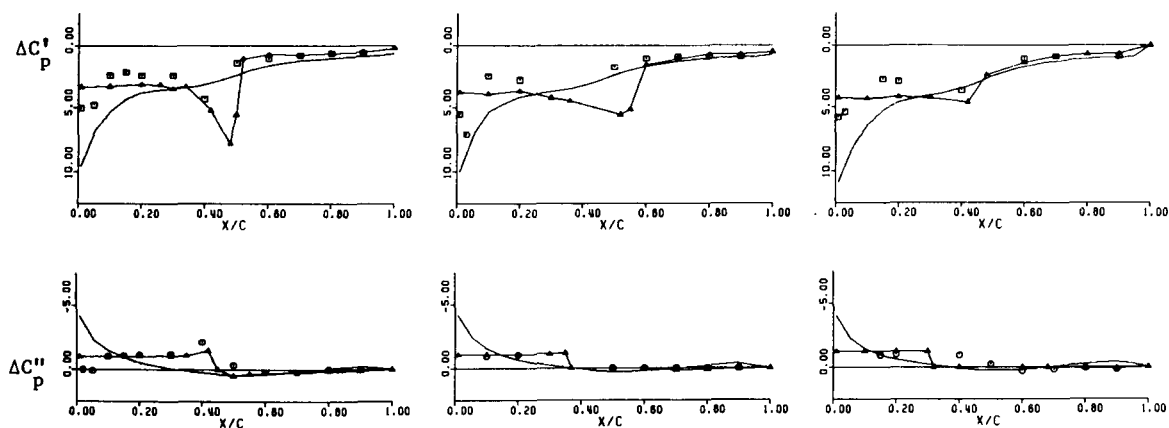
(B) NLR Measured Data Input

Fig. 8 NORTHROP F-5 WING Comparison of Steady Pressure Distributions, In-phase and Out-of-phase Pressures at 18% Spanwise Locations: Pitching Oscillation about Mid Root-Chord at Mach Number M_∞ = 0.95 and Reduced Frequency k_c = 0.528.
(———— Present TES Method; —△— XTRAN3S/Ames; ▣ Real and ⊙ Imaginary - NLR/Tijdeman et al. Measured Data)

150

(A) <u>LANN WING</u>   Upper Surface

(B) <u>LANN WING</u>   Lower Surface

Fig. 9   <u>LANN WING</u>   Comparison of In-phase and Out-of-phase Pressures at Five Spanwise Locations :
Pitching Oscillation about 62% Root-Chord at Mach Number M_∞ = 0.82 and Reduced Frequency
k_c= 0.205
(———— Present TES Method; —△— XTRAN3S/Malone; ▣ Real and ⊙ Imaginary - NLR/Horsten et al.
Measured Data)

151

SEC 5   SEC 6

$\Delta C'_p$

$\Delta C''_p$
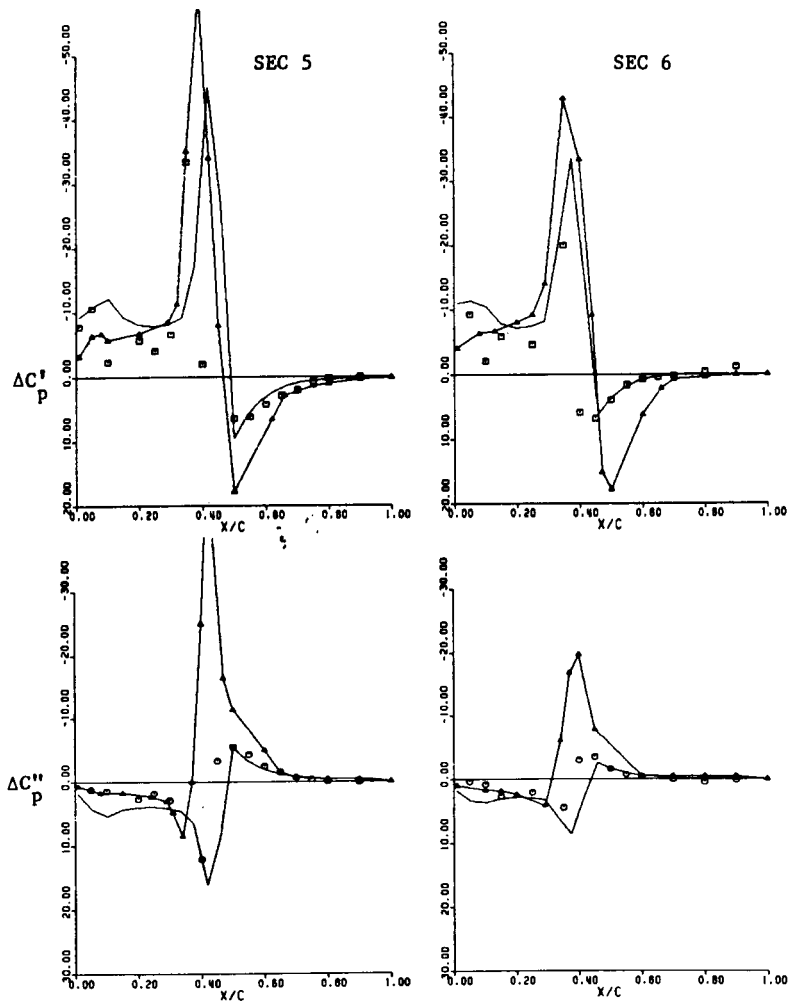
(A) <u>LANN WING</u> Upper Surface [Continued]

$\Delta C'_p$

$\Delta C''_p$
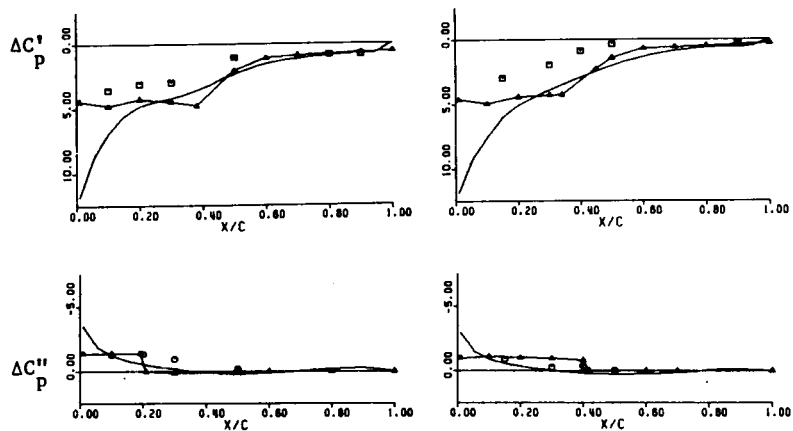
(B) <u>LANN WING</u> Lower Surface [Continued]

Fig. 9 <u>LANN WING</u> [Continued]

RAE AGARD TAILPLANE:

ASPECT RATIO	:	AR=2.41
TAPER RATIO	:	TR=0.27
MACH NUMBER	:	M_∞=0.90
MEAN INCIDENCE	:	α_0=0°
REDUCED FREQUENCY:		k_c=0.422
PITCHING AXIS	:	x_0=68.2% ROOT CHORD
OSCILLATION AMPLITUDE:		α_1=0.4°
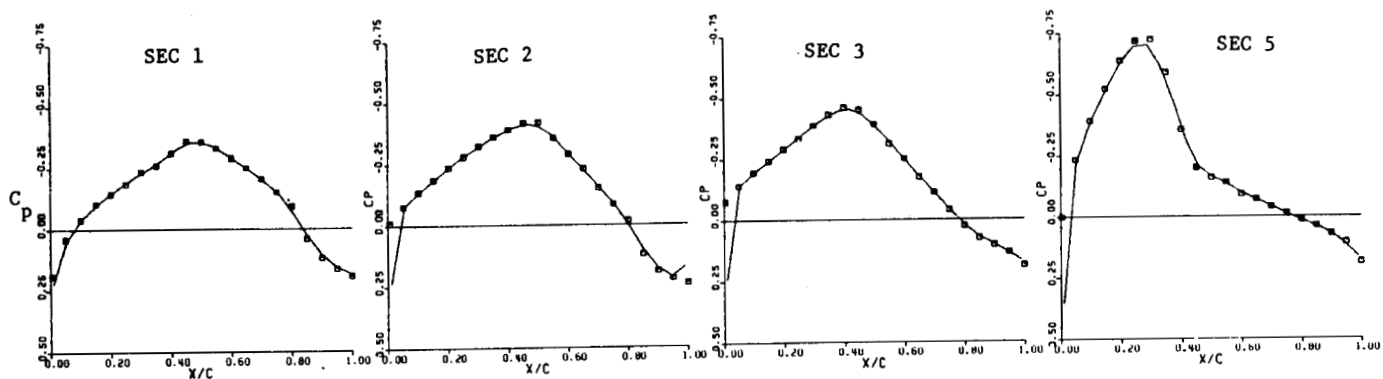
(A) Steady Pressure Distributions
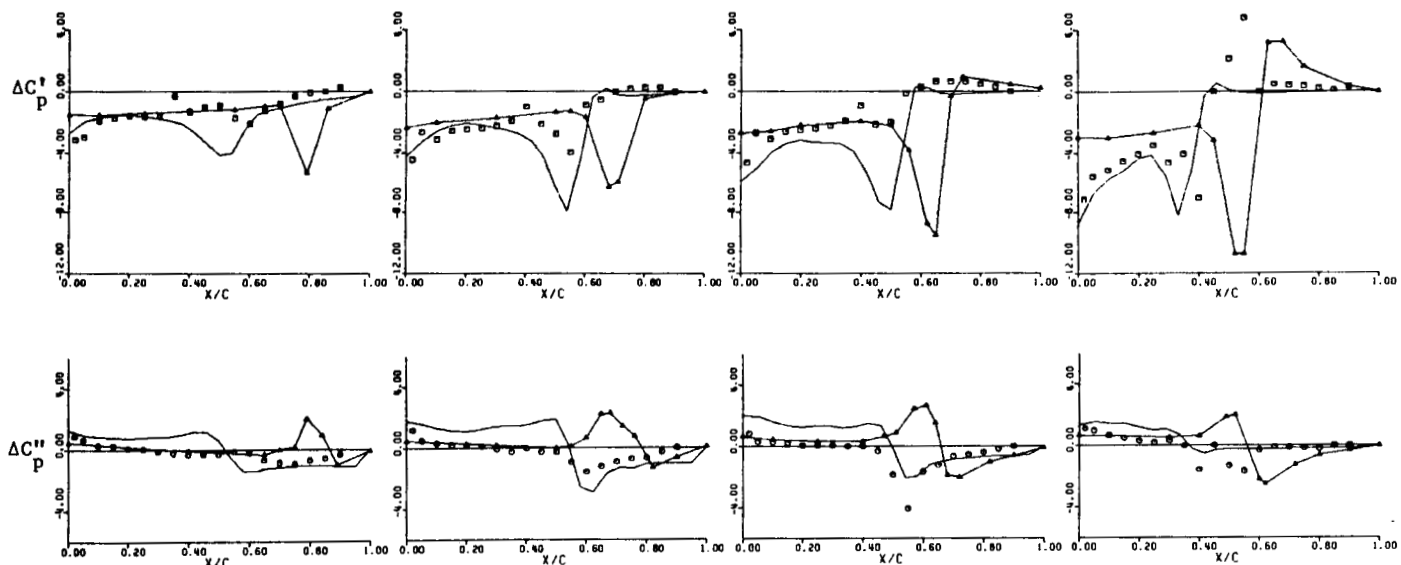
(B) In-phase and Out-of-phase Pressures

Fig. 10 RAE AGARD TAILPLANE:
(A) Steady Pressure Inputs and Equivalent-Airfoil Pressure Outputs at Four Spanwise Locations
(▣   RAE Measured Data Input; ———— Equivalent-Airfoil Output)
(B) Comparison of In-phase and Out-of-phase Pressures
(———— Present TES Method; —△— XTRAN3S/Bennett et al.; ▣ Real and ⊙ Imaginary
-RAE Measured Data)

153

(A) Steady Pressure Distribution

(B) Pressure Magnitude

(C) Phase Angle

Fig. 11 AGARD STANDARD RAE WING WITH OSCILLATING FLAP
(A) Steady Pressure Inputs and Equivalent-Airfoil Pressure Outputs at 45% Spanwise Location at
Mach Number M_∞ = 0.90 and Mean Incidence α_0 = 0°
(⊡ GACBOPPE Code Input; ———— Equivalent-Airfoil Output)
(B) Pressure Magnitude and
(C) Phase Angle on Upper Surface of 45% Spanwise Location for AGARD RAE Wing with Oscillating
Flap at Mach Number M_∞ = 0.90 and Reduced Frequency k_c = 0.705 with Flap Amplitude δ = 1°
(———— Present TES Method; ––––––Isogai's Full Potential Code; O + ✳ RAE Measured Data)

154

ORIGINAL PAGE IS
OF POOR QUALITY

(A) 18% Spanwise Location (Section 1)

(B) 51% Spanwise Location (Section 3)
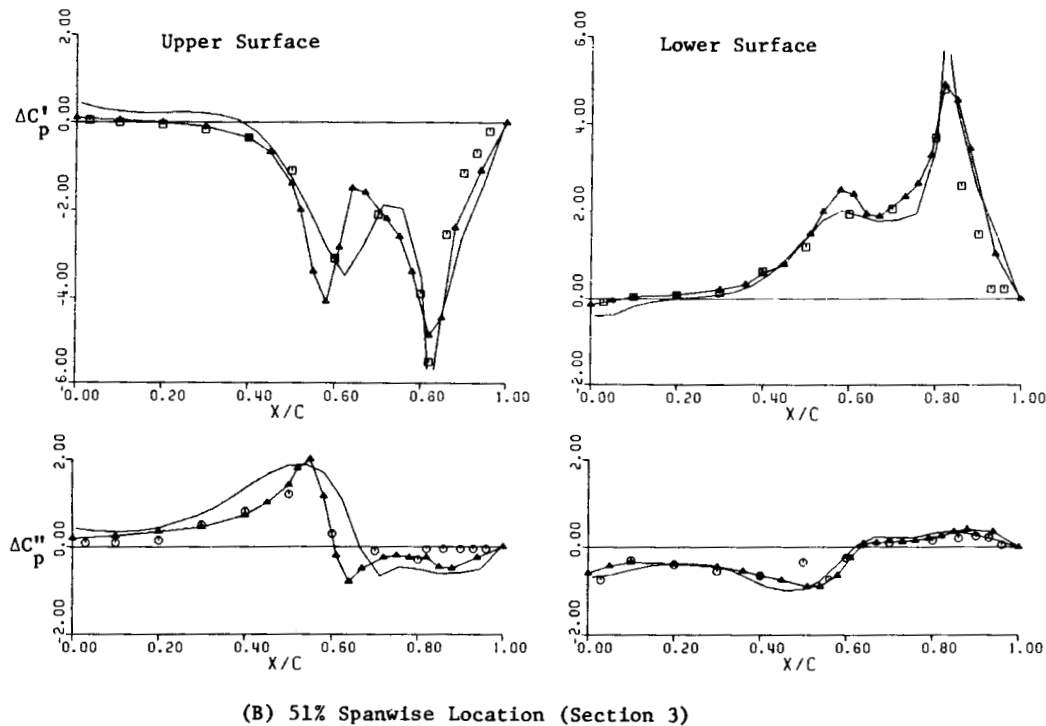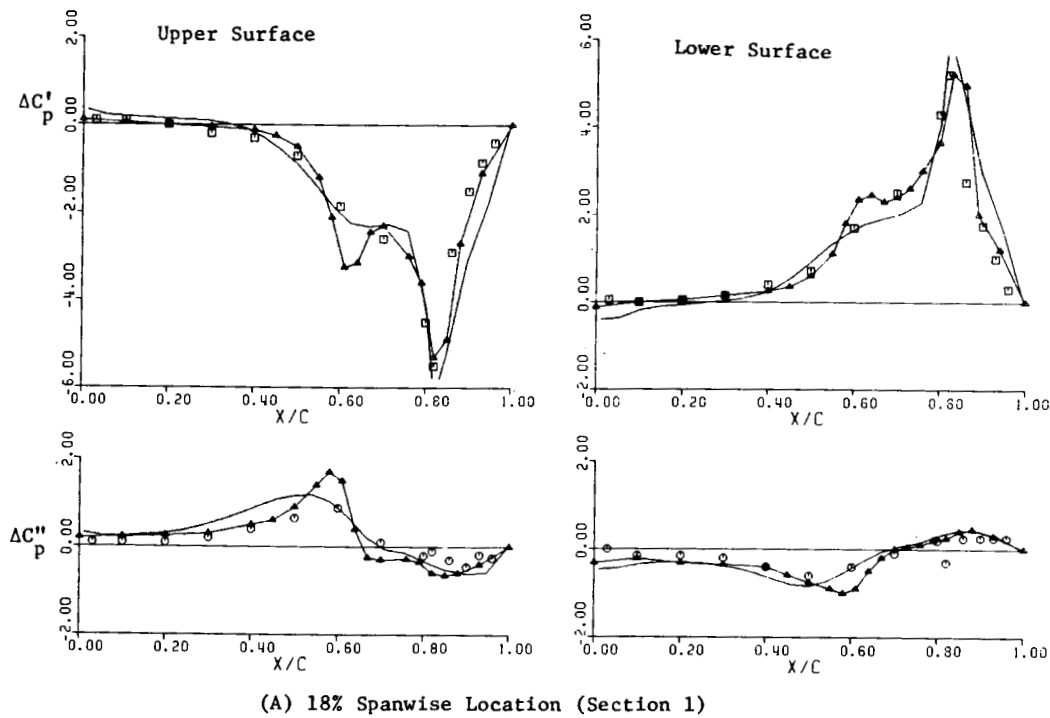
Fig. 12   NORTHROP F-5 WING WITH OSCILLATING FLAP
Comparison of In-phase and Out-of-phase Pressures with Hinge Line at 82% Chord at
Sections 1 and 3.
(———— Present TES Method; ——△—— XTRAN3S/Sotomeyer; ⊡ Real and ⊙ Imaginary
- NLR/Tijdeman et al. Measured Data)

155

APPLICATION OF A FULL POTENTIAL METHOD TO AGARD STANDARD AIRFOILS

WOODROW WHITLOW, JR.
UNSTEADY AERODYNAMICS BRANCH
NASA LANGLEY RESEARCH CENTER

OUTLINE

An outline of the presentation is shown here. First, the motivation for performing this research is discussed. Next, the formulation of an isentropic full potential method is presented, followed by a nonisentropic method. Since the methods that are presented use body-fitted grids, methods for modeling the motions of dynamic grids are presented. Computed results for the NACA 0012 and NLR 7301 airfoils are shown. Summary statements about this effort are presented, and some conclusions are made.

O MOTIVATION

O ISENTROPIC FULL POTENTIAL

O NONISENTROPIC FULL POTENTIAL

O DYNAMIC GRIDS

O RESULTS (NACA 0012, NLR 7301)

O SUMMARY

O CONCLUSIONS

MOTIVATION

One of the most important uses of methods that calculate unsteady aerodynamic loads is to predict and analyze the aeroelastic responses of flight vehicles. Currently, methods based on transonic small disturbance (TSD) potential aerodynamics are the the primary tools for aeroelastic analysis. Theoretically, TSD methods are limited to thin bodies undergoing small amplitude motions. Full potential (FP) methods do not have these limitations, but flow solutions obtained using isentropic potential theory--TSD or FP--can be highly inaccurate and even multivalued. This is because isentropic potential methods do not model the effects of entropy that is produced when shock waves are in the flow field. Thus, the goal of this effort is to develop an unsteady full potential method that models the effects of shock-generated entropy.

O TRANSONIC SMALL DISTURBANCE THEORY IS THE PRIMARY AERODYNAMIC TOOL FOR ANALYZING TRANSONIC AEROELASTIC PHENOMENA

O TSD LIMITED TO THIN BODIES UNDERGOING SMALL AMPLITUDE MOTIONS

O SOLUTIONS FROM ISENTROPIC POTENTIAL THEORY CAN BE HIGHLY INACCURATE AND MULTIVALUED

O GOAL OF THE PRESENT EFFORT IS TO DEVELOP AN UNSTEADY FULL POTENTIAL METHOD THAT MODELS NONISENTROPIC EFFECTS

ISENTROPIC FULL POTENTIAL
(GENERALIZED COORDINATES)

Shown here is the formulation of the isentropic full potential method in generalized coordinates. The first equation is the continuity equation in strong conservation form, where τ is computational time, and ξ and ζ are the computational coordinate directions around and normal to the airfoil, respectively. Density ρ is given by the expression in the second equation, where γ is the ratio of specific heats, M is free stream Mach number, ϕ is the velocity potential, and the nondimensional physical time is denoted by t. The variables U and W are the contravariant velocities in the ξ and ζ directions, respectively. The metrics of the body-fitted grid are A_1, A_2, and A_3. The Jacobian of the coordinate transformation is given by J, and $\hat{\rho}$ is the density divided by the Jacobian. The density, biased to introduce artificial viscosity and capture shock waves, is denoted by $\tilde{\rho}$.

$$\hat{\rho}_\tau + \left(\frac{\tilde{\rho}U}{J}\right)_\xi + (\hat{\rho}W)_\zeta = 0$$

$$\rho = \left\{ 1 + \frac{\gamma-1}{2}[M^2 - 2\phi_\tau - (U+\xi_t)\phi_\xi - (W+\zeta_t)\phi_\zeta] \right\}^{\frac{1}{\gamma-1}}$$

$$U = \xi_t + A_1\phi_\xi + A_2\phi_\zeta \qquad\qquad W = \zeta_t + A_2\phi_\xi + A_3\phi_\zeta$$

$$J = \xi_x\zeta_z - \xi_z\zeta_x$$

$$\hat{\rho} = \frac{\rho}{J} \qquad\qquad\qquad \tilde{\rho} = \text{biased density}$$

160

ISENTROPIC FULL POTENTIAL
(FACTORIZATION)

The isentropic full potential formulation is linearized and factored as shown in this figure. Here, L_ξ and L_ζ represent differential operators in the ξ and ζ directions. The right side of the factored equation is the discretized form of the continuity equation plus some other terms not shown. The subscripts i and j represent grid points in the ξ and ζ directions, respectively, and the superscripts n and n-1 represent computational time levels. Solutions for ϕ are advanced in time by adding the potential from the previous time step ϕ^n to the correction $\Delta\phi$.

$$L_\xi L_\zeta \Delta\phi = \frac{h^2}{\beta^n}[(\frac{\hat\rho^n - \hat\rho^{n-1}}{h})_{i,j} + (\frac{\widetilde{\rho U}}{J})^n_{i+1/2,j} -$$

$$(\frac{\widetilde{\rho U}}{J})^n_{i-1/2,j} + (\hat{\rho W})^n_{i,j+1/2} - (\hat{\rho W})^n_{i,j-1/2}] + \ldots$$

$$\Delta\phi = \phi^{n+1} - \phi^n$$

$$h = \Delta\tau$$

$$\beta = \frac{\rho^{2-\gamma}}{J}$$

FLUX BIASED DIFFERENCING

The flow equations are discretized spatially using flux biased differencing. Artificial viscosity, necessary to capture shock waves, is introduced into the difference equations by defining the biased density ρ as shown in the figure. The $(\rho q)^-$ term is the difference between the actual flux ρq and the sonic flux $\rho^* q^*$ in supersonic regions and is zero in subsonic regions. Expressions for the total speed q, sonic speed q^*, and sonic density ρ^* are shown in the figure.

$$\tilde{\rho} = \frac{1}{q}[\rho q - \Delta\xi(\rho q)_{\xi}^-]$$

$$(\rho q)^- = \rho q - \rho^* q^* \qquad q > q^*$$

$$\qquad\qquad 0 \qquad\qquad q \leq q^*$$

$$q^2 = A_1\phi_{\xi}^2 + 2A_2\phi_{\xi}\phi_{\zeta} + A_3\phi_{\zeta}^2$$

$$q^{*2} = \frac{2}{\gamma+1}[1 + \frac{\gamma-1}{2}(M^2 - 2\phi_{\tau} - 2\xi_t\phi_{\xi} - 2\zeta_t\phi_{\zeta})]$$

$$\rho^* = (q^{*2})^{\frac{1}{\gamma-1}}$$

162

CHARACTERISTICS OF FLUX BIASED DIFFERENCING

Flux biased differencing (a) accurately tracks sonic conditions and automatically specifies the correct amount of artificial viscosity, (b) produces no velocity overshoots at shock waves, allowing for larger time steps for unsteady calculations, (c) produces well defined, monotone shock profiles with a maximum two point transition between the upstream and downstream states, and (d) dissipates expansion shocks, ruling out solutions with such nonphysical characteristics.

O AUTOMATICALLY SPECIFIES CORRECT AMOUNT OF ARTIFICIAL VISCOSITY

O ALLOWS FOR LARGER TIME STEPS

O PRODUCES TWO POINT SHOCK WAVES

O DISSIPATES EXPANSION SHOCKS

NONISENTROPIC DENSITY

To model the jump in entropy across shock waves, the density downstream of shock waves is modified to $\rho_i e^{-\Delta s/R}$. The entropy jump is a function of the normal Mach number upstream of the shock wave M_n. The isentropic density is given by the expression in the figure and is the same as that shown in the formulation of the isentropic potential method. When the expression for the nonisentropic density is inserted into the continuity equation, the equation at the bottom of the figure is obtained. Except across shock waves and wakes, the last part of that equation vanishes. Thus, except at those locations, it is necessary only to solve the classical full potential equation.

$$\rho = \rho_i e^{\frac{-\Delta s}{R}} \qquad \Delta s = f(M_n^2)$$

$$\rho_i = (1 + (\frac{\gamma-1}{2})[M^2 - 2\phi_\tau - (U+\xi_t)\phi_\xi - (W+\zeta_t)\phi_\zeta])^{\frac{1}{\gamma-1}}$$

$$e^{\frac{-\Delta s}{R}}[\hat{\rho}_{i\tau} + (\frac{\tilde{\rho_i}U}{J})_\xi + (\hat{\rho_i}W)_\zeta] + \rho_i e^{\frac{-\Delta s}{R}}\frac{D}{Dt}(\frac{\Delta s}{R}) = 0$$

164

NONISENTROPIC FULL POTENTIAL
(FACTORIZATION)

When nonisentropic effects are modeled, the factored equation becomes as shown at the top of the figure. The nonisentropic biased density for U > 0 is given by the expression at the bottom of the figure.

$$L_\xi L_\zeta \Delta\phi = \frac{h^2}{\beta^n}\left[\frac{(\hat{\rho_i}e^{\frac{-\Delta s}{R}})^n_{i,j} - (\hat{\rho_i}e^{\frac{-\Delta s}{R}})^{n-1}_{i,j}}{h} + (\frac{\tilde{\rho}U}{J})^n_{i+1/2,j} - (\frac{\tilde{\rho}U}{J})^n_{i-1/2,j}\right.$$

$$\left. + (\hat{\rho_i}e^{\frac{-\Delta s}{R}}W)^n_{i,j+1/2} - (\hat{\rho_i}e^{\frac{-\Delta s}{R}}W)^n_{i,j-1/2}\right] + ...$$
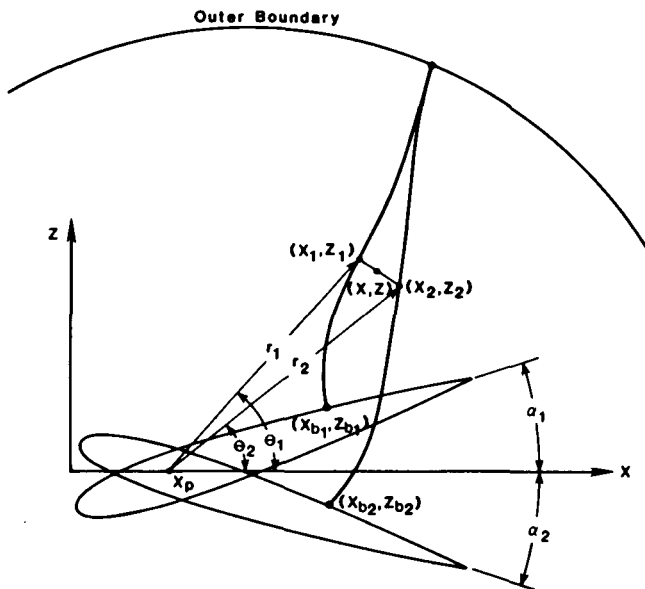
$$\tilde{\rho}_{i+1/2,j} = (\rho_i e^{\frac{-\Delta s}{R}})_{i+1/2,j} + \frac{1}{q_{i+1/2,j}}(\rho_i q - \rho^* q^*)_{i-1/2,j}$$

DYNAMIC GRIDS

To apply the airfoil surface boundary conditions at the instantaneous surface position requires a new grid at each time step. For this work, the body-fitted grids were generated using an elliptic method. Using this method, the resources required to generate the grids can be more than those necessary to do the aerodynamic calculations. Thus, an efficient grid interpolation method is used to generate the required grids. To simulate harmonic motions, the elliptic method is used to calculate grids at the extreme airfoil positions, and the grids for all other airfoil positions are generated using linear interpolation. Interior grid points are redistributed at each time step, while points on the outer boundary remain fixed.

The figure shows grid interpolation for an airfoil pitching about a point x_p. A polar coordinate system centered at x_p is used. Using the subscripts 1 and 2 to denote the minimum and maximum pitch angles, the position of each grid point at any time τ is given by the expressions for $r(\tau)$ and $\theta(\tau)$. The interpolated grid points are then obtained from the expressions for $x(\tau)$ and $z(\tau)$ given in the figure.

O   ASSUME LINEAR VARIATION BETWEEN EXTREME POSITIONS

O   OUTER BOUNDARY FIXED

$$r(\tau) = r_1 + \frac{\alpha(\tau) - \alpha_1}{\alpha_2 - \alpha_1}(r_2 - r_1)$$

$$\theta(\tau) = \theta_1 + \frac{\alpha(\tau) - \alpha_1}{\alpha_2 - \alpha_1}(\theta_2 - \theta_1)$$

$$x(\tau) = r(\tau)\cos\theta(\tau) + x_p$$

$$z(\tau) = r(\tau)\sin\theta(\tau)$$

166

NACA 0012
STEADY FLOW SOLUTIONS
M = 0.84, α = 0°

This figure shows steady pressures that are calculated on the NACA 0012 airfoil using the isentropic and nonisentropic full potential (FP) methods and an Euler method for M = 0.84, α = 0°. For this airfoil, the flow conditions are in the region where multiple solutions are known to occur. The isentropic FP result is asymmetric with negative lift. The Euler solution is symmetric with zero lift. The nonisentropic FP calculation yields a symmetric, nonlifting pressure distribution that shows good agreement with the Euler pressures. Thus, the nonisentropic FP method eliminates the phenomenon of multiple flow solutions.
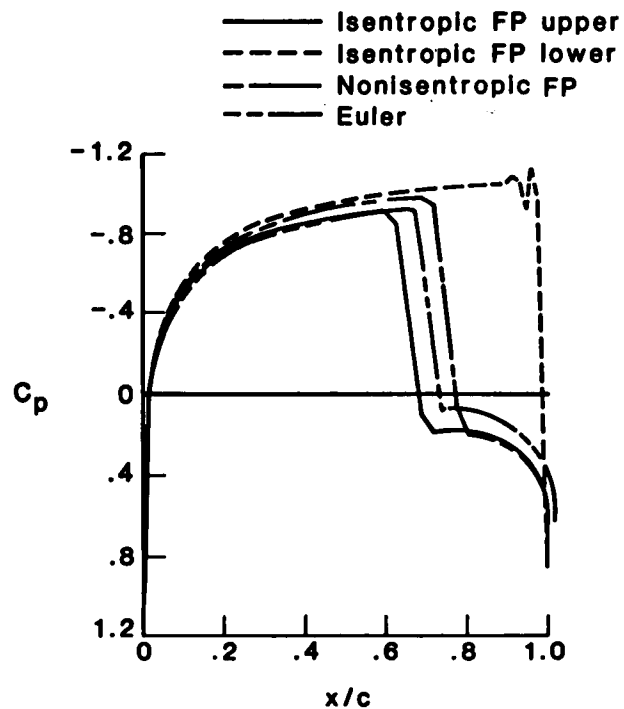
NACA 0012
ISENTROPIC COMPUTATIONS
M = 0.755, α = 0.016° + 2.51°SIN(Kτ), K = 0.814

This figure shows comparisons of calculated isentropic transonic small disturbance and full potential (FP) unsteady pressures with experimental data. Generally, the FP pressures are in good agreement with experiment, but the shock wave is too strong and located too far aft on the airfoil.

168
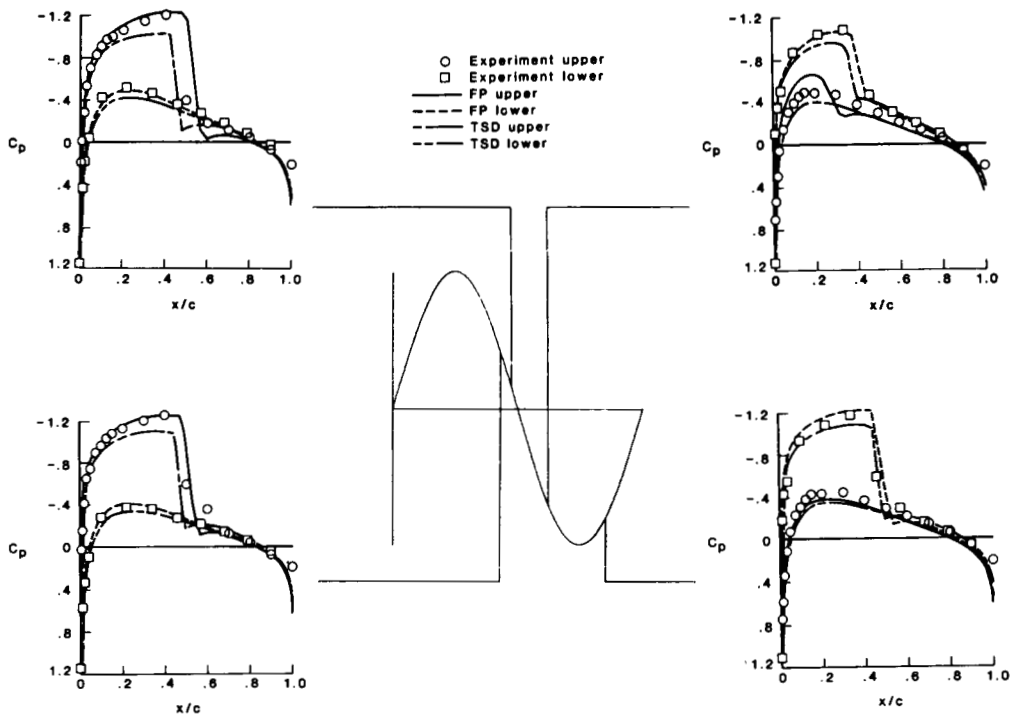
NACA 0012
NONISENTROPIC COMPUTATIONS
M = 0.755, α = 0.016° + 2.51°SIN(Kτ), K = 0.0814

This figure shows comparisons of isentropic and nonisentropic full potential (FP) pressures with experimental data. Generally, the effects of modeling the shock-generated entropy are to weaken the shock wave and move it forward on the airfoil. As a result, the nonisentropic FP calculations show improved agreement with the experimental data.
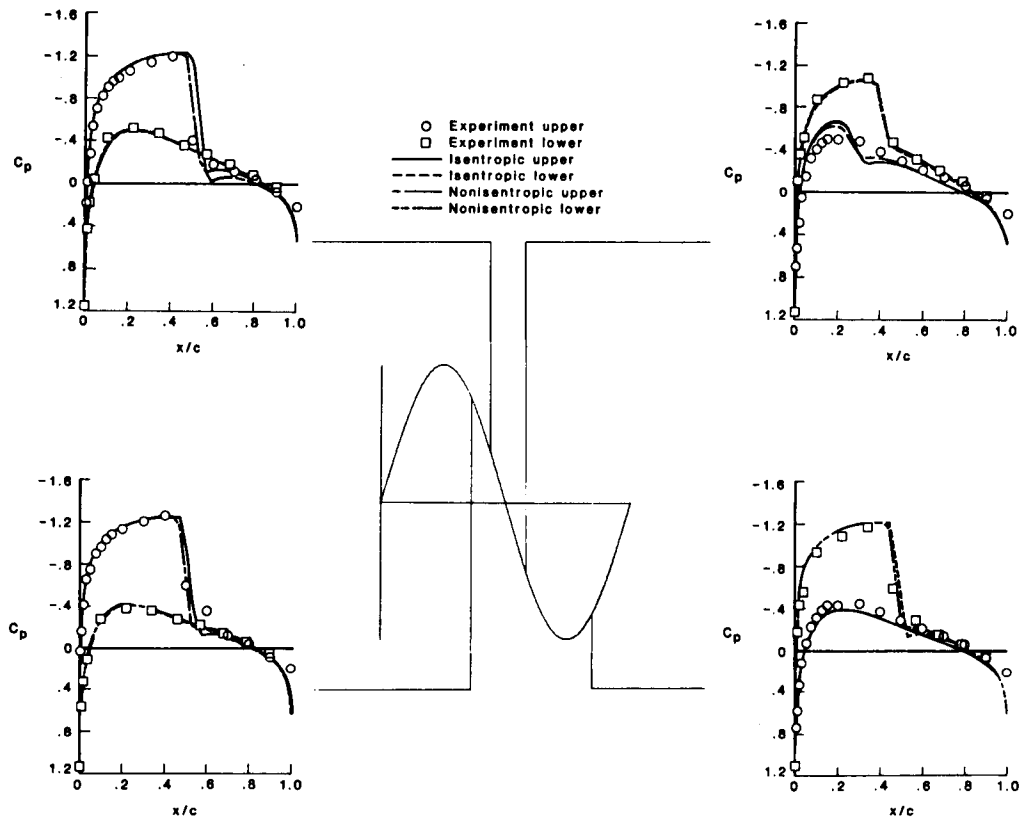
NLR 7301
STEADY STATE PRESSURES
M = 0.721, α = -0.19°

Shown in this figure are comparisons of the full potential (FP) pressures with Euler calculations and experimental data for the NLR 7301 airfoil at M = 0.721, α = -0.19°. For this case, the effects of shock-generated entropy are small, and the two FP solutions are nearly identical. Thus, the isentropic and nonisentropic FP calculations are shown as one line, designated "FP". Results obtained using the potential methods show very good agreement with experimental data and with the Euler calculations. The shock location is slightly upstream of the experimental location and slightly downstream of the location predicted by the Euler method.
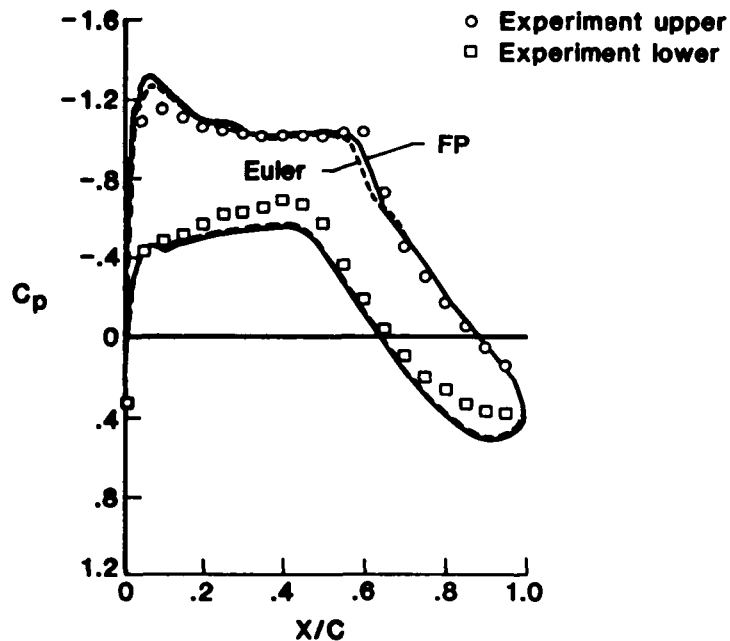
NLR 7301
STEADY STATE PRESSURES
M = 0.7, α = 2°

This figure shows a comparison of isentropic potential and Euler pressures on the NLR 7301 airfoil for M = 0.7, α = 2°. The shock wave calculated with the isentropic method is too strong and located too far aft on the airfoil, suggesting that this case is outside the range of validity of the method.

Legend:
—— Isentropic FP upper
---- Isentropic FP lower
o Euler upper
□ Euler lower
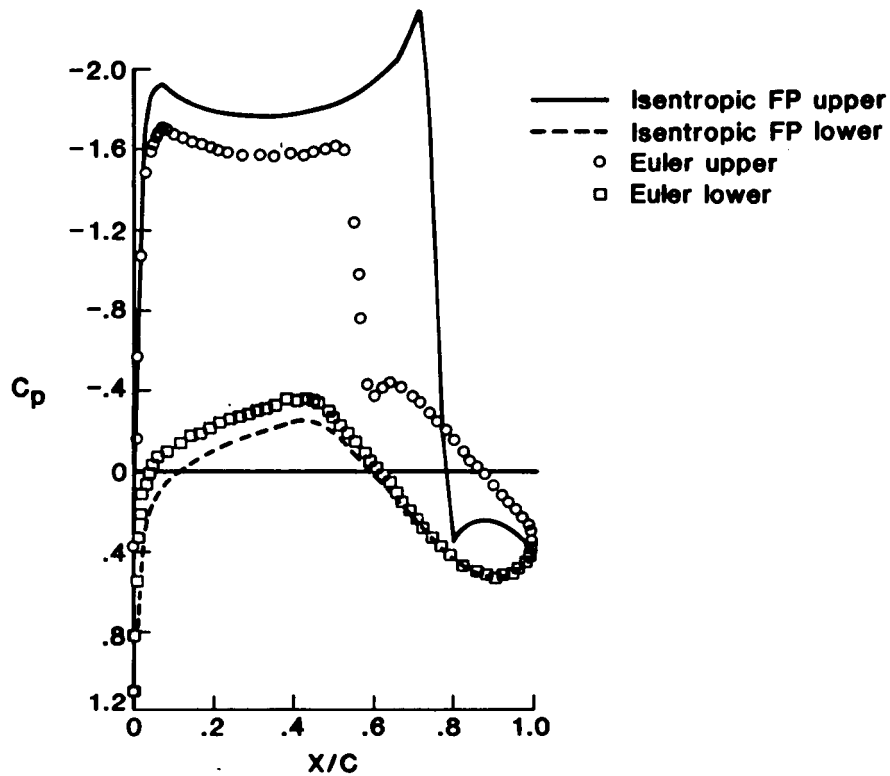
NLR 7301
STEADY STATE PRESSURES
$M = 0.7$, $\alpha = 2°$

Modeling the nonisentropic effects brings the potential flow solution into good agreement with the Euler results. The shock waves differ in location by only 3 percent chord and have nearly the same strength. In addition, the agreement of pressures on the lower surface is excellent.

Legend:
- ——— Nonisentropic FP upper
- - - - Nonisentropic FP lower
- o Euler upper
- □ Euler lower
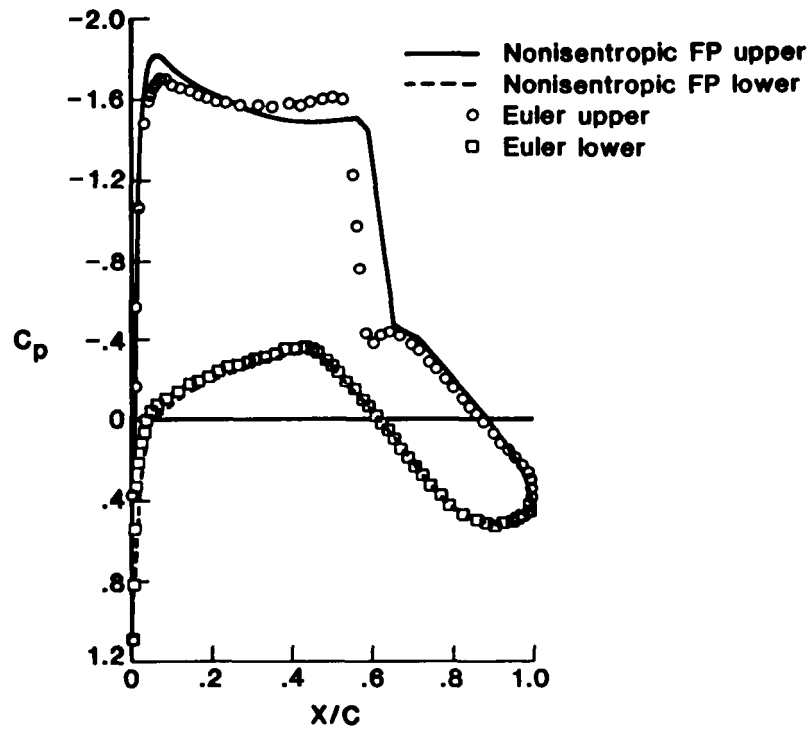
SUMMARY

An unsteady full potential method for calculating flows with strong shock waves has been presented. The method uses approximate factorization to advance the solutions in time and a linear interpolation method to model dynamic grid motion. Calculated results were presented for the NACA 0012 and NLR 7301 airfoils.

O   PRESENTED AN UNSTEADY FULL POTENTIAL METHOD FOR FLOWS WITH STRONG SHOCKS

O   USED APPROXIMATE FACTORIZATION TO ADVANCE SOLUTIONS IN TIME

O   USED LINEAR INTERPOLATION TO MODEL DYNAMIC GRIDS

O   PRESENTED ISENTROPIC AND NONISENTROPIC CALCULATIONS FOR NACA 0012 AND NLR 7301 AIRFOILS

CONCLUSIONS

From the results that were presented, it can be concluded that nonisentropic potential methods more accurately model Euler solutions than do isentropic methods. The primary effects of modeling shock-generated entropy are (1) to eliminate multiple flow solutions when strong shock waves are in the flow field and (2) to bring the strengths and locations of computed shock waves into better agreement with those calculated using Euler methods and those measured during experiments.

O   MODELING NONISENTROPIC EFFECTS RESULTS IN A POTENTIAL
    METHOD THAT MORE ACCURATELY MODELS EULER SOLUTIONS

O   PRIMARY EFFECTS OF MODELING SHOCK-GENERATED ENTROPY

    - MULTIPLE SOLUTIONS ELIMINATED

    - COMPUTED SHOCK WAVES IN BETTER AGREEMENT WITH
      EULER SOLUTIONS AND EXPERIMENT

FULL POTENTIAL UNSTEADY COMPUTATIONS
INCLUDING AEROELASTIC EFFECTS

Vijaya Shankar
Rockwell International Science Center
Thousand Oaks, California

Hiroshi Ide
Rockwell Aircraft Operations
Los Angeles, California

SUMMARY

A unified formulation is presented based on the full potential framework coupled with an appropriate structural model to compute steady/unsteady flows over rigid/flexible configurations for across the Mach number range (subsonic to supersonic). The unsteady form of the full potential equation in conservation form is solved using an implicit scheme maintaining time accuracy through internal Newton iterations. A flux biasing procedure based on the unsteady sonic reference conditions is implemented to compute hyperbolic regions with moving sonic and shock surfaces. The wake behind a trailing edge is modeled using a mathematical cut across which the pressure is satisfied to be continuous by solving an appropriate vorticity convection equation. An aeroelastic model based on the generalized modal deflection approach interacts with the nonlinear aerodynamics and includes both static as well as dynamic structural analyses capability. Figure 1 shows a schematic of the coupling process. Some of the topics to be discussed are 1) mechanism for coupling the aerodynamic and the aeroelastic equations, 2) update of geometry and grid at each time level to maintain time accuracy, and 3) prediction of flutter point dynamic pressure.

Results are presented for rigid and flexible configurations at different Mach numbers ranging from subsonic to supersonic conditions. The dynamic response of a flexible wing below and above its flutter point is demonstrated.
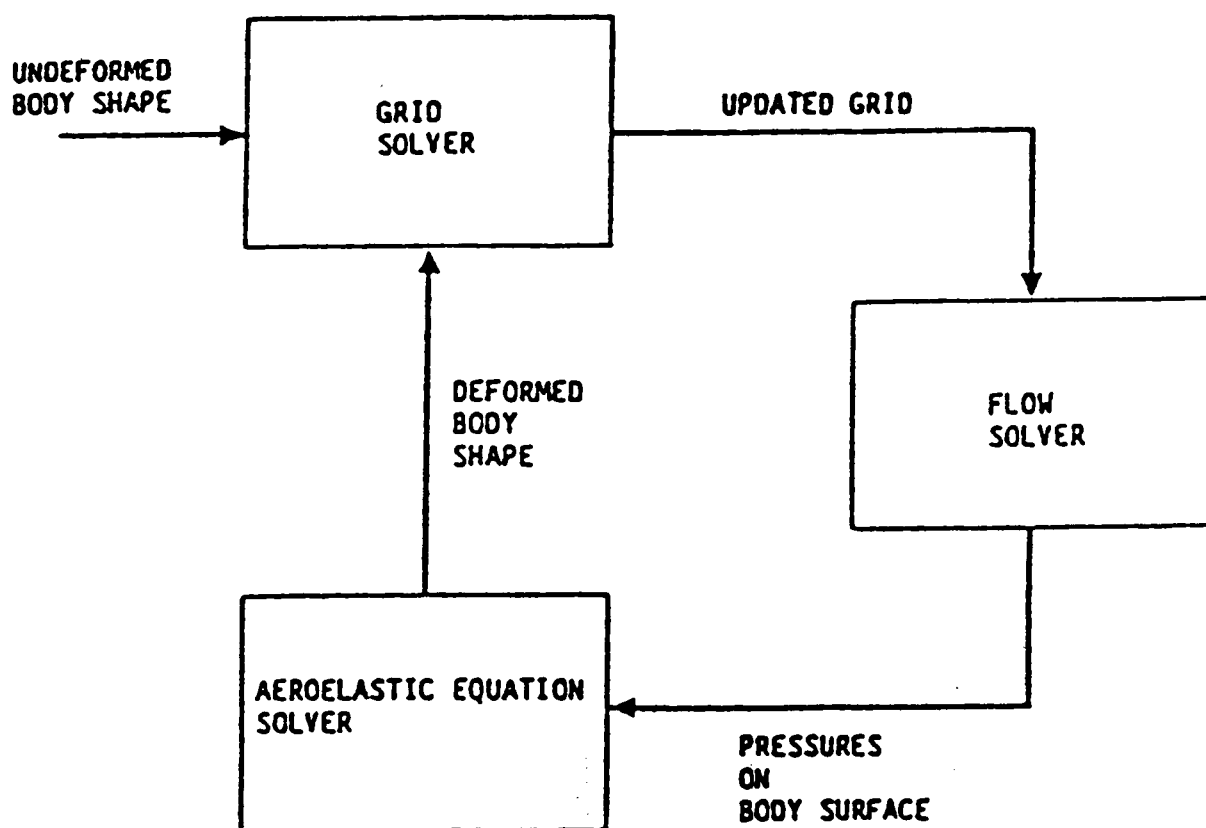
Fig. 1. Schematic of CFD/Aeroelastic Coupling

AERODYNAMIC FORMULATION

The conservation law form of the time–dependent full potential equation cast in an arbitrary coordinate system (τ, ζ, η, ξ) is written as

$$\bar{\rho}_\tau + \bar{E}_\zeta + \bar{F}_\eta + \bar{G}_\xi = 0$$

where

$$
\begin{aligned}
\bar{\rho} &= \frac{\rho}{J} \\
\bar{E} &= (\rho\zeta_t + E\zeta_x + F\zeta_y + G\zeta_z)/J \\
\bar{F} &= (\rho\eta_t + E\eta_x + F\eta_y + G\eta_z)/J \\
\bar{G} &= (\rho\xi_t + E\xi_x + F\xi_y + G\xi_z)/J
\end{aligned}
\tag{1}
$$

and J, Jacobian for the transformation, is given by

$$J = \partial(\tau, \zeta, \eta, \xi)/\partial(t, x, y, z).$$

The density ρ is given by Bernoulli's law

$$
\rho^{\gamma-1} = 1 - \frac{\gamma-1}{2}M_\infty^2 \big[2\phi_\tau + (U + \zeta_t) \\
+ (V + \eta_t)\phi_\eta + (W + \xi_t)\phi_\xi - 1\big]
\tag{2}
$$

where U, V, and W are the contravariant velocities.

Associating the subscripts i,j,k with the ζ,η,ξ directions, a numerical approximation to Eq. (1) can be written in the semidiscrete conservation law form given by

$$
\begin{aligned}
\left(\frac{\rho}{J}\right)_\tau &+ \left(\widetilde{E}_{i,j,k+1/2} - \widetilde{E}_{i,j,k-1/2}\right) \\
&+ \left(\widetilde{F}_{i,j+1/2,k} - \widetilde{F}_{i,j-1/2,k}\right) \\
&+ \left(\widetilde{G}_{i+1/2,j,k} - \widetilde{G}_{i-1/2,j,k}\right) = 0
\end{aligned}
\tag{3}
$$

where $\widetilde{E}, \widetilde{F}, \widetilde{G}$ are representative fluxes approximating the real fluxes $\bar{E}, \bar{F}, \bar{G}$ of Eq. (1).

NEWTON ITERATION

In terms of the velocity potential, Eq. (3) can be represented as

$$R(\phi) = 0 \tag{4}$$

where ϕ is the unknown to be solved at every grid point (i, j, k) in the current $(n + 1)$ time plane. The Newton iteration for solution to Eq. (4) is

$$R(\phi_*) + \left(\frac{\partial R}{\partial \phi}\right)_{\phi=\phi_*} \cdot \Delta\phi = 0 \tag{5}$$

where ϕ_* is the currently available ϕ at the $(n + 1)$ level and $\Delta\phi = \phi - \phi_*$. At convergence, $\Delta\phi$ will approach zero driving ϕ to ϕ^{n+1}. (See Fig. 2).
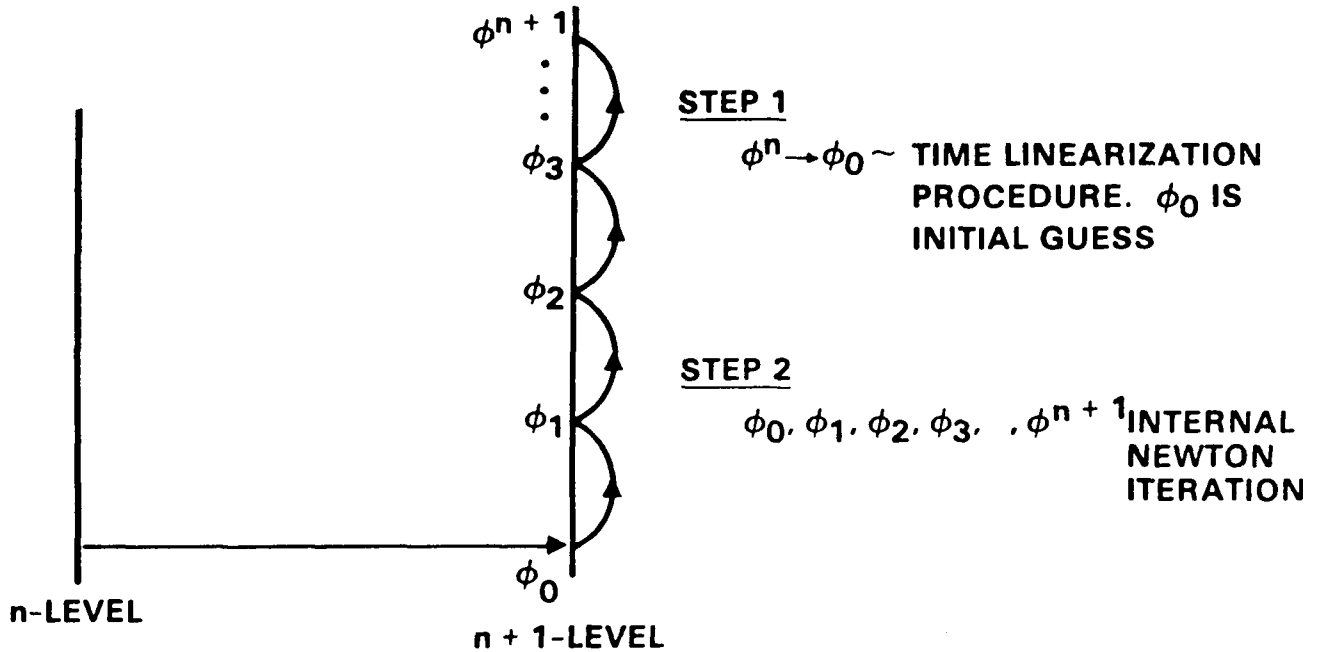

Fig. 2. Update of ϕ Based on Newton Iteration

TIME LINEARIZATION

Treatment of $\frac{\partial}{\partial \tau}\left(\frac{\rho}{J}\right)$ in Eq. (1)

$$\frac{\partial}{\partial \tau}\left(\frac{\rho}{J}\right) = \frac{(a_1 - b_1)\left\{\left(\frac{\rho}{J}\right)^{n+1} - \left(\frac{\rho}{J}\right)^n\right\} - b_1\left\{\left(\frac{\rho}{J}\right)^n - \left(\frac{\rho}{J}\right)^{n-1}\right\}}{a_1 \Delta \tau_1 - b_1(\Delta \tau_1 + \Delta \tau_2)} \tag{6}$$

where

$$a_1 = (\Delta \tau_1 + \Delta \tau_2)^2 \; ; \; \Delta \tau_1 = \tau^{n+1} - \tau^n \; ; \; \Delta \tau_2 = \tau^n - \tau^{n-1} \, .$$

The unknown quantity in Eq. (6) is ρ^{n+1}. Following Eq. (5), this is written as

$$\rho = \rho(\phi_*) + \left(\frac{\partial \rho}{\partial \phi}\right)_{\phi=\phi_*} \Delta \phi \tag{7}$$

where $\Delta \phi = \phi - \phi_*$, and

$$\left(\frac{\partial \rho}{\partial \phi}\right)_{\phi=\phi_*} = \left[-\frac{\rho}{a^2}\left\{\frac{1}{\Delta \tau_1} + U\frac{\partial}{\partial \zeta} + V\frac{\partial}{\partial \eta} + W\frac{\partial}{\partial \xi}\right\}\right]_{\phi=\phi_*} \tag{8}$$

is a differential operator. The speed of sound is denoted by a.

FLUX BIASING

Equation (3) requires evaluation of $\widetilde{E}$, $\widetilde{F}$, and $\widetilde{G}$ at various spatial half node points. As mentioned earlier, $\widetilde{E}$ represents $\bar{E}$ appearing in Eq. (1). The fluxes are defined in the following manner.

$$\widetilde{E} = \tilde{\rho}\frac{U}{J} \quad ; \quad \widetilde{F} = \tilde{\rho}\frac{V}{J} \quad ; \quad \widetilde{G} = \tilde{\rho}\frac{W}{J} \tag{9}$$

where $\tilde{\rho}$ is an upwind biased value of density, designed to produce the necessary artificial viscosity for treatment of hyperbolic regions.

$$\tilde{\rho} = \frac{1}{q}\left[(\rho q) \pm \left\{\frac{U}{Q}\frac{\partial}{\partial\zeta} + \frac{V}{Q}\frac{\partial}{\partial\eta} + \frac{W}{Q}\frac{\partial}{\partial\xi}\right\}(\rho q)^-\right] \tag{10}$$

where $Q = \sqrt{U^2 + V^2 + W^2}$.

The quantity $(\rho q)^-$ appearing in Eq. (10) is defined to be

$$\begin{aligned}(\rho q)^- &= \rho q - \rho^* q^* && \text{if } q > q^* \\ &= 0 && \text{if } q \le q^*.\end{aligned} \tag{11}$$

The quantities $\rho^8 q^*$, ρ^*, and q^* represent sonic values of the flux, density, and total velocity, respectively. These quantities are evaluated at half node grid points. (See Fig. 3).
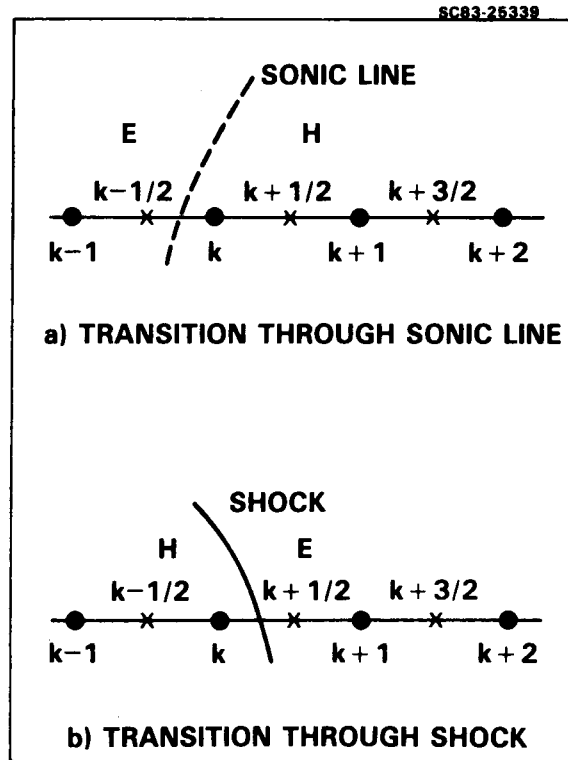

Fig. 3. Notation for Flux Biasing

AEROELASTIC MODEL

The aeroelastic model is based on the generalized modal approach. In the physical space, the structural equation is written as

$$[m]\ddot{z} + [c]\dot{z} + [k] = \{f\}$$

where m, c, k, and f represent the mass, damping, stiffness, and force, respectively. The structural deflection is given by z. Using the generalized mode shape, ϕ, one can rewrite the above equation as

$$M\{\ddot{q}\} + [C]\{\dot{q}\} + [K]\{q\} = \{F\}$$

where M, C, and K are generalized mass, damping, and stiffness matrices and $\{F\}$ is the generalized aerodynamic force. These are defined by

$$M = \phi^T m \phi \quad ; \quad K = \phi^T k \phi \quad ,$$
$$C = \phi^T c \phi \quad , \quad F = \phi^T f \quad \text{and} \quad z = \phi q \quad ,$$

where q is the generalized deflection.

STATIC FLEXIBLE CASE

The flexibility of the structure comes into the calculation through stiffness (K) and generalized mode shapes (ϕ). The steps involved in computing the static flexible equilibrium aerodynamics are given below:

1. Solve rigid aerodynamics for lift force.

2. Solve $Kq = F \Rightarrow \{z\} = [\phi]\{q\}$.

3. Increment $\{z\}$ in smaller steps and compute modified aerodynamic force, Figure 4.

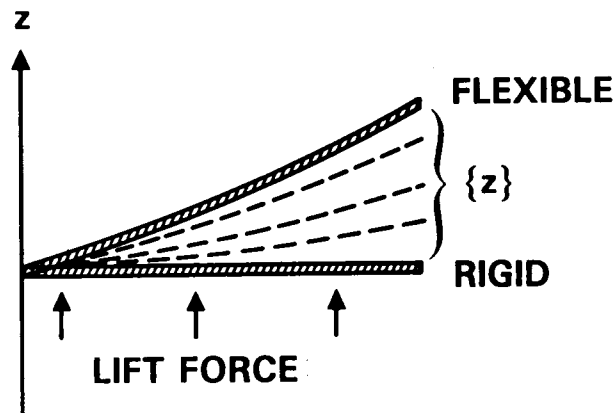4. Repeat Step 2.

5. Continue until $\{z\}$ and lift converge.

Fig. 4. Incremental Shape Change for Static Flexible Calculation

DYNAMIC FLEXIBLE CASE

The aerodynamics and the structural response are computed in a time accurate fashion using internal Newton iterations. The various steps involved in this computation are

1. Compute rigid aerodynamics.

2. Compute static flexible for a given dynamic pressure Q.

3. Set up an initial perturbance by perturbing either q or $\dot{q}$ of any mode.

4. Solve $M\ddot{q} + C\dot{q} + Kq = F \Rightarrow \{z\}$.

5. Compute x_T, y_T, z_T on the surface.

6. Define x_T, y_T, z_T for each field grid point allowing their values to go to zero at outer boundary, Figure 5.

7. Compute new grid location $x^{n+1} = x^n + x_T \Delta\tau, \cdots$ and new metrics.

8. Converge aerodynamics using internal Newton iteration.

9. Repeat Step 4. (For prediction of flutter Q gradually vary Q and monitor generalized modal deflections.)
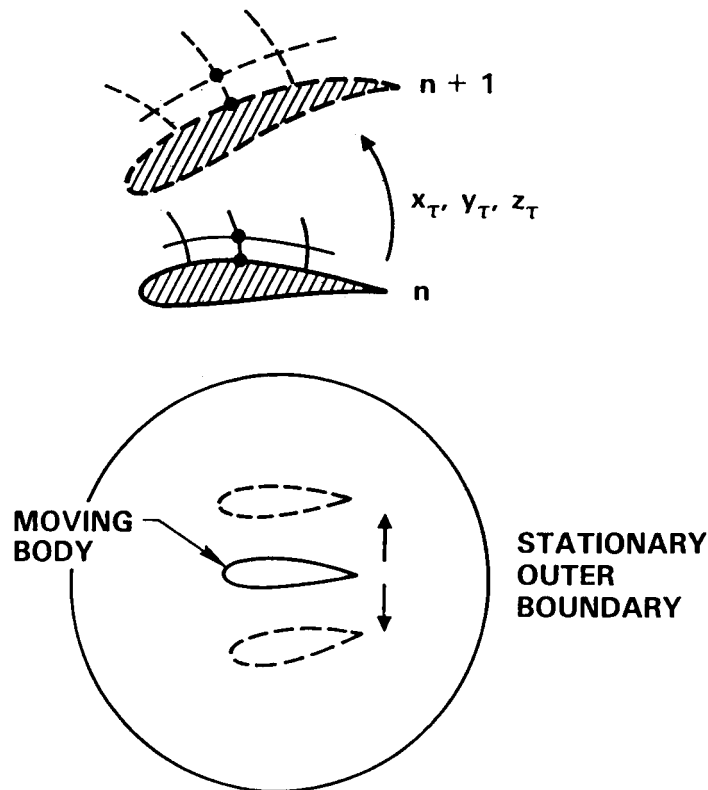
Fig. 5. Grid Update for Dynamic Flexible Calculations

OTHER FEATURES OF AERODYNAMIC/AEROELASTIC PROCEDURE

- Aerodynamics solved by triple approximate factorization scheme $\frac{\partial R}{\partial \phi} = L_\zeta L_\xi L_\eta$

- Wake cut modeled by unsteady vorticity convection equation

- Implicit boundary conditions

- Internal Newton iteration for time accuracy.

Code Capabilities

- Static Rigid

- Dynamic Rigid

- Static Flexible

- Dynamic Flexible

FLEXIBLE WING MODEL

Figure 6 shows the planform shape of a flexible low aspect ratio fighter wing. A sectional airfoil profile is also shown in Fig. 6. Note that there are two bumps in the lower section which are due to the leading edge and trailing edge control surface actuators. This model was designed and built by Rockwell and currently is being tested in NASA Langley Research Center's 16 foot TDT wind tunnel.
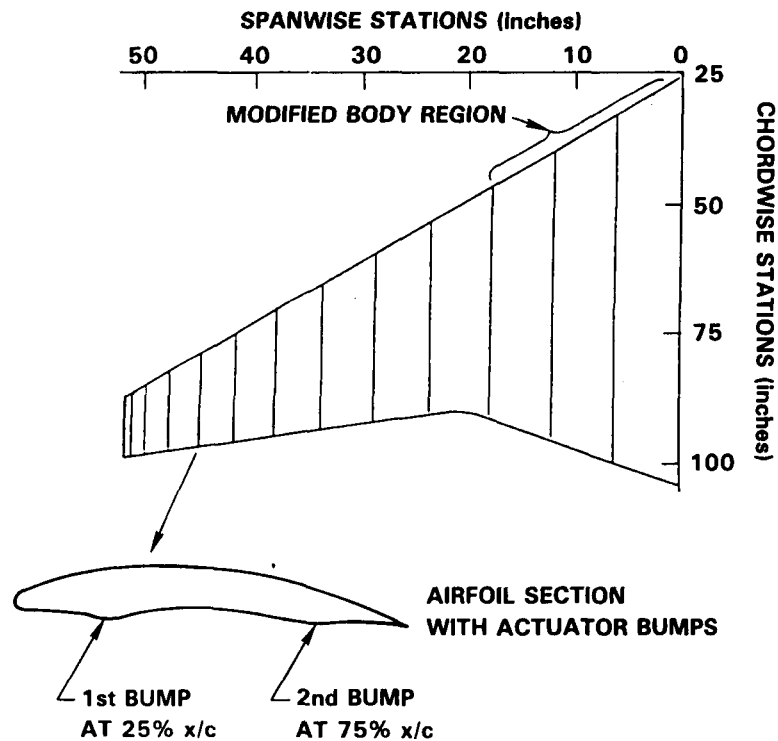
Fig. 6. Planform Shape of a Flexible Fighter Wing

NATURAL MODE SHAPES

Figure 7 shows the first ten natural frequency mode shapes for aeroelastic analysis. Mode shapes are prescribed at every grid point on the wing surface.

| MODE 1 | MODE 2 | MODE 3 | MODE 4 | MODE 5 |
| 6.33 Hz | 10.27 Hz | 13.92 Hz | 22.73 Hz | 32.73 Hz |

| MODE 6 | MODE 7 | MODE 8 | MODE 9 | MODE 10 |
| 35.48 Hz | 40.71 Hz | 52.75 Hz | 54.03 Hz | 55.96 Hz |
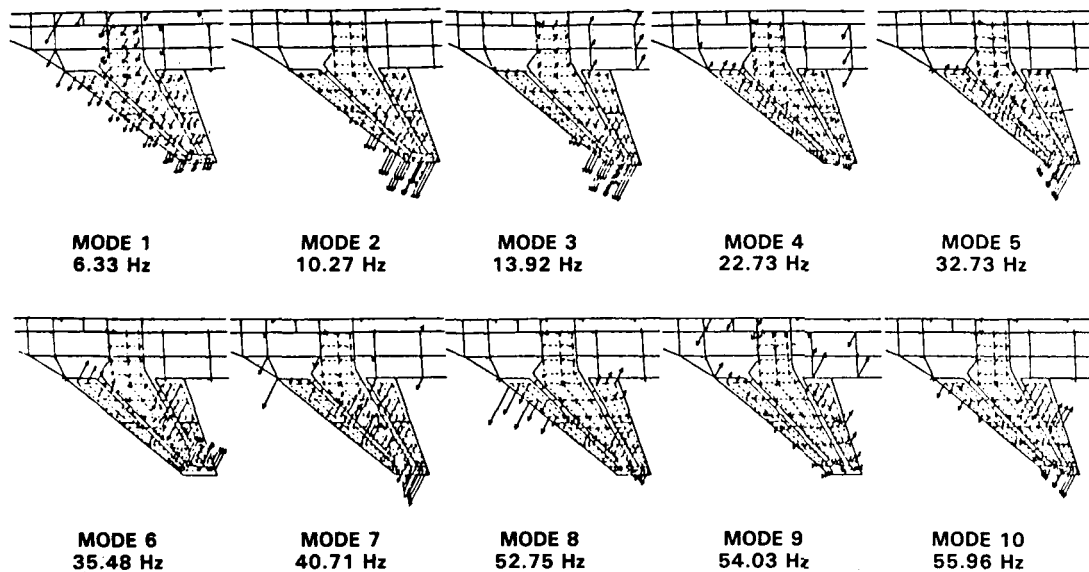
Fig. 7. Selected Mode Shapes for Aeroelastic Analyses

RESULTS FOR STATIC FLEXIBLE CASE

Figure 8 shows results for a static flexible computation at $M_\infty = 1.15$, $\alpha = 6°$ for two different dynamic pressure conditions. $Q = 0$ corresponds to the rigid case. The deflected shape of the wing for $Q = 288$ psf shows the nose down rotation of the airfoil near the wing tip resulting in tip load reduction. This is essential for the wing to be aeroelastically stable.

GEOMETRY   UPPER C_p LOWER C_p

RIGID (Q = 0)

DEFLECTED SHAPE   UPPER C_p LOWER C_p

FLEXIBLE (Q = 288 psf)

Fig. 8. Static Flexible Computation, $M_\infty = 1.15$, $\alpha = 6°$

C_L VERSUS α FOR STATIC FLEXIBLE

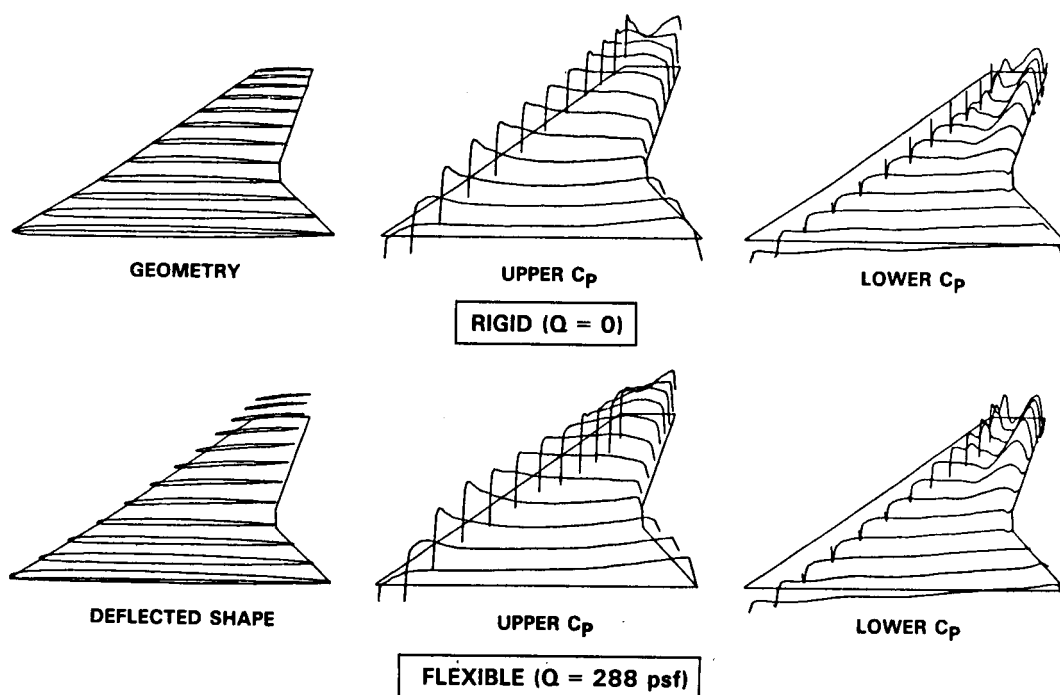The C_L versus α curves at two different Mach numbers are shown in Fig. 9. Table 1 shows the change in total lift coefficient between rigid and flexible cases for different Mach numbers, angles of attack, and Q conditions.

M	α	Q(psf)	$C_{L_{test}}$	$C_{L_{flex}}$	$C_{L_{rigid}}$
1.05	1.6	335	0.0785	0.0800	0.1450
1.15	0.5	230	0.0433	0.0400	0.0685
0.90	0.0	220	0.0446	0.0441	0.0637

Table 1. Comparison of Lift Coefficients between Rigid and Flexible Calculations
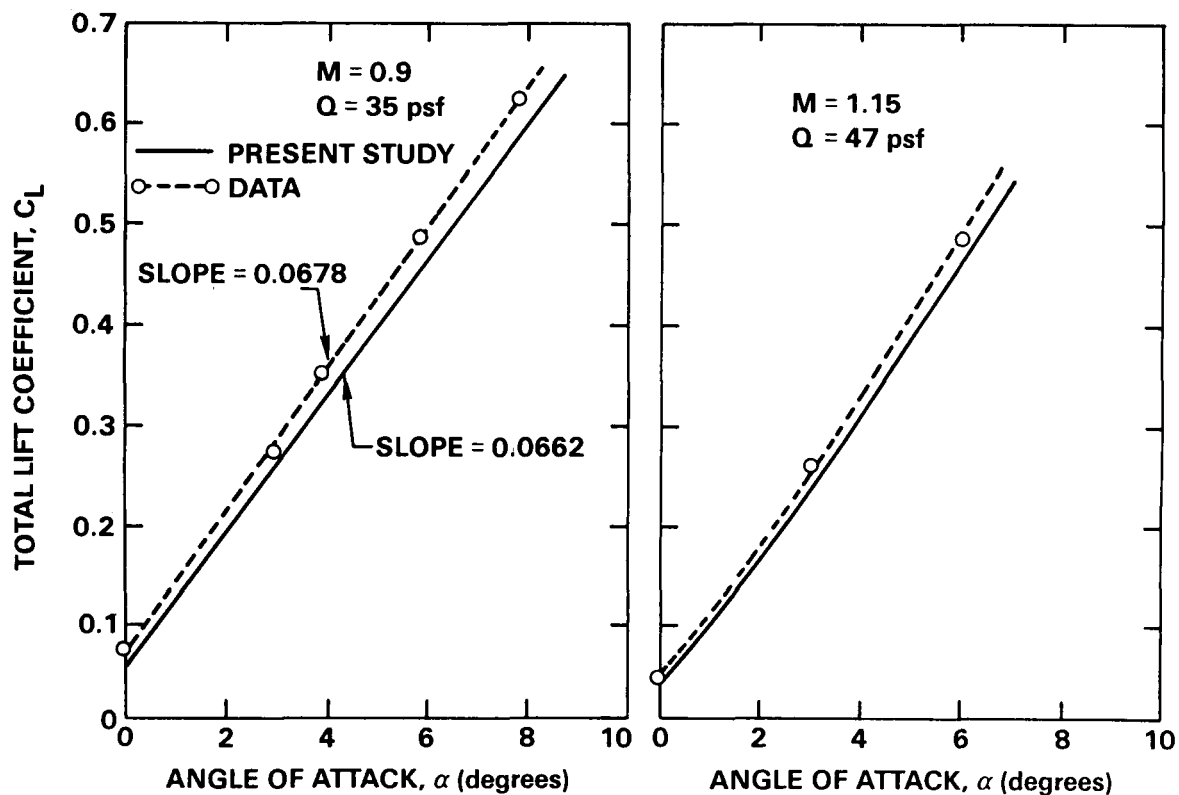
Fig. 9. C_L versus α for the Flexible Wing

STATIC FLEXIBLE WITH DEFLECTED CONTROLS

Figure 10 shows a similar static aeroelastic calculation with leading and trailing edge control surfaces deflected. Also shown are the surface chordwise pressure distributions at various span stations and a cross section of the wing with deflected control surfaces. The span stations where the deflected control surfaces are present are drastically altered.
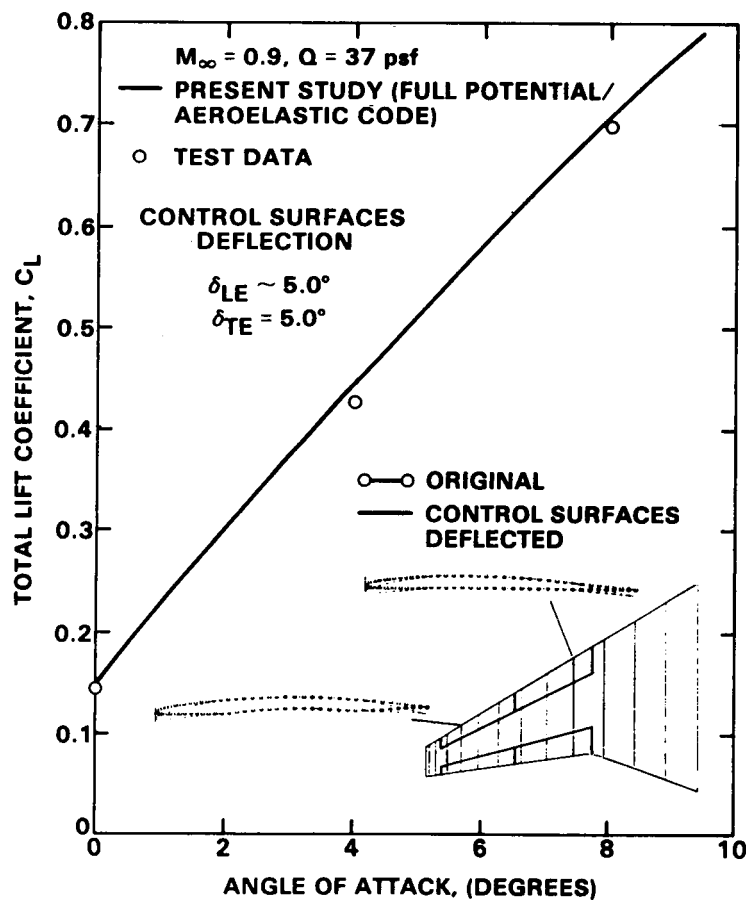
Fig. 10. Static Aeroelastic Computations with Deflected Control Surfaces

DYNAMIC FLEXIBLE CASE

Figures 11–13 show results for dynamic aeroelastic computations at three different dynamic pressures (Q). Figure 11 is for $Q < Q_{\text{Flutter}}$. The structure is aerodynamically stab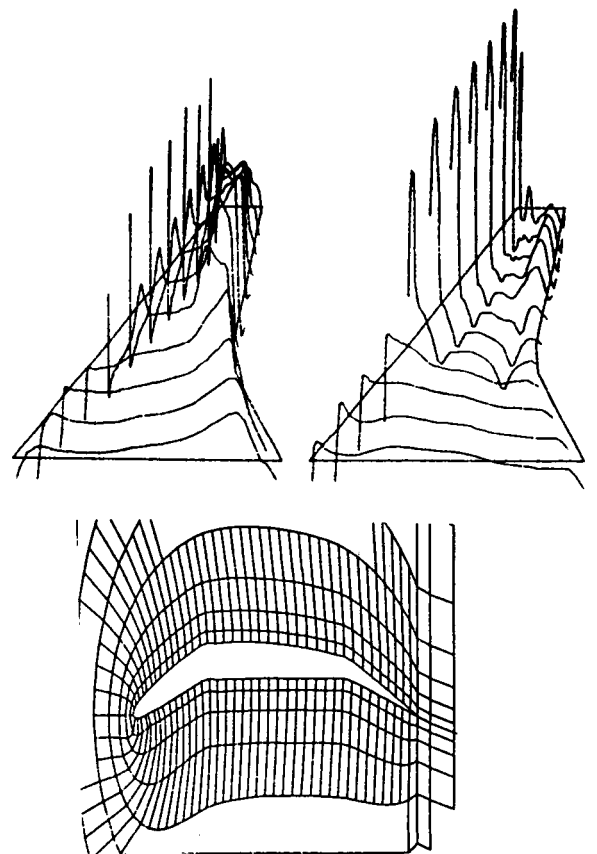le as shown by the decaying amplitudes of various quantities. Figure 12 is exactly at the flutter dynamic pressure. The value for the flutter Q was obtained by the nonlinear aerodynamics/aeroelastic code through numerical search. Exactly at the flutter Q, the dynamic response of the structure does not decay as shown by results of Fig. 12. Figure 13 illustrates the structural response above the flutter Q. The structure is aerodynamically unstable as shown by the growing amplitudes of various quantities.
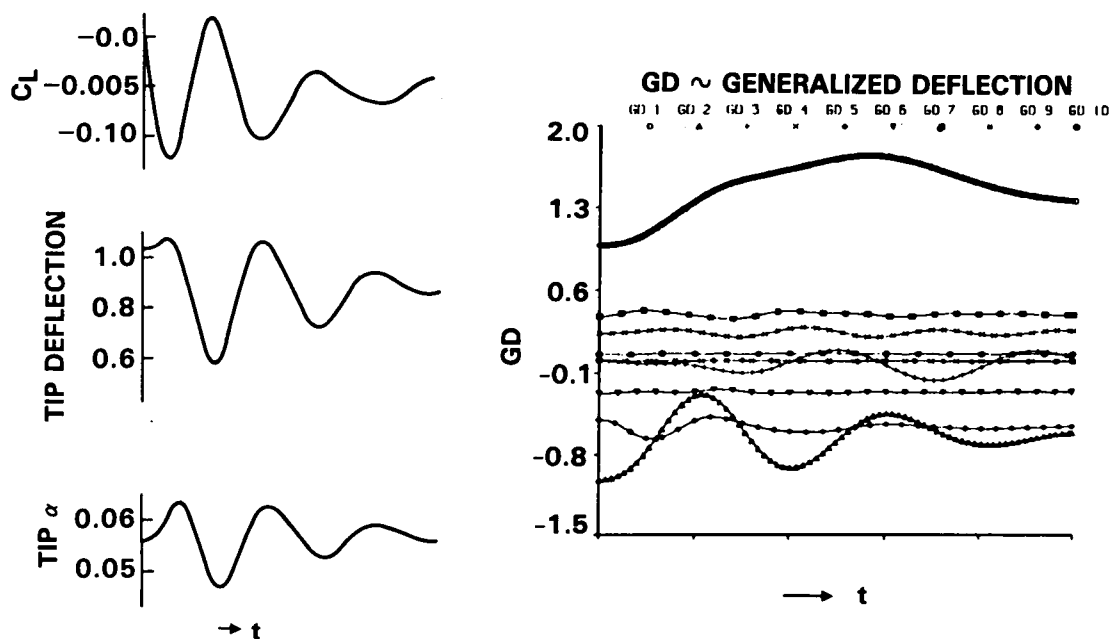
Fig. 11. Dynamic Flexible Computation – below Flutter, $M_\infty = 1.15$, $\alpha = 0°$, $Q = 360$ psf

Fig. 12. Dynamic Flexible Computation – at Flutter Point, $M_\infty = 1.15$, $\alpha = 0°$, $Q = 490$ psf
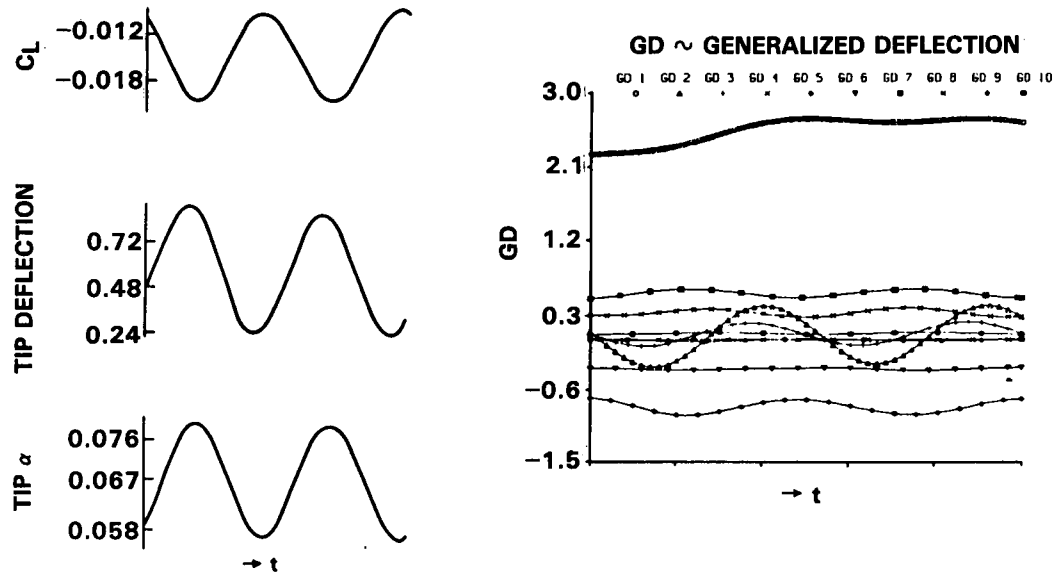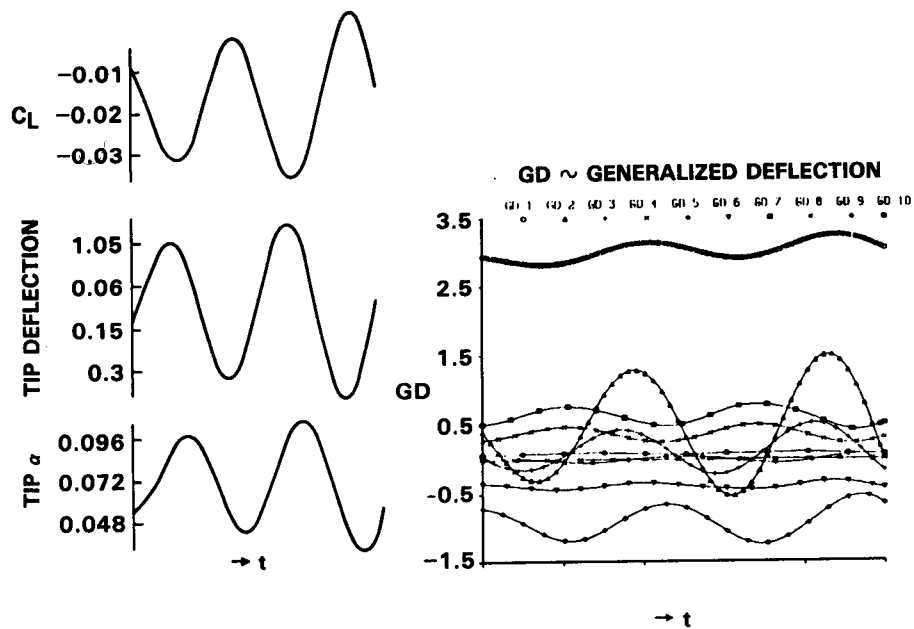

Fig. 13. Dynamic Flexible Computation – above Flutter, $M_\infty = 1.15$, $\alpha = 0°$, $Q = 550$ psf

191

FLUX-VECTOR SPLITTING FOR UNSTEADY CALCULATIONS ON DYNAMIC MESHES

W. Kyle Anderson
James L. Thomas
Christopher L. Rumsey
NASA Langley Research Center

The method of flux-vector-splitting used in the current study is that of Van Leer[1]. The fluxes split in this manner have the advantage of being continuously differentiable at eigenvalue sign changes and this allows normal shocks to be captured with at most two interior zones, although in practice only one zone is usually observed. The fluxes as originally derived, however did not include the necessary terms appropriate for calculations on a dynamic mesh. The extension of the splitting to include these terms while retaining the advantages of the original splitting is the main purpose of the present investigation. In addition, the use of multiple grids to reduce the computer time is investigated. A subiterative procedure to eliminate factorization and linearization errors so that larger time steps can be used is also investigated.

PURPOSE

- Extend the Van Leer method of flux vector splitting for use on moving meshes

- Investigate the use of multiple grids to reduce computer time

- Use of multigrid with a sub-iterative procedure to eliminate factorization and linearization errors

The upwind differencing in the present work is achieved through the technique of flux-vector-splitting where the fluxes are split into forward and backward contributions according to the signs of the eigenvalues of the Jacobian matrices, and differenced accordingly. The split-flux differences are implemented as a flux balance across a cell corresponding to MUSCL (Monotone Upstream-Centered Schemes for Conservation Laws) type differencing[2]. Here, the fluxes at each cell interface are formed from the metric terms at the cell interface, and the state variables are obtained by upwind-biased interpolation of the conserved variables.

FLUX VECTOR SPLITTING

- Split fluxes into forward and backward contributions
  $$F(Q) = F^+(Q^-) + F^-(Q^+)$$

- Use upwind biased approximation to spatial derivatives

- Van Leer splitting
  - Continuously differentiable
  - Allows shocks to be captured with at most two (usually one) interior zones

195
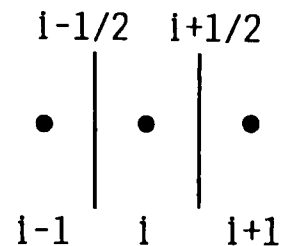
In order to facilitate the derivation of the split fluxes, it is convenient to revert to the one-dimensional Euler equations on a moving grid. The one dimensional Euler equations express the conservation of mass, momentum, and energy for an inviscid, nonconducting gas in the absence of external forces. The flux is written as a function of the density, speed of sound, local Mach number relative to the moving grid, and the mesh speed.

ONE DIMENSIONAL EULER EQUATIONS

$$\hat{F}(\rho,a,M;\hat{\xi}_t) = \left\{ \begin{array}{l} \rho a M \\[2em] \rho a^2\left(M^2 + \dfrac{1}{\gamma} - \dfrac{\hat{\xi}_t M}{a}\right) \\[2em] \rho a^3\left(\dfrac{M}{\gamma-1} + \dfrac{M^3}{2} - \dfrac{M^2\hat{\xi}_t}{a} + \dfrac{\hat{\xi}_t^2 M}{2a^2} - \dfrac{\hat{\xi}_t}{\gamma a}\right) \end{array} \right\}$$

$$M = \frac{U + \hat{\xi}_t}{a} = \text{Mach number relative to moving grid}$$

196

In deriving the splittings for a dynamic mesh, several requirements are placed on the split fluxes: these requirements are identical to those originally imposed by Van Leer for the fixed grid equations, with an additional constraint requiring simply that for zero grid speed the split fluxes revert to those for a stationary grid. Eight requirements are ultimately placed on the split fluxes of which the five most important ones are shown.

REQUIREMENTS FOR VAN LEER SPLITTINGS

- $\hat{F}(\hat{Q};\hat{\xi}_t) = \hat{F}^+(\hat{Q};\hat{\xi}_t) + \hat{F}^-(\hat{Q};\hat{\xi}_t)$

- $\partial\hat{F}^+/\partial\hat{Q}$ must have all eigenvalues ≥ 0
  $\partial\hat{F}^-/\partial\hat{Q}$ must have all eigenvalues ≤ 0

- $\partial\hat{F}^{\pm}/\partial\hat{Q}$ must be continuous

- $\partial\hat{F}^{\pm}/\partial Q$ must have one eigenvalue vanish for subsonic Mach numbers

- $\hat{F}^+(\hat{Q};\hat{\xi}_t) = \hat{F}(\hat{Q};\hat{\xi}_t)$ for $M \geq 1$
  $\hat{F}^-(\hat{Q};\hat{\xi}_t) = \hat{F}(\hat{Q};\hat{\xi}_t)$ for $M \leq -1$

With the Mach number defined relative to the grid, the mass flux has the same form as that of the fixed grid equations. Therefore the splitting of the mass flux for a moving grid is the same as for the fixed grid equations. The momentum flux is split in a similar fashion.

SPLITTING THE FLUX VECTORS

● Mass flux has identical form as for a stationary grid

$$f_1^{\pm}(\rho,a,M) = \pm \frac{\rho a}{4}[M \pm 1]^2$$

● Momentum flux

$$f_2^{\pm}(\rho,a,M;\hat{\xi}_t) = f_1^{\pm} a \left[\frac{\gamma-1}{\gamma}M \pm \frac{2}{\gamma} - \frac{\hat{\xi}_t}{a} \right]$$

The formation of the energy flux can now be obtained from a combination of the split mass and momentum fluxes. The formation of the energy flux in this manner insures its degeneracy, thereby guaranteeing shock structures with no more than two interior zones.

SPLITTING THE FLUX VECTORS

- Energy flux formed from combination of mass and momentum fluxes ensures degeneracy

$$f_3^{\pm}(f_1, f_2; \hat{\varepsilon}_t) = c_1 \frac{(f_2^{\pm})^2}{f_1^{\pm}} + c_2 f_2^{\pm} \hat{\varepsilon}_t + c_3 f_1^{\pm} \hat{\varepsilon}_t^2$$

$$c_1 = \frac{\gamma^2}{2(\gamma^2 - 1)} \qquad c_2 = \frac{1}{\gamma^2 - 1} \qquad c_3 = \frac{1}{2(\gamma^2 - 1)}$$

- Degenerate flux guarantees shock structures with no more than two interior zones (generally one)

The eigenvalues of the Jacobians of the split fluxes are shown for an exemplary grid speed. All eigenvalues of F^+ are non-negative while all the eigenvalues of F^- are non-positive. In addition, each has one eigenvalue vanishing for subsonic Mach numbers. The differentiability of the fluxes is also indicated in the figure since the eigenvalues are representative of the derivatives of the fluxes in canonical form and all are continuous over the Mach number range.

EIGENVALUES OF $\partial \hat{F}^{\pm} / \partial \hat{Q}$ $(\hat{\xi}_t = 0.5)$
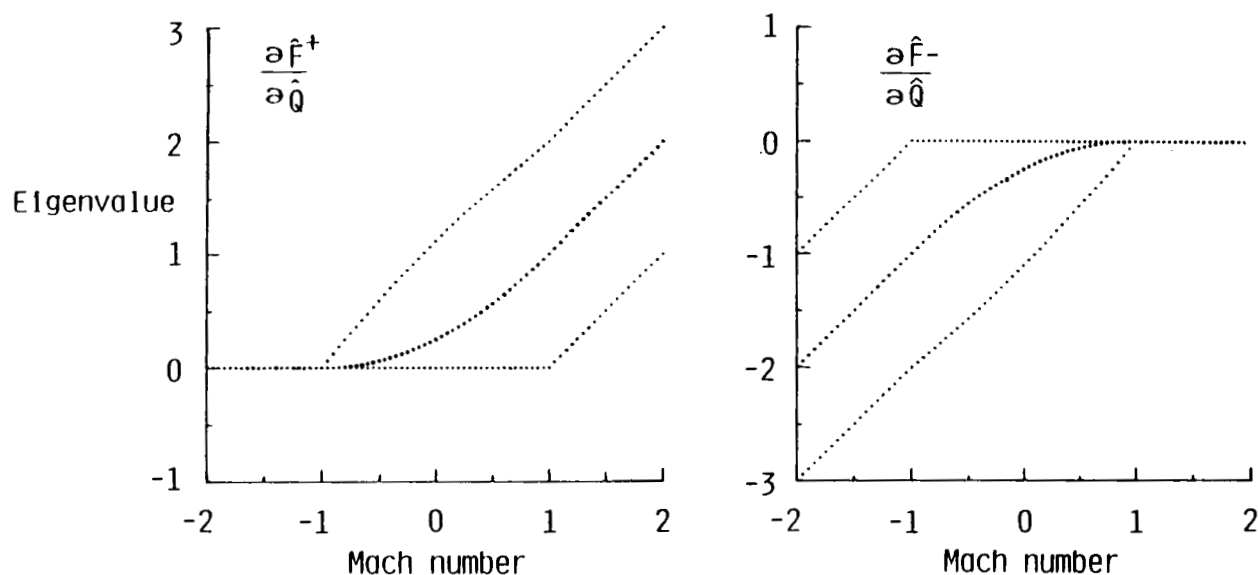
The method used to advance the solution in time is an implicit finite volume method[3]. Since implicit methods allow much larger time steps than explicit methods, the allowable time step is dictated more by the physics of the flow than by stability considerations. The scheme can be either first or second order accurate in time and either first, second or third order accurate in space. Since upwind differencing is employed, no explicitly added artificial viscosity is needed and is therefore not used.

TIME ADVANCEMENT ALGORITHM

- Backward time implicit algorithm
  - Approximate factorization
  - First or second order time accurate
- Finite volume implementation
- No explicity added artificial viscosity
- Explicit boundary conditions

The basic algorithm utilizes approximate factorization to obtain the solution at each time step. For three dimensions the algorithm is implemented in three steps, one for each spatial direction. Using first order spatial differencing on the implicit side of the equation, the scheme requires the solution of a system of block tridiagonal equations in each coordinate direction and is completely vectorizable since the operations in each factor are independent of the other two. For unsteady calculations, several sub-iterations can be used at each time step to eliminate unwanted factorization and linearization errors.

THREE-DIMENSIONAL ALGORITHM

$$\left[\left(I + \frac{\phi}{2}\right) + \Delta t \delta_\xi^- \hat{A}^+ + \Delta t \delta_\xi^+ \hat{A}^-\right] \Delta \hat{Q}^* = -\Delta t \hat{L}(\hat{Q}^\ell)$$

$$\left[\left(I + \frac{\phi}{2}\right) + \Delta t \delta_\eta^- \hat{B}^+ + \Delta t \delta_\eta^+ \hat{B}^-\right] \Delta \hat{Q}^{**} = \left[I + \frac{\phi}{2}\right] \Delta \hat{Q}^*$$

$$\left[\left(I + \frac{\phi}{2}\right) + \Delta t \delta_\zeta^- \hat{C}^+ + \Delta t \delta_\zeta^+ \hat{C}^-\right] \Delta \hat{Q}^\ell = \left[I + \frac{\phi}{2}\right] \Delta \hat{Q}^{**}$$

$$\hat{Q}^{\ell+1} = \hat{Q}^\ell + \Delta Q^\ell$$

$$\phi = 0 \quad \text{first order time}$$

$$\phi = 1 \quad \text{second order time}$$

Steady computations are compared with experiment for the F-5 fighter wing at four freestream Mach numbers and an angle of attack of zero degrees. The mesh used in the computations is a 129×33×33 C-H mesh corresponding to 129 points along the airfoil and wake, 33 points approximately normal to the airfoil, and 33 points in the spanwise direction, 17 of which are on the wing planform. For each Mach number, an inboard and outboard span station are shown, corresponding to y/s=0.174 and y/s=0.8412, respectively where y is the coordinate in the spanwise direction and s is the wing semi-span. The results are generally in good agreement with the experimental data at both span stations for all Mach numbers.

F-5 STEADY PRESSURE DISTRIBUTIONS

$\alpha = 0°$ y/s = 0.1740

——— Theory 129x33x33
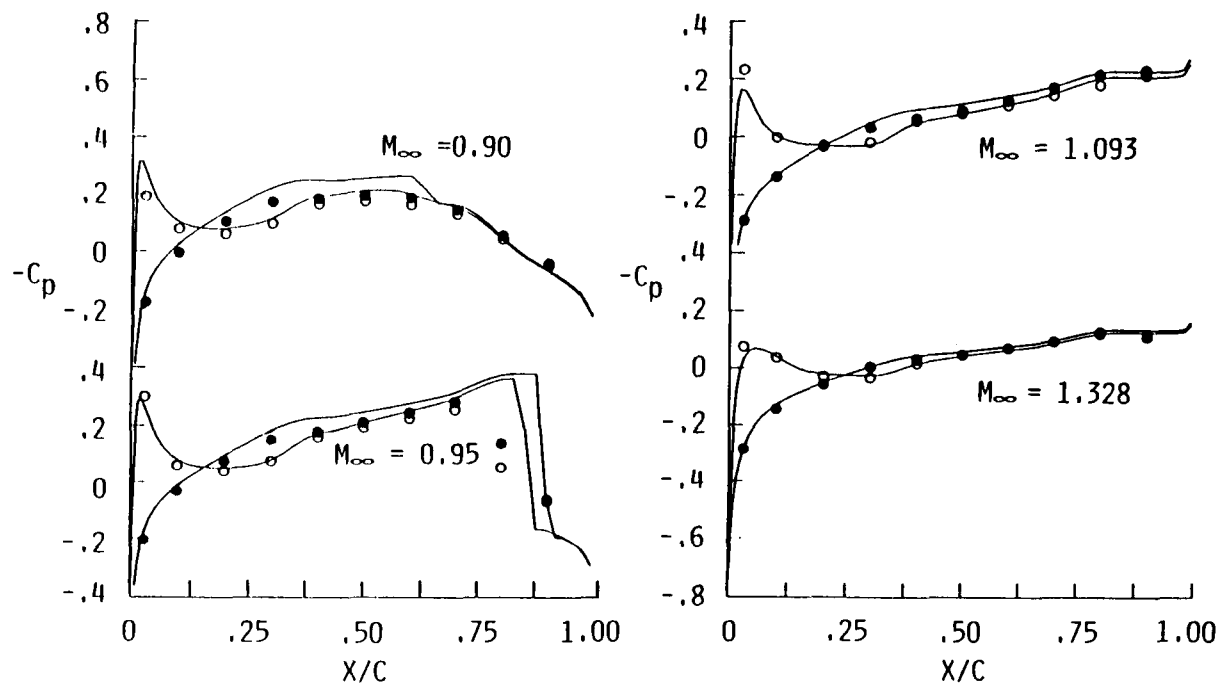
o   Experiment

F-5 STEADY PRESSURE DISTRIBUTIONS

$\alpha = 0°$ y/s = 0.8412

——— Theory 129x33x33
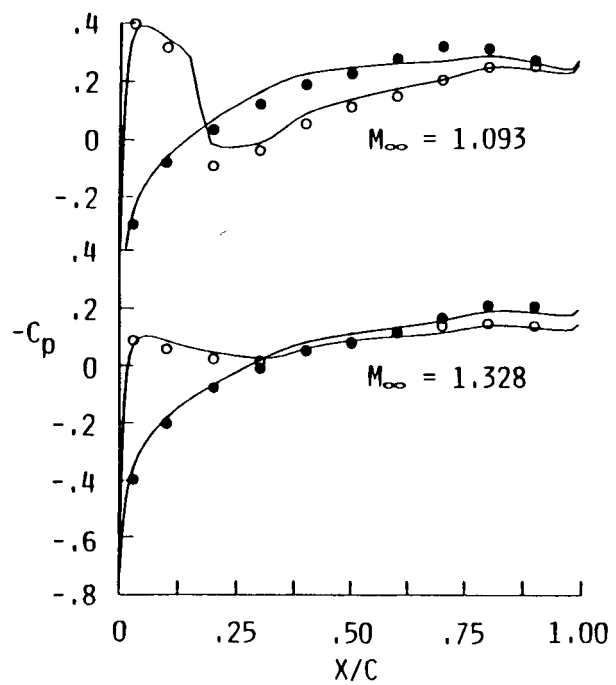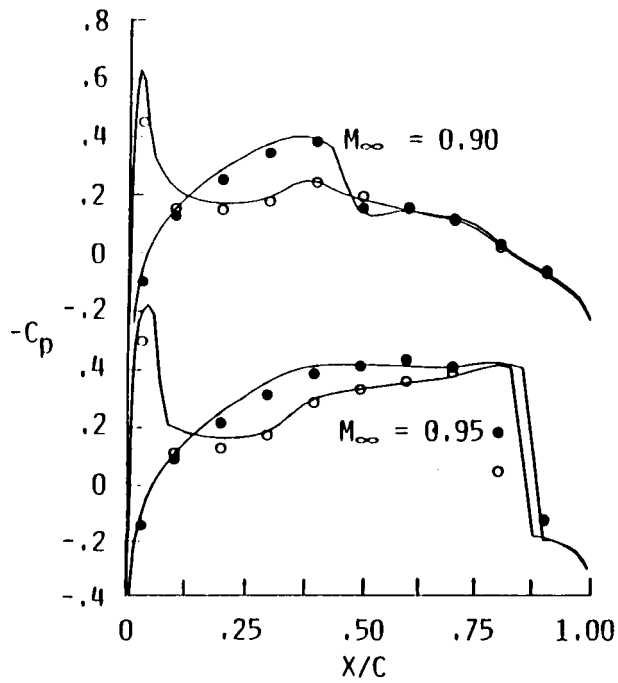
o Experiment

Computational results using both flux-vector-splitting and flux-difference-splitting[4] are compared with experimental data for an NACA 0012 airfoil undergoing forced pitching oscillations. The freestream Mach number is 0.755, the reduced frequency is 0.1628 (based on chord), and the mean and dynamic angles of attack are 0.016 and 2.51 degrees respectively. The results were obtained on a 193×33 C-grid using a time step of 0.10 requiring approximately 500 time steps to compute each pitching cycle. The computed pressures using both flux-vector-splitting and flux-difference-splitting compare well with the experiment at all angles of attack in the cycle shown. The shocks are all captured very sharply with no oscillations. Results for the negative angles of attack are similar.

UNSTEADY PRESSURE DISTRIBUTION

NACA 0012 M_∞= 0.755 k= 0.1628
α_0= 0.016 α_1= 2.51
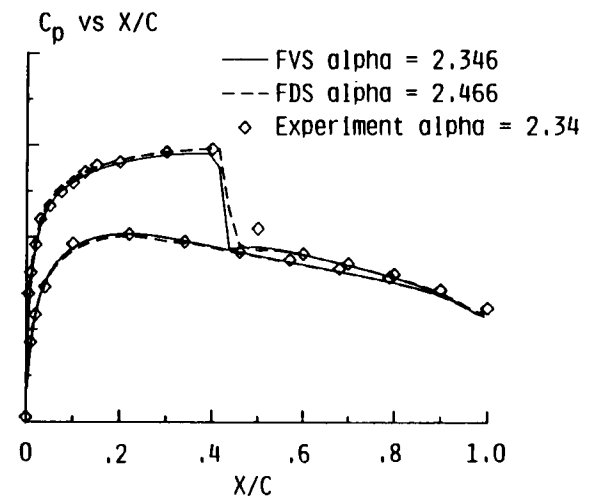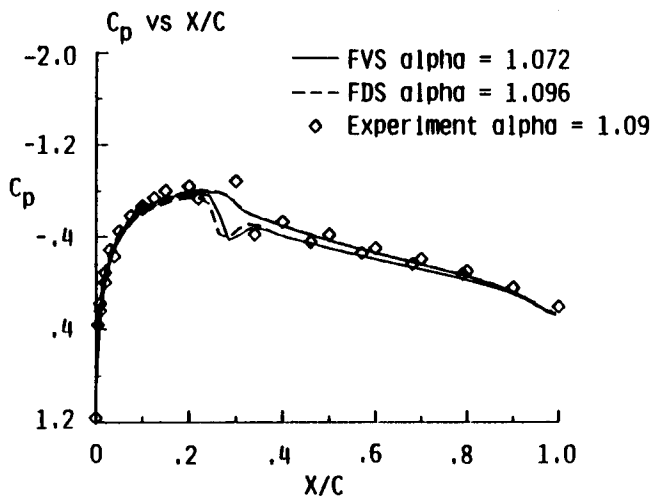
UNSTEADY PRESSURE DISTRIBUTION

NACA 0012 M_∞= 0.755 k= 0.1628
α_0= 0.016 α_1= 2.51
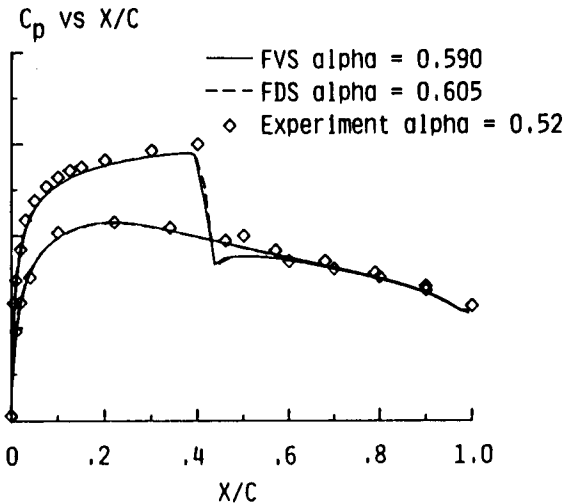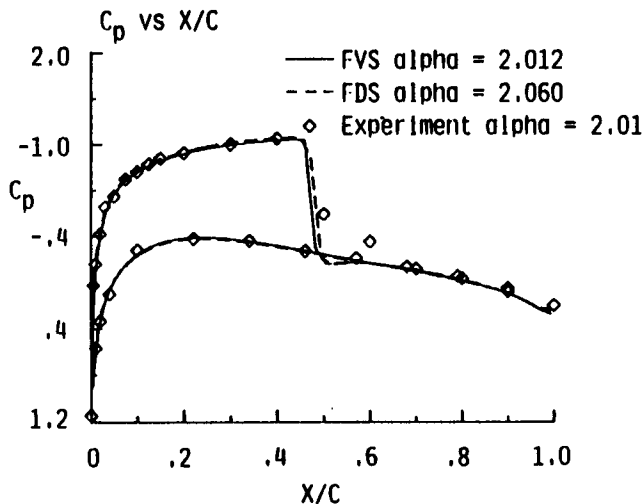
Although the time step allowed by the implicit method is much larger than that allowed by explicit methods, the time steps used may still be relatively small so that resolving the motion requires extensive computational effort, especially for three-dimensional flows where the number of grid points used in the discretization of the flowfield may be large. The multiple grid method has proven to be effective in reducing the computaional work for steady flows, although little work has been done for unsteady flows. Jesperson[5] has shown that the multigrid concept could be used to advance the solution in time on coarser meshes while maintaining first order accuracy in time. The impetus is in reducing the computer time by performing some of the calculations on coarser meshes where fewer operations are required.

NONITERATIVE USE OF MULTIPLE GRID LEVELS

- Advance solution on coarser grids where computations are inexpensive

- Addition of relative truncation error between fine grid and coarser grid maintains high order spatial accuracy
$$M_1(\hat{Q}_1^{n+1} - \hat{Q}_1^n) = -\Delta t \, [\hat{L}_1 \, (\hat{Q}_1^n) - \tau_1]$$

- First order temporal accuracy

Results are shown comparing calculated lift and moment coefficients against experimental data for the pitching NACA 0012 airfoil previously described. Also shown in the figure are results obtained using the noniterative multiple grid technique for the time accurate calculations. The lift and moment calculations are in excellent agreement between the single level and two level cases. With three levels, however, the pitching moment exhibits slightly larger disagreement with the single level results.

UNSTEADY FORCES AND MOMENTS

NACA 0012 $M_\infty = 0.755$ $k = 0.1628$
$\alpha_0 = 0.016$ $\alpha_1 = 2.51$

Lift vs alpha

Moment vs alpha

— 1 level DT=0.1
--- 2 levels DT=0.1
—- 3 levels DT=0.1
△ Experiment
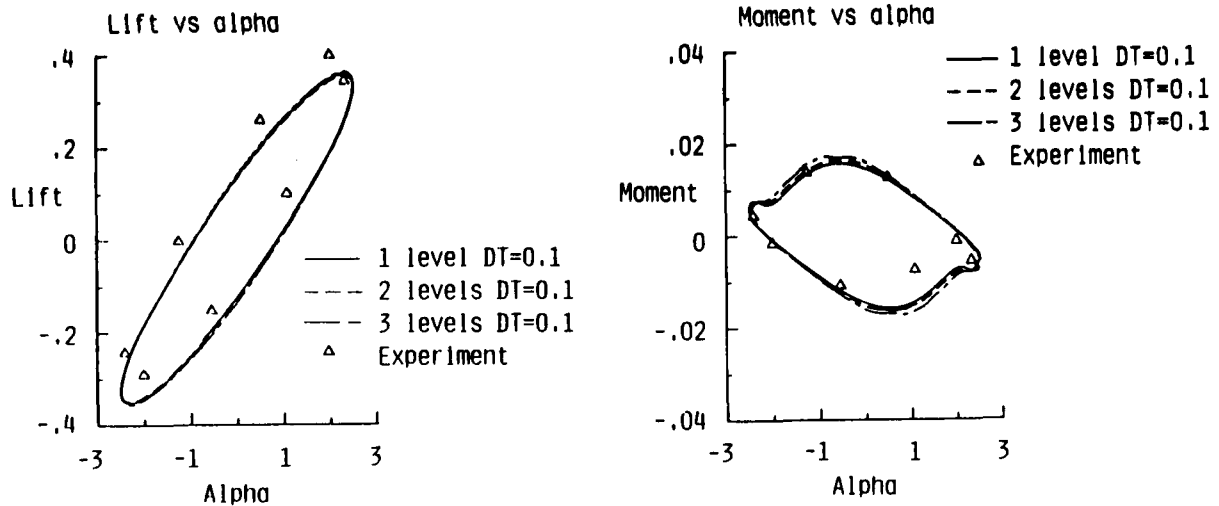
Pressure results are shown at one point in the pitching cycle when one, two, and three grids are used. As seen, the pressure distributions between the single level and two level cases are virtually indistinguishable; the pressures obtained using three grid levels, however, differ somewhat from the other two, particularly at the base of the shock. The explanation for this lies partly in the fact that each of the coarse grids is influenced strongly by the residual on the finest grid. Therefore, as the number of grid levels is increased, the residual which is driving the problem has been evaluated at an earlier point in the cycle. When only two grids are employed, the residual on the fine grid can be evaluated at the correct angle of attack in the cycle so that no lag in the residual exists.

PRESSURE DISTRIBUTION FOR SINGLE AND MULTIPLE GRIDS

NACA 0012 $M_\infty = 0.755$ $k = 0.1628$

$\alpha_0 = 0.016$ $\alpha_1 = 2.51$

——— 1 level alpha = -0.52
- - - 2 levels alpha = -0.56
——- 3 levels alpha = -0.52
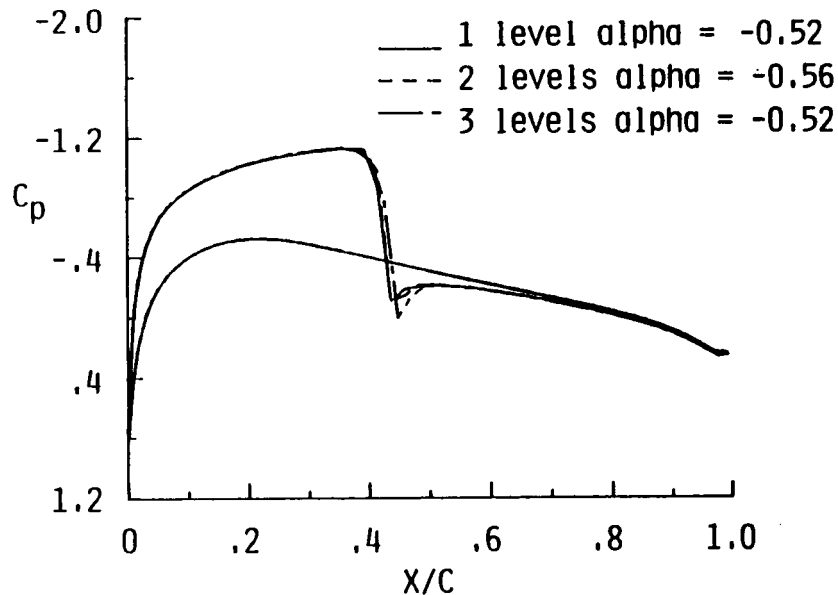
Results indicate that the use of multiple grids can give reasonably accurate results while decreasing the computer time. Use of more than two grid levels, however, leads to increasing errors.

NONITERATIVE USE OF MULTIPLE GRID LEVELS

- Solution using two grid levels are virtually identical to single grid solution

- Two time steps are taken with only a slight increase in cost over a single step

- Use of more than two grids leads to increasing errors

Unsteady results for the F-5 wing are compared with experiment at a freestream Mach number of 0.95 undergoing forced pitching motion where the mean angle of attack is zero degrees, the unsteady amplitude is 0.532 degrees, and the reduced frequency based on root chord is 0.264. The results have been computed on a 129×33×33 mesh using two grid levels and a time step of 0.05 on each grid requiring approximately 250 fine grid time steps per pitching cycle. The real and imaginary components of the pressure coefficients are compared with experiment at two span stations. As before, the results show reasonable comparison with experiment. However, the characteristic pressure spike at the shock is somewhat aft of the experimental results indicating that viscous effects may be important.

UNSTEADY PRESSURE FOR F-5 WING

$M_\infty = 0.95$ $k = 0.264$ $\alpha_0 = 0$ $\alpha_1 = 0.532$
$y/s = 0.1740$

Real component

Imaginary component

UNSTEADY PRESSURE FOR F-5 WING

$M_\infty = 0.95$ $k = 0.264$ $\alpha_0 = 0$ $\alpha_1 = 0.532$

$y/s = 0.8412$

Real component

Imaginary component
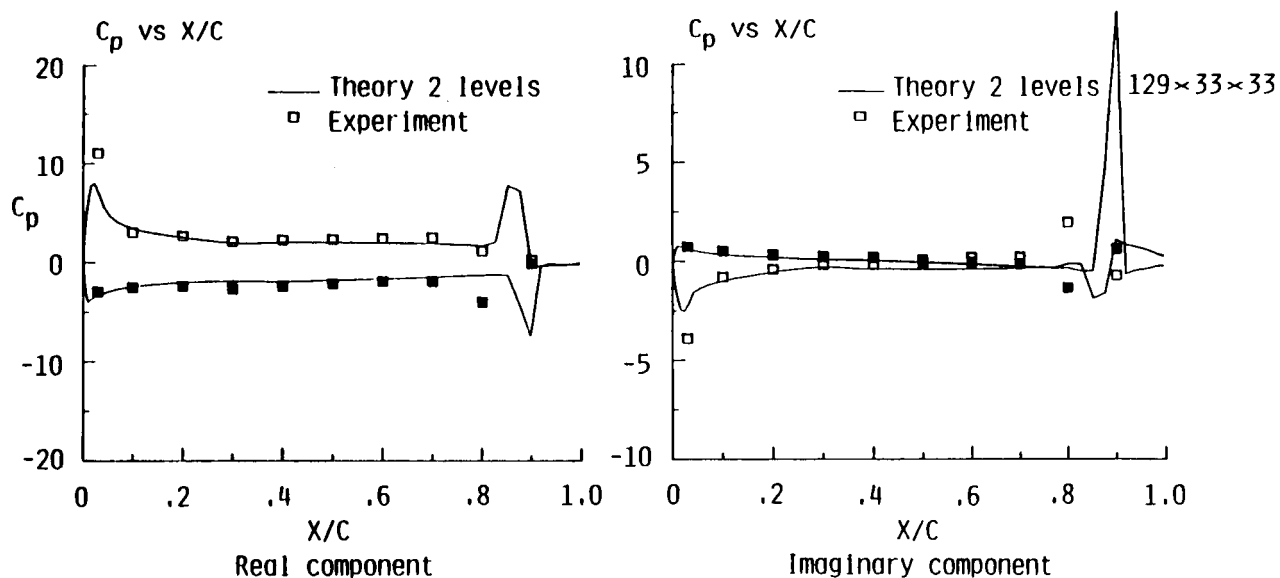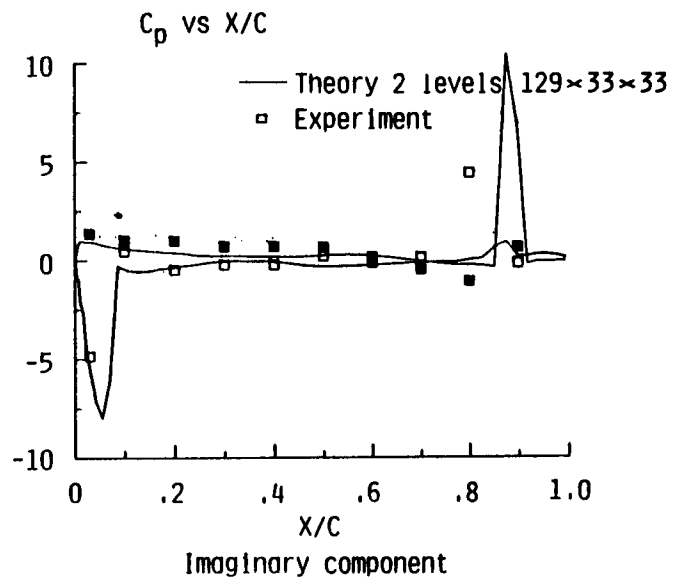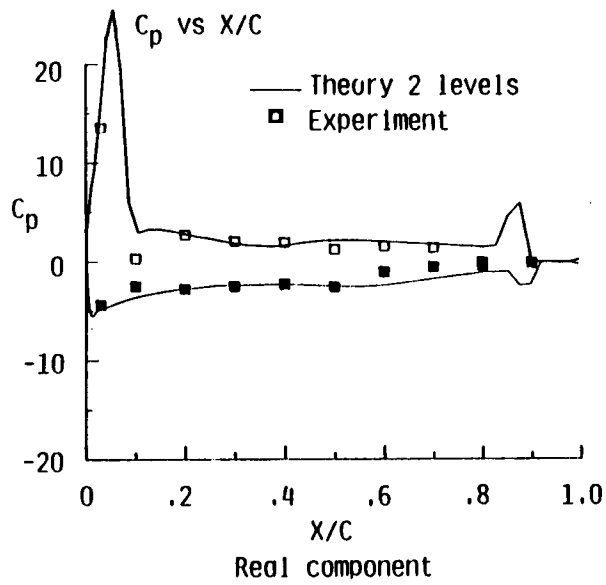
At each time step, several iterations of the algorithm may be carried out in order to eliminate factorization and linearization errors. These subiterations may be done using a multigrid method to accelerate the convergence at each time step. The benefits of the subiterations are observed to be generally offset by the extra computational work required at each time step.

ITERATIVE MULTIGRID ALGORITHM

$$M \, (\hat{Q}^{l+1} - \hat{Q}^l) = -\Delta t L(Q^l)$$

- Repeated iterations at each time step will eliminate factorization and linearization errors so larger time steps can be taken

- Use of multigrid method accelerates convergence

- Benefits of larger time step generally offset by extra computational work

- May be more beneficial for incomplete linearizations or with "frozen" flux Jacobians

CONCLUSIONS

- Van Leer method of flux vector splitting extended for use on dynamic grids

- Use of coarser grids result in substantial reduction of computer time with virtually no loss in accuracy

- Use of multigrid to eliminate factorization and linearization error only marginally beneficial

- Results compare favorably with experiment for two and three dimensional test cases

References

1. Van Leer, B.: Flux Vector Splitting for Euler Equations. Lecture Notes in Physics, Vol. 170, 1982, pp. 501-512.

2. Van Leer, B.: Towards the Ultimate Conservative Difference Scheme V., A Second Order Sequel to Gudonov's Method. Journal of Computational Physics, Vol. 32, 1979 pp. 101-136.

3. Anderson, W.K., Thomas, J.L., and Rumsey, C.L., Extension and Application of Flux-Vector-Splitting to Unsteady Calculations on Dynamic Meshes. AIAA 87-1152-CP, Presented at 8th Computational Fluid Dynamics Conference, June 9-11, Honolulu, Hawaii.

4. Roe, P.L.: Approximate Riemann Solvers, Parameter Vectors, and Difference Schemes. Journal of Computational Physics, Vol. 43, 1981 pp. 357-372.

5. Jesperson, D.C.: A Time-Accurate Multiple Grid Algorithm. AIAA 85-1493, July 1985.

UNSTEADY TRANSONIC FLOW

USING EULER EQUATIONS

Dave M. Belk
L. Bruce Simpson
Air Force Armament Laboratory
Eglin Air Force Base, Florida

Outline

An implicit, two-factor, split flux, finite volume Euler equations solution algorithm is applied to the time-accurate solution of transonic flow about an NACA0012 airfoil and a rectangular planform supercritical wing undergoing pitch oscillations. Accuracy for Courant numbers greater than one is analyzed. Freezing the flux Jacobians can result in significant savings for steady-state solutions; the accuracy of freezing flux Jacobians for unsteady results is investigated. The Euler algorithm results are compared with experimental results for an NACA 0012 and a rectangular planform supercritical wing (Figure 1).

- **ALGORITHM**

- **TIME ACCURACY FOR COURANT NUMBERS GREATER THAN ONE**

- **FREEZING FLUX JACOBIANS**

- **COMPARISON WITH EXPERIMENT**
  - **NACA0012**
  - **RECTANGULAR SUPERCRITICAL WING**

Figure 1

Three Dimensional Euler Equations

The Euler equations model inviscid flow with entropy and vorticity being generated by shocks. Many unsteady flows of practical interest require that viscous effects be included. One advantage of the Euler equations solution algorithm is that it is easily extended to include viscous effects.

The three-dimensional time-dependent Euler equations in conservation form are written in a general time-dependent boundary conforming curvilinear coordinate system. This time-dependent coordinate transformation provides for a dynamic grid that can follow the motion of the body (Figure 2). The details of this transformation are given in Reference 1.

$$\frac{\partial q}{\partial t} + \frac{\partial f}{\partial x} + \frac{\partial g}{\partial y} + \frac{\partial h}{\partial z} = 0$$

where

$$q = \begin{bmatrix} \rho, & \rho u, & \rho v, & \rho w, & e \end{bmatrix}^T$$

TIME DEPENDENT COORDINATE TRANSFORMATION

$$\xi = \xi(x, y, z, t) \qquad \tau = \tau(t)$$

$$\eta = \eta(x, y, z, t)$$

$$\zeta = \zeta(x, y, z, t)$$

$$\frac{\partial Q}{\partial \tau} + \frac{\partial F}{\partial \xi} + \frac{\partial G}{\partial \eta} + \frac{\partial H}{\partial \zeta} = 0$$

Figure 2

Algorithm

An implicit split flux finite volume solution algorithm for the Euler equations is obtained. Flux Jacobians with superscript L correspond to information propagating in the positive curvilinear coordinate direction, and flux Jacobians with superscript R correspond to information propagating in the negative curvilinear coordinate direction. The equation is then factored into two factors as discussed by Whitfield in Reference 2. The first equation of the two-pass scheme requires the solution of a sparse lower block triangular system by a simple forward substitution, while the second equation requires the solution of a sparse upper block triangular system by a simple backward substitution.

This algorithm is first-order accurate in time and second order accurate in space. A simple modification to use three point backward time differencing will result in second order time-accuracy (Figure 3).

- **FINITE VOLUME**

- **FLUX SPLIT**

- **IMPLICIT**

$$[\ I + \Delta \tau \ (\ \delta \xi^{i} \ A^{L \cdot} + \delta \xi^{i} \ A^{R \cdot} + \delta \eta^{i} \ B^{L \cdot} + \delta \eta^{i} \ B^{R \cdot} + \delta \zeta^{i} \ C^{L \cdot} + \delta \zeta^{i} \ C^{R \cdot}) \ ] \ \Delta Q^{n} = - \Delta \tau R^{n}$$

WHERE

$$R^{n} \equiv \delta \xi^{e} \ F^{n} + \delta \eta^{e} \ G^{n} + \delta \zeta^{e} \ H^{n}$$

- **TWO-PASS**

$$[\ I + \Delta \tau \ (\ \delta \xi^{i} \ A^{L \cdot} + \delta \eta^{i} \ B^{L \cdot} + \delta \zeta^{i} \ C^{L \cdot}) \ ] \ X^{n} = - \Delta \tau R^{n}$$

$$[\ I + \Delta \tau \ (\ \delta \xi^{i} \ A^{R \cdot} + \delta \eta^{i} \ B^{R \cdot} + \delta \zeta^{i} \ C^{R \cdot}) \ ] \ \Delta Q^{n} = X^{n}$$

Figure 3

NACA0012   221 x 20   'C' Grid

All of the Euler computations for the NACA0012 airfoil used the 221 x 20 'C' algebraic grid shown below. The grid was generated using Joe Thompson's grid generation code (Reference 3). See Figure 4.
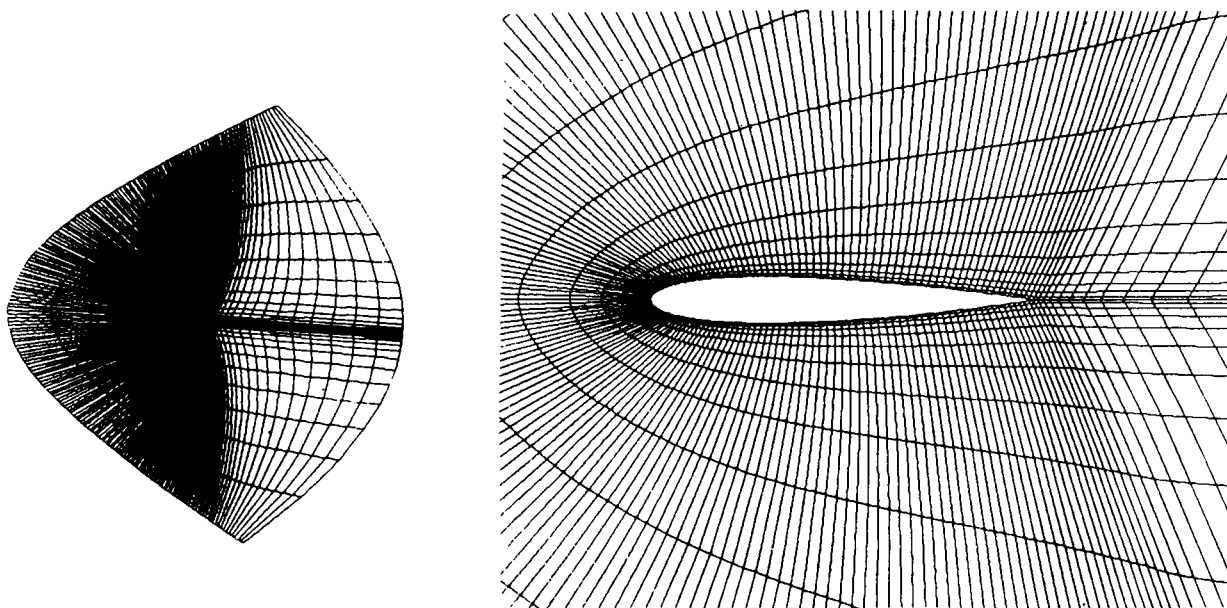
NACA0012 221 x 20 'C' Grid

Figure 4

NACA0012 Lift Coefficients

Calculations were made for a NACA0012 airfoil at Mach = 0.755 oscillating in pitch about the 1/4 chord point with a reduced frequency of k = (ωc/V) = 0.1628. The airfoil had a mean angle of attack = 0.016 degrees and an unsteady alpha = 2.51 degrees. Steady state solutions were obtained at the mean conditions prior to an abrupt start of the oscillatory motion. The calculations were performed for four complete cycles of motion. The figure below shows lift coefficient vs time for three different time step sizes. DTMIN = 0.01 gave 5000 time steps per cycle of motion and corresponds to a maximum Courant number of 10. DTMIN = 0.10 was 500 time steps per cycle of motion and corresponds to a maximum Courant number of 100. DTMIN = 0.20 was 250 time steps per cycle of motion and corresponds to a maximum Courant number of 200. Lift coefficients were only slightly different for the various time step sizes (Figure 5).

M=0.755, k=0.1628, MEAN ALPHA=0.016, UNSTEADY ALPHA=2.51
221X20 ALGEBRAIC 'C' GRID
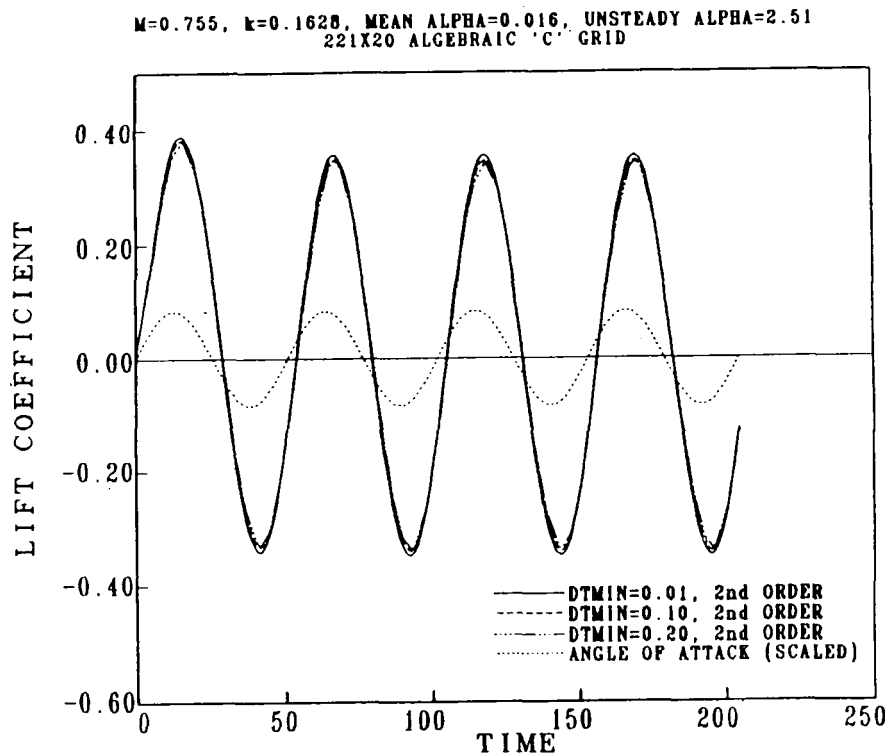
Figure 5

NACA0012 Unsteady Pressure Distributions
340° of Oscillatory Motion

After 340° of oscillatory motion, the angle of attack is increasing through
-0.84 degrees. A shock has formed on the lower surface near the 44% chord location.
At this point in the motion, the shock is nearly stationary and of maximum strength.
The figure below shows the coefficient of pressure distribution along the airfoil.
Calculations were done using both first and second order time-accurate differencing
and various time step sizes. The results show that all the methods are nearly
equivalent for this case (Figure 6).

M=0.755, Unsteady Alpha=2.51, Mean Alpha=0.016, k=0.1628, 221X20 'C' Grid
Two Pass Algorithm
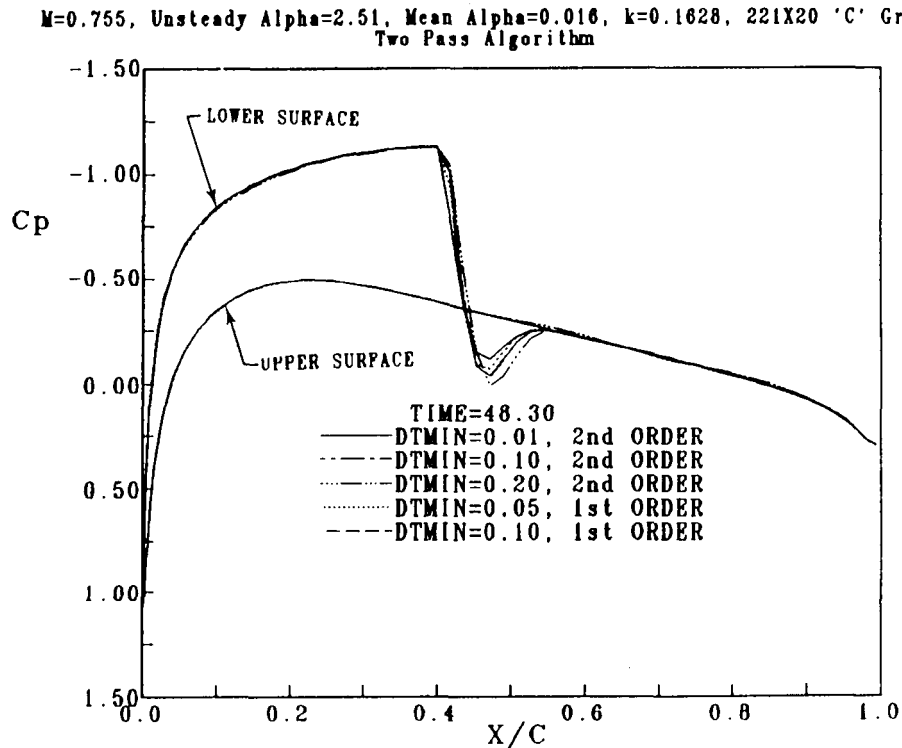
340° OF OSCILLATORY MOTION,   INCREASING THROUGH -0.84°

Figure 6

NACA0012 Unsteady Pressure Distributions
25° of Oscillatory Motion

Shortly after the next cycle of motion begins, the shock on the lower surface starts to collapse and move forward. As the angle of attack increases through 1.09°, the shock speed becomes maximum. The figure below shows coefficient of pressure along the airfoil for first and second order differencing and the same time step sizes as in Figure 5. Very little difference is observed between first and second order solutions, but considerable difference in the shock location is noted for different time step sizes. However, as noted previously, the difference in lift coefficient is relatively small (Figure 7).

M=0.755, Unsteady Alpha=2.51, Mean Alpha=0.016, k=0.1628, 221X20 'C' Grid
Two Pass Algorithm
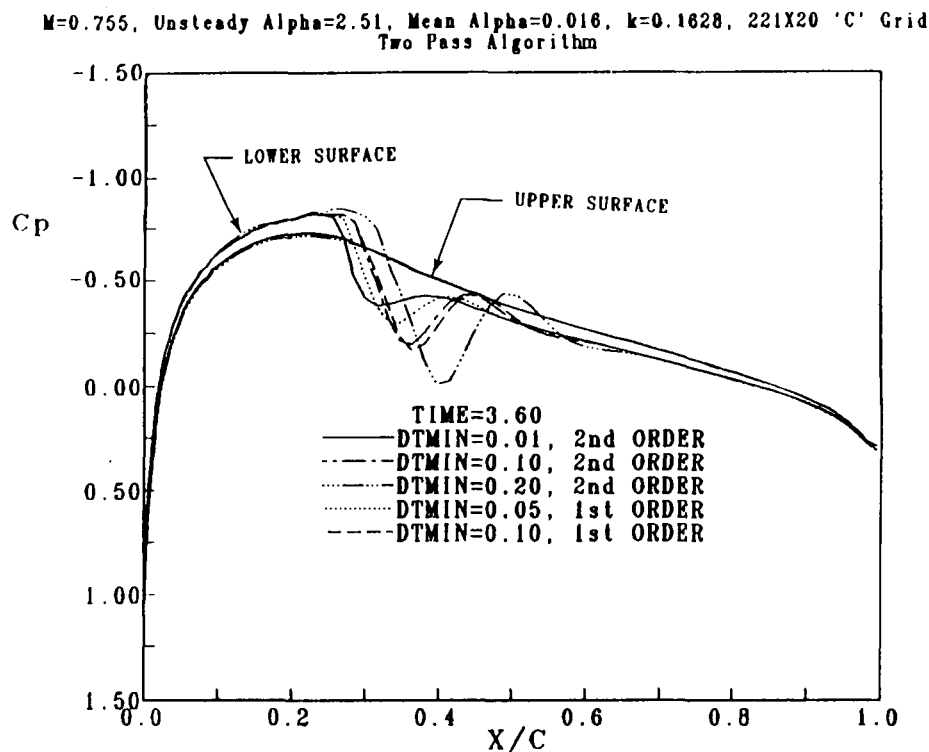
25° OF OSCILLATORY MOTION, INCREASING THROUGH 1.09°

Figure 7

222

Shock Location

Defining the shock location as the axial location where the pressure coefficient equals the critical pressure (for Mach = 0.755, $C_p^* = -0.5143$), the figure below shows shock location given at different time step sizes. The figure shows that the shock location appears asymptotic to a value as the time step decreases. This indicates that reduction of the time step size below 0.01 should not be expected to change the shock location appreciably (Figure 8).
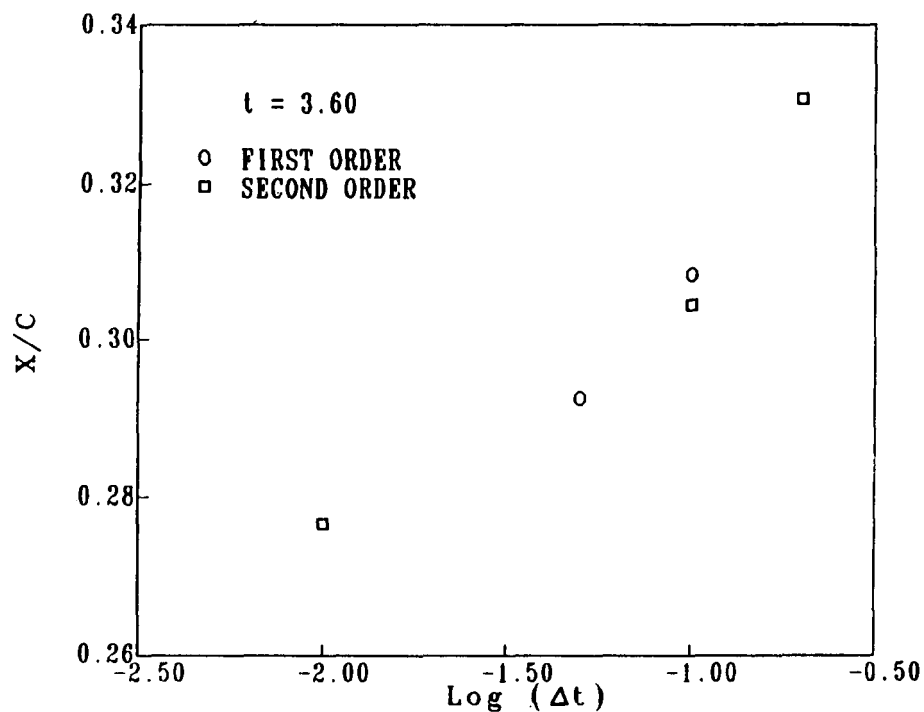
SHOCK LOCATIONS GIVEN BY DIFFERENT TIME STEP SIZES

Figure 8

Freezing the Flux Jacobians for Steady State Conditions

The implicit equations to be solved have the flux Jacobians as coefficients. Since the flux Jacobians, A^L, A^R, B^L, etc., are functions of the current values of Q, they should be updated at each time step. However, D. L. Whitfield has shown steady calculations in which he did not update (froze) the Jacobians and at convergence obtained identical results with calculations updating the Jacobians each time step. The table below shows the obvious computational savings by not doing the extra calculations each time step (Figure 9).

$$A^L = \frac{\partial F^L(Q)}{\partial Q}, \quad A^R = \frac{\partial F^R(Q)}{\partial Q}, \quad B^L = \frac{\partial G^L(Q)}{\partial Q}, \quad \cdots$$

	CYCLES	CPU SEC	MWD	RESID	$\dfrac{\text{CPU SEC}}{\text{POINT} \cdot \text{CYCLE}}$
IMPLICIT UPDATING JACOBIANS	250	3492	3.26	10^{-4}	$7.8 \cdot 10^{-5}$
IMPLICIT FREEZING JACOBIANS	250	1527	3.26	10^{-4}	$3.4 \cdot 10^{-5}$

(8 BLOCK FINNED BODY CALCULATION)

Figure 9

Freezing the Flux Jacobians for Unsteady Calculations

The effect of freezing the Jacobians for unsteady calculations were studied using the oscillatory NACA0012 as the test case. The conditions tested were the same as previously shown. The table below again shows the obvious savings from updating every 10th step (which equates to 3.6° of oscillatory motion) and for never updating the Jacobians. The case listed as never updated used Jacobians from the steady state condition just prior to start of motion. Other cases tried were Jacobians from the freestream starting conditions, updating every 25th step and updating every 50th step. Each of these resulted in stability problems (Figure 10).

JACOBIAN UPDATE FREQUENCY	STEPS	CPU SEC	CPU SEC POINT STEPS	PERCENT
Every Step	4510	1716	8.61×10^{-5}	100%
Every 10th Step	5400	1382	5.79×10^{-5}	67%
Never Updated	5400	1311	5.49×10^{-5}	64%

NACA0012 PITCHING ABOUT 1/4 CHORD

Figure 10

Effect of Frozen Jacobians on Lift Coefficient

Lift coefficient vs time for each of the two frozen Jacobian cases which proved to be stable are compared with the solution from updating every time step. All three solutions used 1st order time-accurate algorithm and a time step size of 0.05. One cannot discern a difference in the three curves shown below (Figure 11).

M=0.755, Unsteady Alpha=2.51, Mean Alpha=0.016, k=0.1628, DT=0.05

Figure 11

NACA0012 Unsteady Pressure Distributions
25 Degrees

A plot of pressure coefficient along the body for the three cases at 25 degrees of oscillatory motion is shown below in Figure 12. This is the same flow condition described earlier, when the angle of attack is increasing through 1.09 degrees and the shock speed is near a maximum as the shock on the lower surface collapses. Very little difference is noted in the three curves with the only perceivable difference being in the shock location similar to the results shown in Figure 7.

M=0.755, Unsteady Alpha=2.51, Mean Alpha=0.016, k=0.1628, 221X20 'C' Grid
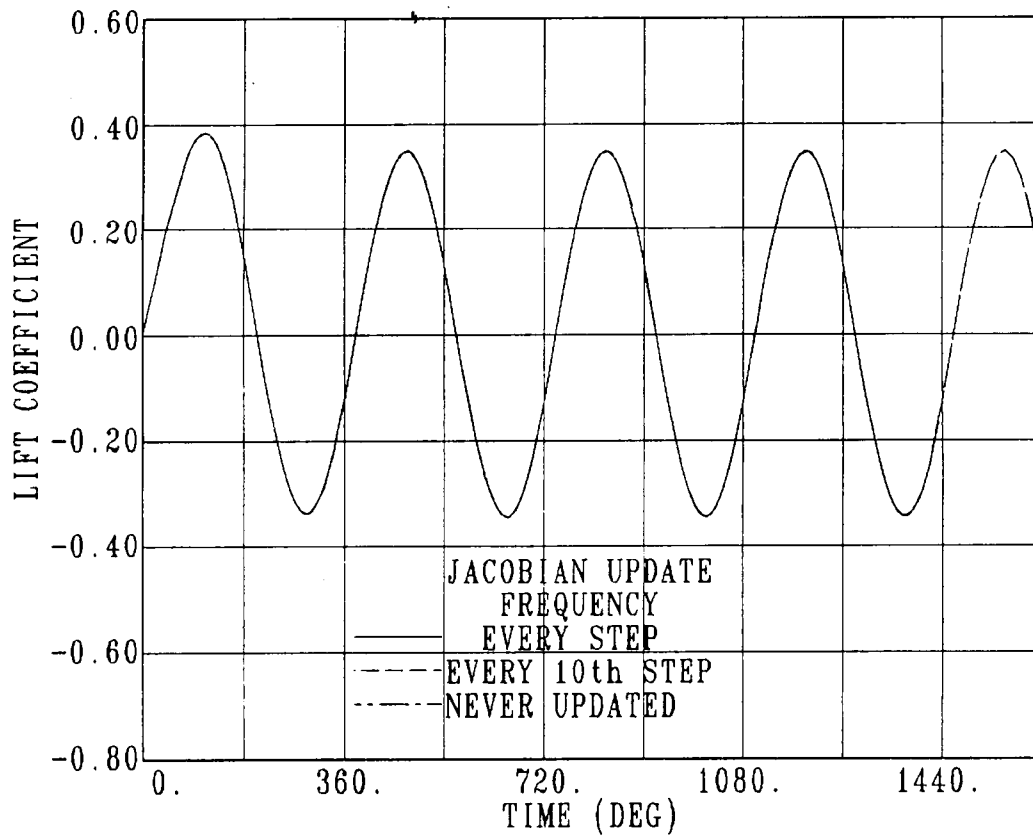Two Pass Algorithm, DT=0.05, 1st-Order in Time
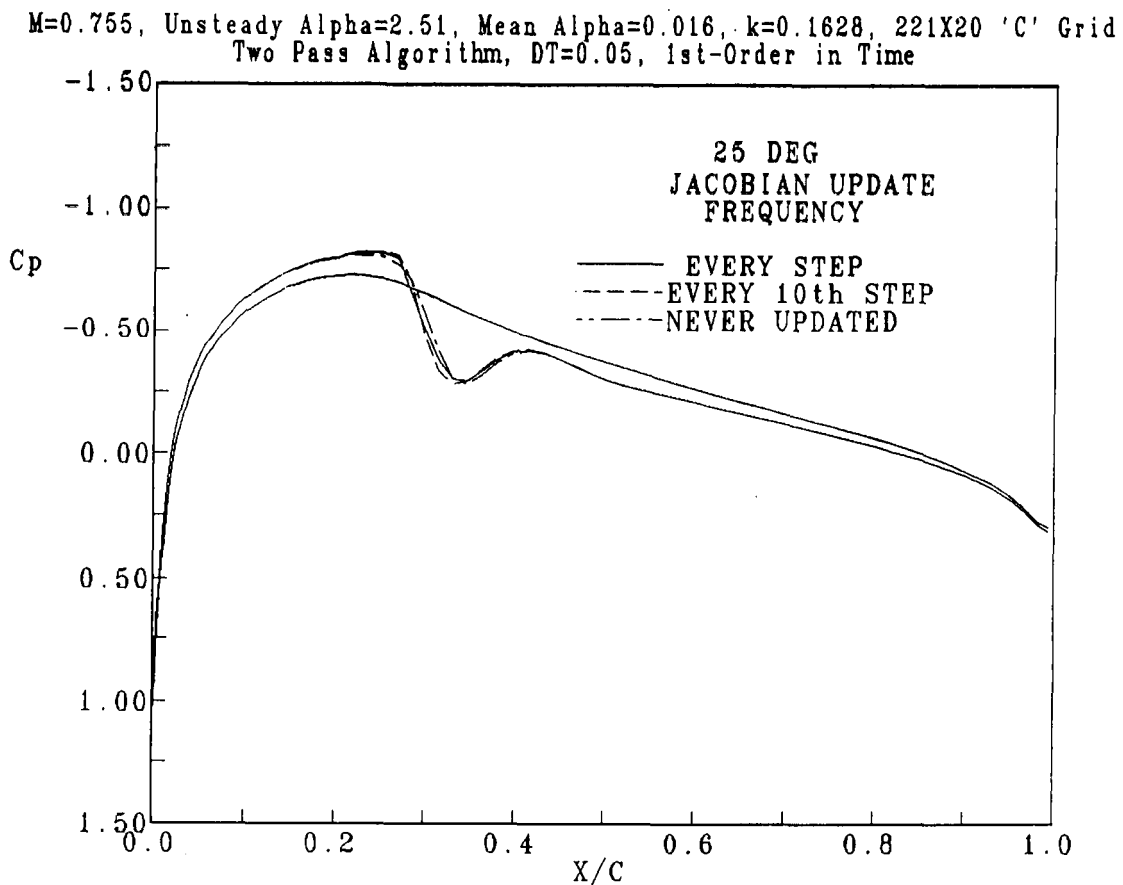
Figure 12

NACA0012 Unsteady Pressure Distributions
70 Degrees

A plot of pressure coefficient along the body for the three cases at 70 degrees of oscillatory motion is shown below. This condition is when angle of attack is increasing through 2.37 degrees and the shock on the upper surface is strengthening and moving downstream. Again, the three solutions are identical except at the shock location. Note that the never updated Jacobian shows a slight ringing action near the shock (Figure 13).

M=0.755, Unsteady Alpha=2.51, Mean Alpha=0.016, k=0.1628, 221X20 'C' Grid
Two Pass Algorithm, DT=0.05, 1st-Order in Time

Figure 13

A comparison of calculated lift coefficients with the experimental results of Landon (Reference 4) is given in Figure 14. The expe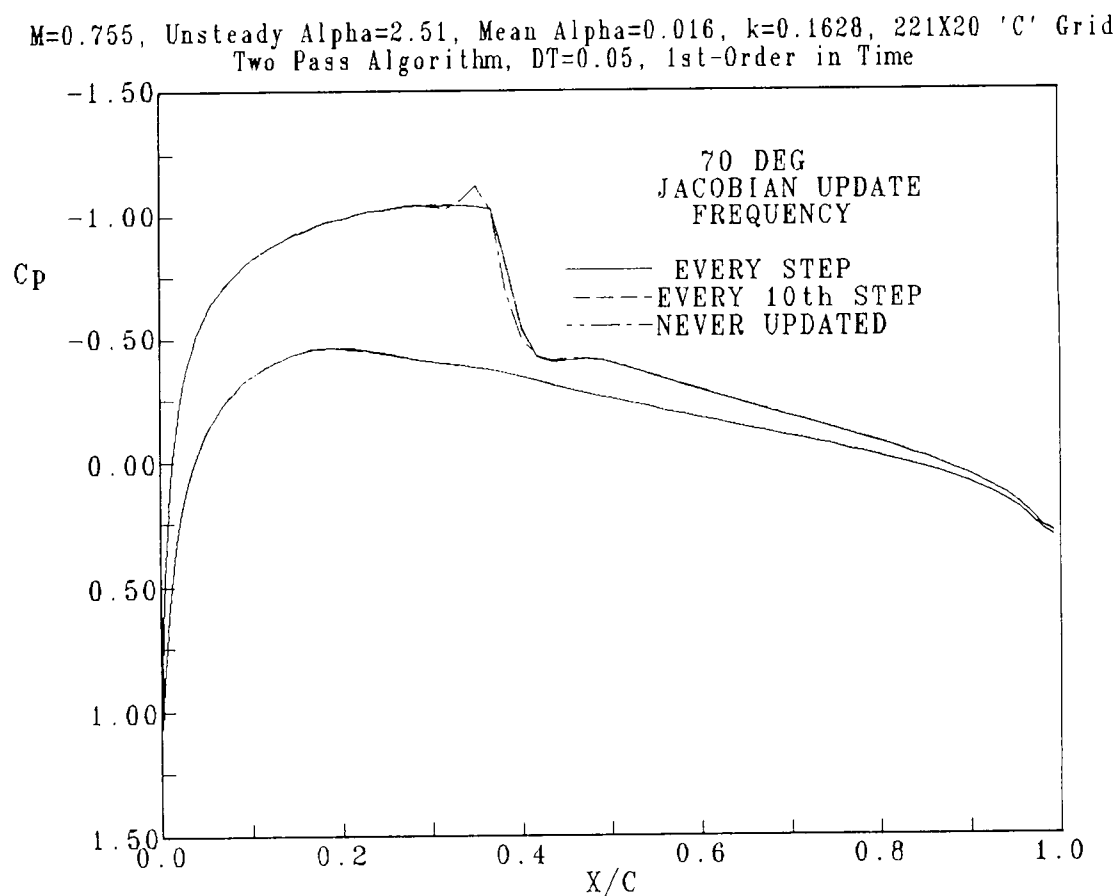rimental results were given for one cycle of motion and are duplicated through four cycles on the figure to compare to the calculations. Examination of experimental lift coefficient reveals a bias towards positive lift not consistent with the small mean angle of attack reported for the symmetric airfoil. A correction to the mean angle of attack was calculated to account for this bias. The following figures show calculations using both the nominal angle of attack of 0.016 degrees and the 'corrected' angle of attack of 0.375 degrees. The freestream Mach is 0.755, reduced frequency is 0.1628, and the unsteady angle of attack amplitude is 2.51 degrees.

M=0.755, k=0.1628, UNSTEADY ALPHA=2.51
221X20 ALGEBRAIC 'C' GRID
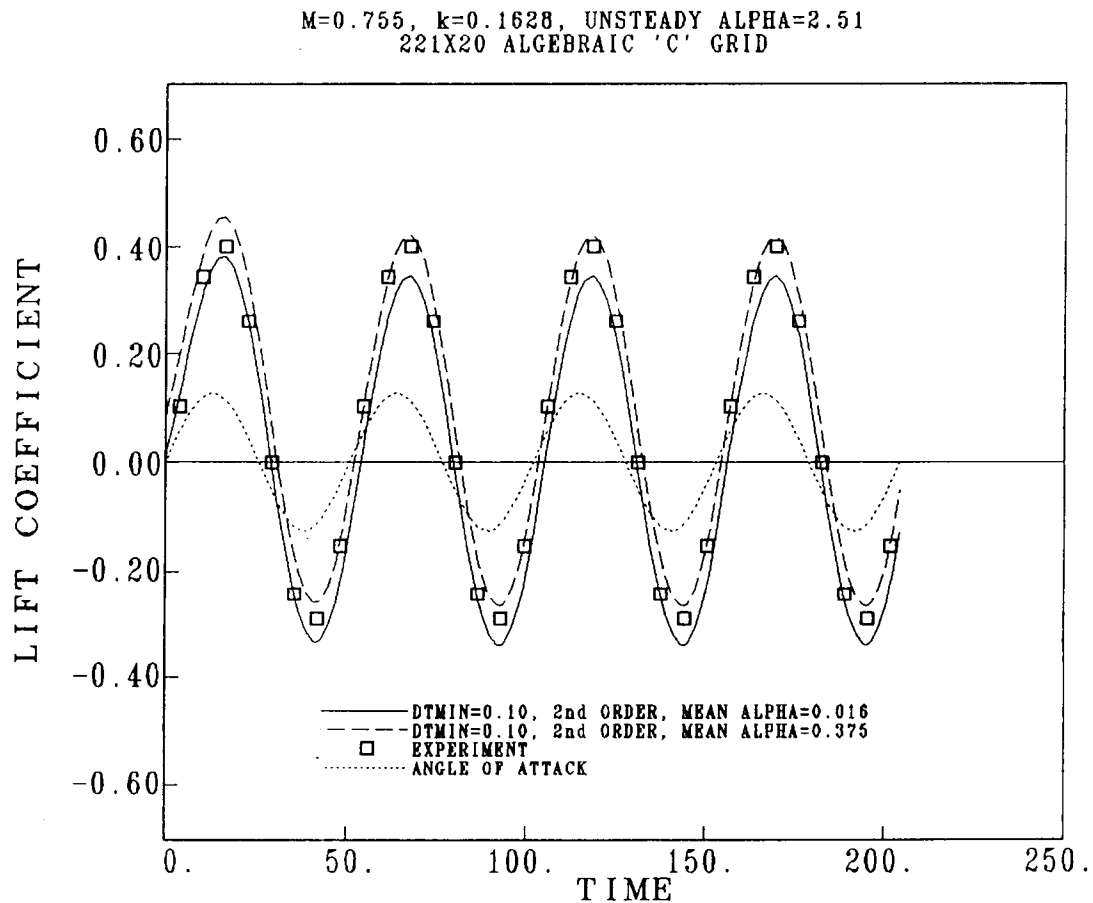

Figure 14

Moment coefficients do not compare with experiment as well as lift, particularly for the negative moments. The 'corrected' mean alpha of 0.375 did not improve the comparison (Figure 15).

M=0.755, k=0.1628, MEAN ALPHA=0.016, UNSTEADY ALPHA=2.51
221X20 ALGEBRAIC 'C' GRID
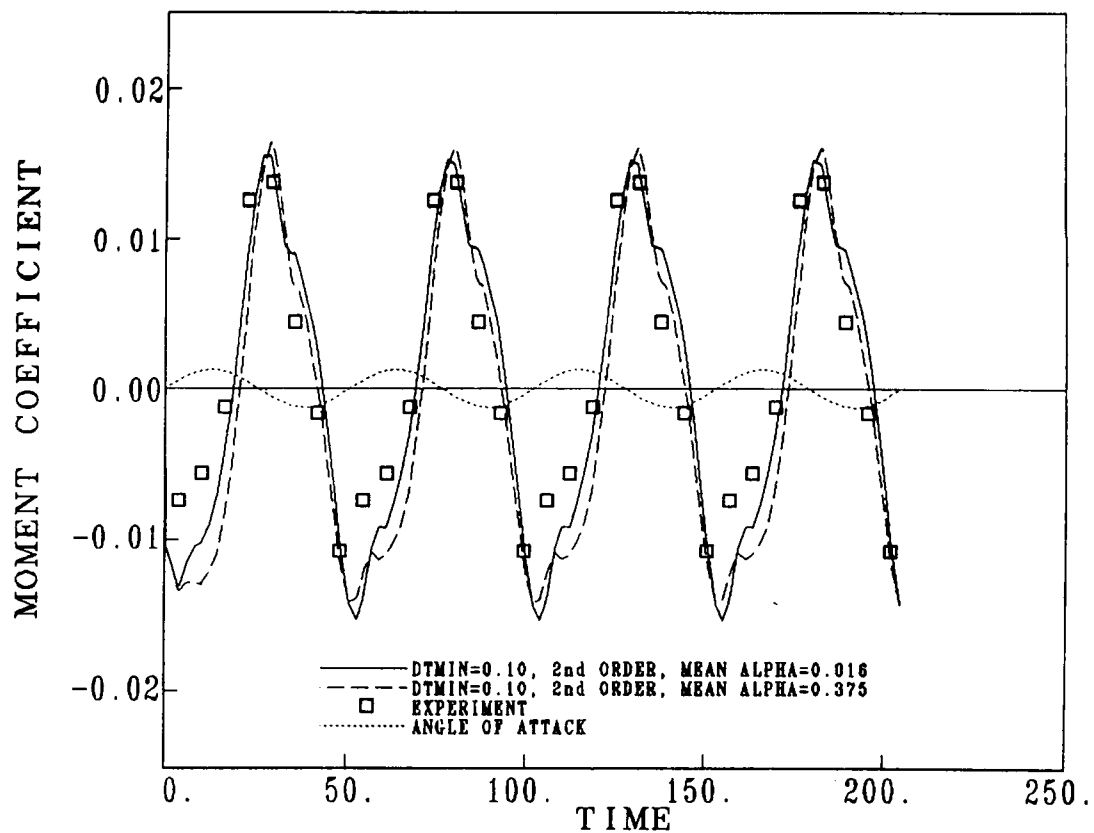
Figure 15

NACA0012 Unsteady Pressure Distributions

The comparison of calculated and experimental pressure distributions is shown in Figures 16 through 21.

M=0.755, Unsteady Alpha=2.51, Mean Alpha=0.016, k=0.1628, 221X20 'C' Grid

TIME=3.59737

EXPERIMENT
□ UPPER SURFACE
◇ LOWER SURFACE
——— DTMIN=0.10, 2nd ORDER
------ DTMIN=0.10, 2nd ORDER, MEAN ALPHA=0.375

Figure 16

M=0.755, Unsteady Alpha=2.51, Mean Alpha=0.016, k=0.1628, 221X20 'C' Grid

TIME=9.98737

EXPERIMENT
□ UPPER SURFACE
◇ LOWER SURFACE
——— DTMIN=0.10, 2nd ORDER
------ DTMIN=0.10, 2nd ORDER, MEAN ALPHA=0.375

Figure 17

231

NACA0012 UNSTEADY PRESSURE DISTRIBUTIONS
M=0.755, Unsteady Alpha=2.51, Mean Alpha=0.016, k=0.1628, 221X20 'C' Grid

TIME=16.345

EXPERIMENT
UPPER SURFACE
LOWER SURFACE
DTMIN=0.10, 2nd ORDER
DTMIN=0.10, 2nd ORDER, MEAN ALPHA=0.375

Figure 18

NACA0012 UNSTEADY PRESSURE DISTRIBUTIONS
M=0.755, Unsteady Alpha=2.51, Mean Alpha=0.016, k=0.1628, 221X20 'C' Grid

TIME=22.735

EXPERIMENT
UPPER SURFACE
LOWER SURFACE
DTMIN=0.10, 2nd ORDER
DTMIN=0.10, 2nd ORDER, MEAN ALPHA=0.375

Figure 19

NACA0012 UNSTEADY PRESSURE DISTRIBUTIONS
M=0.755, Unsteady Alpha=2.51, Mean Alpha=0.016, k=0.1628, 221X20 'C' Grid
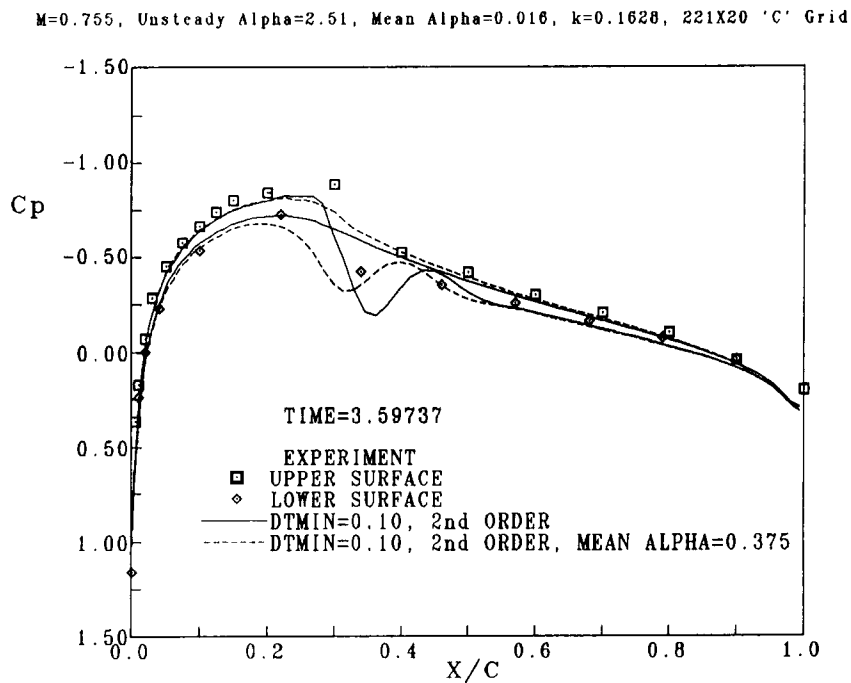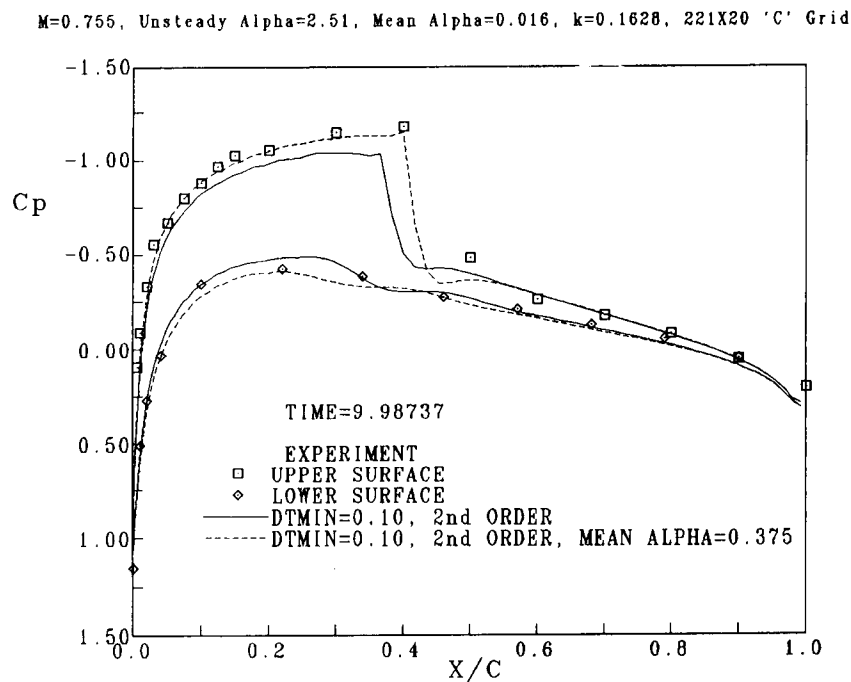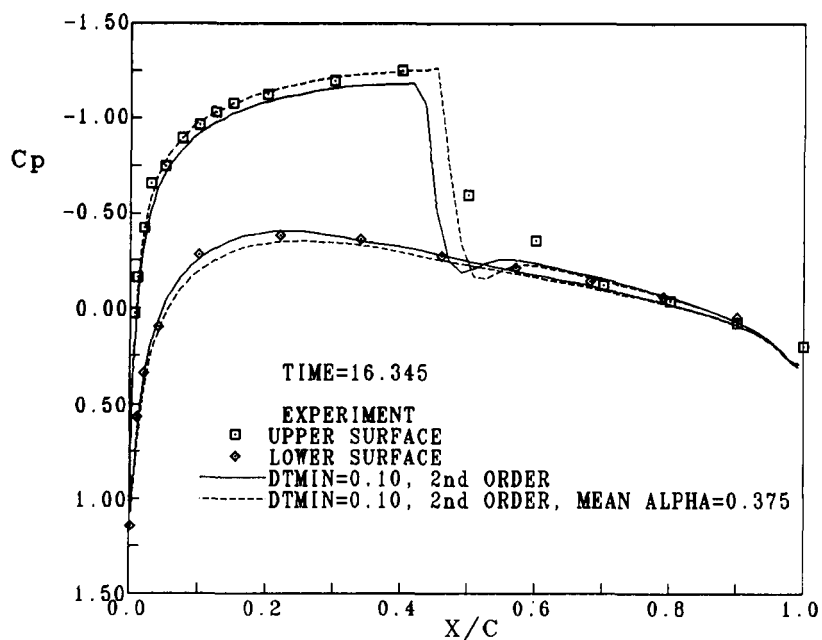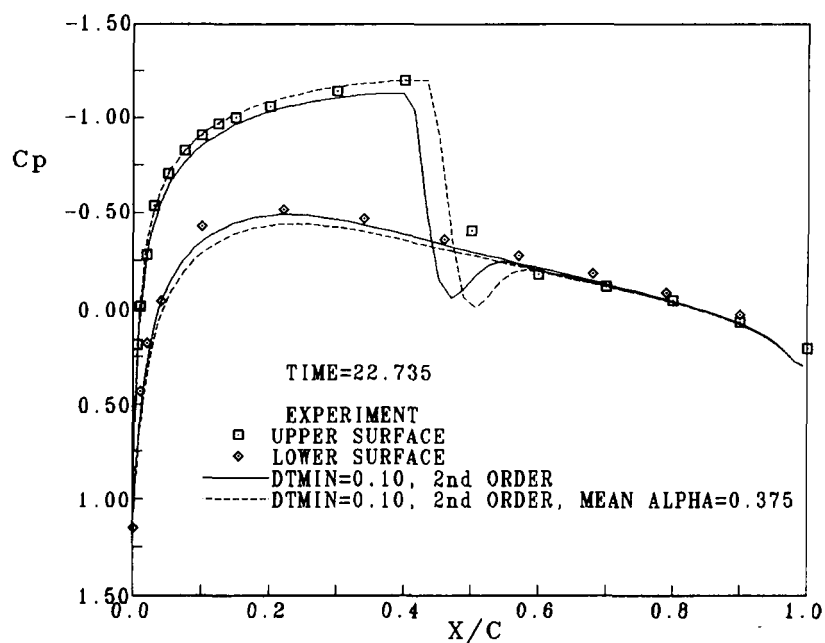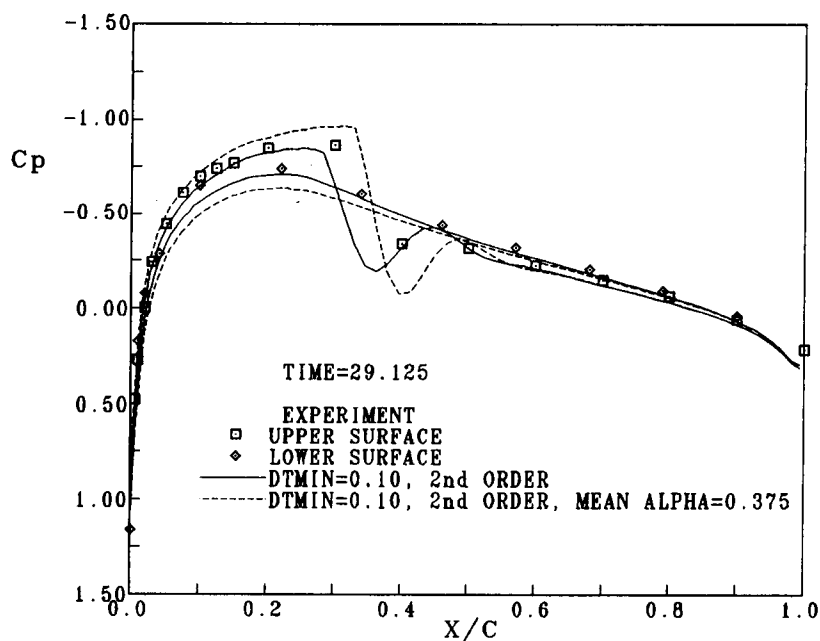

Figure 20

NACA0012 UNSTEADY PRESSURE DISTRIBUTIONS
M=0.755, Unsteady Alpha=2.51, Mean Alpha=0.016, k=0.1628, 221X20 'C' Grid
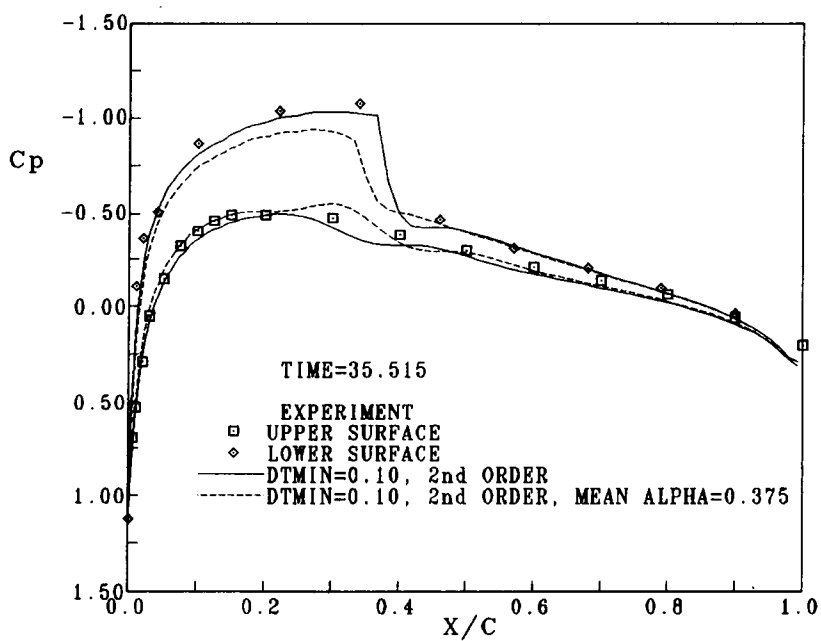

Figure 21

Rectangular Supercritical Wing

Euler calculations were performed to compare to the experimental results of Ricketts, et al (Reference 5). Calculations at a higher reduced frequency, k = 0.714, compare similarly to those presented here, k = 0.358. At higher Mach numbers, however, the comparison was much poorer due to mislocation of the shock by the inviscid Euler code. The time step size used resulted in 360 time steps per cycle of motion for the k = 0.358 case. Maximum Courant numbers near 500 occurred in the vicinity of the wing tip for this time step size. Fourier analysis of the third cycle of oscillation yielded the magnitude and phase of the unsteady pressures shown on subsequent figures. The three cycles of motion used 6357 seconds on a CRAY X-MP (Figure 22).

- EXPERIMENT BY RICKETTS, SANDFORD, WATSON, AND SEIDEL NASA TM 85765, AUG 84

- RECTANGULAR PLANFORM, ASPECT RATIO 4 (FULL SPAN)

- 12% THICK SUPERCRITICAL AIRFOIL

- OSCILLATORY PITCH ABOUT 46% CHORD

- CONDITIONS
  - MACH 0.70
  - 4 DEGREES MEAN ALPHA
  - ONE DEGREE UNSTEADY ALPHA
  - REDUCED FREQUENCY = 0.358 = $\frac{c\omega}{V_\infty}$

Figure 22

The wing calculations were carried out on a grid broken into four blocks to obtain the solution using only 2.6 million words of memory. The entire grid has dimensions 101x25x27. Block I contains all points below the wing, Block II contains points wrapping around the wing tip, Block III contains all points above the wing, and Block IV contains all points downstream of the wing (Figure 23). The method used to obtain time-accurate solutions on blocked grids is described in Reference 6. Motion of the wing is modelled by pitching the entire grid containing the wing as a rigid body using the time-dependent coordinate transformation described earlier.
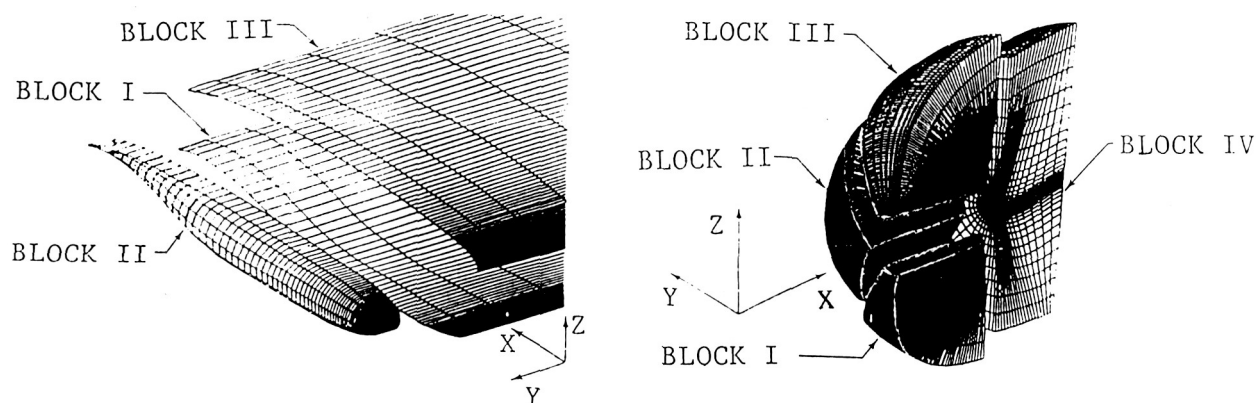
Figure 23

Rectangular Wing Pressures
at 60% Semispan

Steady pressures compare fairly well. There is a slight overshoot at the
leading edge and the captured shock is aft of the experimental location (Figure 24).
Unsteady pressure magnitude compares well except that the shock spike is downstream
of the experimental location. Unsteady pressure phase calculations show excellent
agreement up to the highly cambered trailing edge where the experiment and
calculation differ slightly (Figures 25 and 26).
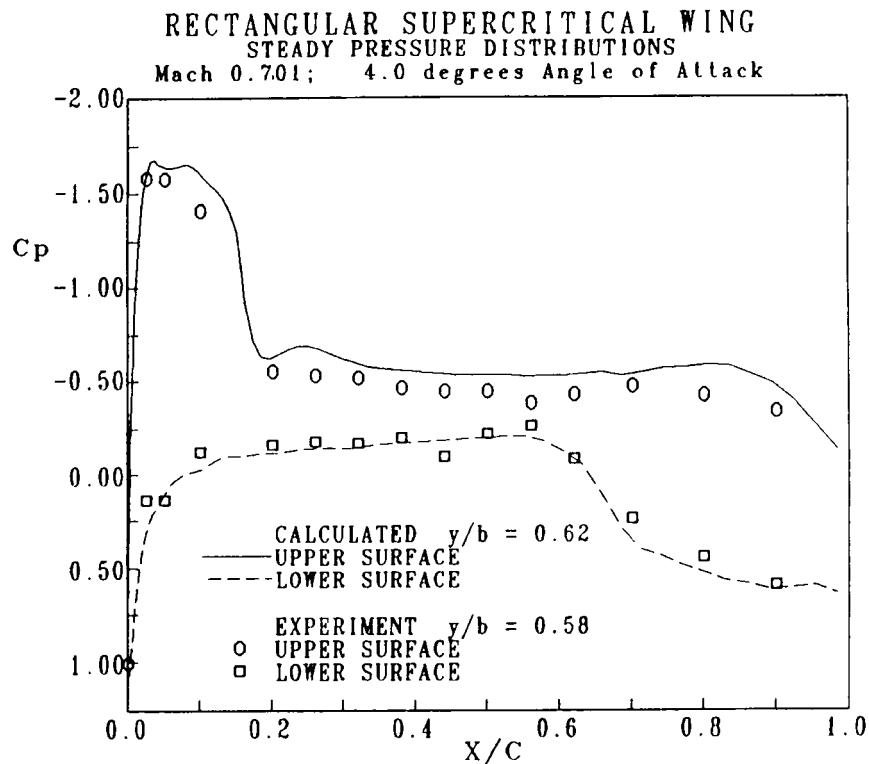
Steady Pressure at 60% Semispan

Figure 24

RECTANGULAR SUPERCRITICAL WING
UNSTEADY PRESSURE DISTRIBUTIONS
Mach 0.7; 4 deg Steady Alpha; 1 deg Unsteady Alpha

MAGNITUDE AT 60% SEMISPAN

Figure 25

RECTANGULAR SUPERCRITICAL WING
UNSTEADY PRESSURE DISTRIBUTIONS
Mach 0.7; 4 deg Steady Alpha; 1 deg Unsteady Alpha

PHASE AT 60% SEMISPAN

Figure 26

237
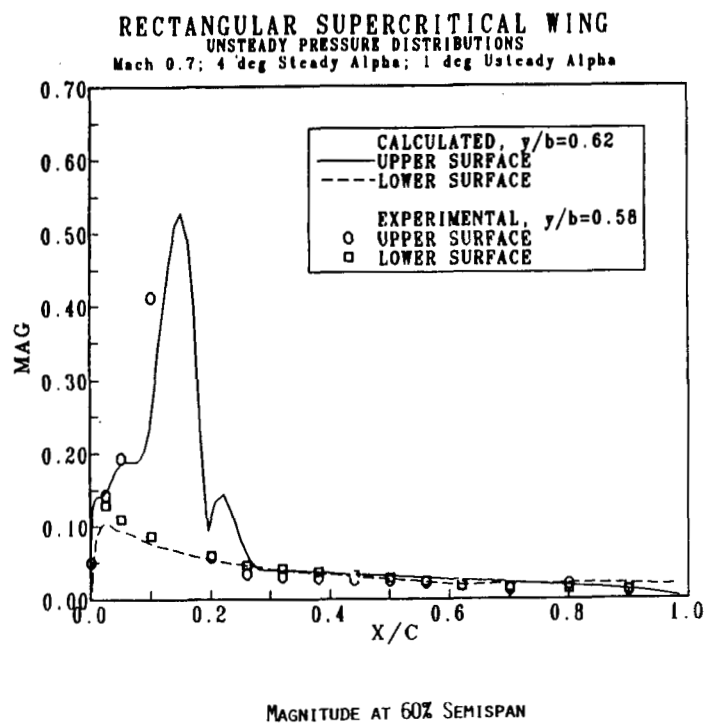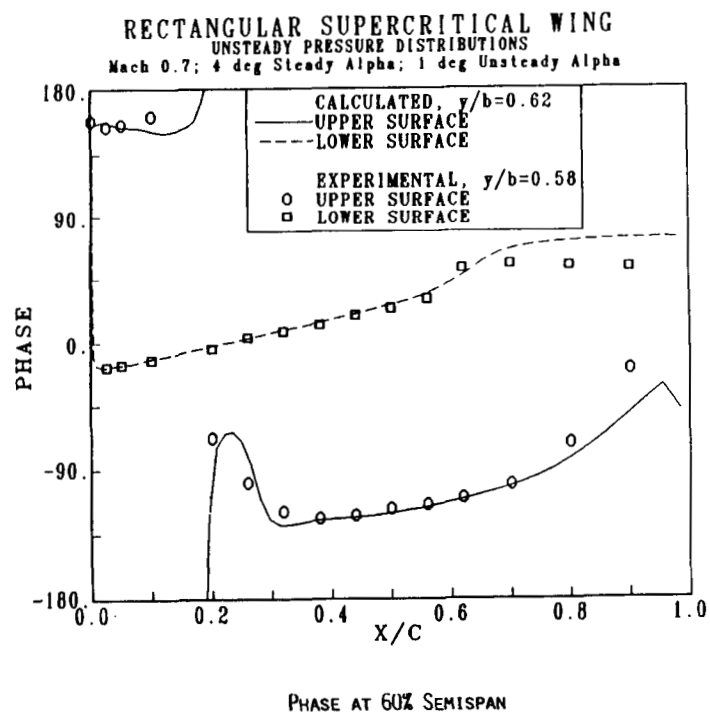
Rectangular Wing Pressures
at 95% Semispan

Steady pressures shown in Figure 27 underexpand slightly in the leading edge region but follow the experimental results very closely thereafter. The peak in unsteady pressure magnitude shown in Figure 28 near the leading edge is likewise calculated to be smaller than experiment. Phase results shown in Figure 29 are in excellent agreement.

RECTANGULAR SUPERCRITICAL WING
STEADY PRESSURE DISTRIBUTIONS
Mach 0.701; 4.0 degrees Angle of Attack
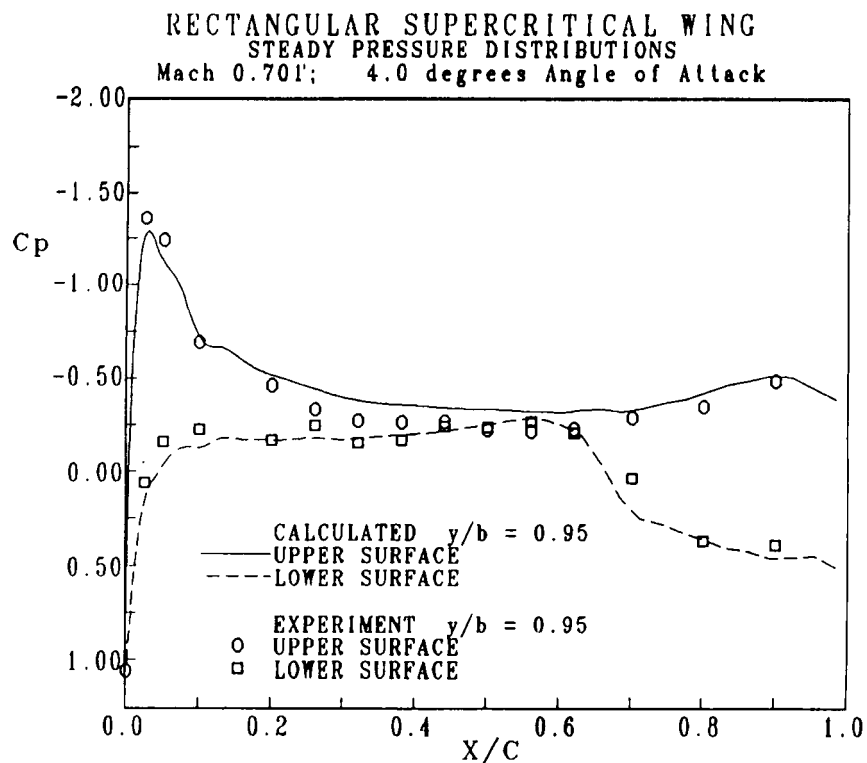
STEADY PRESSURE AT 95% SEMISPAN

Figure 27

RECTANGULAR SUPERCRITICAL WING
UNSTEADY PRESSURE DISTRIBUTIONS
Mach 0.7; 4 deg Steady Alpha; 1 deg Usteady Alpha

MAGNITUDE AT 95% SEMISPAN

Figure 28

RECTANGULAR SUPERCRITICAL WING
UNSTEADY PRESSURE DISTRIBUTIONS
Mach 0.7; 4 deg Steady Alpha; 1 deg Unsteady Alpha

PHASE AT 95% SEMISPAN

Figure 29

CONCLUSIONS

- TIME-ACCURACY CAN BE OBTAINED AT
  COURANT NUMBERS MUCH GREATER THAN ONE

- FOR THE CASE PRESENTED, FREEZING FLUX
  JACOBIANS HAD LITTLE EFFECT ON TIME-ACCURACY

- EULER CALCULATIONS COMPARE WELL WITH NACA0012
  AND SUPERCRITICAL WING EXPERIMENT

- VISCOSITY REQUIRED TO ACCURATELY MODEL
  SUPERCRITICAL WING

Figure 30

List of References

1. Belk, D.M., "Unsteady Three-Dimensional Euler Equations on Dynamic Blocked Grids," Dissertation, Mississippi State University, August 1986, available as AFATL-TR-86-74, October 1986.
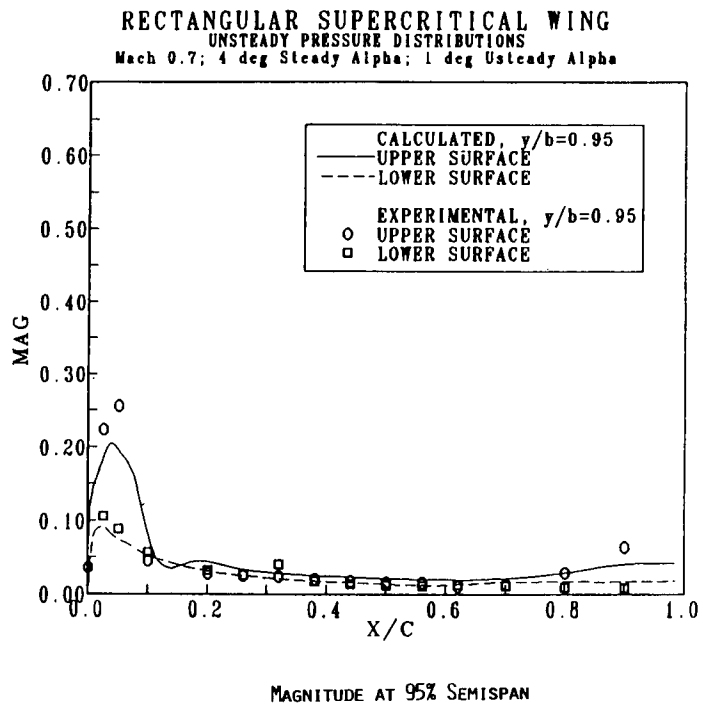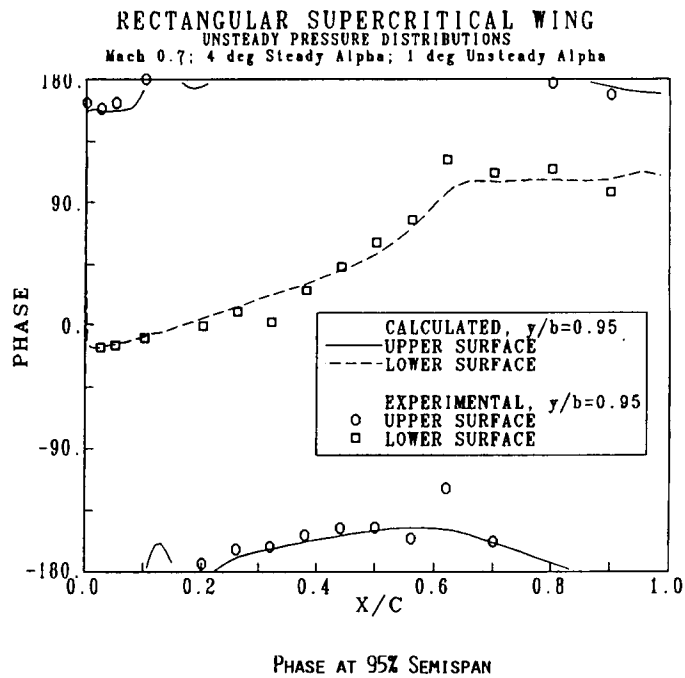
2. Whitfield, D.L., "Implicit Upward Finite Volume Scheme for the Three-Dimensional Euler Equations," MSSU-EIRS-ASE-85-1.

3. Thompson, J.F., "A Composite Grid Generation Code for General Three-Dimensional Regions," AIAA Paper 87-0275, January 1987.

4. Landon, R.H., "NACA0012. Oscillatory and Transient Pitching," Compendium of Unsteady Aerodynamic Measurements, AGARD-R-702, August 1982.

5. Ricketts, R.H., Sandford, M.C., Watson, J.J., and Seidel, D.A., "Subsonic and Transonic Unsteady- and Steady-Pressure Measurements on a Rectangular Supercritical Wing Oscillated in Pitch," NASATM85765, August 1984.

6. Belk, D.M. and Whitfield, D.L., "Time-Accurate Euler Equations Solutions on Dynamic Blocked Grids," AIAA-87-1127-CP, AIAA 8th Computational Fluid Dynamics Conference, Honolulu, Hawaii, June 9-11, 1987.

AGARD STANDARD AEROELASTIC CONFIGURATIONS
FOR DYNAMIC RESPONSE

E. Carson Yates, Jr.
NASA Langley Research Center
Hampton, Virginia

GUIDELINES FOR PRELIMINARY ASSESSMENT

Since emphasis is on the transonic speed range, special importance is placed on configurations for which available data are sufficient to define accurately a transonic flutter boundary. Only configurations with clean, smooth surfaces are considered suitable. Segmented models or models with surface-slope discontinuities (e.g., beveled flat plate) are inappropriate. Excluded also, in general, are configurations and data sets that involve behavior that is uncertain or not well understood, uncertain model properties, or known sensitivities to small variations in model properties. These may represent challenging research opportunities but do not seem appropriate as standard configurations.

- Emphasis on transonic speed range

- Configurations with clean, smooth surfaces

  - Isolated surfaces now

    - Two- and three-dimensional
    - With or without control-surface deflections
    - Conventional or supercritical airfoils

- Well-defined configurations/data sets

  - Geometrical properties
  - Structural properties
  - Flow properties

- Subcritical-response data as well as flutter data

- Exclude:

  - Complicated shapes and flow

  - Configurations/tests likely to involve

    - Flow separation
    - Uncertain model properties
    - Uncertain behavior
    - Sensitivity to variations in model properties

RESPONSE TO SURVEY

Several years ago, the AGARD Structures and Materials Panel selected two-dimensional and three-dimensional standard lifting-surface configurations (refs. 1 and 2) to provide a common basis for comparison of pressures and forces calculated by the emerging transonic unsteady aerodynamic codes in order to assess how well these methods model the essential flow physics. It is appropriate now to designate a similar set of configurations as "standard" for the comparison of transonic flutter characteristics and dynamic response (either forced or turbulence-excited) in order to assess how well these codes do the job for which they were intended, namely, predict aeroelastic behavior. In order to assess the suitability of configurations already tested and the associated data for designation as "standard", a survey of AGARD member countries has been conducted to seek candidates for the prospective set. The results of that survey were given in reference 3 and are summarized here along with the initial selection of a standard configuration.

The survey produced no particular surprises in terms of the unexpected abundance or deficiency of specific kinds of data and information. It was no surprise, for example, that suitable data do not appear to be available from the industry. The high-aspect-ratio transport-type wings that have been flutter tested generally had pylon-mounted nacelles attached and hence are not considered suitable for the initial set of standard configurations. Similarly, the low-aspect-ratio fighter-type models generally had stores attached. Clean-wing configurations have been tested for flutter clearance but were not often taken to hard flutter points in order to preserve the model for subsequent tests with a variety of store configurations.

● No particular surprises

● Suitable data not available from industry

    ● High-aspect-ratio wings have nacelles

   ● Low-aspect-ratio wings have stores

RESULTS

The examination and assessment of configurations and data sets suggested in the course of the survey have led to the delineation of seven configurations which appear to be suitable for use as AGARD standards. All of the configurations are isolated clean wings tested in slotted-throat tunnels. With the exception of the tunnel-spanning two-dimensional configuration, all were side-wall-mounted semispan models. No significant flow separation appears to have occurred during the tests, and the angles of attack, static deformations, and motions were small enough to minimize that concern. However, adequate experimental data sets presently exist for only three of these configurations.

● Seven configurations appear suitable for AGARD standards

   ● Four swept wings
   ● Two unswept wings
   ● One two-dimensional wing

●All were

   ● Isolated, clean wings
   ● Wall-mounted semispan models (except 2D)
   ● Tested in slotted-throat tunnels

●Adequated experimental data sets exist for only three of these
    configurations

The first configuration to be tentatively accepted as an AGARD standard
is designated "Wing 445.6". Wing 445.6 identifies the shape of a set of
sweptback, tapered research models which were flutter tested in both air and
Freon-12 gas in the 16 foot x 16 foot NASA Langley Transonic Dynamics Tunnel
(ref. 4). The first digit of this numerical designation is the aspect
ratio; the second and third digits indicate the quarter-chord sweep angle;
and the last digit is the taper ratio. These wings had NACA 65A004 airfoil
sections with no twist nor camber, and were tested at zero angle of attack
(fully symmetrical conditions). They were of solid homogeneous
construction. For testing, each wing was cantilever-mounted from the tunnel
wall with no simulated fuselage. The wing root was thus immersed in the
wall boundary layer. Since the model was cantilevered, however, little
motion occurred near the root so that portion of the wing contributed
very little to the generalized aerodynamic forces driving the flutter
motion. Consequently, the effect of wall boundary layer on measured
flutter characteristics should not be significant as long as the boundary-
layer thickness is a small fraction of the model span, as it was for these
tests.

——— First torsion mode

- - - - Second bending mode

—— —— Second torsion mode
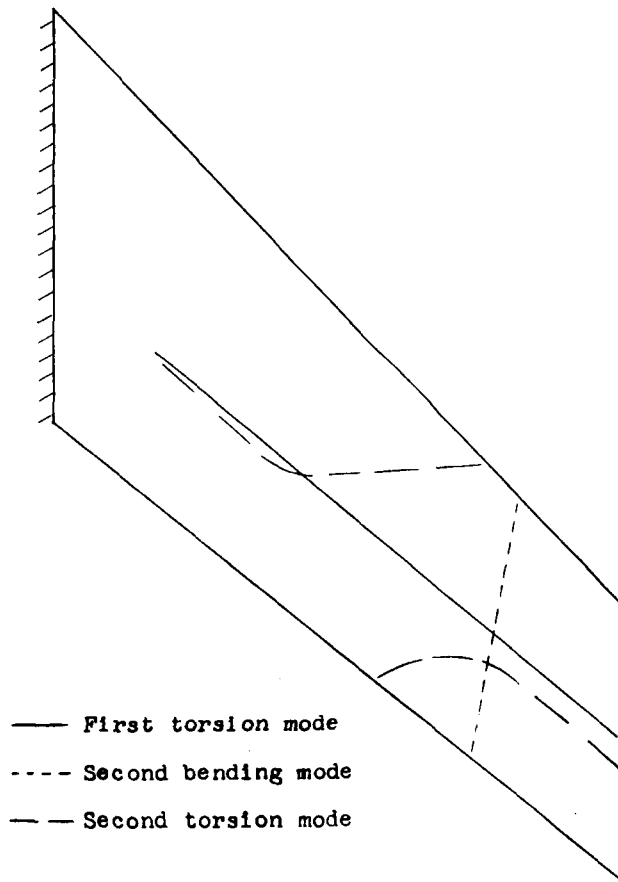
MASS RATIOS FOR WING 445.6

This configuration and associated data are recommended for several reasons. The tests in air and freon covered a very wide range of mass ratio (8.5 to 260 overall as shown here). At Mach number 1.0, mass-ratio values were about 12, 34, and 250, the last two values being for models of uniformly reduced stiffness.
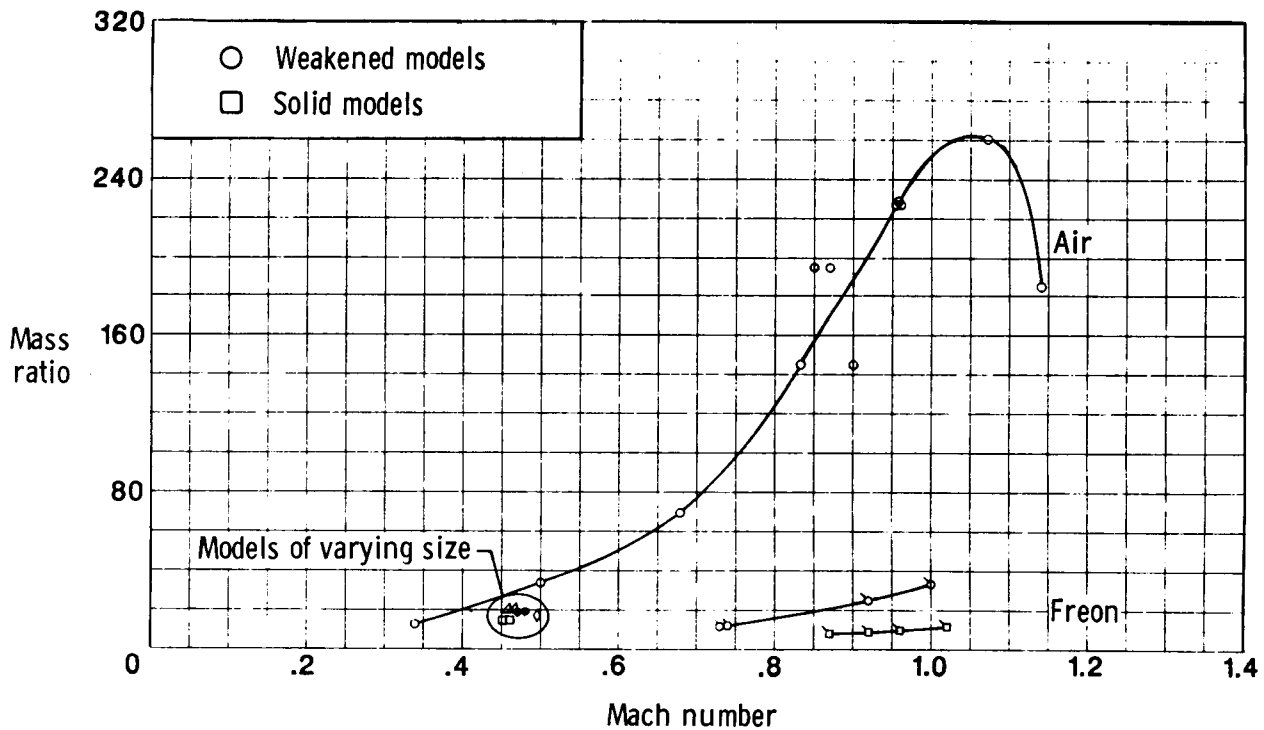
FLUTTER-SPEED INDEX FOR WING 445.6

The transonic dip is defined, including the supersonic side, and data extend also well into the subsonic range. Very good repeatability of data was shown. Flow over the wing was not complicated by the interference effect of a simulated fuselage. Moreover, since the model and flow were fully symmetrical, the flutter data are not complicated by the effects of static aeroelastic deformation. Finally, note that a limited amount of data was obtained with models of different sizes and with a sting-mounted full-span model, but only in the low subsonic range.
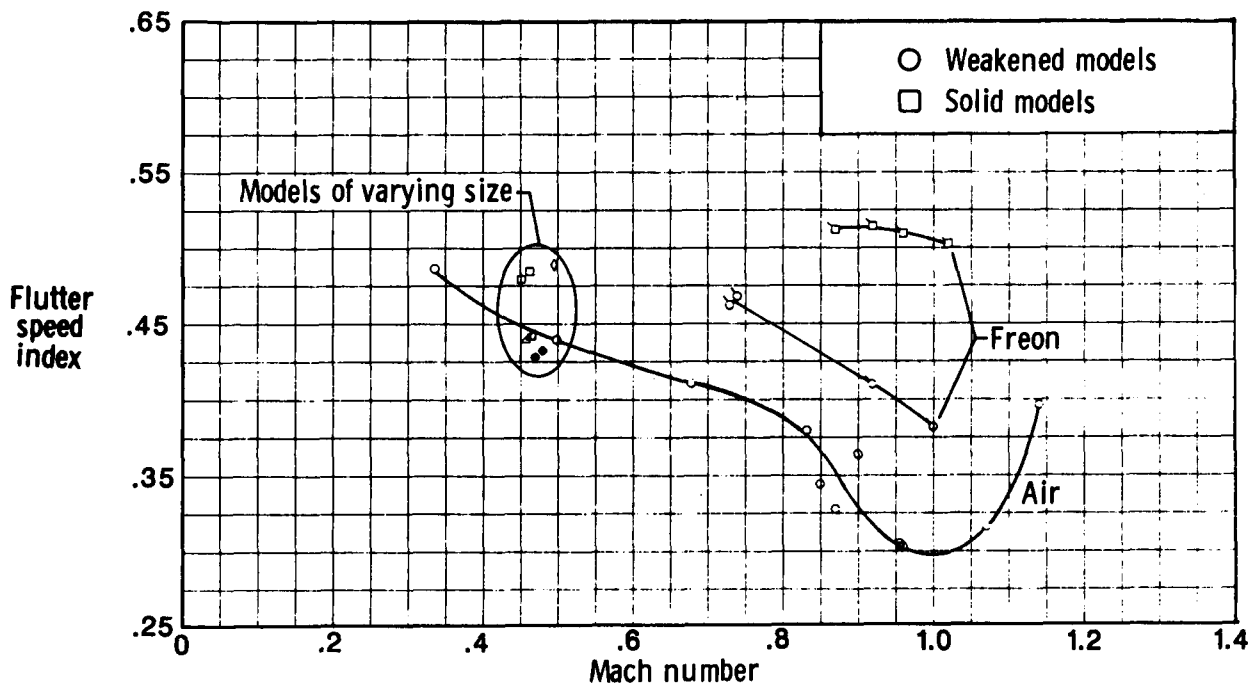
The features that make wing 445.6 attractive as a standard configuration are summarized in this figure.

Reasons recommended:

- No twist, camber, angle of attack - therefore, no static aeroelastic deformation
- Cantilever-mounted with no fuselage - therefore, no interference flow
- Tests covered large range of mass ratio
- Transonic dip fully defined
- Good repeatability of flutter data

Information not available:

- Mode shapes not measured, but have been calculated

The TF-8A wing and associated data sets constitute the most complex of the candidate configurations considered in reference 3. Two models of this wing were tested in air and in Freon-12 (refs. 5 and 6). The models were mounted on a half fuselage for testing and were as nearly identical as possible except one had a supercritical airfoil, and the other had a conventional airfoil. The data obtained in Freon for both wings for angles of attack near zero (ref. 5) show little scatter, extend well into the subsonic range, and include a well-defined transonic dip. Moreover, the flutter boundary for the wing with supercritical airfoil has been closely predicted by modified strip analysis (ref. 6). A limited amount of flutter data obained in air for the supercritical wing at angles of attack between $0°$ and $3°$ (ref. 7) shows a drastically detrimental effect of angle of attack, even at only one or two degrees. The unconventional shape of the flutter boundary for nonzero angle of attack has been shown by modified-strip-analysis calculations to be generated by large variations in mass ratio (refs. 7 and 8), although static aeroelastic deformation apparently has an influence as well.
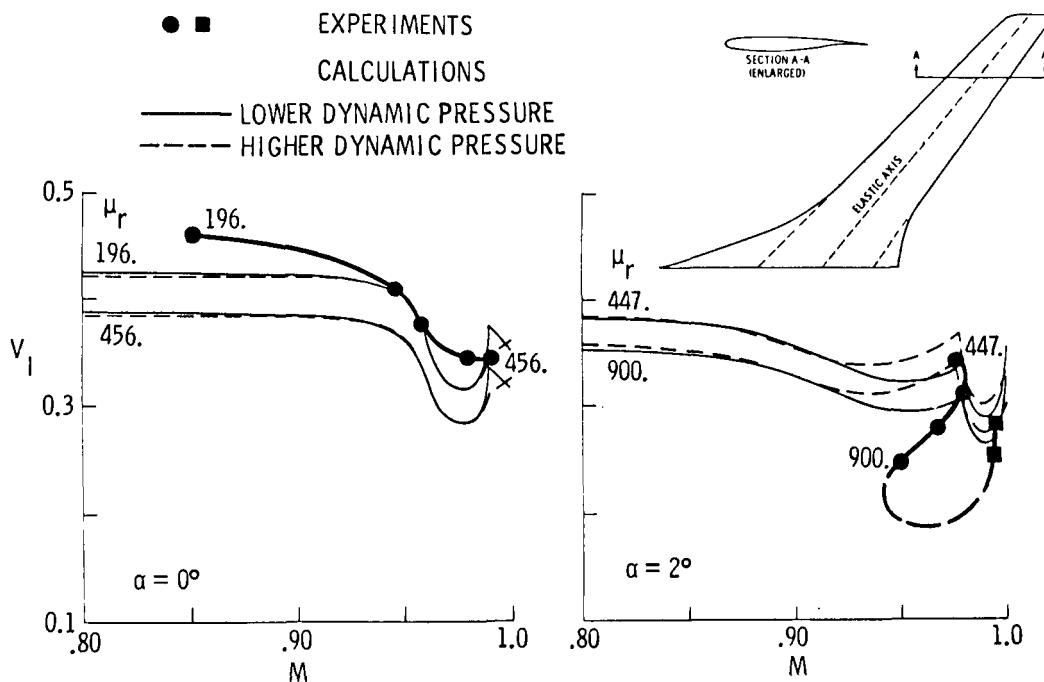
The features that make the TF-8A wing models attractive as standard configurations are súmmarized here. Note that calculation of flutter characteristics for these models should include also calculation of the aeroelastically deformed shape and associated static loading about which the flutter oscillation occurs (refs. 7 and 8).

Reasons recommended:

- Data for wings with conventional and supercritical airfoils
- Flutter boundary well defined, including transonic dip
- Tests covered large range of mass ratio
- Data include effects of nonzero angles of attack
- Shapes, frequencies, and generalized masses for six modes measured

The high-aspect-ratio supercritical transport-type wing shown here has been studied extensively at NLR Amsterdam (refs. 9 and 10). This research wing was tested in the presence of a simulated fuselage, but was attached at the root to an X-section flexure which added a pitch degree of freedom to the usual deformations of the wing itself. The flexure, in turn, was attached to a turntable in the tunnel wall which permitted changes in angle of attack. The torsional stiffness of the wing itself appears to be sufficiently high to avoid twisting deformations large enough to cause any significant amount of flow separation.
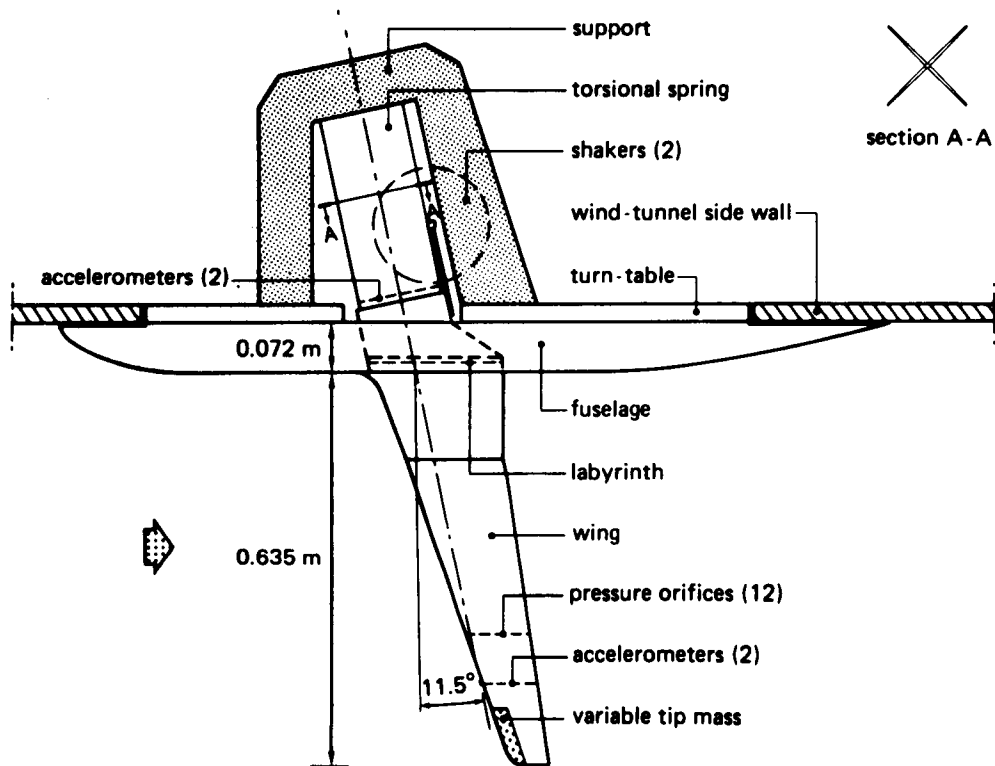
Global view of flutter model and support.

FLUTTER CHARACTERISTICS OF SUPERCRITICAL TRANSPORT WING

The flutter tests of this wing were performed with great care and precision. A considerable amount of subcritical-response data appears to have been taken during the approach to flutter conditions. The exceptionally large number of flutter points obtained show very little scatter and are sufficient to define with great accuracy the transonic flutter boundaries for nominal angles of attack of $-0.35°$, $0.85°$, and $2.05°$. It is particularly noted that the double transonic dip shown for $2.05°$ is remarkably like that calculated for the TF-8A wing at $2.00°$ (ref. 7). The flutter boundaries for the supercritical transport wing, however, do not show the backward turn which was found experimentally for the TF-8A wing at positive angles of attack.
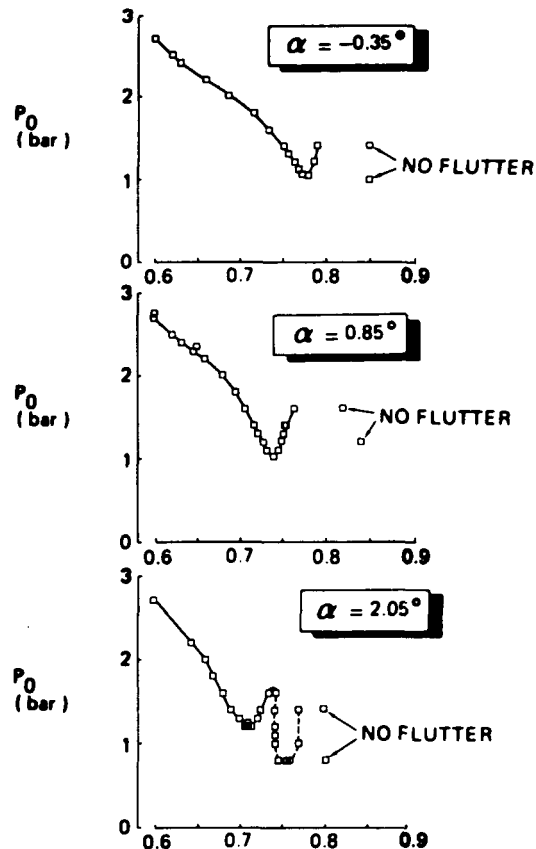
The features that make the supercritical transport wing attractive as a standard configuration are summarized here.

Reasons recommended:

- Flutter boundary very well defined, especially transonic dip

  Many flutter points, little scatter

- Subcritical-response data taken

- Data include effects of nonzero angles of attack

The assessment of available and needed data and information given here is based on a perception of requirements for the establishment of AGARD standard configurations, not on research needs. The two are, of course, closely related, however. Three rather obvious general comments are pertinent: First, high-Reynolds-number data are obviously needed for all types of configurations for closer simulation of aircraft flight conditions. These data are also needed for standard configuration/data sets. Second, data are needed for configurations which incorporate some degree of control-surface deflection in their modes of motion. In the absence of suitable control-surface data of this type, control-surface effects must be evaluated by comparisons of calculations with measured aerodynamic data (e.g., refs. 2 and 11). Third, in any subsequent tests of the recommended configurations or other prospective candidates, subcritical-response data should be recorded as flutter is approached. These data are needed to assess the accuracy and validity of calculated subcritical response (which may be amplitude-sensitive) as well as to provide information for the continuing assessment of methods for extrapolating to flutter points. Static aeroelastic deformation should also be measured, if at all possible.

Based on a perception of requirements for AGARD standard configurations, not on research needs

- High-Reynolds-number data are needed for all types of configurations

  - For closer simulation of aircraft flight conditions
  - For closer, more valid comparisons with calculations by

    - Inviscid-flow theories
    - Viscous/inviscid interaction methods
    - Navier-Stokes solutions

- Data are needed for configurations with control-surface deflections

  - For assessment of calculated contol-surface behavior and influence on flutter

  - For active-control studies

- In future tests subcritical-response data and static aeroelastic deformations should be recorded as flutter is approached

Moderate-to-High-Aspect-Ratio Wings.- The three configurations listed provide reasonably adequate representation of moderate-to-high-aspect-ratio wings at moderate Reynolds numbers. Some pecularities in the effect of angle of attack on the transonic dip for supercritical wings have been delineated; models still exist for further testing as needed.

Low-Aspect-Ratio Swept Wings.- The greatest current deficiency appears to exist for low-aspect-ratio (fighter-type) swept wings. As indicated previously, design-related testing of such models in clean-wing configuration has usually not been taken to hard flutter points. Flutter tests are needed for low-aspect-ratio highly-swept wings at zero to moderately high angles of attack. The free-vortex-dominated flow over such wings is known to increase structural loads and decrease flutter speeds relative to those for attached flows. Methods for calculating such flows at transonic speeds, steady and unsteady, are emerging, and experimental data are needed for validation.

Two-Dimensional Wings.- The survey did not reveal the existence of any transonic flutter data for two-dimensional wings. However, planned tests of the MBB-A3 supercritical airfoil at DFVLR Göttingen and at NASA Langley may provide the needed data sets.

- Moderate-to-high-aspect-ratio wings:

  - Wing 445. 6, TF-8A wing, supercritical transport wing provide reasonably adequate standards for

    - Moderate Reynolds numbers
    - Conventional and supercritical wings with and without twist and camber
    - Effects of zero and nonzero angles of attack
    - Subcritical response data exist

- Low-aspect-ratio swept wings:

  - Greatest deficiency in configurations and data indicated by survey
  - Flutter tests are needed for low-aspect-ratio highly swept wings at zero to moderately high angle of attack (free-vortex-dominated flow)

- Two-dimensional wings:

  - No transonic flutter data appear to exist
  - Imminent tests at DFVLR and NASA should fill need

SYMBOLS

M freestream Mach number

P_o freestream stagnation pressure

V_I flutter-speed index

α steady-state (or mean) angle of attack at wing root

μ_r mass ratio

REFERENCES

1. Bland, S. R.: AGARD Two-Dimensional Aeroelastic Configurations.
   AGARD-AR-156, 1979.

2. Bland, S. R.: AGARD Three-Dimensional Aeroelastic Configurations.
   AGARD-AR-167, 1982.

3. Yates, E. Carson, Jr.: Preliminary Report on Candidates for AGARD
   Standard Aeroelastic Configurations for Dynamic Response. Presented
   at the 61st Meeting of the AGARD Structures and Materials Panel,
   Oberammergau, Federal Republic of Germany, September 9-13, 1985.
   Available as NASA TM-89142, 1987.

4. Yates, E. Carson, Jr.; Land, Norman S.; and Foughner, Jerome T.,Jr.:
   Measured and Calculated Subsonic and Transonic Flutter Characteristics
   of a 45° Sweptback Wing Planform in Air and Freon-12 in the Langley
   Transonic Dynamics Tunnel. NASA TN D-1616, 1963.

5. Farmer, Moses G.; Hanson, Perry W.; and Wynne, Eleanor C.: Comparison
   of Supercritical and Conventional Wing Flutter Characteristics.
   NASA TM-72837, 1976.

6. Yates, E. Carson, Jr,; Wynne, Eleanor C.; Farmer, Moses G.; and
   Desmarais, Robert N.: Prediction of Transonic Flutter of a
   Supercritical Wing by Modified Strip Analysis. Journal of Aircraft,
   Vol. 19, No. 11, November 1982, pp. 999-1004.

7. Yates, E. Carson, Jr.; Wynne, Eleanor C.; and Farmer, Moses G.:
   Effects of Angle of Attack on Transonic Flutter of a Supercritical
   Wing. Journal of Aircraft, Vol. 20, No. 10, Oct. 1983, pp. 841-847.

8. Yates, E. Carson, Jr.; and Chu, Li-Chuan: Static Aeroelastic Effects on
   the Flutter of a Supercritical Wing. In "Static Aeroelastic Effects
   on High Performance Aircraft." AGARD CP-403, 1986. Available also as
   NASA TM-89132, 1987.

9. Houwink, R.; Kraan, A. N.; and Zwaan, R. J.: Wind-Tunnel Study of the
   Flutter Characteristics of a Supercritical Wing. Journal of Aircraft,
   Vol. 19, No. 5, May 1982, pp. 400-405.

10. Persoon, A. J.; Horsten, J. J.; and Meijer, J. J.: Measurement of
    Transonic Dips in the Flutter Boundaries of a Supercritical Wing in
    a Wind Tunnel. Journal of Aircraft, Vol. 21, No. 11, November 1984,
    pp. 906-912.

11. Anon: Compendium of Unsteady Aerodynamic Measurements. AGARD Report
    No. 702, 1982.

Report Documentation Page

1. Report No.	2. Government Accession No.	3. Recipient's Catalog No.
NASA CP-3022, Part 1		

4. Title and Subtitle	5. Report Date
Transonic Unsteady Aerodynamics and Aeroelasticity — 1987	February 1989
	6. Performing Organization Code

7. Author(s)	8. Performing Organization Report No.
Samuel R. Bland, Compiler	L-16532
	10. Work Unit No.
	505-63-21-01

9. Performing Organization Name and Address	11. Contract or Grant No.
NASA Langley Research Center Hampton, VA 23665-5225	
	13. Type of Report and Period Covered

12. Sponsoring Agency Name and Address	Conference Publication
National Aeronautics and Space Administration Washington, DC 20546-0001	14. Sponsoring Agency Code

15. Supplementary Notes

16. Abstract

This two-part document contains copies of the text and figures for the papers presented at the Symposium on Transonic Unsteady Aerodynamics and Aeroelasticity — 1987, held at the NASA Langley Research Center on May 20-22, 1987.

The papers are grouped in five subject areas as follows:

(1) Transonic small disturbance theory for complete aircraft configurations
(2) Full potential and Euler equation methods
(3) Methods for vortex and viscous flows
(4) Aeroelastic applications
(5) Experimental results and cascade flows

17. Key Words (Suggested by Author(s))	18. Distribution Statement
Unsteady aerodynamics Transonic aerodynamics Aeroelasticity	Unclassified - Unlimited Subject Category 02

19. Security Classif. (of this report)	20. Security Classif. (of this page)	21. No. of pages	22. Price
Unclassified	Unclassified	267	A12